

5-AMINOLEVULINIC-INDUCED PROTOPORPHYRIN IX FLUORESCENCE AS
AN INTRAOPERATIVE BIOMARKER FOR BRAIN TUMORS: DETECTION
METHODS AND BIOLOGICAL CORRELATES

A Thesis

Submitted to the Faculty

in partial fulfillment of the requirements for the

degree of

Doctor of Philosophy

by

PABLO ANDRES VALDES QUEVEDO

Thayer School of Engineering

Dartmouth College

Hanover, New Hampshire

June 2011

Examining Committee:

Co-Chairman _____
Keith D. Paulsen
Co-Chairman _____
David W. Roberts
Member _____
Brent T. Harris
Member _____
Frederic Leblond
Member _____
Brian W. Pogue
Member _____
Jeffrey N. Bruce

Brian W. Pogue
Dean of Graduate Studies

Abstract

Brain tumors account for ~2% of all cancers, with gliomas accounting for ~70% of all brain tumors. Evidence suggests that extent of resection provides both a quality of life and survival benefit to patients. Recent work has shown the utility of using 5-aminolevulinic acid (ALA)-induced protoporphyrin IX (PpIX) fluorescence-guided resection (FGR) for increased tumor removal. Briefly, the patient is given a dose of ALA prior to surgery, which leads to overproduction of PpIX in tumor, and provides fluorescence contrast to distinguish normal from tumor intraoperatively.

Although ALA-induced PpIX FGR has shown promise in high-grade gliomas, current studies show a limited sensitivity of PpIX for accurate detection, even in high-grade gliomas. Furthermore, the literature suggests that PpIX is not an accurate biomarker for other tumor histologies, specifically, low-grade gliomas. Current limitations in detection technologies, lack of systematic study of the targeting capabilities of PpIX, and lack of understanding of the biological basis for PpIX, makes further study of ALA-induced PpIX for FGR in neurosurgery a topic of clinical relevance.

Here we present work investigating both the targeting potential of PpIX in brain tumors and an exploration into important biological correlates of PpIX accumulation. First, we elucidate on the significant tumor detection limitations using the state-of-the-art in clinical PpIX fluorescence imaging. We elaborate on the utility of performing quantitative FGR, demonstrating the broad targeting potential of PpIX beyond high-grade gliomas, and develop a combined approach to FGR using additional optical cancer biomarkers for improved detection.

We then provide a systematic analysis on the biological correlates of PpIX

accumulation in tissue. We examined gliomas using gene expression analysis and histopathological techniques, to elucidate a correlation between tumor aggressiveness, e.g., increased proliferation, angiogenesis, migration, and PpIX accumulation. This provides a stronger biological rationale for use of PpIX as a broad targeting agent in FGR, further informing resection decisions.

The work presented in this thesis provides a rationale for *quantitative* fluorescence guided resection, showing the broad targeting potential of PpIX across a range of tumor histologies, the targeting potential of PpIX for distinguishing degree of anaplasticity, and important biological correlates of this fluorescence guidance mechanism.

Acknowledgements

I have been extremely blessed with two wonderful advisors, Dr. David. W. Roberts and Dr. Keith D. Paulsen; both have made my experience as a Ph.D. student at Dartmouth a most rewarding time for intellectual pursuits, intra- and inter-personal growth, and increased passion for biomedical research.

I am extremely grateful to Dr. Roberts, who has exemplified the model of a neurosurgeon physician-scientist, balancing his family life, academic, administrative, and clinical duties, meanwhile maintaining a very fruitful research enterprise with long-standing relationships with researchers at Thayer Engineering. With the long-term goals of becoming a neurosurgeon physician-scientist myself, I could not have asked for a better mentor and role model.

I am extremely grateful to Dr. Paulsen for taking me under his wing as a Thayer Ph.D. student, always with a door open, and more importantly, always encouraging and promoting new ideas. Keith exemplifies the key characteristics for a successful, modern-era researcher - always asking questions, always strengthening professional relationships, and always pushing the boundaries of research. His spirit of innovation and collaboration is something I wish to exemplify in my own career.

I would like to thank Dr. Brent T. Harris, with whom I worked through a research project in his lab during medical school, and now through my Ph.D. at Thayer. I have approached Brent many times asking for insight on lab, academics as well as personal and professional relationships. Most importantly, Brent always has had time to talk and provide support, whether for technical or professional questions, or just to hear the musings of an eager, young investigator.

I would like to thank Dr. Leblond, who is always eager to discuss current and future research ideas. Fred brings a spirit of inspiration and energy to our research enterprise that can only help to make our work successful. I would also like to thank Dr. Pogue,

who has always been available for questions about my work as well as academics. Brian's willingness and ability to listen and help students has positively impacted my time at Thayer.

I would also like to thank our collaborators at the University of Toronto, Brian Wilson and Anthony Kim. The collaborative enterprise between Dartmouth and Toronto has been very fruitful. Working with Tony and Brian has been very rewarding, and I look forward to continued collaboration with them in the days to come.

I am very grateful to all my friends and colleagues. Valerie has provided invaluable support and always probing conversations on both the professional and personal levels, and for that I am forever thankful. My friends in South Street have provided a most needed outlet, for which I am very grateful. I would also like to thank all my other friends at Thayer and the Medical School as well as colleagues in Neurosurgery, which have been invaluable during these years at Thayer, providing support, encouragement, and/or diversion from work.

Last, but of course, not least, I would like to thank my family – mother, father, brother, and sister. I would like to extend my most genuine and heartfelt sense of gratitude to my mother, Xinia Quevedo de Valdes and my father, Oscar Valdes. It is because of them and their never-ending support, love, encouragement, and belief that I can do whatever I put my mind to, which has made this thesis possible. It is because of the love and support my mom and dad have given me, coupled with their life-long lessons on work ethic, relationships, and respect, that I have been able to reach this point in my life.

Dedication

To my mom, Xinia Quevedo de Valdes, and my dad, Oscar Valdes

Table of Contents

Abstract.....	ii
Acknowledgments	iv
Dedication.....	vi
Table of Contents.....	vii
List of Tables	x
List of Figures.....	xii
List of Acronyms	xiv
1. <u>CHAPTER 1. INTRODUCTION</u>	1
1.1 Project Rationale.....	1
1.2 Background.....	1
1.2.1 Introduction.....	1
1.2.2 Factors to consider in intraoperative and in vivo fluorescence detection.....	7
1.2.3 Contrast mechanisms for intraoperative in vivo fluorescence detection	26
1.2.4 Fluorescence detection technologies in the operating room.....	34
1.2.5 Intraoperative neurosurgical applications of fluorescence technologies	41
1.3 Summary	47
1.4 Thesis Organization	47
2. <u>CHAPTER 2. FLUORESCENCE-GUIDED RESECTION OF MALIGNANT GLIOMA: RELATIONSHIPS BETWEEN ALA-INDUCED PPIX FLUORESCENCE, MR IMAGING FEATURES, AND NEUROPATHOLOGICAL PARAMETERS</u>	53
2.1 Introduction.....	53
2.2 Methods	54
2.2.1 Patient Selection	54
2.2.2 Surgical Procedure.....	56
2.2.3 Neuropathology	59
2.2.4 Data Analysis and Image Processing.....	60
2.3 Results.....	62
2.3.1 Association Between Intraoperative Fluorescence and MR Image Features.....	63
2.3.2 Association Between Intraoperative Fluorescence and Neuropathology	64
2.4 Discussion.....	68
2.5 Conclusions.....	73
3. <u>CHAPTER 3. INTRAOPERATIVE ALA-INDUCED PPIX FLUORESCENCE OF GLIOMAS USING PRE-OPERATIVE AND MODEL-DEFORMED MR IMAGING</u>	75
3.1 Introduction.....	76
3.2 Methods	76
3.2.1 Patients.....	76
3.2.2 Coregistered Fluorescence-Guided Resection Procedure.....	76
3.2.3 Intraoperative Brain Deformation Procedure	77
3.2.4 Tissue Processing and Analysis.....	78
3.2.5 Deformation Model.....	78
3.2.6 Data Analysis	84

3.3 Results.....	84
3.4 Discussion.....	89
3.5 Conclusions.....	94
4. <u>CHAPTER 4. PRE-CLINICAL PHARMACOLOGICAL TREATMENT FOR ENHANCEMENT OF ALA-INDUCED PpIX FLUORESCENCE IN MURINE MODEL OF GLIOMA.....</u>	95
4.1 Introduction.....	95
4.2 Methods	97
4.2.1 Cell Culture.....	97
4.2.2 Animal Model.....	98
4.2.3 Chelation Therapy and PpIX Fluorescence Quantification	98
4.2.4 Image Analysis	99
4.3 Results.....	100
4.4 Discussion.....	103
4.5 Conclusions.....	105
5. <u>CHAPTER 5. DIAGNOSTIC CAPABILITIES OF A QUANTITATIVE APPROACH FOR ALA-INDUCED PpIX FLUORESCENCE-GUIDED RESECTION OF INTRACRANIAL TUMORS.....</u>	107
5.1 Introduction.....	107
5.2 Methods	108
5.2.1 Patient Selection	108
5.2.2 Intraoperative Probe.....	108
5.2.3 Surgical Procedure.....	111
5.2.4 Histopathology.....	113
5.2.5 Data Processing.....	113
5.2.6 Statistical Analysis	114
5.3 Results.....	114
5.4 Discussion.....	122
5.5 Conclusions.....	124
6. <u>CHAPTER 6. QUANTITATIVE MULTIPLE BIOMARKER OPTICAL APPROACH FOR INTRAOPERATIVE GUIDANCE IN FLUORESCENCE-GUIDED RESECTION OF GLIOMAS.....</u>	126
6.1 Introduction.....	126
6.2 Methods	128
6.2.1 Patient Selection	128
6.2.2 Surgical Procedure.....	128
6.2.3 <i>In Vivo</i> Optical Probe Measurements and Quantification	130
6.2.4 Neuropathological Assessment.....	135
6.2.5 <i>In Vivo</i> Optical Data Analysis	135
6.2.6 Diagnostic Algorithm	140
6.3 Results.....	144
6.3.1 Neuropathology	144
6.3.2 <i>In Vivo</i> Optical Data	144
6.3.3 Diagnostic Algorithm Classification	151
6.4 Discussion.....	153
6.4.1 Optical Strategies for Brain Tumor Surgery.....	153
6.4.2 Summary of Raw Optical Data.....	155
6.4.3 Summary of Model-derived Optical Spectra	156

6.4.4 Summary of Optical Biomarkers	158
6.4.4 Summary of Diagnostic Algorithm.....	161
6.5 Conclusions.....	163
7. <u>CHAPTER 7. GENE EXPRESSION PROFILE CHANGES IN ALA-INDUCED PpIX IN VISIBLY FLUORESCENT TISSUE COMPARED TO NON-VISIBLY FLUORESCENT TISSUE</u>	165
7.1 Introduction.....	165
7.2 Methods	166
7.2.1 Patients and Samples	166
7.2.2 RNA Isolation and Gene Expression Microarray Analysis	167
7.2.3 Histopathology and <i>Ex vivo</i> PpIX Quantification.....	168
7.3 Results.....	170
7.3.1 Neuropathology and <i>Ex Vivo</i> PpIX Quantification.....	170
7.3.2 Gene Expression Profile of PpIX Fluorescent GBM Samples	180
7.4 Discussion.....	190
7.5 Conclusions.....	193
8. <u>CHAPTER 8. ALA-INDUCED PpIX CONCENTRATION CORRELATES WITH TISSUE HISTOPATHOLOGICAL MEASURES OF MALIGNANCY</u>	195
8.1 Introduction.....	195
8.2 Methods	195
8.2.1 Specimen Acquisition	197
8.2.2 Histopathology.....	199
8.2.3 Immunohistochemistry	200
8.2.4 Ex Vivo PpIX Fluorimetry	201
8.2.5 Statistical Analysis.....	203
8.3 Results.....	204
8.3.1 Patient and Data Characteristics	204
8.3.2 Association Between Intraoperative Visible Fluorescence, C_{PpIX} , and PI...206	
8.3.3 Correlation Between Intraoperative Visible Fluorescence, C_{PpIX} , and PI ...208	
8.3.4 Correlation Between C_{PpIX} , and Quantitative Histopathological Parameters of Malignancy	209
8.4 Discussion.....	209
8.5 Conclusions.....	216
9. <u>CHAPTER 9. CONCLUSIONS AND FUTURE DIRECTIONS</u>	217
9.1 Conclusions.....	217
9.2 Future Directions	231
<u>Appendices</u>	234
Automated 3D rigid and non-rigid image registration graphical user interface	234
<u>References</u>	240

List of Tables

Table 2.1: Summary of characteristics of the 11 patients with a newly diagnosed GBM.	56
Table 2.2: Statistical measures for summarizing the predictive relationship for protoporphyrin fluorescence tissue histopathology	65
Table 2.3: Two-way tables of association	67
Table 3.1: Overview of fluorescence-guided resection using PpIX and brain shift for the whole-brain.....	86
Table 3.2: Statistical measures.....	86
Table 3.3: Technologies for intraoperative updating during brain surgery.....	92
Table 4.1: Mean PpIX fluorescence coefficient of variation and GFP and PpIX fluorescence contrast.....	102
Table 5.1: Diagnostic variables.....	118
Table 5.2: ROC analysis for C_{ppIX} as a diagnostic variable.....	119
Table 6.1: Receiver operating characteristic (ROC) analysis of three diagnostic tests.....	152
Table 6.2: Summary of ROC analysis of diagnostic algorithm.....	152
Table 7.1: Samples for gene expression microarray analysis	170
Table 7.2: List of gene expression profile changes in PpIX fluorescence guided resection.....	171
Table 7.3: List of over-expressed genes in PpIX fluorescent tissue.....	174
Table 7.4: List of under-expressed genes in PpIX fluorescent tissue.....	181
Table 7.5: Gene expression changes of genes associated with cellular proliferation.....	182
Table 7.6: Gene expression changes of genes associated with immune response.....	185

Table 7.7: Gene expression changes of genes associated with cellular locomotion.....	186
Table 7.8: Gene expression changes of genes associated with cell death.....	187
Table 7.9: Gene expression changes of genes associated with ECM interactions.....	188
Table 7.10: Gene expression changes of genes associated with angiogenesis.....	189
Table 8.1: Summary of patient characteristics.....	197

List of Figures

Figure 1.1: Surgical applications of fluorescence detection in the operating room.....	7
Figure 2.1: Images of a right parietal lesion in patient 3.....	56
Figure 2.2: Diagrams of the 95% confidence intervals of the mean of MR image measures.....	63
Figure 2.3: Percentage bar graphs of fluorescence and neuropathological parameters....	68
Figure 3.1: Cross-sectional images of intraoperative 3D US from patient 1.....	81
Figure 3.2: Schema of brain deformation model.....	83
Figure 3.3: Pre-operative, updated, and intraoperative images of patient 1.....	85
Figure 3.4: Test results for biopsy specimens.....	88
Figure 3.5: Gadolinium-enhanced pre-operative and post-operative T1-weighted MR images.....	89
Figure 4.1: U251-GFP coronal brain sections.....	101
Figure 4.2: Chelation treatment effects are shown with a box and whisker diagram of PpIX fluorescence contrast in tumor tissue for both control and DFO treatment groups.....	103
Figure 5.1: In vivo spectroscopic measurements of ALA-induced PpIX fluorescence during intracranial tumor resection surgeries.....	115
Figure 5.2: Concentration of ALA-induced PpIX, C_{PpIX}	117
Figure 5.3: ROC analysis of intraoperative detection of ALA-induced PpIX.....	120
Figure 6.1: Conceptual map.....	138
Figure 6.2: SVM algorithm.....	139

Figure 6.3: Raw reflectance and fluorescence spectra.....	146
Figure 6.4: Model-derived optical spectra.....	148
Figure 6.5: Model-derived optical biomarkers.....	150
Figure 7.1: Gene expression profile changes in ALA-induced PpIX GBM tissue.....	184
Figure 8.1: Illustrative examples of PpIX fluorescence characteristics and proliferative potential of low- and high-grade gliomas.....	202
Figure 8.2: Intraoperative visible fluorescence, PpIX concentrations, and proliferation index.....	205
Figure 8.3: PpIX concentration and quantitative histopathological parameters of malignancy.....	208
Figure Appendix A1: Registration Selection.....	235
Figure Appendix A2: Directory Selection.....	236
Figure Appendix A3: Fixed and Moving Stack Selection.....	237
Figure Appendix A4: Registration Type and Image Visualization.....	238
Figure Appendix A5: Registration Parameters.....	239

Fluorescence-guided Resection	FGR
5-Aminolevlunic acid	ALA
Protoporphyrin IX	PPIX
Glioblastoma multiforme	GBM
Low-grade glioma	LGG
High-grade glioma	HGG
Recurrent glioma	RCG
Meningioma	MEN
Metastasis	MET
Receiver operating characteristic	ROC
Area under the curve	AUC
Positive predictive value	PPV
Negative predictive value	NPV
Support vector machine	SVM
Optimal cutting temperature	OCT
Green fluorescent protein	GFP
Deferoxamine	DFO
Region of interest	ROI
World Health Organization	WHO
Nicotinamide adenine dinucleotide	NADH
Flavin adenine dinucleotide	FAD
Extracellular matrix	ECM

Chapter 1. Introduction and Overview

1. 1 Project Rationale

The main objective of this thesis is to explore the role of 5-aminolevulinic acid (ALA)-induced protoporphyrin IX (PpIX) as an intraoperative fluorescent biomarker for neurosurgical resection of brain tumors. Specifically, this thesis will explore two main aspects of ALA-induced PpIX in fluorescence-guided surgery to subsequently inform the neurosurgical community on the detection capabilities and biological correlates of ALA-induced PpIX in brain tumors.

The rationale for this thesis is to systematically elaborate on and address the following: 1) the extent of and limitations to ALA-induced PpIX fluorescence based detection in brain tumors; and 2) the biological basis of PpIX as an intraoperative biomarker for brain tumors that would inform detection technologies. Overall, the goal of this thesis is to provide a biologically and technologically informed approach in ALA-induced PpIX fluorescence guidance as an adjuvant for improved resection of brain tumors.

1.2 Background

1.2.1 Introduction

In neurosurgical resection of brain tumors, the goal of treatment is to maximize extent of tumor resection meanwhile minimizing surgical insult to normal, viable brain tissue. Initial reports measuring extent of resection and its effect on patient survival showed a benefit in patient survival with maximization of tumor removal. With the advent of

advanced imaging technologies and more systematic clinical studies that investigated the relationship between extent of tumor resection and survival benefit, opinion became split regarding the actual survival benefit of maximal tumor resection. Nevertheless, evidence suggests that maximizing extent of resection provides not just a quality of life benefit to the patient, but also a significant survival advantage⁹⁻¹⁵. A recent, randomized phase III multicenter trial using fluorescence-guided resection (FGR) for brain tumors showed a significant 6-month progression free survival as well as an overall survival benefit for patients undergoing complete resection compared to incomplete resection of contrast-enhancing tumor on T1-weighted MR¹²⁻¹⁴. This study provided level 2b evidence that maximizing extent of tumor resection provides a significant survival advantage to patients. Furthermore, not only does maximizing extent of tumor resection provide a significant survival advantage, but it also provides a quality of life advantage to the patient. Thus, the goal of the neurosurgeon is to maximize resection of tumor meanwhile sparing normal functioning brain tissue.

Conventional neurosurgical technologies for tumor resection involve the use of 3-dimensional, image-guidance systems that provide intraoperative guidance to the neurosurgeon¹⁶. These systems use pre-operative MR or CT images, and by means of specialized tracking technologies (e.g., optical or magnetic-based), are able to relate the location of surgical tools tracked intraoperatively to pre-operative images. As the surgeon operates, he is able to use cross-sectional MR images (i.e., sagittal, coronal, axial) displayed intraoperatively and relate his current position in the operating room to the radiological information provided by MR. That is, these systems function as an intraoperative GPS system guiding the surgeon throughout the patient's anatomy. One

major limitation with current image-guidance systems is their inability to account for intraoperative brain shift and deformation as a result of CSF drainage, brain movement due to gravity, and removal of brain tissue¹⁶⁻²¹. As such, the accuracy of image-guidance degrades as surgery progresses, leading the surgeon to rely less on pre-operative imaging information to help him navigate the surgical cavity (i.e., navigation accuracy degrades).

Numerous efforts have gone into addressing this navigational loss of accuracy that plagues conventional image-guidance systems. One major effort involves use of intraoperative imaging (e.g., intraoperative MR, CT or US) to provide updated images of the current surgical field to the image-guidance systems^{1-8,22}. For example, an intraoperative MR sequence will be acquired halfway through surgery, and these images will then be loaded onto the image-guidance system. In this way the surgeon has an updated view of the surgical field that more accurately represents the patient anatomy. In addition to intraoperative imaging, biomechanical models to update pre-operative images have also been developed. In these cases, data acquired intraoperatively drive a biomechanical model that updates or “warps” pre-operative images, providing the surgeon with updated images for navigation^{17,18,20,21,23,24}.

Both efforts, intraoperative imaging and biomechanical models, provide the surgeon a new set of images with an updated view of the surgical field. Nevertheless they are both prone to certain limitations and challenges. The use of intraoperative imaging, depending on the modality used, presents various challenges including: significant interruption of surgical flow, specialized equipment and/or personnel, limitations in patient positioning, no real-time feedback, and significant prolongation of surgical time. Further, biomechanical models also face limitations such as: no real-time feedback, need for

intraoperative data, computational time costs, and assumption of the accuracy of the modeling results. As a result of the limitations presented by current image guidance systems and current efforts to compensate for loss of navigational accuracy, there still remains a need for technologies that will provide optimal neurosurgical guidance.

One development in neurosurgical guidance that provides real-time intraoperative information without loss of accuracy due to brain deformation is fluorescence-guidance¹²⁻

^{15,24-44}.

Fluorescence-guidance uses fluorescent properties in tissue, both exogenous and endogenous, to increase contrast and better distinguish between normal and abnormal tissues. Used as an adjunct to existing surgical methodologies, fluorescence-guidance can provide more specific information in real-time and at a relatively low cost and with minimal disruption to surgical workflow. Fluorescence-guided surgery has seen great advances in the development of instrumentation for detection of tissue fluorescence (e.g., surgical microscopes modified for fluorescence imaging, point spectroscopy, intra-operative confocal microscopy). In addition, fluorescence-guidance has been a catalyst for the growing field of targeted-fluorophore development and validation⁴⁵. Fluorescence methodologies used in the operating room combine the expertise of numerous individuals, including but not limited to, expertise in instrumentation, light transport physics and modeling, fluorophore synthesis and bio-conjugation, pre-clinical validation using animal models, biostatistics, surgical and clinical needs, and bench-to-bedside translation of new technologies. The promising surgical benefits and interplay of technical expertise makes the development of fluorescence methodologies for *in vivo* and intra-operative applications an important clinical and research challenge.

To date, the most widely used form of fluorescence-guidance for brain tumor resection in neurosurgery uses the prodrug, ALA^{13-15,24,26,33,38-41}. Patients are administered an oral dose of ALA prior to surgery. Tumor tissue takes up ALA leading to a selective and specific accumulation of the fluorescent molecule, PpIX, in neoplastic tissue^{40,46-48}. The surgeon is then able to use the fluorescent properties of PpIX by exciting this fluorophore with blue light, and visualizing the red fluorescent emissions^{39,40}. Since PpIX accumulation displays selectivity to tumors, the surgeon can use this red fluorescence to identify tumor tissue, whereas tissue that has not significantly accumulated PpIX (e.g., normal brain) will not display significant red fluorescence.

A major advantage of this technology is that it provides the neurosurgeon with intraoperative, real-time information regarding the location of tumor tissue within the surgical field. Fluorescence-guidance delineates tumor margins with real-time spatial accuracy, unlike image-guidance systems in which navigational accuracy degrades as surgery progresses. In this way fluorescence-guidance is not plagued by intraoperative brain deformation. This technology provides the neurosurgeon with a practical surgical tool with which he can seamlessly switch from conventional white light resection mode to blue light, fluorescent mode. In current implementations, all that is required is a simple oral dose administration of a well-tolerated peptide drug and a conventional surgical microscope modified for fluorescence imaging. The surgeon can then navigate through the surgical field as usual, and when necessary use fluorescence-guidance to aid the resection.

FGR of brain tumors is an exciting technology with many appealing advantages, but it also faces limitations that need to be properly dealt with so the neurosurgeon will have

an optimal guidance technology. For example, preliminary data suggest that ALA-induced PpIX FGR is limited in both its ability to provide fluorescence detection of some tumor types and tissues as well as displaying low negative predictive values (<30%) and sensitivities with current modified surgical microscopes for GBMs (e.g., low-grade gliomas)^{24,38,44,49}. Further, drug side effects (e.g., possible increase in liver function tests, phototoxicity) and contraindications can make a patient an unacceptable candidate for the procedure. To summarize, some disadvantages of ALA-PpIX FGR are: surface fluorescence detection only with no volumetric fluorescence information, drug contraindications and side effects, sensitivity of current fluorescence-detection technologies and limitation in the range of detectable tumor types and tissues.

Given this general overview of the need for maximizing tumor resection and ALA-induced PpIX FGR of brain tumor, we will now elaborate on the basic principles and factors to take into consideration in surgical fluorescence methodologies. We will discuss the major fluorophore contrast mechanisms in clinical use, both exogenous (e.g., 5-aminolevulinic acid-induced protoporphyrin IX (ALA-induced PpIX), indocyanine green (ICG)) and endogenous (e.g., nicotinamide adenine dinucleotide, flavins, amino acids). Further, we elaborate on current instrumentation approaches used in the clinical setting (e.g., surgical microscopes modified for fluorescence imaging, point spectroscopy) and their basic instrumentation setup (Fig. (1.1)). At the end, we provide an overview of fluorescence methodologies in neurosurgery. This introductory section will provide a thorough and necessary overview of work and issues to consider to place the rest of the work presented in this thesis in the appropriate context.

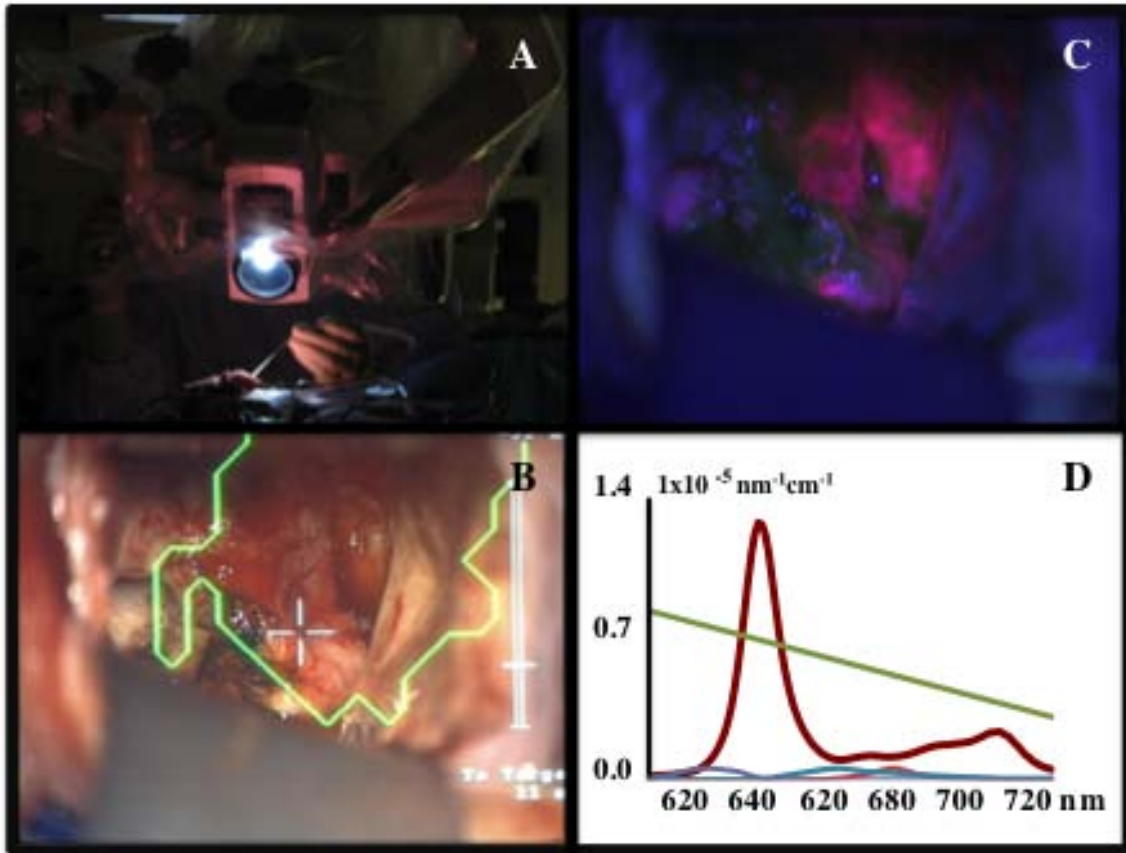


Figure 1.1. Surgical applications of fluorescence detection in the operating room. A) Conventional surgical microscope during a brain tumor resection procedure with corresponding. B) Corresponding bright field image and C) ALA-induced PpIX fluorescence image of the surgical field. D) Spectral data acquired using an intraoperative point spectroscopy fiber-optics probe. A typical PpIX (red), autofluorescence (green), and PpIX photoproducts (blue, purple and orange lines) spectrum are shown (x-axis: emission wavelength, y-axis: fluorescence intensity).

1.2.2 Factors to Consider in Intraoperative and In Vivo Fluorescence Detection

The clinical utility of fluorescence detection for intra-operative localization and surgical guidance relies on the premise that tissue fluorescence provides sufficient and accurate (i.e., sensitive and specific enough) contrast to distinguish between tissues⁵⁰⁻⁵⁵. As such, achieving sufficient and accurate contrast is the primary goal of fluorescence methodologies for intra-operative applications. To achieve this goal, the following four major factors need to be taken into account when considering fluorescence detection for a particular application of interest: the physical properties of the contrast agent, the biological nature and origin of tissue contrast, the interaction of light with tissue and the available light illumination and detection instrumentation. Each of these factors is discussed in this section.

1.2.2.1 Physical properties of fluorescent molecules

Luminescence is an optical phenomenon that consists of light emission from a molecule in an excited state, with two forms being phosphorescence and fluorescence. Phosphorescence occurs when the transition to the ground state (i.e., non-excited state) is forbidden, meanwhile fluorescence occurs in cases where the transition is quantum mechanically allowed. As a result, the main difference between fluorescence and phosphorescence is the average decay time of the excited molecules, which occurs on a smaller scale for fluorescence. In fact, average fluorescence lifetimes are typically of the order of ps to ns, while average decay times for phosphorescence processes are usually between 1ms and 1000ms⁵⁶.

Fluorescent molecules are characterized by excitation and emission spectra. The excitation spectrum of a molecule is a measure of its ability to absorb light at different

wavelengths. Excitation spectra values at a given wavelength, also referred to as the extinction coefficient of the molecule, are often quoted in units of $\text{cm}^{-1}\text{M}^{-1}$, where the molarity, M , refers to the number of moles per liter of solution. The number of molecules within a given volume is commonly quantitated by its molecular mass (g/mol), which is another important property to consider when studying a particular dye. Fluorophore absorption spectra have excitation bands with a peak where the absorption is the largest. However, the increased complexity of the molecular structure of some biological molecules results in more complex absorption spectra, e.g., with several peaks and flat regions. For example, porphyrins have five absorption peaks ranging from the visible to the near-infrared (NIR) part of the electromagnetic spectrum. On the other hand, quantum dots can be engineered to have wide spectrally flat regions, thereby providing the opportunity to excite different species of them using a range of wavelengths; that is, when they are designed to have non-overlapping spectra^{56,57}.

Fluorophores are also characterized by an emission spectrum, which is typically independent of the excitation wavelength, λ_{ex} . The relative amplitude of measured emission spectra can be interpreted as the probability that a fluorophore excited at λ_{ex} will emit a photon at the emission wavelength, λ_{em} . However, emission is always red-shifted with respect to excitation, meaning that λ_{ex} is smaller than λ_{em} . This is referred to as the Stokes shift, $\Delta\lambda = \lambda_{\text{em}} - \lambda_{\text{ex}}$. The energy that appears to be lost in the emission process (i.e., the energy of excitation photons is always larger than the energy of the emission photons) is in fact absorbed through transient vibrational states. For simple molecules the emission spectrum is a mirror-image of the absorption spectrum, although this is not the case for most complex organic fluorophores. Similar to excitation spectra, the emission

spectrum of a dye can have several peaks and flat regions depending on the complexity of the molecular structure of the fluorophore and the nature of its interactions with the intra- or extra-cellular chemical environment^{56,57}.

Photon emission is not the only possible decay mode for a fluorescence molecule. In fact, the brightness of a given molecule is determined by its quantum efficiency, which is a measure of the relative contribution of radiative to non-radiative decay events. Typically, quantum efficiencies can range from values close to unity (e.g., for bright dyes) down to values several orders of magnitude lower. For example, dyes such as cyanine and Alexa Fluor dyes have quantum yields between 0.2 and 0.6, while an organic molecule like PpIX has a quantum yield typically smaller than 0.01. Another important parameter is the photobleaching characteristics of a molecule. In some cases photobleaching can essentially be regarded as a measure of the amount of time a dye fluoresces when excited continuously. This is actually only true very approximately, often in biphasic and therefore non-linear cases. At the molecular level, this can be regarded as the permanent alteration of the chromophore structure, thereby making it non-fluorescent.

As described in this section, lifetime, extinction coefficients, excitation and emission spectra, quantum yield and photobleaching are important intrinsic fluorophore characteristics to consider when evaluating their usefulness for a specific surgical application. The advantage of using fluorescence contrast to guide surgery is that its detection can be highly specific. Further, detection strategies can be used which make this approach extremely sensitive, with the potential to maximize the accuracy and completeness of surgical resection. However, which dyes are accessible in a surgical

context is, in most instances, imposed by the nature of the biological tissue or the degree to which an exogenous optical contrast agent can be effectively delivered to its target.

1.2.2.2 Biological origin of fluorescence contrast

Perhaps the most important aspect to consider when using fluorescence detection in the operating room is the specificity and sensitivity associated with the detected signals. From a biological standpoint, specificity and sensitivity are determined by the nature and origin of the biological process under study. Fluorophores with the potential to be used in surgical applications can be divided into two main categories depending on whether they are 1) endogenous to tissues, or whether they 2) accumulate following administration of an exogenous compound. In the case of exogenously-induced fluorescence, accumulation of fluorescent molecules in tissue can result from either administration of the fluorophore itself or from administration of a compound that acts as a precursor to a fluorescent molecule in a cellular pathway relevant to the application of interest⁵⁶⁻⁵⁸.

The main factor that will affect the utility of a fluorophore for surgery is the degree of specificity to the pathological process of interest. In general, a fluorophore might be highly specific for a particular disease, (e.g., targeted-fluorescent antibody to an over-expressed surface receptor) but might not be able to accumulate to significant levels in the tissue under study to provide sufficient contrast (e.g., molecules too large to cross leaky tumor blood vessels)^{45,51,59}. This might be due to, for example, tissue-specific properties that do not permit significant fluorophore diffusion to the tissue of interest, (e.g., decreased targeted-antibody passage through the blood-brain barrier⁶⁰). The lack of

sufficient fluorophore accumulation in diseased tissue consequently leads to low contrast to distinguish between normal and abnormal tissues. Another major problem that might be encountered with fluorophores (e.g., fluorescein) is non-specific accumulation in tissue (i.e., labels non-diseased tissue⁵⁰). In such cases, the fluorophore's fluorescent properties are ambiguous in distinguishing normal from abnormal tissues. For example, in the case of cancer imaging, passive targeting with blood pool agents such as indocyanine green (ICG) will generate contrast mainly through the enhanced permeability and retention (EPR) effect.

A non-exhaustive list of *in vivo* molecular barriers to exogenous agents includes: rapid binding to plasma proteins, rapid excretion through kidneys, liver metabolism, and inability to cross the blood-brain barrier. Therefore, successful delivery of a fluorescent agent to its intended target is affected by a wide variety of factors, which relate to its biochemical interaction with highly complex native molecular processes and structures. These aspects make the discovery of effective optical contrast agents extremely challenging. However, advantages of using exogenously-induced fluorescence include the potential to use biochemical engineering techniques to produce dyes, which simultaneously provide contrast for other imaging modalities (i.e., multi-modal capabilities), have multiplexing capabilities, are activatable by specific cellular processes, have multi-targeting potential, are useful for photodiagnosis and have therapeutic potential (e.g., phototherapy, chemotherapy).

The use of endogenous fluorescent molecules does not suffer from the same biological delivery barriers as exogenous dyes. Moreover, clinical translation of imaging methodologies that use endogenous fluorescence contrast do not need to address concerns

relating to the potential toxicity of exogenous dyes. However, the attainable levels of fluorescence from endogenous molecules are typically smaller than those achieved with exogenous agents. Moreover, the specificity of the autofluorescence of a given molecule to a disease process is usually limited and often confounded by the fluorescence emanating from fluorophores present in surrounding normal tissue and/or present within the pathogenic tissue itself. This is partly due to the large number of different molecules that naturally fluoresce in tissue, making it difficult to distinguish between different species solely based on fluorescence intensity images⁵¹.

Perhaps the key aspect that will affect the fate of fluorescence-guided surgery is the extent to which clinical translation of specific and sensitive optical molecular markers will be achieved in the future. To date, the major fluorescent markers with institutional approval for human studies are ICG, ALA (and ALA derivatives) and fluorescein. However, there is substantial ongoing work in different groups, which focuses on the development of novel agents, with the vast majority still at the pre-clinical stage.

1.2.2.3 Information content and the role played by intrinsic tissue properties

An attractive feature of fluorescence is that distinct fluorophore species can be distinguished based on their excitation and emission spectra as well as by their quantum efficiency, polarization and lifetime. This implies that fluorescence detection can in principle be performed in such a way as to exploit those characteristics for diagnostic purposes. Moreover, the intrinsic properties of fluorescent molecules are affected by the biochemical, cellular and extra-cellular environment in which they accumulate. Consequently, fluorescence measurements can indirectly provide information about

functional, biochemical and structural changes associated with the molecular signatures of different pathologies. In particular, a vast body of work in optical tissue analysis has been concerned with measuring fluorescence absorption and/or excitation spectra in order to evaluate the relative proportion of different fluorophore species in tissues. Other analyses have been concerned with using *in situ* measurements of the fluorophore lifetime in order to discriminate between different tissue types (e.g., distinguishing between normal and malignant tissue)⁶¹⁻⁶³. The biochemical properties of the fluorophore, such as whether it is hydrophilic or lipophilic, will influence the nature of chemical interactions with native molecules. This will in turn affect the nature of the quantum mechanical level structure of the fluorophore (arrangement of vibrational and rotational quantum levels for the ground state as well as for the excited states) potentially leading to different lifetimes, quantum efficiencies and changes in the absorption and emission spectra^{56-58,64}.

Another factor that is of critical importance when considering surgical applications based on fluorescence detection is the impact of intrinsic tissue optical properties. Propagation of light in biological tissue can be modeled by assuming that individual photons propagate stochastically into the medium as they would inside a finite-sized lattice where each site is associated with a given probability for two different physical processes to occur. Namely, photons can either be absorbed, or they can be scattered away from the site. The physical quantity that is used to quantify the probability of absorption is the absorption coefficient, μ_a , in units of inverse length, usually cm^{-1} . According to the Beer-Lambert law, as it propagates into a purely absorbing medium, light intensity is exponentially attenuated, with the exponent approximately fixed the

product of the pathlength traversed by light, in cm, and the absorption coefficient. However, biological tissue is not purely diffusive but rather highly scattering, due to the cellular architecture and its microscopic building blocks such as membranes, organelles and proteins. Further, proteins in the extra-cellular matrix also contribute to scattering. For modeling, each scattering site is associated with two physical quantities, namely, the scattering coefficient, μ_s and the phase function. The scattering coefficient, with units of inverse length, can be regarded as the probability of a scattering event to occur, relative to the probability associated with an absorption event. The phase function, which is a function of scattering angle, refers to the probability that a photon will be scattered in a given direction. Phenomenologically, scattering contributes further to light attenuation in tissue as a result of diffusion. Modeling is often a committed step in extracting quantitative information from fluorescence measurements performed in surgery. Light transport in highly scattering media can be simulated with great accuracy by solving the so-called radiative transfer equation (RTE), which is a function of the absorption and scattering coefficients as well as the phase function. Monte Carlo simulations are also used for the same purpose, leading to comparable levels of modeling precision with less mathematical rigor. From a practical point of view, these modeling approaches require the resolution of a complex mathematical equation or the simulation of billions of photon events, which is computer intensive and in some case, typically not feasible for providing real-time information to surgeons. Moreover, to be useful, fluorescence simulations based on either the RTE or Monte Carlo approach require knowledge not only of absorption and scattering, but also of the phase function, which is difficult to obtain in practice. However, most biological tissues have been shown to be highly forward scattering with

scattering angles that can, on average, be approximated by $\langle \cos \theta \rangle = 1 - g$, where g , the anisotropy factor, is approximately 0.9. Moreover, for most biological tissues, in the red/NIR range the scattering coefficient is much smaller than absorption. Physically, in tissue this implies that over distances of a few millimeters, photons will on average go through a large number of scattering events before being absorbed. The important conclusion that follows is that light transport in biological tissue can be approximated as a diffusive process as long as the distance between illumination and detection points is larger than a few millimeters and that scattering is significantly larger than absorption. In fact in this limit the RTE simplifies to the so-called diffusion equation which is much less computationally intensive to solve, and thus potentially compatible with real-time workflow in the operating room. Moreover, the diffusion equation is a function of two rather than three tissue parameters, namely, the absorption coefficient, and the reduced scattering coefficient, $\mu_s' = \mu_s(1-g)$. Numerical, or in the case of simple tissue geometries, analytical solutions to the diffusion equation can be an integral part of data processing software that comes with clinical fluorescence detection systems^{56-58,64,65}.

Absorption and scattering properties are tissue-specific and depend on their microscopic composition, namely the concentration and distribution of the main tissue absorbers and scatterers^{51,66}. As analysis of unstained tissue sections with an optical microscope demonstrates, most microscopic structures are transparent to the naked eye. Proteins such as hemoglobin and melanin have significant extinction coefficients in the visible. Water is another potentially important molecule for tissue studies but with a very low absorption in the visible and near-infrared (NIR); that is, up to about 900 nm where its absorption sharply peaks making it a more important contributor than blood. Lipids

also contribute to absorption, but their influence on tissue absorption can usually be ignored. The effect of melanin as an absorber is significant in skin but for intra-operative applications skin is not involved because the field-of-view is an open surgical cavity. The main absorbing molecules in tissue are hemoglobin in its oxygenated and in its deoxygenated forms, i.e., oxy-hemoglobin and deoxy-hemoglobin, respectively. The high absorption of these molecules in the visible part of the electromagnetic spectrum is such that fluorescence excitation in the visible is typically limited to under a millimeter from the tissue surface. This explains why fluorescence surgical applications using visible light are only sensitive to superficial tissue. However, the absorption spectrum of both oxy-hemoglobin and deoxy-hemoglobin drops by at least two orders of magnitude in the NIR, i.e., after a wavelength of $\lambda=600$ nm. Biological tissue is translucent to NIR light, because the absorption is usually much smaller than scattering which for several applications justifies the use of the diffusion equation to model light transport^{57,58,65,67}.

Tissue optical properties will affect the utility and efficiency of fluorophores in fluorescence detection technologies, by determining the degree of penetration of excitation light and fluorescence emissions that escape the tissue^{68,69}. Different tissues will face distinct challenges when applying fluorescence detection technologies, given the different tissue compositions. Effects of tissue optical properties will influence the choice of fluorophores, classification algorithms to decouple the effects of tissue optical properties, and fluorescence detection technologies for tissue interrogation. Interestingly, there have been studies using intra-operative reflectance measurements to assess the level of different proteins in tissue based on the detected spectral signature of the signals. In particular, such approaches can be used to determine the oxygenation status of different

tissue areas during surgery by evaluating blood saturation based on multi-spectral measurements. It has also been shown that the complexity of the spectral signature of native molecules such as hemoglobin can lead to detectable modifications of the fluorescence spectra. Detection and quantification of these deformations has been shown to lead to a simple and rapid method for estimating the depth of fluorophores in tissues.

Although absorption and scattering of native molecules and structures can be useful to increase intra-operative information available for diagnostic purposes, the usual interpretation is that diffusion is a nuisance that limits the depth sensitivity of optical instruments to 1-2 cm. In fact, diffusion is the reason why optical imaging can only be regarded as a whole-body imaging approach for imaging small rodents⁵⁴. Further, endogenous tissue autofluorescence will affect the sensitivity and specificity of fluorescence detection approaches. This can be minimized by exciting fluorophores with NIR light, since the extinction coefficients of most native molecules is considerably reduced compared to visible light. Nevertheless, methodologies that account for autofluorescence, other major fluorophores present and tissue optical properties are needed to maximally exploit fluorescence detection methods. A promising approach to significantly increase the sensitivity and specificity of fluorescence methodologies uses light-transport modeling to account for variations in intrinsic tissue optical properties on the fluorescence emission spectrum, yielding a fluorescence spectrum that can be used to directly quantify the fluorophore of interest, providing the surgeon with a tool for more accurate tissue identification (see, e.g., ⁷⁰).

1.2.2.4 Fluorescence imaging and detection: a technology overview

The last major factor is the capabilities and limitations of currently available instrumentation for fluorescence detection, (e.g., point spectroscopy, fluorescence imaging, confocal microscopy) of which no particular method has yet emerged as a consensus, given the trade-offs in information provided by each individual technology, impact on surgical workflow, and limitations in instrumentation and algorithm development^{13,39,45,50-53,55,57,71-76}. Understanding the basic instrumentation setup as well as the principle advantages and disadvantages of currently available clinical technologies for fluorescence detection will inform the surgeon on what is feasible. Further, it will inform the surgeon regarding possible venues for improvement. For example, if the surgeon desires a broad overview of the surgical field with the caveat of decreased information and sensitivity (e.g., full spectral data) using current technological advances, they might want to use a modified surgical microscope adapted for broad-beam fluorescence imaging. Nevertheless, if the surgeon desires greater sensitivity and more fluorescence data per area sampled for diagnostic purposes, but with the caveat of increased time and smaller areas for interrogation, he might want to use a point spectroscopic approach. This approach provides increased sensitivity, but limited spatial detection⁵¹. Further, a sufficient signal-to-noise ratio is necessary for any fluorescence technology to provide enough contrast for tissue identification, but although promising, many approaches will not be feasible in the operating room, given that a major requirement for intra-operative fluorescence technologies is compatibility with surgical workflow.

The use of optical imaging and detection in the operating room is advantageous when compared to other intra-operative approaches such as MR- and CT-based. There are three main reasons for this, namely, the relatively low-cost of the technology, the non-invasive

and non-hazardous nature of light, and, the ability to provide surgeons with functional and potentially molecular information relating to tissues of interest in real-time. However, as pointed out above, an important limitation associated with optical imaging is the limited depth sensitivity allowing interrogation of tissue from a few hundred microns with visible light up to a centimeter or two with NIR light. There are several factors influencing which technological developments can be incorporated into the surgical workflow. Perhaps the most basic of these requirements is imposed by the geometry of the operating field. In fact, fluorescence detection or imaging of a surgical cavity can most easily be attained using epi-illumination, often also referred to as reflectance. In this type of setup, fluorescence light emitted from the tissue is collected from the same side as the light that was used for excitation. This is in contrast with trans-illumination detection in which light is detected after having traversed the interrogated tissue (i.e., light emitted from tissue is collected from the opposite side as the light used for excitation). Trans-illumination, however, is only practical in situations where the light paths traversed are small and/or the attenuation caused by absorber molecules is small. Optical imaging in trans-illumination mode has been implemented in the past for, e.g., breast and finger joint imaging. Another drawback of reflectance imaging is that detected signals are strongly biased towards fluorescent events occurring close to the tissue surface. This is caused by the exponential attenuation of light in tissue due to diffusion^{57,58,65,67}.

There is no particular method that has been adopted as a standard for use as a fluorescence detection modality in the operating room. However, the development of any fluorescence-guidance tool always includes an excitation light source, a light detector (photodetector) and light filters. For illumination of the surgical cavity, the spectral

distribution of the excitation light must be chosen to significantly overlap the absorption spectrum of the fluorophore of interest. However, while a spectrally broad illumination spectrum might lead to increased fluorescence signals, caution must be exercised in order to maintain an acceptable level of specificity. Criteria to consider when choosing a light source are its ability to deliver significant light intensity within a narrow range of wavelengths and in a short amount of time with time scales compatible with the surgical workflow. Of course, there are limits to the light dose that can be administered for photodiagnosis, but in cases where this is a concern tissue light exposure can be controlled with variable optical attenuators or neutral density filters.

Typically, fluorophore excitation can be accomplished using arc lamps (also referred to as gas-discharge lamps), light-emitting diodes (LED) or lasers. Because of their monochromatic capabilities, LEDs and lasers can be used to excite fluorophores around a specific wavelength, while lamps are typically associated with larger bandwidths. Consequently, fluorescence excitation with lamps usually involves the use of band-pass filters or monochromators. In general, light delivery methods can be divided into two categories, namely, broadbeam and contact illumination. Broadbeam illumination is used in situations where imaging of the surgical cavity is performed for fields of view up from a few centimeters squared. Broadbeam illumination can be implemented with an existing surgical microscope, in which case imaging is consistent with existing spatial constraints relating to the inclusion of a new tool in surgery. In this case the field-of-view can be identical to that of the conventional optical microscope, which is convenient from a practical point-of-view. Broadbeam can also be implemented within a hand-held instrument such as an endoscope. In this case the surgeon needs to hold the instrument

during imaging. An endoscope-type system can introduce limitations when compared to surgical microscopes such as smaller field-of-views and the requirement for post-processing tools allowing registration between the endoscopic images and those acquired with other intra-operative modalities, including a surgical microscope. However, well-conceived endoscopes can potentially deliver more light to tissue as well as image areas of the cavity that might not be accessible to a surgical microscope. In part because of the divergence of the output light, lamps and LEDs are commonly used for broadbeam imaging. Contrary to those light sources, the output of a laser is a beam with a small diameter (typically less than a few millimeters) and low divergence. Using lasers for broadbeam imaging therefore requires the use of optical components allowing for the collimation of the beam followed by lenses used to de-focus the beam onto the surface. The other type of illumination setup used for intra-operative fluorescence detection is contact illumination using optical fibers to deliver light to tissue. This method is used for the development of hand-held fiber-optics probes as well as intra-operative catheters.

Fluorescence detection following excitation of tissue can be done in a variety of manners, but in general, includes the spectral selection of light components prior to detection using light filtering mechanisms to exclude from the signal as much of the excitation light as possible. This can be accomplished using long-pass absorption filters, but is more often done using dichroic filters, also referred to as interference filters. The cut-off wavelength of these filters is usually selected to be spectrally separated from the excitation wavelengths to reduce as much as possible the excitation light bleed-through that can compromise the ability of the system to detect small photon fluxes. For multi-spectral applications requiring the detection of light at specific wavelengths, band-pass

interference filters can be used. A disadvantage of these filters is that for non-normal light incidence attenuation diminishes considerably and the bandwidth of the filter increases, thereby potentially diminishing the detection specificity. In some surgical applications, mainly contact measurements, a spectrograph can be used in conjunction with a photodetector. Another type of filtering method that is often used alongside fluorescence filters is a polarizer, which allows rejection of light having a specific polarization state. These are usually used for imaging in epi-illumination geometry to avoid specular light to contribute to the detected signal by bleed-through across the fluorescence filters. This is accomplished by using two linear polarizers with a 180 degrees separation to reject specular light, which retains the original polarization: one on the illumination side and one on the detection side.

The choice of a light detector will vary depending on which application is considered. The most commonly used detection mechanism for fluorescence imaging is based on charge-coupled-device (CCD) chips. CCDs are advantageous for imaging because they allow for simultaneous detection of a large number of pixels that can be optically projected onto the desired surgical field-of-view. Scientific-grade CCDs can be chosen which have imaging frame rates compatible with the intra-operative workflow in terms of acquisition time. The well-depth and digitizer can also be chosen to provide a high dynamic range of up to 16-bits, which is an important characteristic quantifying the range of largest over the smallest signal that can be measured simultaneously. Another important factor is the sensitivity of the CCD chip, which is defined as the minimal photon flux that can be detected above the noise floor for the detector. The sensitivity of a regular CCD is limited but can be improved by using internal gain mechanisms

implemented in electron-multiplying-CCDs (EMCCD), electron-bombarded-CCDs (EBCCD) and intensified-CCDs (ICCD). However, as seen below, internal gain CCDs are probably not required for most surgical applications. Other light detection systems with internal gain include photomultiplier tubes (PMT) and avalanche photodiodes (APD)⁵⁸.

One important characteristic to consider when choosing a detector is the signal-to-noise (S/N) level it can provide and how it relates to the detection requirements of the particular targeted application. The fluorescence signal associated with the biological process of interest is always going to be corrupted by some type of noise, among which the principal sources are: photon noise, dark current noise, readout noise and background signal. Dark current noise and readout noise are sources of noise inherent to the detection system which limit its sensitivity to the detection of low photon fluxes. Dark current is a thermal effect generated by electrons excited in photocathodes, anodes and dynodes of detection systems in the absence of any light sources. For scientific-grade CCDs, this effect can be made negligible by cooling the chip. Readout noise is attributable to the amplifiers used in the process of transferring the electrons accumulated on the CCD chip unto a digital image. Another source of noise encountered is amplification noise introduced by statistical fluctuations of the internal gain in an EMCCD, ICCD, APD and PMT. While the internal gain of a detector increases its sensitivity to low signals, the amplification noise typically decreases the S/N for large photon fluxes as well as diminishing the dynamical range of the detector⁵⁸.

The sources of noise considered thus far are associated with the intrinsic characteristics of a detector. However, there are sources of noise from photon sources

that are directly related to photon fluxes targeted for detection. Photon noise, often referred to as shot-noise, is an intrinsic characteristic of any detected signal associated with the stochastic nature of light. This is usually the dominant source of noise for large photon fluxes. However, perhaps the most important source of noise for fluorescence-guided imaging consists in the non-specific signals associated with background light. In general, background light, namely fluorescence that is not specific to the targeted pathological process, can be divided into two components: tissue auto-fluorescence or non-specific accumulation of fluorophores in normal tissue. In general, this non-specific contribution to the signal will limit the sensitivity by establishing a limit regarding the lowest signal levels that can be measured and specifically related to the pathological process of interest. Another source that contributes to the decrease in S/N for low signals is the bleed-through of non-desired light components through the fluorescence filters. Excitation light can be a source of bleed-through for low fluorescence levels, but this can be negligible for most intra-operative fluorescence imaging applications because of the presence of tissue autofluorescence and non-specific accumulation of fluorophores. Also, in general it is usually not practical to expect surgical procedures to be performed under pitch-black conditions, so a certain degree of background light should always be expected. This could be another source of noise impacting the detection of low levels of fluorescence^{58,67}.

In brief, extrinsic (e.g., specificity, sensitivity, tissue delivery) and intrinsic (e.g., excitation/emission profile, quantum yield) fluorophore properties, intrinsic tissue optical properties (e.g., absorption, scattering, tissue autofluorescence), and fluorescence detection instrumentation are key factors when considering surgical fluorescence

methodologies. A combined effort that takes advantage of expertise in clinical utility, physiological understanding, fluorophore uptake and light properties, light-tissue interactions, and instrumentation is necessary in developing and applying the optimal intra-operative fluorescence methodology. That is, surgeons, basic scientists, and engineers can develop the most innovative and effective fluorescence methodologies if they combine their various areas of expertise for a particular pathophysiological application.

1.2.3 Contrast Mechanisms for Intraoperative and In Vivo Fluorescence Detection

Although this review focuses on clinical methods and applications of fluorescence-guided surgery, it is important to note that some of the most innovative, and experimental studies occur at the pre-clinical phase before proceeding into clinical use. For example, some of the latest developments in targeting agents for more sensitive and specific diagnostics are currently used in animal models. Researchers are investigating antibodies or peptides tagged with fluorophores for specific targeting of cancer cells^{45,54,77}. Quantum dots or nanoparticles with unique optical, electric, and/or magnetic properties are also attracting widespread interest in biology and medicine^{50,78}. Another research area in molecular imaging consists in the development of activatable probes that fluoresce only in the presence of specific enzymes, which modify their native conformational structure. One important aspect that is often considered in the development of novel fluorescent markers is the requirement that they have excitation spectra in the NIR. As mentioned above, if used in clinical applications, these probes might potentially allow the development of fluorescence-guidance surgery tools that are sensitive to pathologies

buried up to a few centimeters below the tissue surface. Most of these pre-clinical contrast agent developments, however, are years away from translation into the clinic. Below, we focus on the main contrast mechanisms currently in surgical use: ALA, ICG, and endogenous fluorescence. In some countries agents are approved for routine use for specific types of surgical procedures. For example, ALA is approved in Germany and Japan for photodiagnosis of intracranial tumors. The objective in this section is to present an overview of some of the most important biological aspects allowing for an assessment of the degree of usefulness of each of these probes for different clinical applications.

1.2.3.1 5-Aminolevulinic Acid

Photodiagnosis and phototherapy using ALA has been in clinical use for over fifty years. Exogenous administration of ALA overrides the heme biosynthetic pathway, resulting in increased production and accumulation of PpIX. The clinician or researcher is able to detect PpIX, a naturally occurring fluorescent porphyrin, using proper fluorescence detection instrumentation. Although ALA-induced PpIX has been studied for decades, the specific mechanisms for selective ALA-induced PpIX over-expression and accumulation in cells have not been fully elucidated. In what follows, we provide an overview of the work that has been done in an effort to understand the molecular basis of PpIX over-expression in cells.

PpIX, a product of the heme biosynthetic pathway, is a fluorescent compound with its main excitation peak in the blue at around $\lambda_{\text{ex}}=400$ nm with four accompanying secondary excitation maxima at longer wavelengths, including a peak in the NIR at $\lambda_{\text{ex}}=635$ nm. Selective over-expression and accumulation of PpIX after exogenous ALA

administration, with subsequent differences in fluorescence intensity of tissues, enables the use of this biomarker for fluorescence-guided therapy, principally for the resection of intracranial tumors⁶⁷.

The heme biosynthetic pathway is essential to the function of aerobic cells, with levels of activation that vary drastically between different cells and tissues, and an ultimate end point being the production of heme, a prosthetic group involved in the transfer of diatomic gases (e.g., oxygen) and electrons. Briefly, in the first step of the heme biosynthetic pathway, localized on the inner mitochondrial membrane, ALA-synthase catalyzes the conversion of ALA from glycine and succinyl CoA. The second step is a rate limiting one in which ALA is translocated into the cytosol for the synthesis of porphobilinogen by the metalloenzyme 5-aminolevulinate dehydrase. This is also a committed step in the reaction, guaranteeing conversion to PpIX^{46,67}.

In the third step, porphobilinogen deaminase and uroporphyrinogen III co-synthase form the skeletal structure of porphyrinogen. Still in the cytosol, decarboxylation occurs by uroporphyrinogen decarboxylase forming coproporphyrinogen III. Coproporphyrinogen III is subsequently translocated into the intermembrane space of the mitochondrial. Further decarboxylation and oxidation occurs by coproporphyrinogen oxidase to form protoporphyrinogen IX, with the subsequent conversion to PpIX being strongly oxygen dependant. The final step in heme synthesis involves insertion of an iron (II) ion onto PpIX by ferrochelatase. Exogenous administration of ALA bypasses the rate-limiting step of ALA-synthase, driving the reaction to the right, resulting in a build-up of PpIX in cells and tissues. PpIX fluorescence emissions from increased levels of accumulated PpIX can be measured to provide significant contrast in distinguishing tissues^{46,67}.

While in this review we focus on ALA and its usage for fluorescence detection in surgery, it is important to mention that ALA is used to a larger extent for photodynamic therapy⁷⁹⁻⁸⁴. ALA is used to photoactivate tissue that produces increased levels of the photosensitizer PpIX. Then, using specific excitation light, the tissue can be targeted for cellular destruction through the release of singlet oxygen atoms. Significantly smaller doses of ALA are used for diagnostic purposes compared to doses used for photodynamic therapy. Whether ALA is used for therapy or diagnostics, the mechanisms of PpIX fluorescence remain the same.

The ALA-induced PpIX system has been used for tumor diagnostics since the 1950's, despite the lack of full understanding of the exact mechanisms underlying the selectivity of PpIX accumulation in some tissues upon exogenous ALA administration. It is likely that an important factor influencing the over-production of PpIX in malignancies is the tumor's biochemical environment. An example of this is the pH of a cell, which is often lower in tumors compared to normal tissue. In fact, some enzymes in the heme synthesis pathway operate optimally at lower pH. Porphobilinogen deaminase, for example, forms the skeletal structure of porphyrinogen at an optimum pH of 6.2-6.4⁸⁵.

Tumor vasculature is another environmental factor that has been implicated in the selective tumor accumulation of PpIX⁸⁶. PpIX synthesis is highly oxygen dependant and tumors often form an elaborate vasculature as a result of increased angiogenesis. An increased supply of oxygen to tissue may thus lead to an increased production of PpIX.

At a cellular level, a tumor cell's metabolic mechanisms are different from normal cells, possibly further explaining their higher PpIX fluorescence levels. Studies that look at lipoproteins in tumors demonstrate increased tumor uptake of certain molecules in the

presence of low-density lipoproteins ⁸⁷. Enzymes and receptors involved in the steps leading up to PpIX synthesis are upregulated in some tumors, which might also contribute to an increase in PpIX production ^{88,89}.

The final step in heme synthesis is dependant on the availability of an iron (II) ion. A decrease in iron supplies as a result of the high metabolic rate of some tumors could lead to a decrease in PpIX conversion to heme, with a subsequent build-up of PpIX⁹⁰. The decreased ferrochelatase activity found in many tumors, could also lead to a PpIX over-accumulation ^{91,92}. There are several possible mechanisms to explain differences in PpIX fluorescence. These mechanisms may also explain the differences found in PpIX fluorescence between various tumor types ⁹³. For now there is not one mechanism that seems to fully explain the selective over-accumulation of PpIX in neoplastic cells and tissues.

ALA can be administered to patients by different routes depending on the therapeutic or diagnostic application of interest. Skin application is mostly used for photodynamic therapy of skin cancers. Systemic administration of ALA is the most common method for fluorescence-guided surgery. ALA can be administered orally to patients 24 hours prior to imaging ⁵⁰ or via intravenous route at half the oral dose ⁹⁴, with many surgical studies administering ALA approximately 2-3 hours prior to surgery. In animal models, ALA is often given intraperitoneally due to ease of administration ^{95,96}. Systemic ALA is cleared in humans through urinary excretion while non-renal clearance occurs mainly through liver metabolism ⁹⁷.

The fastest growing application of ALA for photodiagnosis is as a guide for the resection of intracranial tumors. An important aspect of this application is that ALA has a

limited ability to cross the blood brain barrier after systemic administration⁹⁸⁻¹⁰⁰. In fact, one of the greatest challenges in central nervous system therapy and diagnostics is finding safe, specific and effective molecular probes that can cross this biological barrier. The exact mechanisms for limited ALA entrance into the central nervous system are possibly due to its partially lipophobic nature but selective uptake of ALA into the choroid plexus has been demonstrated at the blood-cerebrospinal fluid boarder¹⁰¹. Complete break down of the blood brain barrier increases ALA delivery to central nervous system tumors. As such, ALA-induced PpIX fluorescence has become an important tool for fluorescence-guided surgery of central nervous system tumors with a compromised blood brain barrier^{38,50,102}. While there are strong benefits to using ALA for the central nervous system, ALA is also used in a variety of other tissues and organs. One disadvantage of using ALA is the lack of complete understanding why different tissues have varying levels of PpIX fluorescence following exogenous ALA administration. A better understanding of these mechanisms will help better predict which tissues, and ultimately which patients, would benefit from using the ALA-PpIX system for fluorescence-guided surgery.

1.2.3.2 ICG

Indocyanine green (ICG) is a water-soluble cyanine derivative originally developed by the Kodak Research Laboratories in 1955. ICG is transported in the blood mostly bound to proteins, however, 2% of ICG is unbound and quickly removed from the vascular system by the liver¹⁰³. Originally thought to bind albumin, ICG was first found to bind to alpha 1-lipoproteins in serum¹⁰⁴. Subsequent work demonstrated that ICG binds high

density lipoproteins strongly, low density lipoproteins moderately, but does not bind albumin¹⁰⁵. The ability of ICG to rapidly bind plasma proteins, coupled to its fluorescent properties, enables it to be an effective tool for blood flow assessment.

ICG was originally designed for the study of cardiac function, since it allows detection of blood flow without influences from fluctuations in blood oxygen saturation. Its ability to bind proteins and travel in the blood makes its use as a blood flow marker possible^{106,107}. Hepatologists soon became interested in using this less invasive method for monitoring liver functions in the intensive care unit¹⁰⁸. Besides being less invasive than other methods at the time, ICG was found to be eliminated by the liver with no detectable renal, non-hepatic splanchnic or systemic elimination¹⁰⁹. Currently, ICG has been exploited for real-time intra-operative procedures in several medical specialties, including ophthalmology, neurosurgery, cardiology, urology, and plastic surgery (see Section 1.2.4 for an overview).

ICG is administered by intravenous injection, and is rapidly bound to plasma proteins. The dye is taken up almost exclusively by the hepatic parenchymal cells and secreted into the bile for clearance.

Since ICG binds plasma proteins, its use is limited to diagnostic studies of the vasculature and lymphatic vessels. In this capacity, ICG is safe¹¹⁰, highly sensitive and particularly suited for diagnostics with no known metabolites¹¹¹. At this time, ICG is the only clinically approved NIR fluorophore with an excitation peak around $\lambda_{\text{ex}}=800$ nm. In part due to its large size ($MM_{\text{ICG}} = 774.96$ g/mol versus $MM_{\text{ALA}} = 167.59$ g/mol) ICG does not cross the blood brain barrier, limiting its use in the central nervous system to study of vasculature. Other disadvantages are specific to patient therapy. For example,

patients cannot undergo radioactive iodide uptake for other diagnostic procedures for a week after ICG treatment. ICG administered by injection contains sodium iodide, which will interact with the radioactive iodide uptake in clinical studies. Further, patients treated with heparin demonstrate a reduced absorbance peak for ICG ¹¹², since heparin preparations often contain sodium bisulfates which reduce the absorption peak of ICG.

1.2.3.3 Endogenous fluorescence

Fluorescence emission arising from endogenous fluorophores is an intrinsic property of cells and their metabolic pathways. Human tissues contain numerous endogenous fluorophores, including enzymes, metabolic co-factors (nicotinamide adenine dinucleotide (NADH), flavins), some amino acids (e.g., tyrosine, tryptophan, phenylalanine), porphyrins as well as structural proteins such as elastin and collagens ^{51,52,55,66,113}. Methods have been developed to use autofluorescence for diagnostic purposes ^{76,114-118}.

As previously mentioned, an advantage of using endogenous fluorescence when compared to exogenously-induced fluorescence is elimination of possible allergic reactions or side effects that might result from administration of an exogenous compound. Endogenous fluorophores may change significantly in their fluorescence properties (concentration, absorption and emission spectra, lifetime, quantum yield) as a result of their environment. The use of appropriate fluorescence detection instruments could potentially discriminate between normal and abnormal tissue based on endogenous fluorescence ^{51,52,55,66}.

1.2.4 Fluorescence Detection Technologies in the Operating Room

Intra-operative use of fluorescence is a developing field offering significant potential advantages for surgical guidance (e.g., increased sensitivity and specificity for tissue identification). Surgical microscopes modified for fluorescence imaging, point spectroscopy, confocal microscopy, fluorescence tomography, and fluorescence endoscopy, are some of the different fluorescence technologies under development or in clinical or pre-clinical use. Some technologies (e.g., *in vivo* fluorescence tomography) are in the pre-clinical development phase, yielding exciting results in animal models, but have not come into clinical use^{50,54}. In this review we focus on the two major instrumentation approaches that have been the workhorse of clinical intra-operative fluorescence technologies to date: surgical microscopes modified for fluorescence imaging and point spectroscopy. Endoscopic methods are a ‘hybrid’ of these two technological approaches, such that the surgeon uses an endoscope to either visualize fluorescence (i.e., similar to fluorescence imaging) or perform spectroscopic interrogation of an area of interest (i.e., similar to conventional point spectroscopy systems). In what follows, we provide an overview of the basic setup for each technology, followed by a discussion of the advantages and disadvantages of each technology that are of relevance to the surgeon.

1.2.4.1 Fluorescence imaging

A greater proportion of clinical studies using fluorescence have employed a surgical microscope modified for fluorescence imaging to improve tissue localization and detection during surgery (see **Section 1.2.4** for an overview). In these studies, surgeons

have used an exogenously-induced fluorescence contrast mechanism, e.g., ALA-PpIX, ICG, mTHPC, to detect regions with visible fluorescence, in contrast to point spectroscopy studies which have taken advantage of differences in both exogenously-induced and endogenous fluorescence (i.e., autofluorescence).

The basic setup of surgical microscopes modified for fluorescence imaging include: 1) an adequate light source for excitation of fluorophore, and 2) appropriate filters for collection of fluorescence emissions^{40,71,74,119}. A standard set up includes white light (bright filed) illumination with a motorized wheel, that when activated for fluorescence imaging, switches from white light illumination to filtered excitation light (e.g., Xenon light filtered to blue-violet 375-440 nm for PpIX excitation⁴⁰ or red-NIR 760-810 nm for ICG excitation⁷⁴). A motorized wheel allows seamless integration of standard white light illumination and fluorescence guidance, such that the surgeon is able to switch from one mode to the other by a simple mechanism⁴⁰.

The second major modification is addition of filters in the observer light path, which allows passage of fluorescence emissions to reach the observer and camera. The usual set up is composed of beamsplitters that allow separation of incoming light to reach both the observer (i.e., surgeon) and a CCD camera for recording purposes. In ALA-induced PpIX fluorescence imaging, red fluorescence emissions (i.e., 600+ nm) are allowed to pass through with special filtering. Further, part of the reflected blue excitation light (e.g., <10%), which allows visualization of non-fluorescent materials (e.g., surgical instruments, PpIX negative tissue), is also allowed to pass through⁴⁰. This filtering setup permits efficient navigation throughout the surgical field, but has a negative impact on instrument sensitivity for detection of ALA-induced PpIX fluorescence emissions. In

ICG fluorescence imaging, a special filter (e.g., 820-860 nm filter) is used to allow mostly ICG fluorescence to be detected^{71,119}. This information is recorded and displayed on video for surgical visualization. A recent ICG NIR fluorescence imaging device captures fluorescence at the wavelengths of interest (i.e., ICG emission wavelengths), and overlays white light images of the surgical field with “pseudocolored” images corresponding to the fluorescence emissions of interest¹²⁰

A major advantage of fluorescence imaging is the ease of use of this technology for the surgeon. Integration of standard white light and fluorescence modalities into fluorescence imaging allows the surgeon to seamlessly switch between white light illumination to fluorescence mode by means of a simple trigger (e.g., a button on the microscope handles) without interrupting surgical flow. The second major advantage of fluorescence imaging is the ability to interrogate a broad area of tissue. The surgeon is able to survey a greater part, if not the whole, surgical field for tissue-specific fluorescence emissions almost instantaneously. Another advantage offered by current fluorescence imaging, especially in neurosurgical applications, is integration of fluorescence capabilities with image-guidance systems. Co-registration of fluorescence imaging with the image-guidance system allows the surgeon to know, within the degree of error inherent to current image-guidance systems, the location of the current microscope field of view relative to pre-operative images used for image-guidance, thus providing volumetric information to the surgeon^{102,121}. The surgeon is then able to seamlessly switch from white light illumination to fluorescence mode and survey large areas of tissue, or even the whole surgical field, without delay or interruption to surgical flow in addition to use of the added volumetric image-guidance information. Integration

of fluorescence capabilities into the surgical microscope has made it an enticing surgical tool and provided some of the most extensive clinical experiences using fluorescence technologies in the operating room.

The disadvantages of fluorescence imaging are intricately tied to the nature of optical imaging of tissue and the instrumentation setup that allows for quick, broad visualization of the surgical field. A disadvantage of current fluorescence imaging is the lack of full spectral data acquisition, which could be further used for quantitative analysis and diagnostic purposes. Current detection capabilities using fluorescence imaging is able to detect visible levels of fluorescence, allowing surgeons to make diagnostic decisions based on visible levels of fluorescence^{38,102,121,122}. Nevertheless, these decisions are based on qualitative determinations of visible fluorescence, compared to a quantitative approach that utilizes the full tissue spectral information for fluorescence diagnosis and quantification. Further, current fluorescence imaging technologies have decreased sensitivities compared to point spectroscopy systems as a result of several factors, including light collection geometries and adaptive filtering (i.e., passage of reflected excitation light for increased visualization of the surgical field). Another limitation, especially in fluorescence imaging for ALA-induced PpIX surgical guidance is the inability to visualize subsurface levels of fluorescence. Currently such systems visualize only surface levels of fluorescence, such that a thin layer of blood will obscure any fluorescent tissue underneath. In ICG fluorescence imaging systems, the surgeon is able to visualize deep within tissue, nevertheless the field of view is still limited. That is, such systems do not provide volumetric fluorescence information, but only surface (or limited subsurface) information, with deeper-seated anomalies going undetected with

fluorescence imaging. As discussed above, this limitation is the result of significant tissue absorption of excitation light (e.g., 405 nm excitation light for PpIX fluorescence imaging), effects of tissue optical properties, nature of light propagation in tissue, and physical and technological limitations of instrumentation detectors.

1.2.4.2 Point spectroscopy

The second major type of technology used in surgical fluorescence detection is point spectroscopy. Point spectroscopy has probed endogenous and exogenously-induced fluorescence in tissues as well as tissue white light reflectance coupled to fluorescence spectroscopy. White light reflectance provides added information regarding tissue morphology, structure, and input data for extraction of tissue parameters (e.g., oxygen saturation, oxy- and deoxy-hemoglobin concentrations)^{51,66}. Point spectroscopy has even been heralded as a possible optical biopsy diagnostic tool to perform quick, intra-operative diagnostic evaluations of small regions of tissue.

The basic instrumentation components of a point spectroscopy system are: 1) a light source, 2) a conduit for transport of excitation and emission light, and 3) a photodetector^{51,66}. Light sources are usually ultraviolet or visible filtered arc lamps and continuous wave or pulsed lasers that provide monochromatic excitation light. Conduits for light collection are either fiber-optic contact probes or lenses used to project light unto the surface for collection, with the former sampling smaller regions of tissue. Detection of incoming light requires spectral dispersion^{51,66}, which uses either a monochromator¹¹³ or spectrograph to separate light into the different wavelengths⁷⁶, or filter sets for discrete spectral bands¹²³. When choosing a light detector, it is important to consider the type of

measurements being made (i.e., single wavelength vs multi wavelength, and single pixel vs multi pixel). Combinations of single or multichannel and appropriate technologies such as PMTs or photodiode arrays will depend on the speed desired for a particular application. For a thorough review of relevant instrumentation details when developing or choosing a point spectroscopy system please see the review by Ramanujam ⁶⁶.

The greatest advantage of point spectroscopy technologies is their ability to acquire more information per area interrogated than fluorescence imaging technologies, since they acquire the full shape and intensity of the fluorescence (as well as reflectance) spectrum^{50,51,118}. This spectral data can inform researchers on the fluorophores present, both their abundance and identity, providing them with the ability to look at numerous fluorescence-based parameters (e.g., intensity of specific fluorophore peaks of interest such as the two fluorescence peak maxima in PpIX – 635 nm and 710 nm, ratios of fluorescence spectral peaks, area under the curve of the fluorescence spectra). Further, using intra-operative point spectroscopy spectral information, tissue specific properties can also be determined (e.g., concentration of oxy- and deoxy-hemoglobin, oxygen saturation levels, tissue absorption and scattering values (i.e., μ_a and μ_s')⁷⁰). The increased amounts of information can be used to apply elaborate classification algorithms to distinguish normal from abnormal tissue (e.g., principle component analysis)^{116-118,124,125}. For example, point spectroscopy clinical studies have used multivariate statistical methods to develop classification algorithms that could distinguish, between, for example, tumor bulk vs normal tissue, or diffuse tumor vs normal tissue, with excellent diagnostic sensitivities and specificities^{116,126}. Further, point spectroscopy provides significantly better sensitivities as well as a quantitative methodology for detecting tissue

fluorescence as a result of instrumentation geometry allowing greater capture of light^{50,51}. This has led to the idea that point spectroscopy might be a type of intra-operative optical biopsy diagnostic tool that might lower the burden of dependence on frozen tissue analysis, which could lead to faster surgical times and decision making when interrogating regions of interest.

A major disadvantage of point spectroscopy technologies is that tissue interrogation is limited to small areas of approximately 50-1000 μm in diameter⁵¹. As such, use of point spectroscopy leads to disruption of surgical flow, since the surgeon has to stop what he is currently doing to interrogate a small region of interest. Upon point spectroscopic interrogation, the surgeon does not get a spectroscopic view of the whole surgical field, but rather, that of a small area of tissue. Surgical disruption and spatially-limited information might be reasons why point spectroscopy has not taken a strong hold as a fluorescence detection technology in surgical practice. Further, although more spectral information provides means for more elaborate classification algorithms to be developed, many such algorithms are not amenable for surgery (i.e., they take minutes to provide information on one small area of interrogated tissue) since they significantly prolong surgical time¹²⁶.

The two major fluorescence detection technologies, fluorescence imaging and point spectroscopy, provide structural and functional information on interrogated tissue using the fluorescent properties of tissue. Fluorescence imaging provides an overview of the complete surgical field, without interruption to surgical flow, but offers limited, qualitative information. Point spectroscopy provides significantly more amounts of fluorescence and tissue-optical properties information in a quantitative manner, with

more diagnostic data per area investigated, but only informs the surgeon on small areas of tissue, with interruption of surgical flow. Currently, fluorescence imaging technologies are the most common fluorescence technologies for intra-operative use compared to point spectroscopy, mostly as a result of the ease of use and lack of interruption of surgical flow.

1.2.5 Intra-operative Neurosurgical Applications of Fluorescence Technologies

In this section we provide an overview of current applications and examples of fluorescence detection methodologies in neurosurgery. The greatest experience in fluorescence-guided surgery has occurred in the neurosurgical operating room. What follows is not an exhaustive overview of the literature, but rather seeks to provide the reader with an understanding of what is currently in clinical use in the neurosurgical operating room.

Fluorescence detection methodologies for neurosurgical applications have focused on tumor tissue characterization and blood flow measurements. In the former, ALA-PpIX has been the major contrast mechanism used, whereas in the later, ICG has been the main fluorophore. The majority of fluorescence methodologies in use to date for neurosurgery rely on real-time imaging^{12,13,25,33,37-40,73,102,121,122,127-132}, with a lesser number of studies completed with spatial information traded for spectrally-resolved point measurements achieving higher sensitivities and specificities^{44,49,61,63,114,115,126,133-136}. Some recent review papers on fluorescence methodologies have reviewed the spectroscopic literature as well^{39,50,137,138}.

The single largest experience using fluorescence methodologies for neuro-oncologic applications has been by Stummer and colleagues^{12,13,37-40,122,132}. The German effort used ALA-PpIX in a prospective study on 52 patients with high grade gliomas, i.e., glioblastoma multiforme (GBM)³⁸, and saw that 63% of patients had complete resection of contrast enhancing tumor on post-operative MR. This prospective study determined that a strong association ($p=0.0014$) exists between residual fluorescence during surgery and residual contrast enhancement on post-operative MR. These results laid the groundwork for a randomized phase III multicenter trial using ALA-PpIX to assess the effectiveness of fluorescence-guided resection looking at the following endpoints: radicality of surgical intervention, progression free survival, overall survival, and morbidity^{13,37}. In the initial assessment on 270 patients, Stummer et al. found that complete resection of contrast-enhancing tumor was achieved in 65% of patients in the fluorescence-guided resection group compared to 36% of patients in the group undergoing conventional white light guided resection ($p<0.0001$). Further, the fluorescence-guided resection group showed a higher 6-month progression free survival compared to the white light guided resection group (41.0% vs 21.1%, $p=0.0003$). In a subsequent analysis of the data in an effort to identify and adjust for bias (i.e., factors that would influence degree of resection), Stummer et al. found that patients without residual tumor survived longer (16.7 vs 11.8 months, $p<0.0001$), providing level 2b evidence that survival depends on complete resection of contrast enhancing tumor in GBM¹³². A radiation therapy oncology group recursive partitioning analysis of these patients further confirmed the causal influence of resection on survival¹². Another phase II clinical study on 36 patients with recurrent glioma treated using ALA, showed that ALA-PpIX

fluorescence has a high positive predictive value for detection of tumor in recurrent gliomas¹³⁹.

There have been various studies in Japan using ALA for spectroscopic identification of gliomas (e.g., anaplastic astrocytomas, diffuse astrocytomas, and GBMs)^{44,49,134}, endoscopic detection¹⁴⁰, intra-operative diagnosis of meningiomas³³, and metastasis¹⁴¹, and fluorescence imaging identification of ventricular wall tumors¹⁴². In the USA, an ongoing clinical trial at Dartmouth-Hitchcock Medical Center^{102,121} and a clinical study in Switzerland²⁶ have also used the ALA-PpIX system and fluorescence imaging for tumor tissue detection of gliomas. Utsuki et al. used PpIX spectral information^{44,134} to identify infiltrative glioma tissue without need for visible fluorescence (i.e., visible red fluorescence under the surgical microscope). Ishihara et al. used spectroscopic analysis of ALA-PpIX fluorescence in gliomas, and found that PpIX fluorescence correlates to cell proliferation (MIB-1 index, $R = 0.929$, $p < 0.001$) and also to microvessel density (CD-31 index, $R = 0.487$, $p = 0.0067$)⁴⁹. These findings suggest that ALA-induced PpIX overproduction is a marker for increased cell proliferation. However, Miyatake et al.¹²⁹ reported areas of positive fluorescence in tissue histologically assessed as radiation necrosis or demyelinating disease but with no tumor cells. The study by Valdes et al.¹²¹ showed that combination of computational modeling to update pre-operative MR images based on intra-operative US images, and ALA-induced PpIX fluorescence-guidance substantially improves the accuracy of resection by eliminating instances of false positives and false negatives. In the work by Roberts et al.¹⁰² the authors studied 11 cases of newly diagnosed GBM, to assess relationships between intra-operative fluorescence, pre-operative MR imaging features, and neuropathological parameters. The conclusions

of this study are two-fold. First, contrast enhancement on pre-operative MR is significantly associated with intra-operative PpIX fluorescence, implying that pre-operative MR image signatures are predictive of intra-operative PpIX fluorescence. Second, the authors found that a strong relationship between tumor aggressiveness (as determined by neuropathological analysis) and PpIX fluorescence exists, with PpIX fluorescence showing a high positive predictive value for tumor tissue. However this study found a low negative predictive value for tumor tissue using visible ALA-induced PpIX, pointing at the need for more sensitive fluorescence detection technologies than the state-of-the-art broad-band wide-field surgical microscope. Eljamel et al.¹²⁷ found that ALA-PpIX fluorescence-guided resection is a feasible and reliable way for identifying pituitary adenomas during transphenoidal surgery in a study of 30 patients with non-functioning macroadenomas, secreting pituitary adenomas and pituitary cysts. In another study, Eljamel et al.²⁵ combined ALA-PpIX and Photofrin fluorescence-guided resection with photodynamic therapy in a single-center phase III clinical trial on 27 patients with GBM, showing a significant survival advantage in patients undergoing combination therapy (i.e., photodiagnosis-based surgery plus photodynamic therapy) compared to the control group using conventional image-guidance and white light guided resection (52.8 vs 24.6 weeks, $p < 0.01$).

A few studies have used other exogenous contrast agents such as fluorescein^{73,128,130,131}, mTHPC¹⁴³, and Photofrin^{25,135}. The first report of fluorescence-guided resection in neurosurgery was by Moore et al.¹³⁰ with fluorescein sodium on 46 patients with brain tumors using the yellow-green fluorescence observed by the naked eye to improve tumor tissue delineation. A few decades later Murray¹³¹ reported on 23

patients with intracranial tumors, with tissue positive for fluorescein fluorescence showing either neoplasia (84.7%) or necrosis (15.3%) demonstrating the value of fluorescein for tissue with an abnormal blood brain barrier. In like manner Kabuto et al.¹²⁸ used fluorescence imaging of fluorescein to more clearly demarcate tumor compared to white light guided resection. Kremer et al.¹⁴⁴ developed a new 5-aminofluorescein labeled albumin conjugate for fluorescence-guided surgery, showing an accuracy (i.e., agreement between fluorescence and histology for tumor tissue) of 83.3% on 16 patients with high-grade gliomas (e.g., GBM, anaplastic oligodendroglioma).

A developing area in neurosurgery research consists in using spectrally-resolved point measurements to probe differences in endogenous fluorescence (e.g., autofluorescence from nicotinamide adenine dinucleotide (NADH), flavins, porphyrins, amino acids, and lipopigments) between tumor and normal tissue^{50,51,57,66}. The largest reported clinical studies using this type of approach for intracranial tumor demarcation have been those by Lin et al.¹³⁶ and Toms et al.¹²⁶. Lin et al. investigated 36 brain tumor patients to assess the value of *in vivo* autofluorescence and diffuse-white light reflectance point spectroscopy in distinguishing infiltrating tumor margins from normal brain tissue. Using a multivariate algorithm to identify the most diagnostically useful classification, the researchers achieved a sensitivity and specificity of 100% and 76%, respectively. The study by Toms et al. included 24 patients with glioma tumors and 11 patients with temporal lobe epilepsy. In agreement with Lin et al., they found that spectrally-resolved fluorescence and white light reflectance achieves a sensitivity and specificity of 80% and 89%, respectively, for discriminating solid tumor from normal tissues, and a sensitivity and specificity of 94% and 93%, respectively, for discriminating infiltrating tumor

margins from normal tissue. Reports have also used differences in fluorescence lifetime between gliomas^{62,63,114} or meningiomas⁶¹ to distinguish tumor from normal tissue.

Another major application of fluorescence imaging in neurosurgery has been in the assessment of blood flow using fluorescein¹⁴⁵ but mostly the NIR exogenous dye, ICG^{119,146-150}. Clinical applications include cerebral aneurysms^{119,147-149,151}, dural fistulae¹⁴⁸, cerebral revascularization in ischemia and moyamoya disease¹⁵⁰, arteriovenous malformations, extracranial-intracranial bypasses^{146,150}, and blood flow assessment in cortical perfusion measurements for malignant stroke¹⁵². Li et al.¹⁴⁷ used ICG angiography in 120 patients with intracranial aneurysms, and identified incomplete clippings and arterial stenosis with the help of ICG angiography¹⁴⁷. In a similar study by Raabe et al., ICG angiography permitted the surgeons simple and quick assessment of vessel patency and aneurysm clipping, with valuable intra-operative imaging of both arterial and venous flow which included small perforating arteries^{148,149}. Woitzik et al. used ICG angiography to assess extracranial-intracranial bypass patency, with visualization of cerebral arteries, bypass grafts, and brain perfusion in such cases as superficial temporal artery-middle cerebral artery bypass surgery and superficial temporal artery-posterior cerebral artery bypass. In this study, ICG angiography identified four nonfunctional superficial temporal artery-middle cerebral artery bypasses, which were successfully revised as well as detection of stenosis proximal to the site of anastomosis¹⁵⁰.

In retrospect, assessment of intracranial blood by means of fluorescence angiography provides the following advantages: 1) real-time assessment of cerebral circulation, 2) simplicity and reliability in use, 3) cost-effectiveness, 4) positive validation by digital subtraction angiography or CT angiography, and 5) complementary use with current

surgical approaches^{119,146-150}. A limitation of ICG angiography is the qualitative nature of the information it provides. Also, when compared to digital subtraction angiography, the field of view (i.e., area and depth sensitivity) presented to the surgeon is limited^{146,148}. As such, fluorescence angiography is promising as an adjunct approach to state-of-the-art approaches such as Doppler ultrasonography or intra-operative digital subtraction angiography, but likely not as its own free-standing intra-operative guidance modality. Similar limitations associated with intracranial fluorescence imaging and spectrally-resolved point measurements imply that in the future these approaches will be used as adjuncts to conventional surgical guidance approaches.

1.3 Summary

In summary, we provided a context for the work on ALA-induced PpIX FGR of brain tumors presented in this thesis. First, we presented an overview of the major factors that need to be taken into account when considering fluorescence detection for a particular application of interest: the physical properties of the contrast agent, the biological nature and origin of tissue contrast, the interaction of light with tissue and the available light illumination and detection instrumentation. We followed by providing an overview of the major fluorescence detection technologies and fluorescence contrast agents in clinical use. Finally, we concluded with a thorough overview of the main neurosurgical applications using fluorescence guidance. As such, this introductory section provided the necessary background for the work presented in this thesis.

1.4 Thesis Organization

The work in this thesis arose out of a need to understand the targeting and detection capabilities of ALA-induced PpIX fluorescence for resection of brain tumors as well as the biological basis for such observed targeting.

Chapter 1 presents an introductory exposition and background on the use of fluorescence and optical technologies for the resection of brain tumors. This chapter first provides an overview of the major factors to consider when using fluorescence for *in vivo* detection, followed by a brief synopsis of the major fluorescent targeting agents in clinical use. It continues with an overview of the major detection technologies in use or under investigation for fluorescence guided resection of brain tumors. Finally, the chapter ends with a thorough review of the current literature on fluorescence-guided surgery for brain tumors, including both wide-field and spectroscopic approaches, as well as optical technologies other than just fluorescence, e.g., diffuse reflectance spectroscopy combined with fluorescence.

Chapter 2 presented our first experience using ALA-induced PpIX for resection of GBM. This chapter provides an initial starting point, or baseline, regarding the two key facets of ALA-induced PpIX fluorescence explored in this thesis. First, it provides an analysis of the detection capabilities of state-of-the-art fluorescence imaging. Second, it provides a baseline on some key biological correlates of PpIX accumulation in GBM. Finally, it further confirms the utility of FGR as an adjuvant to conventional pre-operative MR image-guidance. This chapter resulted in the following publication:
Roberts DW, Valdés PA, Harris BT, Fontaine KM, Hartov A, Fan X, Ji S, Lollis SS, Pogue BW, Leblond F, Tosteson TD, Wilson BC, Paulsen KD. *Coregistered fluorescence-enhanced tumor resection of malignant glioma: relationships between δ -*

aminolevulinic acid-induced protoporphyrin IX fluorescence, magnetic resonance imaging enhancement, and neuropathological parameters. J Neurosurg. 2011 Mar;114(3):595-603. Epub 2010 Apr 9.

Chapter 3 was a continuation of *Chapter 4*, combining FGR with MR image-guidance and ‘model-updated’ MR image-guidance to assess the added value of FGR alone, and in combination with updated MR image-guidance for correctly identifying tumor tissue intraoperatively. This study further informed on the detection limitations and importance of further understanding the biological basis of PpIX accumulation. This chapter resulted in the following publication: Valdés PA, Fan X, Ji S, Harris BT, Paulsen KD, Roberts DW. *Estimation of brain deformation for volumetric image updating in protoporphyrin IX fluorescence-guided resection. Stereotact Funct Neurosurg.* 2010;88(1):1-10. Epub 2009 Nov 12.

Chapter 4 was an initial attempt at improving PpIX fluorescence and associated tumor detection, given the observed sensitivity limitations identified in *Chapter 2* and *Chapter 3*. Here we hypothesized that pharmacological alteration of the heme biosynthetic pathway in a rodent model of glioma would significantly improved the detected levels of PpIX fluorescence, thus improving tumor detection. This chapter resulted in the following publication: Valdés PA, Samkoe K, O'Hara JA, Roberts DW, Paulsen KD, Pogue BW. *Deferoxamine iron chelation increases delta-aminolevulinic acid induced protoporphyrin IX in xenograft glioma model. Photochem Photobiol.* 2010 Mar-Apr;86(2):471-5. Epub 2009 Dec 7.

Chapter 5 was born out of our experience using the state-of-the art in intraoperative fluorescence imaging and the significant limitations associated in accurately detecting

PpIX fluorescence. In our initial experience(s) we observed significant limitations specifically in the sensitivity of current fluorescence imaging for accurate tumor targeting and identification. In this chapter we present a systematic study validating a highly sensitive spectroscopic technique for accurate tumor tissue identification - maximally exploiting PpIX targeting of tumor tissue by taking into account both fluorescence emissions and tissue optical properties. This chapter resulted in the following publication: Valdés PA, Leblond F, Kim A, Harris BT, Wilson BC, Fan X, Tosteson TD, Hartov A, Ji Songbai, Erkmén K, Simmons NE, Paulsen KD, Roberts DW. *Quantitative fluorescence in intracranial tumor: implications for ALA-induced PpIX as an intraoperative biomarker*. **J Neurosurg**. 2011. Epub 2011 Mar 25.

Chapter 6 develops a new and improved diagnostic approach which grows out of our quantitative study for measuring PpIX concentrations *in vivo* presented in *Chapter 5*. Here, we develop a quantitative approach which accounts for multiple biomarkers of relevance to neoplastic processes. We develop a diagnostic algorithm that can significantly improve detection of gliomas – low-grade, high-grade, and recurrent gliomas – compared to both current fluorescence imaging and our single biomarker quantitative approach developed in *Chapter 5*. This chapter resulted in the following manuscript in preparation: Valdés PA, Leblond F, Kim A, Conde OM, Harris BT, Paulsen KD, Wilson BC, Roberts DW. *Comprehensive and quantitative multiple biomarker optical strategy for the resection of low- and high-grade gliomas*. (in preparation, 2011).

Chapter 7 is a more all-encompassing, exploratory study arising out of our work in *Chapter 2*, in which we seek to address the biological basis of PpIX accumulation in

tissue. We present a gene expression microarray analysis of five GBM patients, providing an analysis of the gene expression profile differences of tissues displaying distinct fluorescence characteristics. This chapter informed on both the metabolic and structural changes that form the basis for PpIX accumulation in tissue.

Chapter 8 is a focused study born out of our original work associating visual impressions of PpIX fluorescence, tissue histopathology and our gene expression results. Here we focus specifically on tumor tissue proliferation status and quantitative levels of fluorescence to further understand the role of increased growth and metabolism in accumulation of PpIX. Further, we elaborate on the predictive value of accumulated PpIX levels in tumor tissue for anaplastic regions in both low- and high-grade gliomas. This chapter resulted in the following accepted manuscript to **Neuro-Oncology**: Valdés PA, Kim A, Brantsch M, Niu C, Wilson BC, Paulsen KD, Roberts DW, Harris BT. *δ-aminolevulinic acid-induced protoporphyrin IX concentration correlates with histopathological markers of malignancy in human gliomas: the need for quantitative fluorescence-guided resection to identify regions of increasing malignancy.* (accepted, 2011).

Chapter 9 concludes the work in this thesis. It first provides a summary and interpretation of the results presented in *Chapters 2 – 8*. This chapter concludes with suggestions for future directions, suggesting further investigation into the biological basis of PpIX accumulation in brain tumors and improvements in intraoperative detection technologies for fluorescence guided surgery.

Appendices are added which include a brief description of tools developed for use in processing and analyzing data in the FGR project and the work presented in this thesis.

Additional publications that resulted from studies and work during this thesis are:

Bekelis K, Valdés PA, Erkmen K, Leblond F, Kim A, Wilson BC, Harris BT, Paulsen KD, Roberts DW. *Quantitative and qualitative ALA-induced PpIX fluorescence in skull base meningiomas*. (**Neurosurgical Focus**, 2011 May)

Whitson W, Valdés PA, Harris BT, Paulsen KD, Roberts DW. *Confocal microscopy for the histologic fluorescence pattern of a recurrent atypical meningioma*. (**Neurosurgery**, 2011 Mar 8)

Pogue BW, Gibbs-Strauss S, Valdés PA, Samkoe K, Roberts DW, Paulsen KD. *Review of neurosurgical fluorescence imaging methodologies*. (**IEEE J Sel Top Quantum Electron**, 2010 May;16(3):493-505)

Leblond F, Davis SC, Valdés PA, Pogue BW. *Pre-clinical whole-body fluorescence imaging: review of instruments, methods, and applications*. (**J Photochem Photobiol B**, 2010 Jan 21;98(1):77-94. Epub 2009 Dec 26)

Chapter 2. Fluorescence-guided resection of malignant gliomas: relationships between ALA-induced PpIX fluorescence, MR imaging features, and neuropathological parameters

2.1 Introduction

Clinical use of fluorescence-guidance for resection of malignant gliomas, meningiomas, and metastatic brain tumors has grown in interest over the last decade ^{12,13,25-28,33,35-41,73,122,132,144,153,154}. Trials of intraoperative fluorescence for resection of brain tumors using fluorescein sodium was first reported in 1948 by Moore et. al. ¹³⁰ and later in 1982 by Murray ¹³¹. More recently, fluorescence-guidance has taken advantage of intrinsic metabolic and structural changes that occur within tumors by exploiting the heme biosynthetic pathway and a natural biochemical precursor in that pathway, 5-aminolevulinic acid (ALA) ^{13,26,33,38-41,122,132}. Exogenous administration of ALA overloads the heme pathway and leads to selective accumulation of the fluorescent heme precursor, protoporphyrin IX (PpIX), in neoplastic tissues ^{46,48,155}. Accumulated PpIX levels are sufficiently high that neoplastic tissue can be easily visualized through a surgical microscope adapted to excite PpIX fluorescence ⁴⁰.

By far the largest and most important experience described to date using ALA-induced PpIX fluorescence for intraoperative resection guidance has been the pioneering work of Stummer and the ALA-Glioma Study Group in Germany. They have reported in a series of publications that: 1) complete resection of contrast-enhancing tumor occurred in a greater proportion of patients undergoing fluorescence-guided resection (FGR) compared to standard white-light surgery (65% vs. 36%); 2) a significantly longer 6-

month progression free survival was achieved in the FGR group compared with the control group (41.0% vs. 21.1%)¹³; 3) after accounting for selection and other biases a statistically significant survival advantage for complete versus incomplete resection was seen (median survival time of 16.9 months vs. 11.8 months, $P < 0.0001$)^{12,132}; and 4) a significant association existed between residual contrast on post-operative MRI and residual intraoperative fluorescence³⁸. In addition to the work in Germany, other studies have reported experiences on the uses and limitations of the technology^{24,129,156}.

We hypothesize a correlation between conventional features from co-registered pre-operative MR imaging and intraoperative fluorescence, as well as a correlation between neuropathological parameters and intraoperative fluorescence. In this study we seek to provide initial findings from co-registered ALA-PpIX-induced fluorescence-enhanced surgical resection of malignant gliomas in 11 patients with newly diagnosed GBM, under an IRB-approved, FDA IND protocol, with the goal of establishing the statistical significance of (a) the diagnostic capabilities of qualitative visible fluorescence signatures for tumor tissue identification in ALA-induced PpIX FGR, and relationships between (b) quantitative assessments of MR image signals and the spatially co-registered qualitative fluorescence signatures determined intraoperatively and (c) these same qualitative fluorescence determinations and subsequent neuropathological evaluations of the biopsy specimens taken from these locations.

2.2. Methods

2.2.1 Patient Selection

This study was approved by our IRB, and informed consent was obtained from all patients. Patients with a new pathological diagnosis of GBM operated upon under our fluorescence-guided tumor resection protocol were included in this study. These patients were part of a larger group, inclusion criteria for which were: (1) preoperative diagnosis of presumed low or high grade glioma; (2) tumor judged to be suitable for open cranial resection based on preoperative imaging studies; (3) age equal to or greater than 18 years; and (4) ability to provide informed consent. Exclusion criteria were: (1) pregnancy or breast feeding; (2) history of cutaneous photosensitivity, hypersensitivity to porphyrins, photodermatitis, exfoliative dermatitis, or porphyria; (3) history of liver disease within the last 12 months; (4) ALT, AST, ALP or bilirubin levels greater than 2.5 times the normal limit at any time during the previous 2 months; (5) plasma creatinine in excess of 180 mmol/L; (6) inability to comply with the photosensitivity precautions associated with the study, and (7) serious associated psychiatric illness. Between August 2008 and April 2009 a total of 24 patients were enrolled, 11 of whom were newly diagnosed with GBM and were the subject of this analysis. These were chosen because they shared a common diagnosis, which has been the subject of previous investigations of ALA-induced PpIX FGR. Diagnoses in the remaining 13 patients were: 3 dysembryoplastic neuroepithelial tumors (Grade I), 1 ganglioglioma (Grade I), 1 anaplastic mixed oligoastrocytoma (Grade III), 1 anaplastic oligodendroglioma (Grade III), 1 astrocytic neoplasm (Grade III), 1 atypical anaplastic astrocytoma (III), 2 recurrent GBM (Grade IV), 1 gliosarcoma (Grade IV), and 2 vascular malformations. **Table 2.1** summarizes the patient characteristics of these 11 subjects.

#	Gender	Age	Side	Location	Enhancing Tumor Volume (cc)
1	M	61	Left	Temporoparietal	19.5
2	M	52	Right	Temporal	98.4
3	M	80	Right	Parietal	8.7
4	F	55	Left	Parietal	44.8
5	M	68	Left	Parietal	35.1
6	M	60	Left	Frontotemporal	40.7
7	F	76	Right	Parietal	31.7
8	M	59	Left	Temporal	46.3
9	F	76	Left	Temporal	4.4
10	M	60	Left	Temporoparietal	4.2
11	M	55	Right	Occipitoparietal	35.9

^aM, male; F, female; cc, cubic centimeter

Table 2.1. Summary of characteristics of the 11 patients with a newly diagnosed GBM.

2.2.2 Surgical Procedure

Patients were administered a 20 mg/kg body weight oral dose of 5-aminolevulinic acid (ALA) (DUSA Pharmaceuticals, Tarrytown, NY, USA) dissolved in 100 ml of water approximately three hours prior to the induction of anesthesia. Preoperative, high-resolution, contrast-enhanced T1-weighted axial images (256 x 256 matrix, 124 axial slices, 1.5 mm slice thickness, TE = 3 msec, TR = 25 msec; 0.1 mmol/kg body weight gadolinium-diethylenetriamine pentaacetic acid) were acquired for each subject on the day of the procedure. The operating room was equipped with a Zeiss OPMI Pentero® operating microscope (Carl Zeiss Surgical GmbH, Oberkochen, Germany) enabled with fluorescence imaging and a Medtronic's StealthStation® Treon® (Medtronic, Louisville, CO, USA) for neurosurgical navigation. The Zeiss OPMI Pentero® operating microscope

was modified to include a blue light source for excitation (i.e., a wavelength of 400 nm) and a 620-710 nm BP filter for recording PpIX fluorescence on a sensitive 3-chip CCD camera. The patient's head was positioned in 3-point pin fixation, registered with the image-guidance system using scalp-based fiducials, prepared and draped following standard practice. The Pentero® microscope was co-registered with the navigational system and surgical field, such that the focal point of the microscope was mapped to the patient coordinate system in the OR and its coordinates were displayed in image-space on the StealthStation® image-guidance monitor.

The primary guide for resection was conventional neurosurgical technique with white light illumination assisted by neuro-navigational guidance. Only tissue judged reasonably part of the planned resection volume, or abnormal tissue by other assessments (i.e., texture, non-fluorescent color, etc.) was included in the resection. In no instance was tissue resected on the basis of fluorescence alone. At different times during resection, the surgeon switched to blue light excitation mode and red-shifted filtered collection to visualize fluorescence. Biopsy specimens from image-registered sites within the intended resection volume were collected at the beginning, middle, and end of resection, and digital images in white and blue light modes were recorded concurrently for each biopsy acquisition. Biopsy sites were assigned a fluorescence level by the study surgeon (DWR) of 0-no fluorescence, 1-low fluorescence, 2-moderate fluorescence, or 3-high fluorescence. For each patient, biopsy specimens were collected in both fluorescing and non-fluorescing regions within the preoperatively planned resection volume.

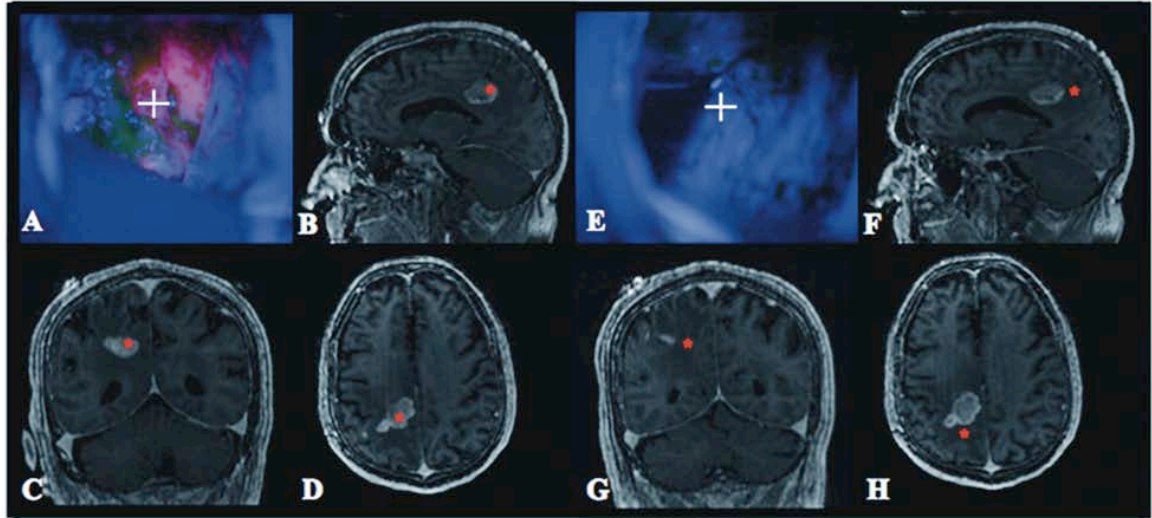


Figure 2.1. Images of a right parietal lesion in patient 3. A) During resection, the surgical cavity displayed a high level of PpIX fluorescence (red) at the focal point of the surgical microscope (white cross hairs). B, C, D) Navigational information localized the focal point to an area of high contrast-enhancement (red asterisk on MR images). E) Later during resection, the focal point of the operating microscope (white cross hairs) is focused on tissue with no observable PpIX fluorescence. F, G, H) Navigational information localized the focal point to an area without contrast-enhancement (red asterisk).

Each excised specimen was immediately separated into three equal parts for further processing as follows: 1) one part was placed in formalin; 2) a second part was placed in Optimal Cutting Temperature (OCT) compound and frozen in liquid nitrogen; 3) the third part was placed in a cryogenic vial and also frozen in liquid nitrogen. For each biopsy specimen, we retrieved the corresponding image-space coordinates provided by the navigational system and matched the coordinates to the corresponding blue and white

light digital images (**Figure 2.1**). Resection of tumor was performed until the surgeon judged from both the image-guidance and surgical microscope systems that no more malignant tissue that could be safely removed was present.

2.2.3 Neuropathology

Neuropathological analysis was performed on formalin fixed paraffin embedded biopsy tissue processed for H&E staining. A single neuropathologist (BTH) analyzed the H&E tissue slides blinded to the pathological diagnoses derived from the main surgical specimen in each case. Three major histological parameters were measured: 1) histopathological score, 2) tumor burden, and 3) necrotic burden. Each H&E tissue section was assigned a histopathological score (0-IV) based on the current WHO grading criteria for the particular neoplasms observed ¹⁵⁷. The following histopathological characteristics were used for each of the biopsies and judged independently regardless of the overall WHO grade assigned: (0) normal or fully necrotic tissue section with no viable tumor cells observed; (I) tissue section with diffusely infiltrating tumor cells (reserved for specific types of glial or glioneuronal neoplasms such as pilocytic astrocytomas, dysembryoplastic neuroepithelial tumors, and gangliogliomas); (II) tissue section with higher number of diffusely infiltrating, pleomorphic cells and no observable necrosis, mitotic figures, or endothelial proliferation; (III) tissue section with highly pleomorphic tumor cells with mitotic figures and no observable necrosis or endothelial proliferation, (IV) tissue section with highly pleomorphic tumor cells with mitotic figures and either observable necrosis and/or endothelial proliferation. In addition, the tumor burden (0-III) for each tissue section was assessed and defined on the basis of the

percentage of area occupied by tumor compared to non-tumor cells in each tissue slide (as estimated by two observers -- BTH, PV). The following tumor burden scores were assigned: (0) normal or fully necrotic tissue section with no observable or viable tumor cells; (I) >0% and ≤33% viable tumor; (II) >33% and ≤67% viable tumor; (III) >67% viable tumor. Necrotic burden (0-III) for each tissue section was assessed and defined on the basis of the percentage of area occupied by necrotic tissue compared to non-necrotic tissue in each slide (as estimated by two observers -- BTH, PV). The following necrotic burden scores were assigned: (0) no observable necrosis; (I) >0% and ≤33% necrosis; (II) >33% and ≤67% necrosis; (III) >67% necrosis.

2.2.4 Data Analysis and Image Processing

Results for each biopsy specimen were arranged according to fluorescence level (0-3), histopathological score, tumor burden, and necrotic burden in two-way tables of association. Sensitivities, specificities, positive predictive values (PPV), negative predictive values (NPV), and odds ratio for fluorescence score were calculated to summarize the strength of association in these tables (**Table 2.2**). A chi-squared statistic (χ^2) was used to estimate the significance of a relationship between fluorescence, histopathological score, tumor burden, and necrotic burden (**Table 2.3**). The Spearman's rank correlation coefficient was calculated to summarize the strength of these relationships.

The following two image measures of contrast-enhancement on MR imaging were used: (1) gadolinium-enhanced signal intensity (GdE) and (2) normalized contrast ratio (nCR). GdE values refer to the absolute MR imaging signal intensity of a T1-weighted

subtraction image volume, i.e., post-contrast image volume minus pre-contrast-injection image volume. Eight (8) MR imaging subtraction image volumes were used in the analysis for GdE (high resolution T1-weighted image volumes prior to gadolinium injection were not available in three cases). The average MRI signal intensity value of a 3 x 3 x 1 voxel (2.8 mm x 2.8 mm x 1.5 mm) centered about the specific image-space coordinates for each biopsy specimen was calculated from the patient specific subtraction image volume to determine the GdE value.

Normalized contrast ratio, a well-established imaging parameter¹⁵⁸, was also used as a metric for MRI signal contrast-enhancement:

$$nCR = \frac{(SI_b - SI_n)}{SI_{bg}} \quad \text{Equation 2.1}$$

where SI_b refers to the MR imaging signal intensity of the image-space coordinates corresponding to a biopsy specimen; SI_n refers to a weighted average MRI signal intensity of gray and white matter; SI_{bg} refers to an average MRI signal intensity of background (in air). MATLAB® software (Version R2008b, The Mathworks, Inc., Natick, MA, USA) was used to automatically calculate the contrast of the voxel in the T1-weighted, post-gadolinium-injection image volume corresponding to each biopsy specimen using the biopsy-specific image-space coordinate transformation provided by the navigation system. Briefly, the average MRI signal intensity value of a 3 x 3 x 1 voxel (2.8 mm x 2.8 mm x 1.5 mm) centered about the specific image-space coordinates for each biopsy specimen was calculated to determine the SI_b values. The weighted average MRI signal intensity value of a 5 x 5 x 3 voxel (4.7 mm x 4.7 mm x 4.5 mm) of gray and white matter was calculated to determine the corresponding SI_n values. The

average MRI signal intensity value of an 11 x 11 x 3 voxel (10.3 mm x 10.3 mm x 4.5 mm) of space outside the patient's head was calculated to determine the SI_{bg} values.

After calculating the voxel GdE and nCR values in the image volume, a systematic region of interest (ROI) thresholding was carried out to improve the accuracy of the navigational information by allowing for the occurrence of intraoperative brain shift. On an axial image, a ROI with a radius of 3 pixels (2.8 mm) centered about the specific image-space coordinates for each biopsy specimen was calculated. All ROIs that did not encompass two (or more) grossly distinct tissue regions as visualized on the co-registered MRI (e.g., necrotic core, contrast-enhancing rim of the tumor, or white matter) were used in the final analysis. Subsequently, each specimen with its corresponding fluorescence level was automatically matched to the corresponding specimen's GdE and nCR values, which were then grouped into a binary system of negative fluorescence (fluorescence level 0) or positive fluorescence (fluorescence level 1, 2, or 3). To accommodate the multiple samples per person, mixed models¹⁵⁹ with random effects for the individual were used to assess a difference in GdE and nCR values between the positive (+F) and negative (-F) fluorescence groups. The 95% confidence intervals of the mean GdE and nCR for the positive and negative fluorescence groups were calculated and plotted. Tumor volume for each patient was determined by manual segmentation of the region enclosed by contrast enhancing tissue on T1-weighted MR image volumes. A P value of <0.05 was considered statistically significant for all tests. Statistical analyses were performed with Stata 10.0 (Stata Corporation, College Station, TX, USA).

2.3. Results

2.3.1 Association Between Intraoperative Fluorescence and MR Image Measures

The 95% confidence intervals of the mean GdE and nCR for the fluorescent and non-fluorescent groups are plotted in Figure 2. For GdE, the mean difference was 8.33 ([95% C.I: 1.42 – 15.24], $P=0.018$), and for nCR the mean difference was 5.15 ([95% C.I: 2.54 – 7.77], $P<0.001$). These results demonstrate a statistically highly-significant difference in GdE and nCR between fluorescent and non-fluorescent samples.

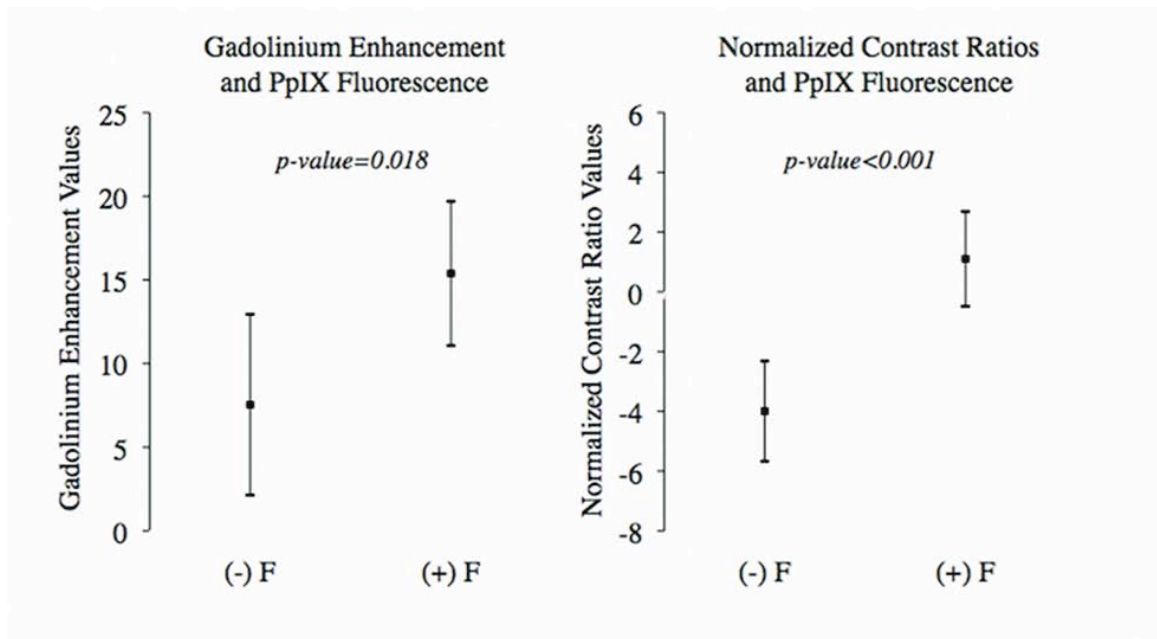


Figure 2.2. Diagrams of the 95% confidence intervals of the mean of MR image measures. (Left) The 95% confidence intervals of the mean for the gadolinium-enhanced signal intensity(GdE) values from subtraction images of both fluorescent (n=57, mean= 15.38 [95% C.I.: 11.07 – 19.69]) and non-fluorescent (mean= 7.54 [95% C.I.: 2.14 – 12.94]) groups (Random-effects mixed model, mean difference = 8.33 [95% C.I: 1.42 – 15.24], $P=0.018$). (Right) The 95% confidence intervals of the mean for the normalized contrast ratio (nCR) of both fluorescent (n=77, mean= 1.10 [95% C.I.: - 0.49 – 2.69]) and

non-fluorescent (mean= -3.99 [95% C.I.: - 5.67 – -2.32]) groups (Random-effects, mixed model, mean difference = 5.15 [95% C.I.: 2.54 – 7.77], P<0.001). The small black square in the middle of the vertical line represents the mean and the whiskers represent the upper and lower 95% confidence limits of the mean.

2.3.2 Association Between Intraoperative Fluorescence and Neuropathological Parameters:

A total of 124 biopsies were collected from the 11 patients with a newly diagnosed GBM. Of these, 86 specimens (69.4% of all specimens) had an observable intraoperative red fluorescence whereas 38 specimens (30.6% of all specimens) did not show any observable fluorescence. Of the 86 specimens with observable fluorescence, 82 were positive for the presence of tumor cells (95.3% of fluorescent specimens), 3 specimens (3.5% of fluorescent specimens) were either fully necrotic or showed abnormal, prominent vasculature, and 1 specimen showed no abnormalities (1.2% of fluorescent specimens). Of the 38 non-fluorescing specimens, 28 (73.7% of non-fluorescent specimens) were positive for the presence of tumor cells, 8 specimens (21.1% of non-fluorescent specimens) were either fully necrotic, showed abnormal, prominent vasculature, or reactive gliosis, and 2 specimens showed no abnormalities (5.3% of non-fluorescent specimens).

Table 2.2. Statistical measures for summarizing the predictive relationship for protoporphyrin fluorescence and tissue histopathology	
	Neoplastic Tissue
Sensitivity	0.75 [0.65 – 0.82]
Negative Predictive Value	0.26 [0.14 – 0.43]
Specificity	0.71 [0.42 – 0.90]
Positive Predictive Value	0.95 [0.88 – 0.98]
Odds Ratio	7.32 [2.13 – 25.21]

Values in brackets denote the 95% confidence intervals

Table 2.2. Statistical measures summarizing the predictive relationship for PpIX fluorescence and tissue histopathology. The sensitivity, negative predictive values, specificity, positive predictive values, and odds ratios of PpIX fluorescence for tissue with the presence of tumor cells (i.e., neoplastic tissue).

In this study, the positive predictive value of observable intraoperative PpIX fluorescence (i.e., the probability that tissue with observable intraoperative PpIX fluorescence is a true positive for the presence of tumor cells) was 0.95 [95% C.I. 0.88 – 0.98], while the negative predictive value (i.e., the probability that tissue without observable intraoperative PpIX fluorescence is a true negative for the presence of tumor cells) was 0.26 [95% C.I. 0.14 – 0.43]. The sensitivity of observable intraoperative PpIX fluorescence (i.e., the probability of having observable intraoperative fluorescence given the presence of tumor cells in the tissue) was 0.75 [95% C.I. 0.65 – 0.82], while the specificity (i.e., the probability of not having observable intraoperative fluorescence given that there are no tumor cells in the tissue) was 0.71 [95 %C.I. 0.42 – 0.90]. An odds

ratio of 7.32 [95% C.I. 2.13 – 25.21] ($P < 0.001$) for tissue with intraoperative PpIX fluorescence to be tumor compared to non-fluorescent tissue further summarizes and confirms the statistically significant association between observable intraoperative fluorescence and tumor tissue. Further, 98.8% of fluorescent tissue (85 out of 86 fluorescent specimens) was abnormal, i.e., neoplastic, fully necrotic, or positive for abnormal, prominent vasculature. The corresponding positive predictive value of observable intraoperative PpIX fluorescence for abnormal tissue was 0.99 [95% C.I. 0.93 – 1.00].

To test for the significance of association between fluorescence levels (0-3) and the three neuropathological parameters under study, chi-squared statistics (χ^2) and P values were calculated (**Table 2.3**). Each biopsy specimen was grouped based on its level of fluorescence (0-3), histopathological score (0-IV), tumor burden (0-III), and necrotic burden (0-III) in two-way tables of association. The chi-squared statistic for fluorescence and histopathological score was 58.8 with a $P < 0.001$; chi-squared statistic for fluorescence and tumor burden was 42.7 with a $P < 0.001$; and chi-squared statistic for fluorescence and necrotic burden was 30.9 with a $P < 0.001$.

Table 2.3. Two-way tables of association.

Vis F	Histopathological Score				Tumor Burden				Necrotic Burden				
	O	II	III	IV	O	I	II	III	O	I	II	III	
-0-	10 (7.6)	14 (14.8)	4 (0.3)	10 (9.4)	10 (7.6)	19 (7.8)	4 (1.3)	5 (8.1)	24 (19.3)	2 (10.1)	1 (1.5)	11 (7.0)	38
-1-	2 (0.1)	0 (2.9)	0 (1.7)	19 (1.7)	2 (0.1)	7 (0.4)	2 (0.9)	10 (0.1)	6 (10.7)	7 (5.6)	0 (0.8)	8 (3.9)	21
-2-	0 (2.3)	1 (1.1)	5 (7.1)	14 (0.0)	0 (2.3)	2 (2.1)	6 (1.4)	12 (1.2)	13 (10.2)	4 (5.3)	1 (0.8)	2 (3.7)	20
-3-	2 (1.9)	2 (2.8)	1 (1.9)	40 (3.2)	2 (1.9)	5 (4.1)	11 (0.8)	27 (2.8)	20 (22.9)	20 (12.0)	3 (1.8)	2 (8.3)	45
	14	17	10	83	14	33	23	54	63	33	5	23	124
$c^2 = 58.8^*$				$c^2 = 42.7^*$				$c^2 = 30.9^*$					

**P < 0.001*

Expected calculated values for each cell are denoted in parenthesis

Table 2.3. Two-way tables of association. Tissue biopsy samples were grouped according to their neuropathological parameter scores and fluorescence level (expected values in parenthesis). A chi-squared (χ^2) statistical analysis was used to assess whether there was a significant association between fluorescence and the neuropathological parameter scores: $\chi^2 = 58.8$ ($P < 0.001$) for fluorescence vs. histopathological score, $\chi^2 = 42.7$ ($P < 0.001$) for fluorescence vs. tumor burden, and $\chi^2 = 30.9$ ($P < 0.001$) for fluorescence vs. necrotic burden.

As histopathological score or tumor burden (i.e., histopathological scores from 0-IV or tumor burden scores from 0-III) for a specimen increased, the proportion of fluorescent samples as well as the levels of fluorescence (0-3) also increased (Figure 3). To quantify this relationship, a Spearman's rank correlation analysis was performed producing correlation coefficients of 0.51 ($P < 0.001$) and 0.49 ($P < 0.001$) for fluorescence and

histopathological score, and for fluorescence and tumor burden, respectively. No statistically significant correlation was observed between levels of fluorescence and necrotic burden by this statistical measure (Spearman's rank correlation coefficient = -0.02, P=0.79).

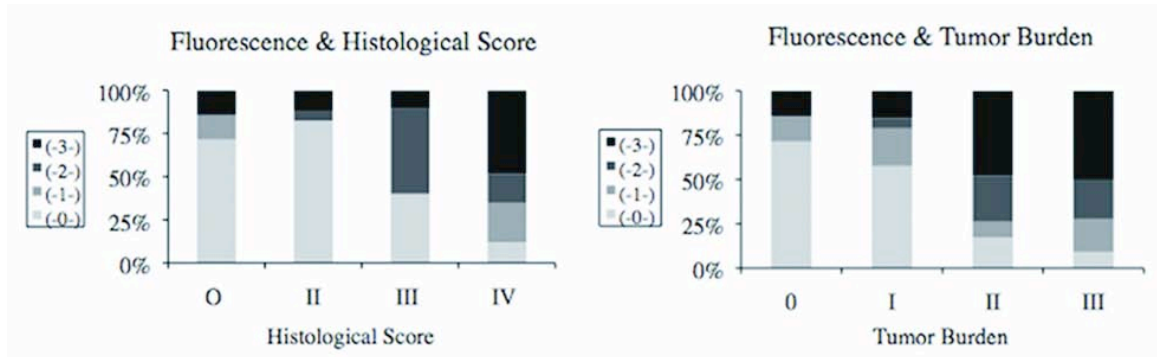


Figure 2.3. Percentage bar graphs of fluorescence and neuropathological parameters. A relationship between qualitative fluorescence levels (0-3) and the two neuropathological parameters was observed. Spearman's rank correlation = 0.51 (P <0.001) for the correlation between fluorescence and histopathological score (left), and 0.49 (P < 0.001) for the correlation between fluorescence and tumor burden (right).

2.4. Discussion

We report initial findings from co-registered ALA-PpIX-induced fluorescence-enhanced surgical resection of malignant gliomas in 11 patients with newly diagnosed GBM, with the goal of establishing the statistical significance of relationships between (a) quantitative assessments of MR image signals and the spatially co-registered qualitative fluorescence signatures determined intraoperatively and (b) these same

qualitative fluorescence determinations and subsequent neuropathological evaluations of the biopsy specimens taken from these locations. Previous studies of ALA-PpIX fluorescence have reported encouraging results in guiding the neurosurgeon to achieve higher percentages of complete tumor resection^{13,38}, which has repeatedly been shown to correlate with patient survival^{9-13,132}. While pioneering in scope, intent and positive outcome for high grade glioma surgery, those studies did not explicitly relate quantitatively, either spatially or in terms of pre-operative MR image contrast characteristics, the relationship between the MRI signature and the degree of intraoperative PpIX fluorescence observed by the neurosurgeon.

One standard feature used to distinguish pathological tissue pre- and post-surgically is contrast-enhancement on MRI after gadolinium injection. In this study we used two measures to quantify contrast-enhancement on T1-weighted image volumes: (1) gadolinium-enhanced signal intensity (GdE) from subtraction image volumes (pre- and post-contrast injection) and (2) normalized contrast ratios (nCR) on T1-weighted, post-gadolinium-injection image volumes. GdE served as a surrogate measure for gadolinium-proper induced changes in the MR images, whereas nCR served as a surrogate measure for what the neurosurgeon most often utilizes in the operating room on T1-weighted, gadolinium-enhanced images. We found evidence of a significant difference in both GdE and nCR between fluorescing and non-fluorescing tissues. PpIX fluorescence can provide the neurosurgeon with real-time information for differentiating tumor from normal tissue, independent of any image-guidance system. The degree to which pre-operative MR image signatures are predictive of intraoperative PpIX fluorescence is of practical importance in understanding the potential role of fluorescence during surgery.

In this study, the odds ratio for intraoperative fluorescence for tumor tissue was highly-favorable (7.32). The positive predictive value for tissue with observable fluorescence to be tumor confirmed the effective accumulation of PpIX in tumor tissue (95%) and abnormal tissue (99%). The sensitivity and specificity of intraoperative fluorescence for tumor tissue were also favorable (75% and 71%, respectively). Similar to previous studies, intraoperative macroscopic fluorescence showed sensitivity limitations. Low negative predictive values (26%) point to the need for improving the detection limit of intraoperative fluorescence imaging. Several groups, including ours, are using intraoperative probes that take advantage of the spectroscopic signature of PpIX (or similar fluorophores) and have signal detection sensitivities that exceed the current surgical microscope^{13,38,44,49,134,135,160}.

Selective accumulation of PpIX in neoplastic tissues may involve changes in intracellular metabolism, increased ALA uptake, vascularization, proliferation, differentiation, or blood brain barrier breakdown⁴⁶. Here, histopathological scores used pathological characteristics to categorize specimens into four distinct levels, in a manner similar to WHO grading of a surgical specimen. This analysis provided a semi-quantitative assessment, analogous to histopathological grading, of the biological aggressiveness of each specimen, and accounts for other biological characteristics such as degree of differentiation, cellular metabolism, and environmental changes. Tumor burden scores offered another important metric, analogous to tumor infiltration, which was used to relate levels of fluorescence to the presence of tumor cells. These parameters were chosen in the present analysis because previous studies have indicated that mitochondrial content and cellular density play a significant role in the selective accumulation of PpIX

⁴⁶. An analysis of association using chi-squared statistics demonstrated a significant relationship between the levels of intraoperative fluorescence and histopathological score ($\chi^2=58.8$, $P < 0.001$), between fluorescence and tumor burden ($\chi^2=42.7$, $P < 0.001$), and between fluorescence and necrotic burden ($\chi^2=30.9$, $P < 0.001$). Spearman's rank correlation analysis provided statistically significant correlation coefficients of 0.51 for fluorescence and histopathological score, and 0.49 for fluorescence and tumor burden, but no statistically significant correlation between fluorescence and necrotic burden. This lack of a direct correlation between degree of fluorescence and necrosis could be attributed to poor fluorescence in heavily necrotic tissue as a result of fewer viable PpIX-producing cells.

The neuropathological analysis increases confidence in the accuracy of intraoperative PpIX fluorescence for abnormal tissue. The data support the idea that biological aggressiveness and burden of tumor cells are important, synergistic factors that explain accumulation of PpIX to observable levels. This study uses parameters, similar to conventional histopathological characteristics, to provide explanatory variables for the selective accumulation of PpIX in resected tumor tissue. These results provide a framework for further understanding PpIX fluorescence, as observed intraoperatively, relative to conventional notions of tumor grading and infiltration.

The Spearman's rank correlation coefficients for histopathological score (0.51) and tumor burden (0.49), however, indicate that while these two variables are important in understanding accumulation of PpIX, other biological characteristics, such as levels of cellular growth, endothelial proliferation, blood brain barrier disruption, and possibly glial-cell phenotype are also likely to be important ^{46,48,155}.

This study adds two major contributions to the neurosurgical literature regarding FGR that differ from previous clinical studies using PpIX fluorescence-guidance. First, this work provides evidence that a strong correlation exists between imaging features on pre-operative MR using patient-specific image-guidance spatial information and intraoperative fluorescence, to the degree that spatially co-registered imaging features on MR are predictive of corresponding intraoperative fluorescence. Second, this work reports that a strong correlation exists between tumor aggressiveness using patient-specific image-guidance spatial information for each biopsy specimen and corresponding intraoperative fluorescence, to the degree that spatially co-registered intraoperative PpIX fluorescence is predictive of tumor aggressiveness. These contributions are of practical importance for the neurosurgical community to integrate FGR into conventional image-guidance.

One limitation of our study is registration error of our image-guidance system and intraoperative brain shift and deformation, with subsequent degradation of navigational accuracy over the course of a surgical procedure. In an attempt to reduce errors in analysis as a result of navigational inaccuracies, we constrained data points using an ROI methodology. Although this methodology reduces this error, it does not completely eliminate it. Second, determination of intraoperative fluorescence in this study is non-quantitative, as it is in all current commercial adaptations of operating microscope systems. Quantitative determination of fluorescence will refine our understanding of the relationship, so that a standard could be applied between patients and across studies. Our group is actively working on this challenge. Further, our group is currently developing a methodology to merge our fluorescence information with our stereovision system²¹ to

create 3-dimensional surface maps of the surgical field, with fluorescence map overlays of these reconstructions onto the MR image-guidance cross-sectional images, using both qualitative and quantitative fluorescence information. Third, current fluorescence surgical systems are sometimes not able to detect low levels of fluorescence (e.g., NPV = 26%), which can lead to a high number of false negatives as was observed in this study (i.e., low negative predictive values). We have developed and are currently in clinical testing phases of an intraoperative probe that quantifies PpIX levels at sub-microgram per milliliter concentrations, with the aim of distinguishing normal from abnormal tumor tissue in a more sensitive manner than our current fluorescence surgical microscope. Lastly, current fluorescence systems detect only fluorescence of surface tissue. Overlying non-fluorescent tissue, including blood or necrotic debris, will prevent visualization of deeper, fluorescing tumor. Systems capable of detecting fluorescing tissue at depth are also under development.

2.5. Conclusions

Analysis of our initial clinical experience with co-registered ALA-PpIX fluorescence-guided tumor resection in 11 patients with newly diagnosed GBM provides evidence for a significant relationship between gadolinium-induced contrast-enhancement on pre-operative MR imaging and observable intraoperative PpIX fluorescence. Further, in newly diagnosed GBM a strong relationship exists between tumor aggressiveness and observable fluorescence. In this study, intraoperative observable fluorescence was shown to have an excellent positive predictive value, but a low negative predictive value. This points to the usefulness and promise of this technology for tumor tissue identification, but

also to the need for more sensitive fluorescence-detection systems. This study reports on the relationships between intraoperative fluorescence and histopathological characteristics analogous to important clinical parameters such as tumor grade and tumor infiltration. It is part of a larger effort to integrate conventional neuro-navigational image-guidance with fluorescence-guidance to increase the probability and consistency of achieving maximal tumor resection.

Chapter 3. Intraoperative ALA-induced PpIX fluorescence of gliomas using pre-operative and model-deformed MR imaging

3.1. Introduction

Fluorescence-guided resection (FGR) for intraoperative, real-time delineation of tumor has been gaining wider acceptance within the neurosurgical community^{12,13,26,38-41,122,132}. Prior to surgery, 5-aminolevulinic acid (ALA) is administered orally, leading to accumulation of protoporphyrin IX (PpIX) in neoplastic tissue. When excited with blue light, tumor tissue accumulating sufficient levels of PpIX displays a red fluorescence^{39,40,122}. FGR provides the neurosurgeon with a surface guidance technology that is not susceptible to intraoperative brain shift, in contrast to conventional image-guidance systems where navigational accuracy is degraded^{18-21,161}. However, not all neoplastic tissue fluoresces to levels observable intraoperatively, leaving some tumor tissue undetected^{26,38,126,156} and subsurface levels of fluorescent tissue are not visible with current surgical microscope systems, requiring the need for complementary 3D volumetric guidance in locating abnormal tissue.

To account for image-guided registration degradation secondary to brain shift, biomechanical models that compensate for brain deformation are currently under development^{20,21,162}. In one form, intraoperative data drives a biomechanical model to estimate the 3D displacement field and subsequently deform the pre-operative MR images (pMR) used for navigation to produce updated MR images (uMR). The uMR provides the neurosurgeon with more accurate MR image correspondence with the current surgical field. A dual-modality, neurosurgical guidance system that incorporates

both FGR and uMR images would offer the neurosurgeon a biomarker of the surgical margin as currently exposed along with coregistered volumetric neuroanatomy that is not degraded by intraoperative brain shift. In this study we present the implementation of a biomechanical deformation model for brain shift compensation in the setting of PpIX fluorescence-guided resection of brain tumors.

3.2. Methods

3.2.1. Patients

Two patients with diagnoses of gliosarcoma (GS) and glioblastoma multiforme (GBM) provided written informed consent for this investigational study and were enrolled in an IRB (Institutional Review Board)-approved study of coregistered fluorescence enhanced tumor resection. Pre-operative (pMR), T1-weighted images (matrix: 256 x 256, 1.5 mm slice thickness) with gadolinium enhancement (0.2 ml/kg gadolinium-diethylenetriamine pentaacetic acid) and scalp-based registration fiducials were acquired for both patients and used for image-guidance. Three hours prior to induction of anesthesia, both patients received a 20 mg/kg body weight oral dose of ALA (DUSA Pharmaceuticals, Tarrytown, NY, USA) dissolved in 100 ml of water.

3.2.2. Coregistered Fluorescence-Guided Resection Procedure

For FGR, a commercial image-guidance system (Treon® StealthStation® Medtronic, Louisville, CO, USA) was coregistered with a surgical microscope offering fluorescence capabilities (Zeiss OPMI Pentero® Carl Zeiss Surgical GmbH, Oberkochen, Germany). The surgical microscope excites with blue light and collects the filtered red

fluorescence emission of PpIX. During a procedure, the surgeon intermittently switched from white light to blue light illumination mode (e.g. see **Figure 3.3**). Eighteen (18) biopsy specimens were collected (9 from Patient 1: GS; 9 from Patient 2: GBM) at the beginning, middle, and end of resection in regions within the bulk of the tumor and tumor margins, and were separated into three parts: one was placed in 10% buffered formalin, one was frozen in a cryogenic vial, and one was frozen in mounting medium (OCT). The navigation system was used to determine the image-space coordinates of each specimen, which was subsequently matched to its corresponding white and blue light digital images.

3.2.3. Intraoperative Brain Deformation Procedure

Prior to the start of surgery, pMR images were rigidly registered to the patient's head in the physical space coordinate system through a fiducial-based registration. At the time of surgery and before craniotomy, the locations of the fiducial markers were digitized using a stylus probe whose location was identified by a 3D tracking system (Polaris System Northern Digital Inc., London ON, Canada) coupled to a workstation dedicated to the deformation modeling. The registration process was used to match the fiducials' physical space-coordinates with the corresponding image-space coordinates. The stylus probe was then placed at two vertical locations to estimate the direction of gravity that was used in the model computations.

After craniotomy, a Philips (Philips Medical Systems, Bothell, WA) iU22 3D ultrasound system (US) was used to collect pre-durotomy and post-durotomy images. The US transducer was tracked by the Polaris System continuously through a rigidly attached

infrared light-emitting tracker to allow for the 3D US images to be registered to the pMR stack^{163,164}.

3.2.4. Tissue Processing and Analysis

Formalin fixed paraffin embedded tissue was processed for H&E staining and analyzed by a single neuropathologist (BTH). The neuropathologist was blinded to the pathological diagnoses from the main surgical specimen and from the intraoperative fluorescence or imaging data. Each biopsy tissue section was analyzed for the presence or absence of tumor cells and was evaluated based on the WHO classification schema¹⁵⁷.

3.2.5. Deformation Model

Briefly, the biomechanical brain deformation model implemented simulates the amount and direction of brain shift and deformation (i.e., displacement) that occurs intraoperatively, by incorporating standard surgical conditions (e.g., direction of gravity) and intraoperative data. Pre-durotomy and immediate post-durotomy US images were used to measure the displacement that occurs in a sub-volume of the brain at the beginning of surgery. They provided sufficient patient-specific intraoperative data, in combination with standard surgical conditions, to drive the biomechanical brain deformation model to estimate displacement for the whole-brain volume which was used to deform the pMR and generate updated MR images (uMR).

A biomechanical brain deformation model computed through the Finite Element Method (FEM) was used to estimate displacement vectors within the whole brain volume. This model can be represented by the following coupled equations, where \mathbf{u} is

the displacement, \mathbf{p} is the pore fluid pressure, and the other parameters symbolize the tissue mechanical properties:

$$\nabla \cdot G \nabla \mathbf{u} + \nabla \frac{G}{1-2\nu} (\nabla \cdot \mathbf{u}) - \alpha \nabla p = (\rho_i - \rho_f) \mathbf{g} \quad \text{Eq. 3.1}$$

$$\alpha \frac{\partial}{\partial t} (\nabla \cdot \mathbf{u}) + \frac{1}{S} \frac{\partial p}{\partial t} - \nabla \cdot k \nabla p - \alpha \nabla p = \Psi \quad \text{Eq. 3.2}$$

These equations are discretized into a matrix form, $\mathbf{Kx} = \mathbf{b}$, where \mathbf{K} is the stiffness matrix, \mathbf{x} is the displacement and pore fluid pressure to be computed, and \mathbf{b} contains the forcing conditions.

The patient's parenchymal volume was isolated within the pMR images using a level set segmentation algorithm ¹⁶⁵. A triangular surface mesh and its corresponding tetrahedral volume mesh were generated using the segmented brain. After patient registration, boundary conditions were assigned to different types of surface nodes as follows: 1) craniotomy nodes were identified using the contour line drawn by the surgeon and were allowed to move freely; 2) brainstem nodes were also allowed to move unconstrained; 3) fluid-drainage was defined by a plane passing through the lowest craniotomy node which was perpendicular to the direction of gravity, with elements below and above being assigned with different parameters (e.g. saturated with fluid or not); 5) a second plane was determined by moving the fluid plane along the direction of gravity by 20 mm. All boundary nodes above this plane except the craniotomy nodes were assigned as contact nodes that are free to move towards or away from the inner surface of the skull and were constrained to motion tangential to the skull, if and when, they moved into direct contact during the displacement computations; 6) other boundary

nodes were assigned as fixed, meaning that they were only allowed to move tangentially with respect to the skull.

Subsequently, a master surface was generated by projecting the brain boundary nodes along the average nodal normal by a specified distance to simulate the inner surface of the skull ¹⁶². The data used to drive the model estimates were the displacements between pre-durotomy and immediately post-durotomy ultrasound images. A mutual-information based rigid registration followed by a B-Spline non-rigid registration was performed to align the pre-durotomy and post-durotomy ultrasound images and compute displacement vectors. **Figure 3.1** shows typical US images from patient 1 pre- and post-durotomy as well as their un- and re-registered overlays which were used to extract intraoperative displacement data. Displacement vectors were mapped from US coordinates to pMR coordinates through a series of transformations and used as data to drive the biomechanical model. To generate a displacement map for model assimilation, the tumor does not have to be well-defined on US per se as long as features exist in both US and MR image volumes which correspond sufficiently well to allow the mutual information registration to occur successfully. Once the displacement map has been generated, the model will assimilate the measured data to produce whole-brain deformation in order to create the model-updated MR images.

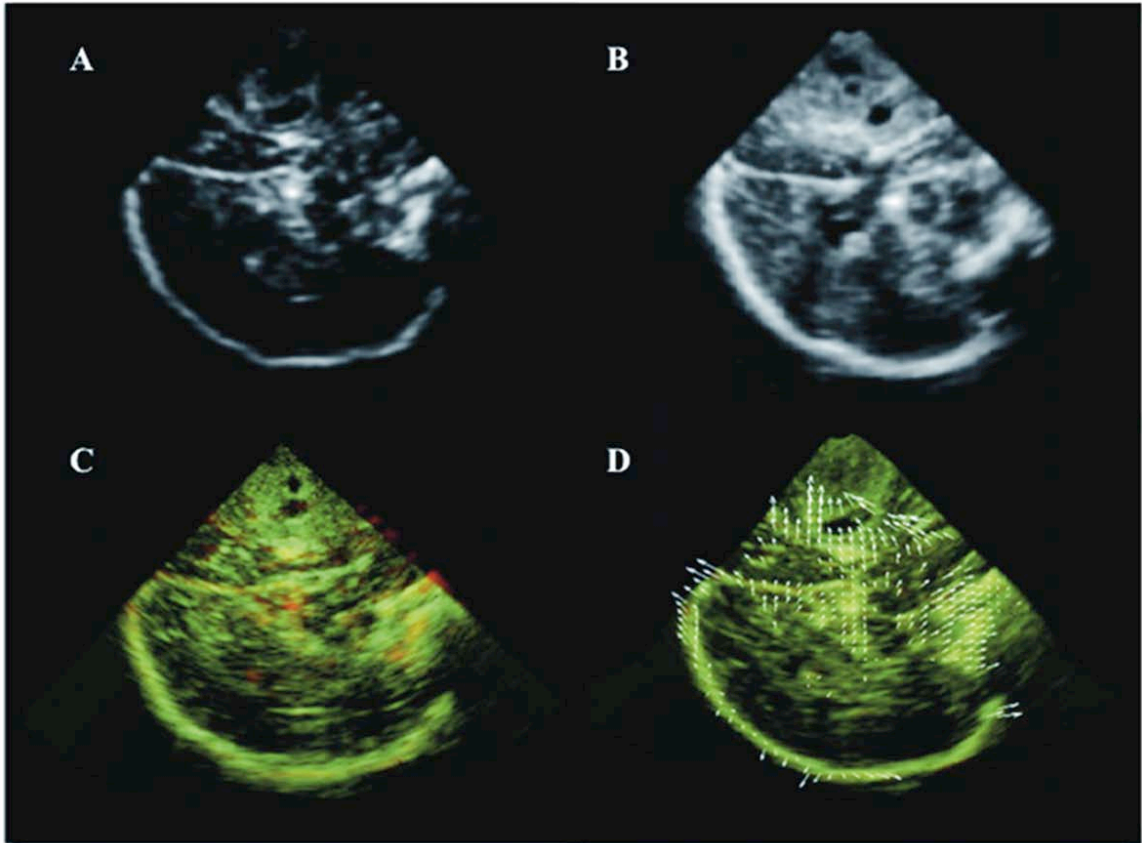


Figure 3.1. Cross-sectional images of intraoperative 3D US from patient 1. US image pre- (A) and post- (B) dura opening. Overlays of US images pre- (red) and post- (green) dura opening (regions appearing in yellow align) are shown in (C) and (D). Apparent misalignment due to brain shift is evident in (C); after both rigid and non-rigid registration with computed displacement vectors (white arrows) is presented in (D).

A generalized least squares inverse method was used to solve the estimation problem by minimizing the difference between measured data, \mathbf{d} , and the model estimate, \mathbf{x} ¹⁸. The model constraint was embedded in the objective function through Lagrange multipliers to form an augmented quadratic expression

$$\Omega = (d - Ax)^T W_\epsilon (d - Ax) + b^T W_b b + \lambda^T (Kx - b) \quad \text{Equation 3.3}$$

where \mathbf{A} is the sampling matrix which computes the model estimate at locations where the measurements were made. W_ϵ is the inverse of the covariance matrix of the misfit, ϵ , between measured data and model estimates, and W_b is the inverse of the covariance of forcing conditions, b .

The objective function is minimized when all derivatives are zero, and the resulting set of equations was solved using the steepest gradient descent algorithm with displacement vectors throughout the whole brain volume as output files^{17,166}. The pMR was then deformed using these displacement vectors and updated MR images (uMR) were generated. A schema of the biomechanical brain deformation modeling process is shown in **Figure 3.2**.

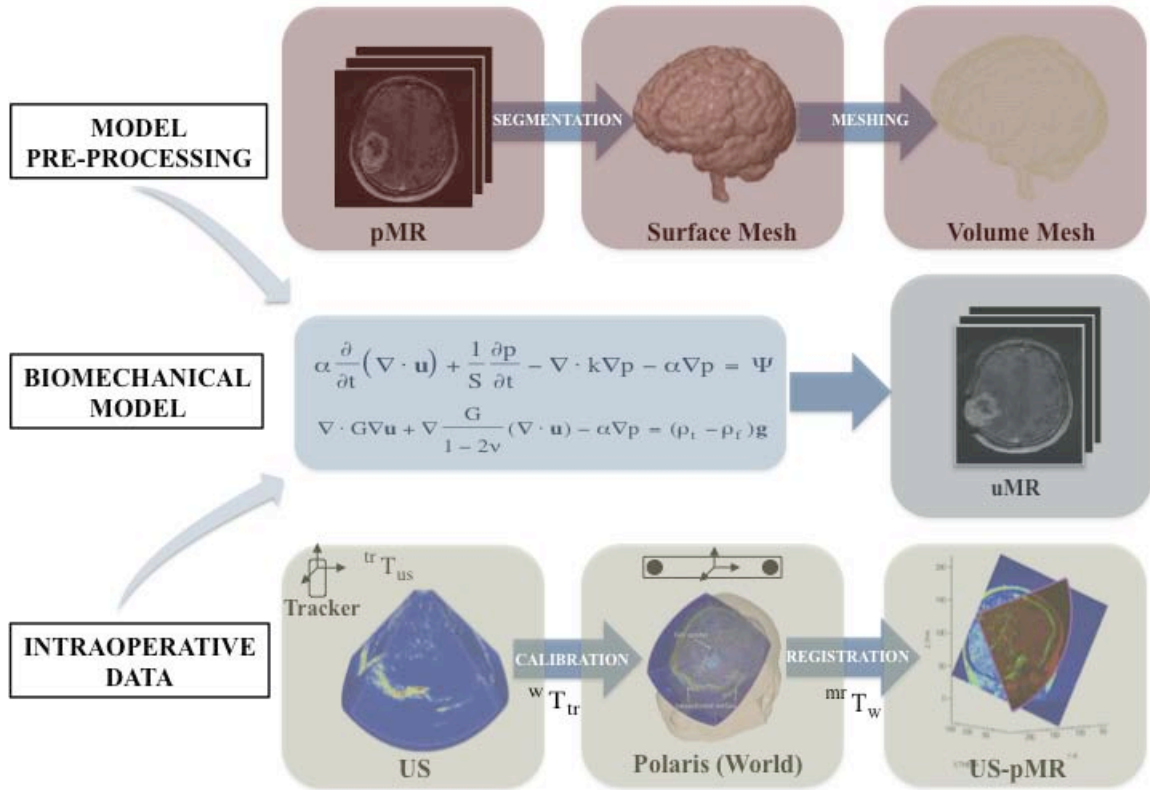


Figure 3.2. Schema of Brain Deformation Model. (Model Pre-Processing) The brain is segmented from the pMR to generate triangular surface and tetrahedral volumetric meshes, and appropriate boundary conditions are assigned. All pre-processing steps are performed prior to surgery. (Intraoperative Data) Tracked 3D US images are acquired pre- and post-durotomy, and are spatially merged with the patient’s head and then re-registered with the pMR. Displacement data are computed from registered pre- and post-durotomy US images to drive a biomechanical model. (Biomechanical Model) Whole-brain deformation is computed based on boundary conditions assigned and intraoperative sparse data provided to generate an updated MRI image volume (uMR).

3.2.6. Data Analysis

Two-by-two tables were used to calculate the following values and statistical measures for FGR alone, image-guidance with (IGW) and without brain shift compensation (IGWO) alone, and FGR coupled with brain shift compensated image-guidance (FGR-IGW): 1) true negatives (TN), 2) false negatives (FN), 3) true positives (TP), 4) false positives (FP), 5) sensitivities, 6) specificities, 7) negative predictive values (NPV), and 8) positive predictive values (PPV). To calculate these measures for FGR, intraoperative red fluorescence was considered a positive test result, whereas absence of fluorescence was recorded as a negative test result. Similarly, to calculate the same values and measures for image-guidance, tissue judged radiologically abnormal from T1-weighted pMR (i.e., pre-operative MRI without brain shift compensation) or uMR (i.e., pre-operative MRI with brain shift compensation) was considered a positive test result, whereas tissue judged radiologically normal from pMR or uMR was scored as a negative test result.

3.3. Results

The two patients in this study displayed distinct patterns of PpIX fluorescence and different degrees of brain shift (**Table 3.1**). The GS and GBM (both WHO Grade IV) cases displayed areas of strong fluorescence as well as gadolinium-enhancing regions on MRI. The GS (brain shift displacement values: mean = 2.9 mm, max = 16.0 mm) surgery had the largest degree of brain shift (**Table 3.2**), whereas the GBM (brain shift displacement values: mean = 0.1 mm, max = 1.4 mm) surgery showed much less brain shift. The deformation model was run on a Linux computer (2.33GHz, 8G RAM) with

500 iterations for patient 1 (GS) and 51 iterations for patient 2 (GBM). The computational cost was less than 30 minutes for patient 1 and less than 6 minutes for patient 2. **Figure 3.3** shows representative pMR, uMR, and white and blue light images of the coregistered focal point of the operating microscope after dural opening during the patient 1 surgery from which it is evident that the fluorescing tumor distended. The uMR views correctly compensate for the post-dural-opening tumor movement whereas their pMR counterparts clearly do not.

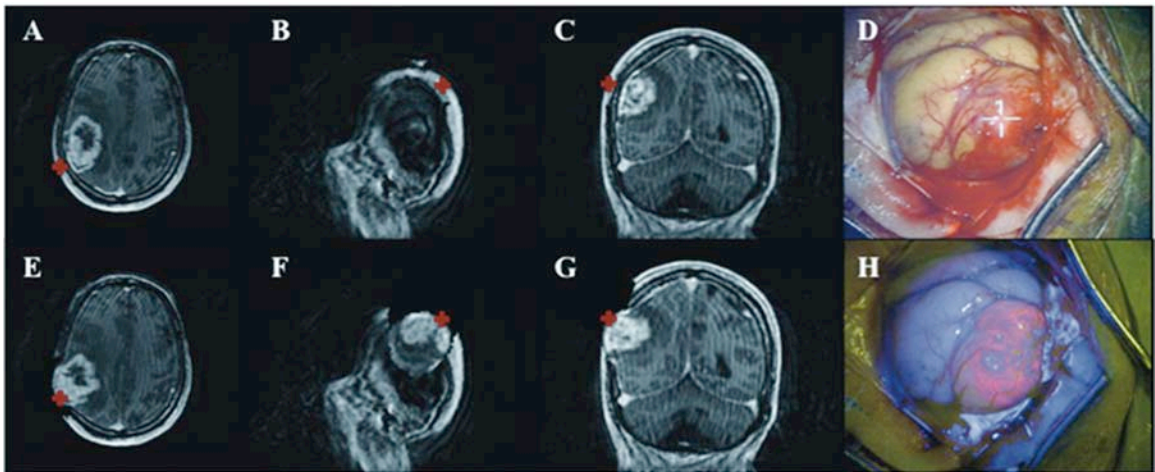


Figure 3.3. Pre-operative, updated, and intraoperative images of patient 1. The top row from left to right (A, B, C) shows pre-operative T1-weighted MRI images post-durotomy without compensation for brain shift (pMR). The bottom row from left to right (E, F, G) shows the updated T1-weighted MRI images immediately post-durotomy with compensation for brain shift (uMR). The surgical microscope was coregistered and tracked by the navigational system. The white light (D) and blue light (H) images corresponding to the tracked coordinates of the microscope focal point in image-space (crosses) are shown. A bulging, highly fluorescent tumor tissue confirmed by pathology

as neoplastic tissue corresponds to an area of contrast-enhancement in the uMR. Compare this area of fluorescent brain tissue to the pMR, which inaccurately points to the scalp region.

Patient	Age (years)	Diagnosis	Tumor Location	Tumor Volume (cc)	Intraoperative Fluorescence	Brain Shift Displacement (mm)	
						mean	max
1	70	Gliosarcoma	Right Parietal	65.95	Yes	2.9	16.0
2	76	Glioblastoma	Left Temporal	4.96	Yes	0.1	1.4

Table 3.1. Overview of fluorescence-guided resection using PpIX and brain shift for the whole-brain. Mean and maximum displacements represent the mean and maximum magnitude of brain shift estimated by the biomechanical model.

Statistical Measures	FGR	IGWO	IGW	FGR-IGW
Sensitivity	0.50	0.69	0.94	1.00
Specificity	1.00	1.00	1.00	1.00
NPV	0.20	0.29	0.67	1.00
PPV	1.00	1.00	1.00	1.00

n=18

Table 3.2. Statistical measures. Sensitivities, specificities, negative predictive values, and positive predictive values were calculated for fluorescence-guided resection (FGR), image-guidance without brain shift compensation (IGWO), image-guidance with brain shift compensation (IGW), and fluorescence-guided resection with brain shift compensation (FGR-IGW).

Sensitivity, specificity, negative predictive values, and positive predictive values for both cases are shown in **Table 3.2**. An increase in the sensitivity and negative predictive value of image-guidance was noted after brain shift compensation (*sensitivity: IGWO = 0.69 vs IGW = 0.94, negative predictive value: IGWO = 0.29 vs. IGW = 0.67*). FGR-IGW showed the best statistical measures for accurately identifying abnormal tissue (*sensitivity = 1.00, negative predictive value = 1.00, specificity = 1.00, positive predictive value = 1.00*). Values for true negative, false negative, and true positive from both cases are graphically displayed in **Figure 3.4**. No false positives were recorded in this study and two biopsies suspected to be tumor were true negatives. The percentage of true positive samples increased (IGWO = 61.1% vs. FGR-IGW = 88.9%) and false negatives decreased (IGWO = 27.8% vs. FGR-IGW = 0.00%) in IGWO vs. FGR-IGW. **Figure 3.5** shows representative pre- and post-operative gadolinium-enhanced, T1-weighted images of both cases.

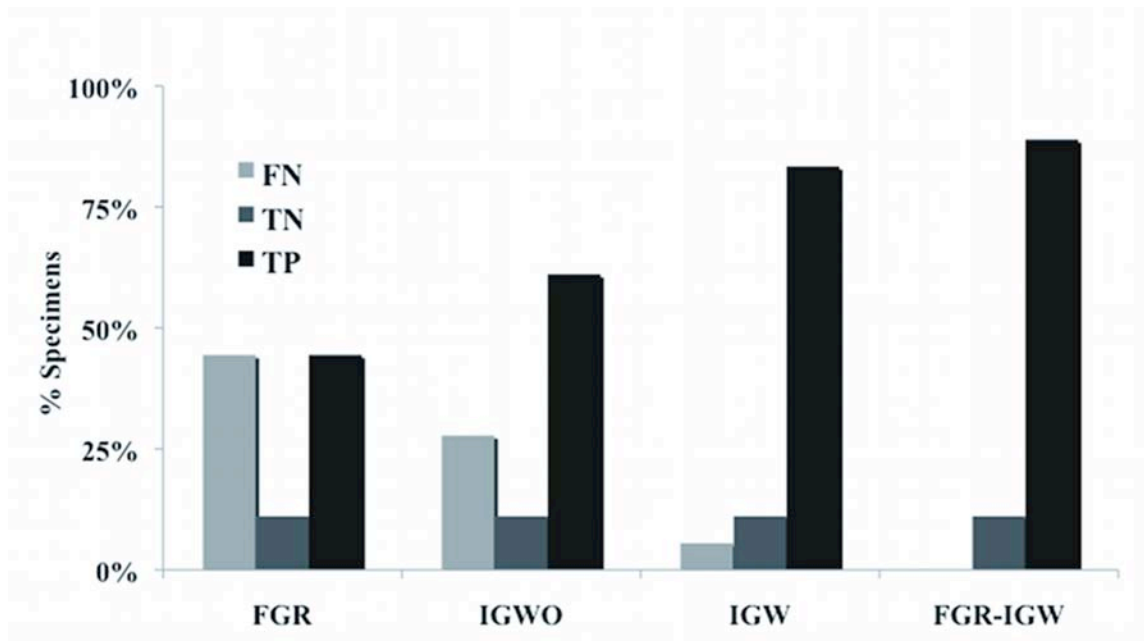


Figure 3.4. Test results for biopsy specimens. Percentage of biopsy specimens (n=18) for fluorescence-guided resection (FGR), image-guidance without brain shift compensation (IGWO), image-guidance with brain shift compensation (IGW), and fluorescence-guided resection with brain shift compensation (FGR-IGW) that were true negative (TN), false negative (FN), and true positive (TP) are shown for both cases. No false positives were recorded in this study.

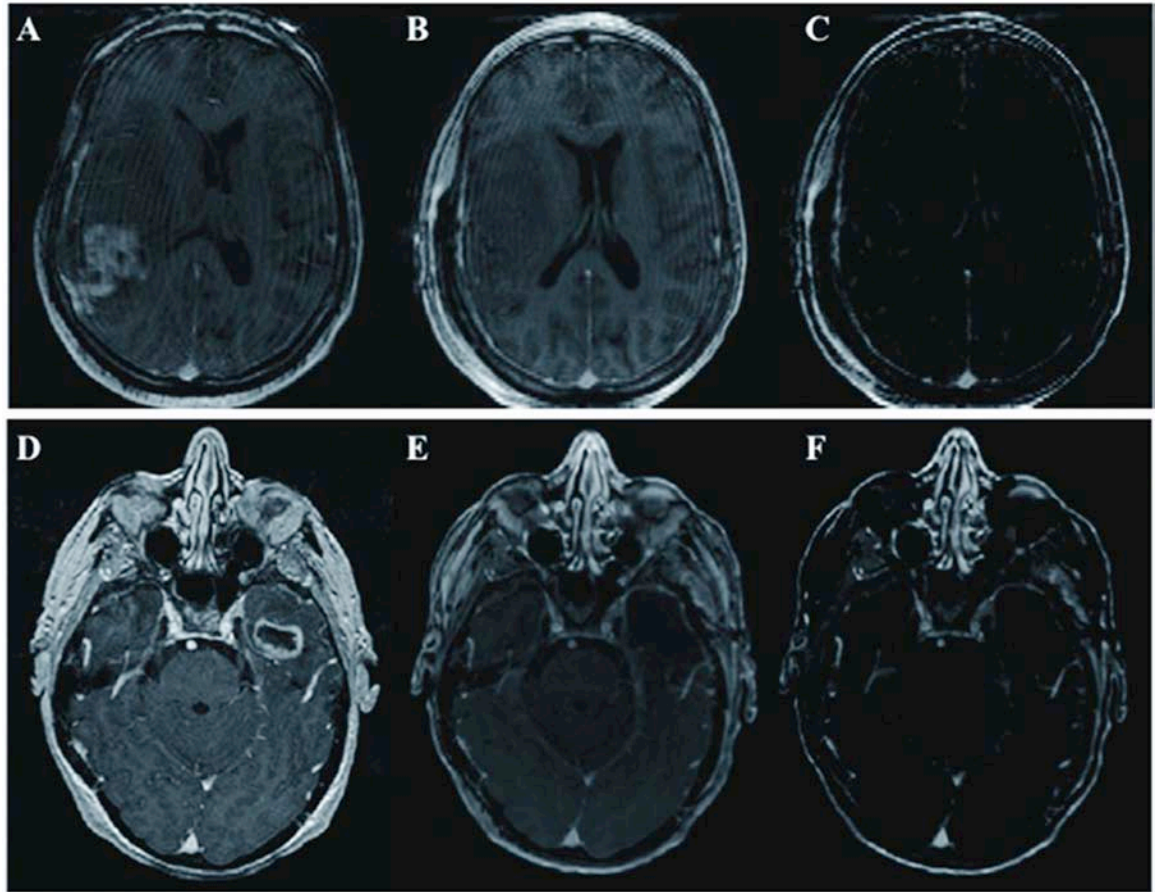


Figure 3.5. Gadolinium-enhanced pre-operative and post-operative T1-weighted MR images. Pre-operative images for patients 1 (A) and 2 (D). Post-operative images for patients 1 (B) and 2 (E). Post-operative subtraction images for patients 1 (C) and 2 (F).

3.4. Discussion

With evidence that extent of tumor resection correlates with patient survival and quality of life^{9-13,132}, intraoperative brain shift poses a major challenge in brain tumor resections using conventional image-guidance technologies. Fluorescence-guided resection (FGR) based on ALA-PpIX has recently gained acceptance as a safe and easy way to aid the neurosurgeon in delineating neoplastic tissues during tumor resection.

FGR is not limited by degradation of registration accuracy due to the intraoperative brain shift that is known to compromise conventional image-guidance systems. However, FGR only provides the neurosurgeon with surface information on the location of neoplastic tissue, and as such, accurate 3D navigation that accounts for intraoperative brain shift is still needed to complement FGR.

Here, we present the implementation of a brain deformation biomechanical model to compensate for intraoperative brain shift in PpIX fluorescence-guided resection of brain tumors. Two surgical cases with different levels of PpIX fluorescence and intraoperative brain shift were studied. FGR-delineated tumor tissue appeared in both the GBM and GS instances. In both surgeries, observable intraoperative fluorescence was mapped only to areas of contrast-enhancing tissue on the uMR, whereas the pMR incorrectly mapped fluorescing tissue to radiologically normal regions (e.g., scalp), which on pathological analysis was demonstrated to be neoplastic. Some biopsy specimens of highly enhancing tissue in patient 1 ($n = 3$) did not display observable fluorescence. In these specimens, a heavy infiltration of mostly the sarcomatous element of the tumor was observed. Meanwhile, tissue sections containing mostly astrocytic elements of the tumor showed intraoperative fluorescence and contrast-enhancement on uMR, suggesting that high-grade glioma tumor cells accumulate more PpIX than high-grade sarcomas.

The uMR images provided more accurate anatomical information increasing both the sensitivity (pMR = 0.69 vs. uMR = 0.94) and negative predictive value (pMR = 0.29 vs uMR = 0.67) of T1-weighted images for surgical correspondence with histologically abnormal tissue (i.e., tissue with the presence of tumor cells). The dual-modality approach using fluorescence signatures with uMR offers a complementary approach that

increased the accurate determination of abnormal tissue in the two cases (**Figure 3.4**). Image-guidance provides the neurosurgeon with accurate 3D volumetric information for navigation based on MR-specific image signatures that are widely used to identify abnormal and resectable tissue. PpIX FGR provides the neurosurgeon with an intuitive guidance tool that delineates tumor tissue in real-time from which the current resection margin can be evaluated. Thus, the dual-modality approach described here takes advantage of pathophysiological changes in tumor cell metabolism (e.g., increased PpIX production and accumulation), blood brain barrier breakdown (e.g., gadolinium enhancement on MRI), and tumor-specific biological signatures (e.g., astrocytic tumors) to improve the accuracy of tumor identification in the OR.

Current technologies for intraoperative updating during brain surgery include intraoperative MRI (iMRI), CT (iCT), and US (iUS). These technologies provide intraoperative feedback to the neurosurgeon, counteracting error in navigational accuracy due to brain deformation^{1-8,167}. Each technology has pros and cons with respect to its costs, limitations and capabilities for tissue contrast, and effects on surgical procedures and workflow that remain to be fully understood and evaluated in the operative setting. In

FGR-IGW	iMRI	iCT	iUS
Pros	Pros	Pros	Pros
High soft-tissue contrast	High spatial resolution ^{1,2}	Mobility of iCT system ^{3,4}	Real-time feedback ^{1,5-7}
3-D image guidance using MRI image features with increased intraoperative accuracy	High contrast resolution ^{1,2}	Capability of monitoring intraoperative complications ^{3,4}	Easy to use instruments ⁷
Mobility of microscope with minimal OR modifications	Better differentiation of normal from abnormal tissue ²	High soft-tissue contrast for contrast enhancing tissue ^{4,5}	Relatively inexpensive costs ⁷
Minimal disruption to surgical workflow	High soft-tissue contrast for non-contrast enhancing tissue ⁵	Minor modifications in OR ^{4,5}	
Real-time feedback of fluorescence characteristics		Use of same instruments and equipment ⁵ Fewer limitations in patient positioning ⁵	
Cons	Cons	Cons	Cons
Detection of only surface fluorescence	No real-time feedback ¹	No real-time feedback ³	Low contrast resolution ^{1,6,8}
Limits in fluorescing tumors using δ -ALA	Interrupts surgical flow ¹	Low contrast resolution ^{1,5}	Low spatial resolution ^{2,6,8}
Model updating dependent on sparse data from US	Prolongs time of surgery ¹	Low spatial resolution ⁵	Restricted field of view due to probe placement ²
Administration of δ -ALA with minimal drug side effects	Special shielded room ^{4,5,8}	Increased radiation dose ^{1,5}	Difficulty interpreting results, requiring specialized user ^{1,5-7}
5-20 minutes for uMR generation	Specialized instruments and equipments ⁵	Interrupts surgical flow ³	Artifacts due to blood, air, and instruments ^{6,7}
	Specialized personnel in the OR ⁵	Low soft-tissue contrast for non-contrast enhancing tissue ^{4,5}	
	Limitations in patient positioning ⁵	Artifacts due to patient positioning devices ⁵	
	High costs ^{4,5,8}	Prolongs time of surgery ⁵	
	Limited access to operating field ⁸		

Table 3.3. Technologies for intraoperative updating during brain surgery. Fluorescence-

guided resection with brain shift compensation (FGR-IGW), and intraoperative MRI (iMRI), CT (iCT), and US (iUS).

this study FGR-IGW combines intraoperative feedback from surface fluorescence with a biomechanical model enabled through iUS to update the pMR, providing the neurosurgeon with real-time feedback on tumor fluorescence coregistered with periodically compensated 3-D uMR views for enhanced neuronavigation.

Although this dual-modality system provides a platform for integrating two powerful guidance technologies, some limitations remain. FGR currently detects only the visually apparent surface levels of fluorescence, since thin layers of blood and/or intervening tissue can obscure subsurface fluorescence emissions. As noted with the GS case, not all tumor tissue produces observable PpIX fluorescence (i.e., sarcomatous element of the tumor). As such, the optimal brain tumor population for efficient use of PpIX FGR needs to be determined. We are currently studying various brain tumor histologies in patients undergoing FGR to determine the most appropriate and relevant biologies for efficient accumulation of PpIX to observable levels. In addition, our group is developing intraoperative fluorescent probes to target non-PpIX-fluorescent tumors. We continue our ongoing efforts to develop a software platform to execute the deformation model intraoperatively as efficiently as possible. Our approach exploits intraoperative US to create a sparse data set to drive the model where one US image is acquired before durotomy, followed by a series of intraoperative US images at different stages during the surgery in order to generate corresponding uMR images ¹⁶⁸. We have also utilized a

stereovision system that can provide surface sparse data to improve the generation of uMR with minimal disruption to surgical workflow^{20,21}.

3.5. Conclusion

We present an implementation of a deformation model guided by intraoperatively acquired data in the setting of PpIX fluorescence-guided resection of brain tumors. FGR was used to delineate and guide the resection of fluorescent tissue visually evident within the surgical field. A biomechanical brain deformation model provided updated MR images by assimilating intraoperative data acquired with 3D iUS that improved the correspondence between the volumetric representation of tumor and the fluorescing biomarker of tumor associated with the surgeon's visual field. Post-operative analysis of fluorescence signatures and the updated MR images were complementary in more accurately identifying tumor tissue confirmed histopathologically from resected specimens. We believe that this dual-modality approach which uses a deformation model that compensates for brain shift coregistered with fluorescence imaging can provide the neurosurgeon with an accurate, intuitive platform that improves intraoperative guidance during tumor resection.

Chapter 4. Pre-clinical pharmacological treatment for enhancement of ALA-induced PpIX fluorescence in murine model of glioma

4.1. Introduction

Malignant gliomas account for approximately 70% of primary brain tumors in the United States ¹⁶⁹. Surgical resection plays an important role in treatment and prognosis of patients with brain tumors, with studies showing a correlation between extent of resection and patient survival ^{11,132,170,171}. Current neurosurgical resection of malignant gliomas includes intraoperative 3-D image guidance. A limitation of current image guidance technologies is the degree of intraoperative brain shift, causing a significant registration error between patient physical space and image space ^{17,18,161}. In recent years, large clinical efforts, mostly in Germany and Japan, have used fluorescence characteristics of tumors after exogenous 5-aminolevulinic acid (ALA) administration to guide neurosurgical resection of brain tumors providing real-time neurosurgical guidance ^{12,13,38,39,41,44,132,156}. While this technique is promising, the fluorescence signal from low-grade tumors and certain tumor types is still below detectable levels, and so methods which might increase the production of protoporphyrin IX (PpIX) generation are still needed. Two major techniques have been used to increase PpIX fluorescence: iron chelation therapy and differentiation therapy (e.g., methotrexate, vitamin D) ¹⁷²⁻¹⁷⁸. In this paper, iron chelation to sequester away available iron in the body is tested to see if this would increase the PpIX signal in glioma tumors.

Exogenous administration of ALA overloads the heme biosynthetic pathway, causing accumulation of PpIX to levels which allow visual detection using commercial surgical microscope systems. Studies have shown that PpIX accumulation is selective to high-grade brain tumor over normal tissue ^{39,40,47,122,179}. The reasons for selective PpIX accumulation after ALA administration are many and the causes likely vary with different tumor types, however in the brain the breakdown of the blood-brain barrier is a major factor in increased delivery of ALA ¹⁷⁹.

The ALA-Glioma Study group used fluorescence-guided resection (FGR) for treatment of glioblastoma multiforme, showing a highly-statistically significant difference in extent of resection between patients undergoing FGR compared to standard white-light guided resection ^{12,13,132}. Although these studies showed an increase in extent of resection using FGR as well as a correlation between extent of resection and patient survival, studies have also shed light on a major limitation in ALA-induced PpIX production for FGR: tumor margins containing diffuse tumor cells accumulate significant levels of PpIX, nonetheless these levels are not high enough to be detected with commercial surgical systems ^{26,38,126,156}. The potential for improved detection through enhancing the signal is always present, however this will likely not be in the area of the total light intensity, but rather in the area of enhanced filtering and fluorescence detection, relative to the excitation light.

Significantly increased PpIX levels at tumor margins might lead to more effective FGR and greater extent of resection of previously undetected tumor tissue. Previous *in vitro* work with prostate cancer cells, brain tumor cells, adenocarcinoma cell lines ^{93,176}, bladder and pancreatic cancer cells ¹⁸⁰, skin cell lines ^{177,181,182}, and *in vivo* work with

bladder epithelium¹⁷⁸ and skin tumors¹⁸¹ used iron chelators to increase levels of PpIX fluorescence. Iron chelation reduces the availability of free iron that would be used by the ferrochelatase enzyme for insertion into the PpIX molecule, thereby increasing the net accumulation of PpIX^{91,93}. In this study we used deferoxamine, a well-known iron chelator in clinical use for over 30 years^{183,184}. Deferoxamine is a hexadentate iron chelator originally isolated from the fungus *Streptomyces pylosus*, which forms ferroxamine, a stable 1:1 chelator-iron complex, with subsequent urinary and biliary excretion. Deferoxamine is administered parenterally with reported doses from 20 mg/kg/day to 360 mg/kg/day, with a limit of 6 g/day^{183,185-188}. Some common adverse effects are: local skin reactions, urine discoloration, neurotoxicity, ototoxicity, and skeletal changes^{184,185}. In this report, the ALA-PpIX fluorescence system was studied in a xenograft glioma model with ex vivo analysis of the enhancement ratio. Animals were treated with deferoxamine, to test the hypothesis that iron chelation therapy leads to significant increases in PpIX fluorescence of gliomas.

4.2. Methods

4.2.1 Cell Culture.

A GFP transfected U251 (U251-GFP) human glioma cell line was used in this study. Cells were cultured in Dulbecco's modified eagle's medium (Cellgro, Mediatech, Herndon, Virginia, USA) with 10% fetal bovine serum (Atlanta Biologicals, Lawrenceville, Georgia, USA) 1% (v/v) penicillin-streptomycin (P-S) prepared from a stock solution of

10,000 IU penicillin and 10,000 g/ml streptomycin (Mediatech). Incubation was done in a humidified environment consisting of 95% air and 5% CO₂ at 37° C.

4.2.2 Animal Model

This study was approved by the Dartmouth College Animal Care and Use Committee (IACUC). Intracranial implantation of U251-GFP cells was performed on 6 week-old male athymic nude mice. Mice were anesthetized using a 90:10 mg/kg ratio mixture of ketamine/xylazine and body temperature was maintained using a heating pad during anesthesia. Skull landmarks were exposed via a small scalp incision on the superior part of the cranium. A 1 mm hole in the cranium located 2 mm anterior to the bregma and 2 mm left of the midline was made with a Dremel drill. A needle was subsequently inserted 2 mm deep into the brain via stereotactic frame guidance, and 1×10^6 cells in 10 ml of PBS were injected over a period of 5 minutes using a Hamilton syringe. The needle was retracted and skull cleaned. The drilled hole was covered with bone wax and the scalp incision closed with Vetbond tissue adhesive (J.A. Webster, Inc., Sterling, Massachusetts, USA). Mice were examined daily to ensure proper healing of the scalp.

4.2.3 Chelation Therapy and PpIX Fluorescence Quantification

Mice were separated into two groups: the deferoxamine (DFO) treatment group and the control group, with both receiving ALA. The DFO group received 200-mg/kg of deferoxamine mesylate (Sigma, St. Louis, Missouri, USA) dissolved in 200 ml deionized water administered i.p. at 11, 12, and 13 days after tumor implantation. An equal volume of deionized water was administered i.p. at 11, 12, and 13 days after tumor implantation to

the control group. At day 14 after tumor implantation 100-mg/kg ALA (Sigma) dissolved in PBS was administered to both groups i.p. Two hours after ALA administration mice were sacrificed, their brains resected whole under dim lighting, and sectioned into 1 mm thick coronal slices. The sectioned faces were placed on a fluorescence plate scanner (Typhoon 9410, GE Healthcare Life Sciences) facing the scanner imaging plane. Measurement of PpIX fluorescence was done with a 633 nm excitation laser and 650 nm long pass emission filter, followed with measurements of tissue GFP fluorescence with a 488 nm laser excitation and 526 nm short pass emission filter.

4.2.4 Image Analysis

GFP and PpIX fluorescence contrast in brain tumors was calculated:

$$FC = \frac{SI_{\text{tumor}} - SI_{\text{bkg}}}{SI_{\text{nl}} - SI_{\text{bkg}}} \quad \text{Equation 4.1}$$

where FC refers to fluorescence contrast of tumor; SI_{tumor} refers to an average signal intensity of a region of known tumor tissue; SI_{bkg} refers to an average signal intensity of background; SI_{nl} refers to an average signal intensity of normal brain in the contralateral hemisphere. The coefficient of variation for PpIX fluorescence was calculated:

$$CV = \frac{SD}{SI_{\text{tumor}}} \quad \text{Equation 2.2}$$

where CV refers to the coefficient of variation of tumor; SD refers to the standard deviation of the signal intensity of a region of known tumor tissue. Assessment of a significant difference of the mean GFP fluorescence contrast, mean PpIX fluorescence contrast, and mean coefficient of variation in PpIX fluorescence between the control and DFO treatment groups was done using an unpaired Student's t-test. A total of ten (10)

mice were studied, five (5) for each group. For each mouse, three different regions of tumor tissue were analyzed to determine the SI_{tumor} , for a total of thirty (30) different tumor tissue regions analyzed. A p-value < 0.05 was considered statistically significant. All statistical analyses were done with Stata 10.0 (Stata Corporation, College Station, Texas, USA).

4.3. Results

Following the treatment with DFO and ALA, and extraction and fluorescence scanning of the samples, the regions to be quantified were identified by the GFP fluorescence, indicating positive tumor regions. The PpIX-positive fluorescent tissues co-localized to areas of GFP-positive fluorescent tissue in mice are shown for an example data set in **Figure 4.1**. The GFP signal is only visible in areas of tumor (right slices) and the PpIX is seen in background normal brain, with highlighted areas in the tumor regions.

Fluorescence intensities were quantified from the GFP positive regions and are listed in the summary data of **Table 4.1**.

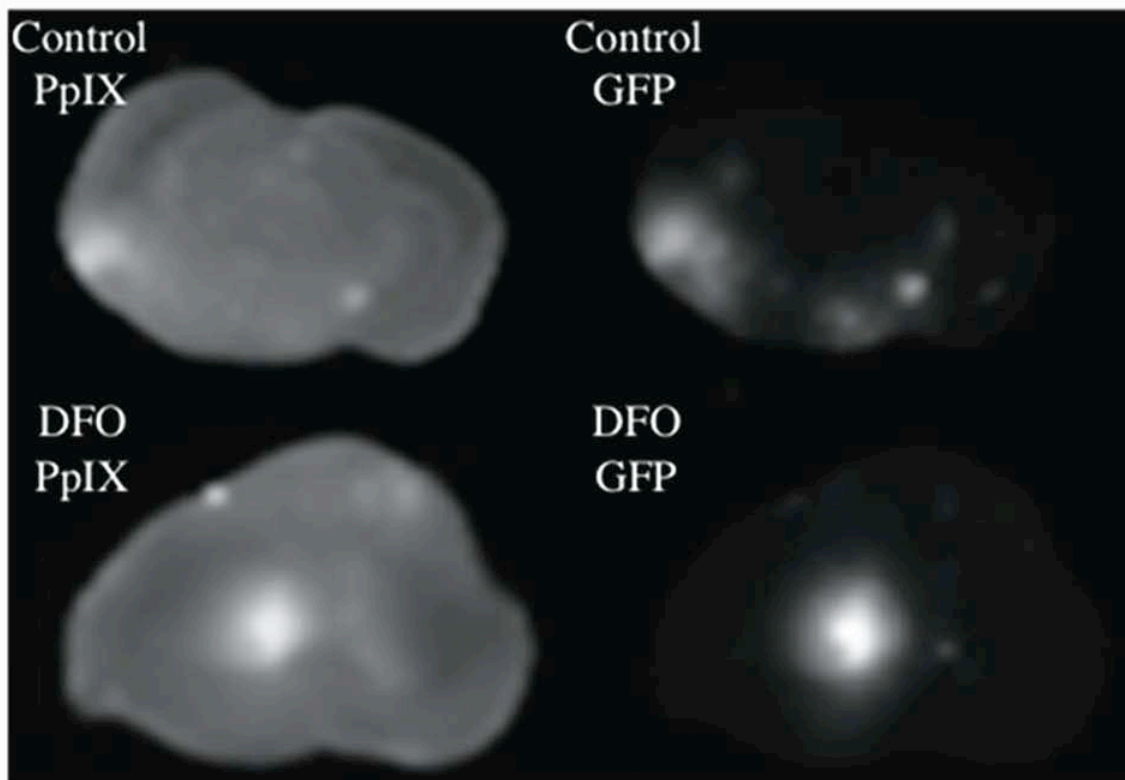


Figure 4.1. U251-GFP coronal brain sections. (Upper) Representative coronal brain section of control animal with PpIX-positive fluorescent tissue co-localized to a fraction of the GFP-positive fluorescent tumor area. (Lower) Representative coronal brain section of DFO-treated animal with PpIX-positive fluorescent tissue co-localized with the majority of GFP-positive fluorescent tissue.

The values for mean GFP fluorescence contrast, mean PpIX fluorescence contrast, and mean coefficient of variation in PpIX fluorescence contrast as well as their corresponding 95% confidence intervals for the DFO and control groups are summarized in **Table 4.1**.

Table 4.1. Mean PpIX fluorescence coefficient of variation and GFP and PpIX fluorescence contrast		
	Mean	95% C.I. of the mean
PpIX Coefficient of Variation		
Control Group	7.4×10^{-2}	$5.1 \times 10^{-2} - 9.7 \times 10^{-2}$
DFO Group	6.3×10^{-2}	$4.1 \times 10^{-2} - 8.4 \times 10^{-2}$
GFP Fluorescence Contrast		
Control Group	7.6	6.1 – 9.1
DFO Group	6.9	6.0 – 7.8
PpIX Fluorescence Contrast*		
Control Group	1.9	1.6 – 2.3
DFO Group	2.9	2.9 – 3.4

*Statistically significant, p-value = 0.0020

Table 4.1. Mean PpIX fluorescence coefficient of variation and GFP and PpIX fluorescence contrast.

The GFP levels (t-test associated P -value = 0.37) and coefficient of variation (t-test associated P -value = 0.44) were not significantly different between control and DFO treatment groups. The PpIX fluorescence values were significantly different between the groups (t-test associated P -value = 0.0020), indicating a difference exists between the control and DFO treatment groups, with a 50% increase in mean PpIX fluorescence contrast after chelation treatment (**Figure 4.2**).

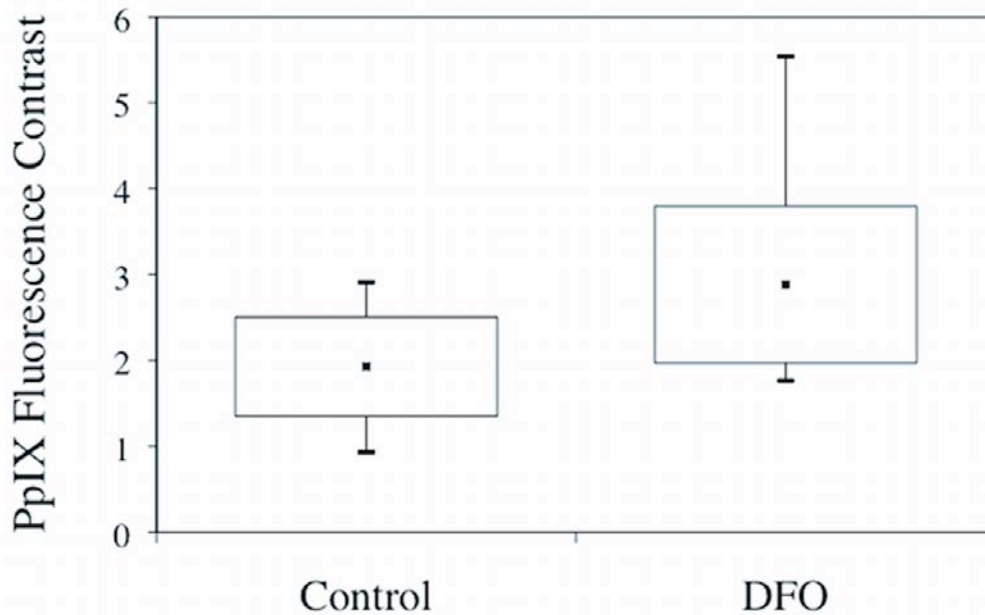


Figure 4.2. Chelation treatment effects are shown with a box and whisker diagram of PpIX fluorescence contrast in tumor tissue for both control and DFO treatment groups. Unpaired Student's t-test associated p-value = 0.0020. Box and whisker diagram represents mean ((\blacksquare) square); +/- 1 standard deviation-top and bottom of each box, respectively; maximum and minimum-vertical bars extending from each box; n=30.

4.4. Discussion

Extent of tumor resection plays an important role in prognosis and survival of patients with malignant gliomas^{9-13,26,132} and FGR of brain tumors is a promising technology to increase the extent of surgical resection of malignant brain tumors^{12,13,26,36,132,144}.

Nevertheless, a major limitation of the ALA-PpIX system for FGR is the lack of detectable levels of PpIX fluorescence at tumor margins using commercial microscope

systems^{26,126,156}. Therefore, methods that increase tumor PpIX contrast are critical for this procedure to gain wider utility.

Here an *in vivo* study was completed using deferoxamine-mediated iron chelation therapy to quantify the increase in levels of PpIX fluorescence after exogenous administration of ALA in a human glioma xenograft model. Deferoxamine was used in this study because of the good safety profile and routine use in clinical practice for treatment of acute and chronic iron overload disease^{184,189}. No significantly adverse drug effects were noticed in the DFO group compared to the control group after deferoxamine administration over a period of three days.

Both control and DFO treatment groups demonstrated co-localization of PpIX and GFP fluorescence. A major cause of varying levels of PpIX fluorescence is the number of viable tumor cells present (e.g., tumor bulk vs. tumor margin). Although animals in this study were injected with the same batch of U251-GFP cells, differential *in vivo* growth of implanted cells might be a confounding factor in quantifying PpIX fluorescence. Indications were that the tumor sizes and locations were not altered by the DFO therapy. With no significant difference in GFP fluorescence contrast, viable tumor cell populations can be assumed to be approximately the same for both groups.

PpIX fluorescence contrast between control and DFO treatment groups was subsequently measured and a statistically significant difference in the mean PpIX fluorescence contrast was determined (t-test associated p-value = 0.0020). These results showed a 50% increase in PpIX fluorescence contrast as a result of iron chelation therapy. In addition, as evidenced by the lack of a statistically significant difference in the mean coefficient of variation in PpIX fluorescence, the increase in fluorescence cannot be

attributed to a more homogeneous production, but appears to be an overall increase throughout the tumor.

It was anticipated that the iron chelator, deferoxamine, would temporarily sequester available iron stores away from tumor cells, thus decreasing the ability of ferrochelatase to reduce PpIX levels¹⁹⁰. The exact mechanisms causing the increased PpIX fluorescence after iron chelation therapy were not investigated, but have been well studied in the past. This proof of concept study sought to establish whether a significant increase in PpIX fluorescence of a malignant glioma model occurs with iron chelation therapy, and if clinical use is warranted. An optimal deferoxamine dose to achieve maximal increase in PpIX fluorescence without significant drug side effects was not determined, but will likely be determined by human clinical factors rather than mouse tolerance levels. Relevant clinical factors affecting selection of optimal deferoxamine dose for enhancing PpIX fluorescence might include but not be limited to: adverse drug reactions, i.e., local skin reactions, organ toxicity, drug counter indications, i.e., concomitant high dose vitamin C and deferoxamine treatment, pregnancy, therapeutic benefit-to-cost ratio, and drug tolerance^{184,188}.

4.5. Conclusions

In summary, exogenous administration of ALA induces selective accumulation of PpIX in brain tumor compared to normal brain tissue. Studies using the ALA-PpIX system for FGR provide exciting results about increases in extent of tumor resection in malignant gliomas. Nevertheless, tumor margins are known to not display detectable levels of fluorescence using commercial surgical microscope systems. This study used

iron chelation treatment in an animal model of malignant glioma, and found a 50% significant increase in PpIX fluorescence contrast. Future studies will seek to find the optimal deferoxamine dose to achieve a maximal increase in PpIX fluorescence. Further work will also test if iron chelation therapy significantly increases PpIX fluorescence in cases of gliomas without an impaired blood-brain barrier.

Chapter 5. Diagnostic capabilities of a quantitative approach for ALA-induced PpIX fluorescence guided resection of intracranial tumors

5.1. Introduction

Biomarkers that are specific to malignancies and can be imaged or otherwise detected during intraoperative procedures hold significant promise in the treatment and management of disease⁴⁵. Indeed, several clinical studies have shown that high-grade gliomas accumulate the endogenous fluorescent biomarker, protoporphyrin IX (PpIX), specifically and in concentrations sufficient for visual detection during surgery under blue light exposure after exogenous administration of 5-aminolevulinic acid (ALA)^{12,13,38,121,139,191-194}. The net effect has been the realization of a tumor-specific biomarker for surgical guidance which has improved completeness of resection of high-grade gliomas and led to statistically significant increases in progression-free survival in this patient population in a randomized, controlled Phase III clinical trial^{12,13,132}. Unfortunately, the same has not been true for lower grade disease where the clinical impact in terms of prolonging survival could be more substantial^{38,194}. Here we show for the first time that concentrations of PpIX exist in intracranial tumors that are below the threshold of human visual perception and that this biomarker, when detected quantitatively, offers classification efficiencies of up to 97% with corresponding sensitivities and specificities greater than 90%, which far exceed the diagnostic performance of the human eye and current fluorescence imaging technologies.

5.2. Methods

5.2.1 Patient Selection

The institutional review board (IRB) governing the participation of human subjects in research at Dartmouth-Hitchcock Medical Center approved our fluorescence-guided intracranial tumor resection protocol. All patients participated under informed consent. Inclusion criteria were preoperative diagnosis of low- or high-grade glioma, meningioma, or metastatic brain tumor; tumor judged suitable for open cranial resection; age equal to or greater than 18 years; and patient ability to provide informed consent. Exclusion criteria included pregnancy or breast feeding; history of cutaneous photosensitivity or, hypersensitivity to porphyrins; photodermatosis, exfoliative dermatitis or porphyria; history of liver disease within the last 12 months; ALT, AST, ALP or bilirubin levels greater than 2.5 times the normal limit at any time during the previous 2 months; plasma creatinine in excess of 180 $\mu\text{mol/L}$; patient inability to comply with the photosensitivity precautions associated with the study; and serious associated psychiatric illness. Patients were administered an oral dose (20 mg/kg body weight) of 5-aminolevulinic acid (ALA) (DUSA Pharmaceuticals, Tarrytown, NY, USA) dissolved in 100 ml of water approximately three hours prior to the induction of anesthesia. Preoperative, high-resolution contrast-enhanced T1- and/or T2-weighted axial images were acquired and used for navigational guidance.

5.2.2 Intraoperative probe

We used a fiber-optic probe connected to a spectrometer to measure the response of brain tissue excited with blue light (wavelength: $\lambda = 405$ nm) followed by interrogation with broadband white light ($\lambda = 450\text{--}720$ nm) delivered through the fiber-optic probe tip in order to compensate for signal losses due to light absorption and scattering by the tissue using novel light-transport modeling methods⁷⁰. The relative contributions of oxy-hemoglobin and deoxy-hemoglobin to the total light absorption were determined *in situ* using the measured white-light reflectance spectrum fitted to a diffusion model of the reflectance where the intrinsic absorption spectra of each of these proteins were assumed to be known.

A mathematical model⁷⁰ was then used to quantify the absolute concentration of PpIX based on the measured fluorescence spectrum. Since the fluorescence measurements are distorted by variations in tissue optical properties, quantitative determination of the concentration of fluorescing molecules requires knowledge of the absorption and scattering spectra of the tissue being sampled. Moreover, PpIX is not the only molecule contributing to the measured fluorescence spectrum (other contributors include tissue auto-fluorescence and photoproducts such as photoporphyrin resulting from PpIX photobleaching¹⁹⁵). However, the spectral shapes of the primary fluorophores of interest are known, which allows spectral decomposition to be used to determine their relative contributions, and in the case of PpIX, the absolute concentration. By incorporating these light-transport modeling methods which eliminate the distorting effects of variations in tissue optical properties and account for the presence of multiple fluorescent species, quantitative measurements of PpIX concentration (C_{PpIX}) can be obtained intraoperatively and *in vivo* with an unprecedented degree of sensitivity and fidelity.

The handheld probe developed for fluorescence and white light reflectance measurements was used intraoperatively⁷⁰. Briefly, four optical fibers, each with a 200 μm diameter core spaced (linearly) 260 μm apart, were bundled into an 18-gauge stainless steel shaft forming the tissue-contact end of the probe. The fibers were connected to the data acquisition system through a 3 m cable. White light reflectance and fluorescence emission spectrum were collected during each measurement following sequential white light (wavelength range from 450-720 nm) and fluorescence excitation light (at 405 nm) exposure through the fiber-optics, with one fiber connected to a spectrometer onboard the data acquisition system.

The absolute concentration of PpIX (C_{PpIX}) was calculated with a light-transport model which extracted the quantitative fluorescence spectrum from the intraoperative recordings. The tissue optical properties (i.e., absorption and reduced-scattering coefficients) were estimated from the white light reflectance to correct for their distorting effects on the fluorescence emission signal by minimizing the error between probe measurements and a spectrally constrained model of the diffuse reflectance in a Levenberg-Marquardt algorithm. The resulting quantitative (and corrected) fluorescence spectrum was estimated from the model and used to determine biomarker (i.e., PpIX) concentration through a fluorescence basis spectrum equivalent to unit concentration ($\mu\text{g/ml}$).

Briefly, the fluorescence model assumed that 1) absorption at the excitation wavelength is much larger than absorption at the fluorescence emission wavelengths (i.e., $\lambda_{a,x} \gg \lambda_{a,m}$ where excitation and emission wavelengths are denoted by the subscripts x and m, respectively) because the fluorescent biomarker's contribution to $\lambda_{a,x}$ is small

when compared to the high absorption of hemoglobin in the range 380 – 450 nm; and 2) fluorescence and reflectance photons travel similar path lengths given the same fiber-optic distance (and $\lambda_{a,x} \gg \lambda_{a,m}$). Under these assumptions, the measured fluorescence, $F_{x,m}$, has a linear relationship with reflectance at the emission wavelength, R_m .

$$F_{x,m} = S R_m \quad \text{Equation 5.1}$$

where S represents the fraction of photons re-emitted as fluorescence which is a function not only of the fluorophore concentration but also the tissue optical properties at the excitation wavelength.

The quantitative fluorescence spectrum was extracted from the spectrally constrained model, yielding an emission spectrum, f , with the distorting effects of variations in optical properties removed. This corrected fluorescence emission spectrum was used to quantify biomarker (i.e., PpIX) concentration, c , through a fluorescence basis spectrum, b , equivalent to unit concentration ($\mu\text{g/ml}$) from the relation,

$$f = b c \quad \text{Equation 5.2}$$

where f and b are column vectors and c is computed by pseudo-inversion as

$$c = (b^T b)^{-1} b^T f \quad \text{Equation 5.3}$$

Generalization to N fluorescent biomarkers, each with different spectra, is possible by forming a basis matrix, $B = [b_1 \ b_2 \ \dots \ b_N]$, composed of the individual basis spectra for each fluorescent biomarker, and calculating biomarker concentrations, $c = [c_1 \ c_2 \ \dots \ c_N]^T$.

5.2.3 Surgical Procedure

The patient's head was prepared and registered with a StealthStation® Treon® image-guidance system (Medtronic, Louisville, CO, USA) following standard practice. A

Zeiss® OPMI Pentero® surgical microscope (Carl Zeiss Surgical GmbH, Oberkochen, Germany) modified for fluorescence-guidance with a 400 nm wavelength source for excitation and a 620-710 nm bandpass filter to record fluorescence emissions on a sensitive 3-chip charge coupled device (CCD) camera, was also co-registered with the surgical field.

At various points during resection, the surgeon switched from white to blue light exposure to visualize fluorescence. Biopsy specimens were collected at the beginning, middle, and end of resection, as well as in both fluorescing and non-fluorescing regions within the preoperatively planned resection volume, and were identified as corresponding to either the center or the edge of tumor. Biopsy specimens were separated into three equal parts for further processing as follows: one part was placed in formalin; another part was placed in Optimal Cutting Temperature (OCT) compound and frozen in liquid nitrogen; and the final part was placed in a cryogenic vial and frozen in liquid nitrogen. Briefly, immediately prior to biopsy acquisition, the surgeon placed the intraoperative probe on the location of the intended specimen and performed the intraoperative probe recordings. Intraoperative probe data was recorded in <0.5 seconds and immediately converted into quantitative PpIX concentrations (i.e., C_{PpIX}) in approximately 2 seconds. Control data was also acquired in each case consisting of spectroscopic measurements in normal brain (of indeterminate sub-types) or normal dura.

Digital images were recorded under white and blue light for each biopsy acquisition and the site was assigned a fluorescence score from 0 to 4 (0 = no fluorescence, 1 = minimal fluorescence, 2 = moderate fluorescence, 3 = high fluorescence, 4 = very high fluorescence) based on the impression of the surgeon (blinded to the quantitative

measurement) of the visible fluorescence before the tissue was removed. Biopsy specimens were immediately separated into three equal parts for further processing. Resection was continued until the surgeon judged that no more malignant tissue that could be safely removed was present.

5.2.4 Histopathology

Histopathological analysis was performed on formalin fixed paraffin embedded biopsy tissue specimens processed for hematoxylin and eosin (H&E) staining. A neuropathologist (BTH) was blinded to the final pathological diagnoses on all cases. Each H&E tissue section was assessed for the presence of tumor cells, necrosis, and reactive astrocytosis, and subsequently classified as normal or abnormal (tumor) tissue based on World Health Organization (WHO) histopathological criteria. Biopsy specimens were classified into five categories: normal tissue, low-grade glioma (WHO grade I or II), high-grade glioma (WHO grade III or IV), meningioma (WHO grade I or II), and metastasis. A sixth diagnostic category, labeled ‘all tumors’, was introduced to group all abnormal biopsy specimens together for comparison with the normal control measurements.

5.2.5 Data Processing

Data processing was performed using MATLAB® software (Version R2009b, The Mathworks, Inc., Natick, MA, USA). The following five diagnostic variables were calculated to determine the diagnostic variable with the best classification efficiency: C_{PpIX} , A_{615} , A_{660} , P_{635} and P_{710} . C_{PpIX} corresponds to the quantitative measurements of PpIX

concentration derived from the light-transport modeling. A_{615} and A_{660} correspond to the total light intensity associated with the integration of the fluorescence emission spectrum from $\lambda = 615$ nm to $\lambda = 740$ nm and from $\lambda = 660$ nm to $\lambda = 740$ nm, respectively, whereas P_{635} and P_{710} refer to the peak intensities of the fluorescence emission spectrum at $\lambda = 635$ nm and $\lambda = 710$ nm, respectively.

5.2.6 Statistical Analysis

Statistical analyses were performed with Stata 10.1 software (Stata Corporation, College Station, TX, USA). Wilcoxon rank-sum (Mann-Whitney) tests were used to compare differences in fluorescence variables between tissue categories. We used receiver operating characteristic (ROC) analysis to summarize the diagnostic performance of the fluorescence variables. The cut-off value with the best discriminative ability was chosen as the point on the curve closest to the upper left corner of the ROC graph¹⁹⁶. Two-sided P value <0.05 are described as statistically significant.

5.3. Results

Briefly, we used a fiber-optic probe connected to a spectrometer to measure the response of brain tissue excited with blue light (wavelength: $\lambda = 405$ nm) followed by interrogation with broadband white light ($\lambda = 450$ – 720 nm) delivered through the fiber-optic probe tip in order to compensate for signal losses due to light absorption and scattering by the tissue using novel light-transport modeling methods⁷⁰. The relative contributions of oxy-hemoglobin and deoxy-hemoglobin to the total light absorption were determined in situ using the measured white-light reflectance spectrum fitted to a

diffusion model of the reflectance where the intrinsic absorption spectra of each of these proteins were assumed to be known.

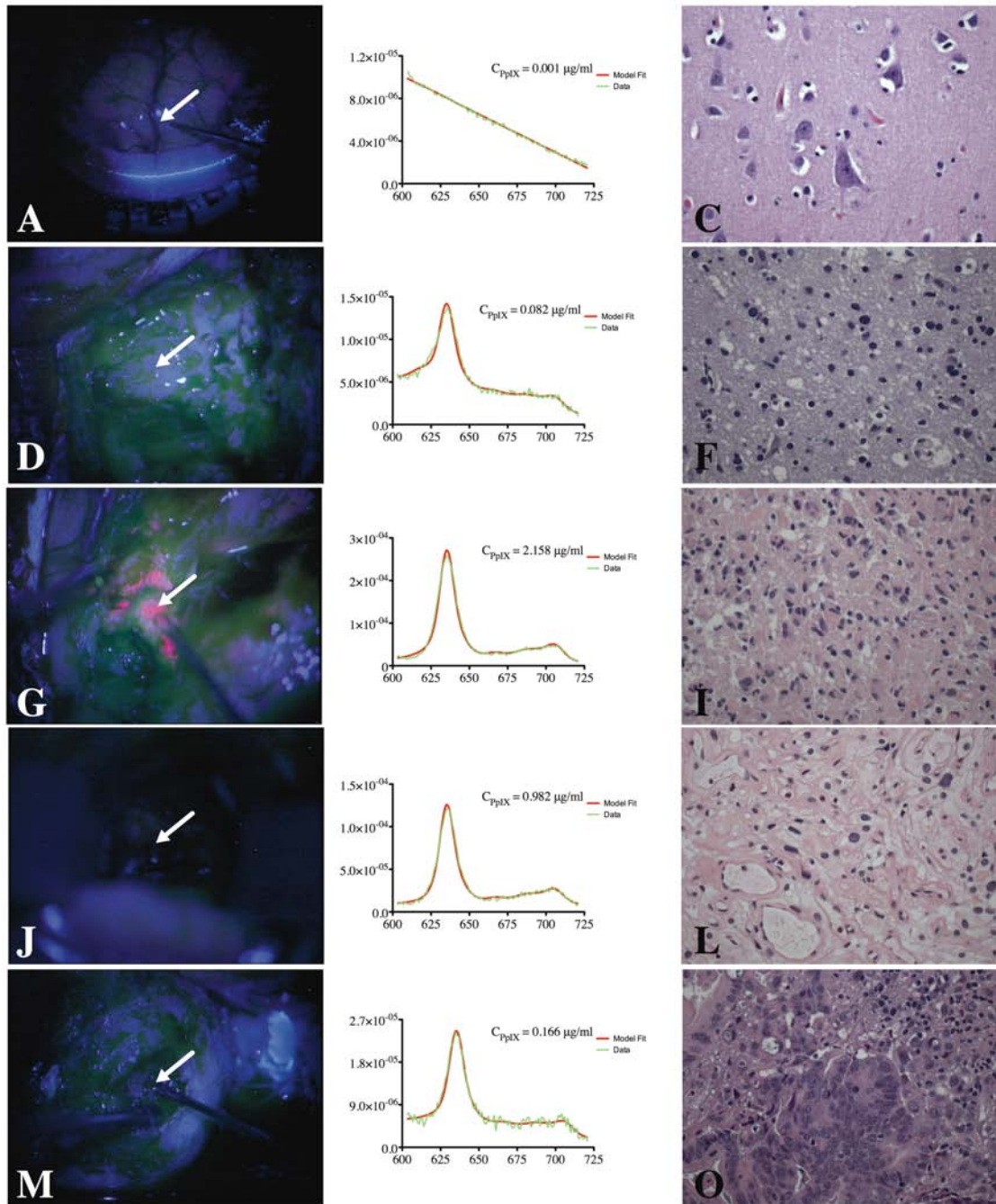


Figure 5.1. In vivo spectroscopic measurements of ALA-induced PpIX fluorescence during intracranial tumor resection surgeries. (Left) Intraoperative fluorescence images of the resection cavity visible to the surgeon through the operating microscope under blue-light exposure. White arrows point to the location of the hand-held probe tip where the spectroscopic measurements and tissue specimens were acquired. (Middle) Quantitative in vivo fluorescence spectra measured at the location of each specimen (the characteristic spectral features of PpIX, i.e., emission peaks at $\lambda = 635$ nm and $\lambda = 710$ nm, are evident). (Right) H&E histological tissue sections of the specimens (40x). From top to bottom: A-C) normal cortex; D-F) low-grade glioma; G-I) high-grade glioma; J-L) meningioma; M-O) metastasis. The high-grade glioma displays visible levels of fluorescence while the low-grade glioma, meningioma, and metastasis exhibit no visible fluorescence; all of the tumor histologies have measurable C_{PpIX} relative to normal cortex, whose spectrum is devoid of the characteristic signal features of PpIX and its associated photoproducts. Ordinate, $\text{nm}^{-1}\text{cm}^{-1}$; abscissa, nm.

A mathematical model⁷⁰ was then used to quantify the absolute concentration of PpIX based on the measured fluorescence spectrum. Since the fluorescence measurements are distorted by variations in tissue optical properties, quantitative determination of the concentration of fluorescing molecules requires knowledge of the absorption and scattering spectra of the tissue being sampled. Moreover, PpIX is not the only molecule contributing to the measured fluorescence spectrum (other contributors include tissue auto-fluorescence and photoproducts such as photoporphyrin resulting from PpIX photobleaching¹⁹⁵). However, the spectral shapes of the primary fluorophores of interest

are known, which allows spectral decomposition to be used to determine their relative contributions, and in the case of PpIX, the absolute concentration. By incorporating these light-transport modeling methods which eliminate the distorting effects of variations in tissue optical properties and account for the presence of multiple fluorescent species, quantitative measurements of PpIX concentration (C_{PpIX}) can be obtained intraoperatively and in vivo with an unprecedented degree of sensitivity and fidelity.

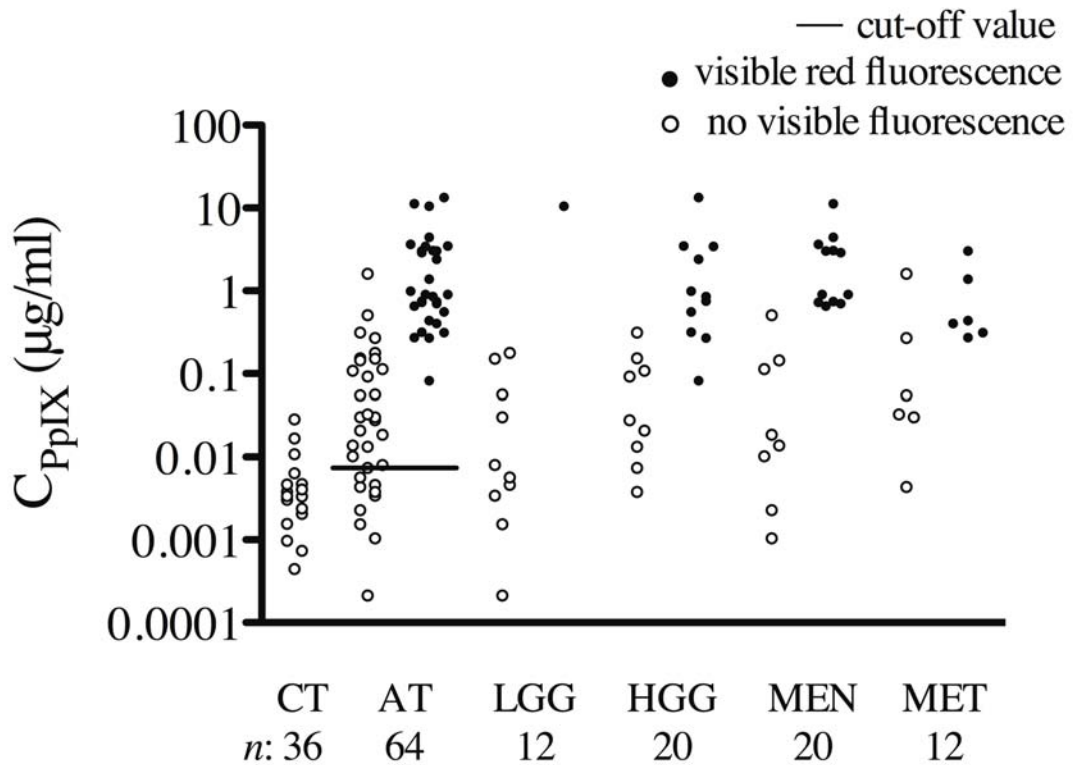


Figure 5.2. Concentration of ALA-induced PpIX, C_{PpIX} . Circles (●) represent the C_{PpIX} value calculated in vivo using the light-transport model for each location where a biopsy specimen was collected, with filled circles representing biopsy specimens with visible fluorescence, (+)F, and open circles representing biopsy specimens with no visible

fluorescence, (-)F. The black line (-) represents the cut-off value determined from the quantitative probe measurements, and n represents the number of locations measured for controls (CT), all tumors combined (AT), and the four tumor categories: low-grade gliomas (LGG), high-grade gliomas (HGG), meningiomas (MEN), and metastases (MET). The ordinate is logarithmic. Statistically significant differences in C_{PpIX} were found between normal and abnormal intracranial tissue: all tumors ($P < 0.0001$), low-grade gliomas ($P < 0.05$), high-grade gliomas ($P < 0.0001$), meningiomas ($P < 0.0001$), and metastases ($P < 0.001$).

Table 5.1. Diagnostic variables

Group	Vis AUC (s.e.)	C_{PpIX} AUC (s.e.)	A_{615} AUC (s.e.)	A_{660} AUC (s.e.)	P_{635} AUC (s.e.)	P_{710} AUC (s.e.)
AT	0.73 (0.03)	0.95 (0.02)	0.54 (0.06)	0.54 (0.06)	0.60 (0.06)	0.57 (0.06)
LGG	0.54 (0.04)	0.75 (0.12)	0.20 (0.11)	0.18 (0.11)	0.32 (0.14)	0.17 (0.11)
HGG	0.78 (0.06)	0.96 (0.03)	0.54 (0.11)	0.54 (0.11)	0.65 (0.11)	0.61 (0.11)
MEN	0.80 (0.06)	0.99 (0.02)	0.70 (0.09)	0.70 (0.09)	0.73 (0.09)	0.73 (0.09)
MET	0.75 (0.08)	0.98 (0.02)	0.63 (0.14)	0.59 (0.15)	0.67 (0.14)	0.67 (0.14)

Receiver operating characteristic (ROC) analysis of each diagnostic variable in the five categories of pathogenic tissues. Vis, qualitative visual imaging; AUC, area under the curve. AT = all tumors, LGG = low-grade gliomas, HGG = high-grade gliomas, MEN = meningiomas, MET = metastases; standard error (s.e.) of the ROC AUC (in parenthesis)

Table 5.1. Diagnostic variables.

Table 5.2. ROC analysis for C_{ppIX} as a diagnostic variable							
Groups	CO ($\mu\text{g/ml}$)	Classification Efficiency (%)	ROC AUC	Sn (%)	NPV (%)	Sp (%)	PPV (%)
AT	0.0074	87	0.95	84	77	92	95
LGG	0.0034	76	0.75	75	57	80	90
HGG	0.0074	93	0.96	95	89	89	89
MEN	0.0010	97	0.98	100	100	93	95
MET	0.0302	95	0.97	92	89	100	100

Summary of ROC analysis of C_{ppIX} as a diagnostic variable. C_{ppIX} threshold values (in $\mu\text{g/ml}$) with corresponding classification efficiencies, AUCs, sensitivities (Sn), negative predictive values (NPV), specificities (Sp), and positive predictive values (PPV) are tabulated. AT = all tumors, LGG = low-grade glioma, HGG = high-grade glioma, MEN = meningiomas, MET = metastases; CO, cut-off value.

Table 5.2. ROC analysis for C_{ppIX} as a diagnostic variable

The majority of work^{52,57,66} using fluorescence spectroscopy as a tissue characterization tool (e.g., in brain tumor studies) has been based on measurements of the raw emission spectrum without correcting for variations in tissue optical properties or the presence of other fluorophores. In order to assess the added value of our quantitative measurements, raw spectroscopic variables were also considered and their relative diagnostic performances were evaluated. Specifically, the variables A_{615} , A_{660} , P_{635} and P_{710} were computed from the raw fluorescence emission spectrum.

Measurements were obtained under an IRB-approved protocol with informed consent during the open cranial surgeries of fourteen (14) subjects with a range of tumor histologies: low-grade (2) and high-grade (3) gliomas, meningiomas (6), and carcinoma of the lung metastases (3). In vivo spectra and corresponding tissue biopsies were

recorded at distinct stages of the surgical procedure and were identified as corresponding to either the center or the edge of tumor in an effort to maximize the sampling extent of each lesion. Tissue samples from each biopsy site were also assessed histologically using hematoxylin and eosin (H&E) staining (**Figure 5.1**). We found a statistically significant increase ($P < 0.05$) in C_{PpIX} across all of the tumor categories when compared to the normal controls. Figure 2 presents C_{PpIX} on a logarithmic scale for each tissue category, since the normal control values of C_{PpIX} can be up to four orders of magnitude smaller than in tumor. The other diagnostic variables – A_{615} , A_{660} , P_{635} and P_{710} – did not show similar potential for discriminating between normal and abnormal intracranial tissue.

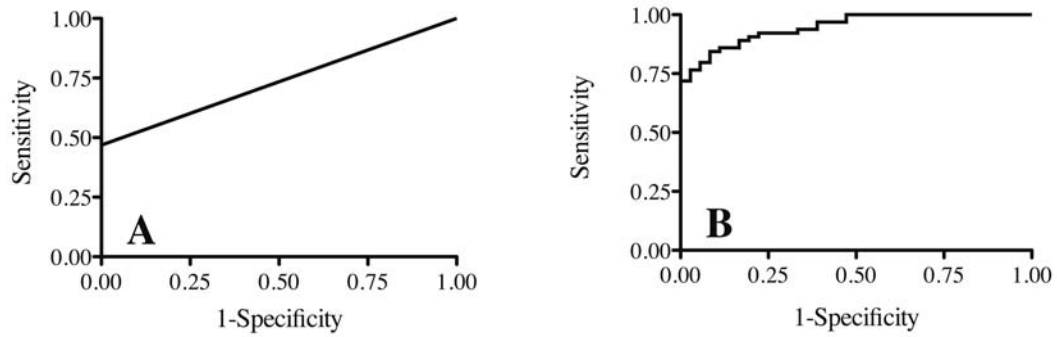


Figure 5.3. ROC analysis of intraoperative detection of ALA-induced PpIX. a) ROC curve for all tumors using visible in vivo fluorescence as a diagnostic variable (AUC = 0.73 (0.03)). b) ROC curve for all tumors using quantitative in vivo PpIX concentration, C_{PpIX} , as a diagnostic variable (AUC = 0.95 (0.02)).

We used ROC analysis¹⁹⁶ to further assess the diagnostic performance of the fluorescence variables listed in **Table 5.1**. We found that C_{PpIX} stood out as the most

accurate diagnostic variable based on an area-under-the-curve (AUC) metric. In fact, C_{PpIX} discriminated abnormal from normal tissue with an AUC of 0.95(0.02) compared to AUCs of 0.54(0.06), 0.54(0.06), 0.60(0.06) and 0.57(0.06) (standard error in parenthesis) for A_{615} , A_{660} , P_{635} and P_{710} , respectively. As summarized in **Table 5.2**, ROC analysis of C_{PpIX} as a diagnostic biomarker resulted in classification efficiencies of 87% for all tumors, 76% for low-grade gliomas, 93% for high-grade gliomas, 97% for meningiomas, and 95% for the metastases group (**Figure 5.3B**).

State-of-the-art clinical detection of PpIX during open cranial tumor resection surgery is based on broad-beam blue light illumination and human visual perception and/or image capture (with a CCD) of the resulting fluorescence observed through the optics of the operating microscope. We have compared the sensitivity and specificity of this qualitative visual imaging approach with the quantitative fluorescence measurements presented here in the same cohort of patients (**Figure 5.3A**). Specimens were assigned a fluorescence score from 0 to 4 (0 = no fluorescence, 1 = minimal fluorescence, 2 = moderate fluorescence, 3 = high fluorescence, and 4 = very high fluorescence) based on the impression of the surgeon (blinded to the quantitative measurement) of the visible fluorescence before the tissue was removed. The optimal classification efficiency was 66% (specificity=100%, sensitivity=47%, positive predictive value=100%, negative predictive value=51%, cut-off value: fluorescence score=1, i.e., minimal level of observed fluorescence) when using the surgeon's visual assessment, compared to a classification efficiency of 87% (specificity=92%, sensitivity=84%, positive predictive value=95%, negative predictive value=77%, cut-off value: $C_{\text{PpIX}} = 0.0074 \mu\text{g/ml}$) when using the quantitative fluorescence measurements in the all tumors category. Further,

more than 81% (57/70) of the quantitative fluorescence measurements that were below the threshold of the surgeon's visual perception were classified correctly in an all tumors analysis. **Figure 5.3** shows ROC curves comparing the qualitative visual approach with the quantitative C_{PpIX} data which is significantly more accurate (quantitative approach: $\text{AUC} = 0.95(0.02)$, visible approach: $\text{AUC} = 0.73(0.03)$; $P < 0.0001$).

5.4. Discussion

Here we show that quantification of fluorescence signals measured intraoperatively and in vivo after accumulation of exogenously-enhanced PpIX yields a highly specific and sensitive biomarker for intracranial tumors that holds promise as a diagnostic indicator for informing resection decisions during neurosurgery. Previous studies have demonstrated that this biomarker accumulates with high specificity and in sufficient concentrations in high-grade glioma to allow visual fluorescence detection, and that this improves resection completeness and concomitantly disease-free survival^{12,13}. However, current fluorescence imaging technologies (including the human visual system) do not take full advantage of the biological targeting of ALA-induced PpIX^{38,46,191,192,194}. More specifically, we have shown that quantitative in vivo measurements based on a light-transport modeling approach, which corrects for the marked distorting effects of variations in tissue optical properties on the fluorescence emission spectrum and intensity, improves substantially the ROC performance of PpIX as a brain tumor diagnostic across a range of histologies.

Our work demonstrates that PpIX fluorescence is a more sensitive and specific biomarker for intracranial tumors than previously appreciated, thus promoting further

work into understanding of the molecular basis of the cellular pathways involved in preferential ALA-induced PpIX accumulation in tumors per se. Importantly, the data presented here demonstrate that the biological targeting of ALA-induced PpIX fluorescence extends to low-grade gliomas with diagnostic fidelity – a finding which reverses current thinking that these tumors are not amenable to fluorescence-guided resection with this particular biomarker^{38,194}.

Currently, intraoperative tumor tissue detection relies on visual white light inspection, pre-operative image-guidance, intraoperative imaging¹⁹⁷ including qualitative observation of fluorescence^{13,191,192}, and/or time-consuming, ex vivo diagnosis by a pathologist¹⁹⁸. Here we show the advantage of a light-transport modeling-based measurement approach compared to four direct but uncorrected spectroscopic metrics for intraoperative fluorescence-based tumor detection. Quantitative PpIX concentration (C_{PpIX}) yielded the best classification efficiency (i.e., 87%) as a diagnostic variable for the category with all tumor histologies with a high specificity (i.e., the probability of classifying tissue as normal tissue given that it is normal tissue) of 92%, a sensitivity (i.e., the probability of classifying tissue as abnormal tumor tissue given that it is abnormal tumor tissue) of 84%, a positive predictive value (i.e., the probability that tissue is abnormal tumor tissue given that it is classified as abnormal tumor tissue) of 95%, and a negative predictive value (i.e., the probability that tissue is normal given that it is classified as normal tissue) of 77%^{192,199}. The derived specificity, sensitivity, negative predictive value, and positive predictive value are dependent on the chosen cut-off value. We have provided the cut-off values (**Table 5.2**) using a standard methodology for determining the optimal classification efficiency¹⁹⁶. One could increase the specificity at the cost of decreasing the

sensitivity of our quantitative fluorescence approach by choosing a different cut-off value. Our quantitative approach also showed superior diagnostic detection of abnormal tissue in intracranial tumors compared to qualitative assessment of the visible fluorescence (classification efficiency: $C_{\text{PpIX}} = 87\%$ vs. visible = 66%; AUC: $C_{\text{PpIX}} = 0.95$ vs. visible = 0.73, $P < 0.0001$).

It is important to note that this study was performed only on individuals with a diagnosis of intracranial tumor. As a result, the prevalence of the disease under study (i.e., the total number of abnormal tumor sites interrogated for analysis divided by the total number of both normal and abnormal sites interrogated) was high. Under certain assumptions (e.g., a truly dichotomous disease status), sensitivity and specificity are independent of disease prevalence, whereas predictive values are highly dependent on disease prevalence¹⁹⁹. The purpose of this study was to demonstrate that our quantitative approach, when compared to the subjective approach in ALA-induced PpIX FGR, provides more accurate tumor tissue identification. Since this technique is intended for use on patients with a presumed preoperative diagnosis of intracranial tumor using conventional neurosurgical technique (e.g., MR image-guidance), prevalence of the disease will always be high, and as such, predictive values would be expected to remain within a diagnostically acceptable, high range. We are currently enrolling more patients to validate the results of our quantitative approach.

5.5. Conclusions

We believe that this quantitative approach for intraoperative in vivo measurement of PpIX concentrations opens the door to real-time delineation and diagnosis of intracranial tumor histologies beyond high-grade gliomas^{13,38,192-194}. We have used this approach as an adjuvant to standard white-light and qualitative fluorescence image-guided resection in the first demonstration of truly quantitative surgical guidance. Further, if the concentration of PpIX can be quantitatively imaged over the entire resection cavity during surgery, the approach is likely to increase not only the completeness of resection but also the frequency with which complete resections can be safely achieved in tumor surgeries, including those for low-grade gliomas, where the impact on patient survival could be substantial²⁰⁰.

Chapter 6. Quantitative multiple biomarker optical approach for intraoperative guidance in fluorescence guided resection of gliomas

6.1. Introduction

Gliomas are the most common primary brain tumors, accounting for over 60% of all cases. More efficient and accurate tumor detection strategies can improve diagnosis, and lead to advances in the treatment and management of disease^{11,67,201-203}. Biomarkers hold therapeutic and diagnostic promise; and in particular, biomarkers for intraoperative tumor detection^{67,191,203,204}, in which extent of resection is a significant factor influencing local recurrence of disease and prognosis^{9,11,13,205}.

Optical methods offer a wide range of detection technologies, and strategies that maximally exploit tumor-specific optical biomarkers have the potential to increase tumor detection accuracies, improving intra-operative *in vivo* diagnostics and therapeutic benefit. For example, high-grade gliomas accumulate the endogenous biomarker protoporphyrin IX (PpIX) following exogenous administration of 5-aminolevulinic acid (ALA), resulting in increased tumor tissue fluorescence. Despite existing applications which detect this highly specific tumor biomarker, state-of-the-art fluorescence detection strategies suffer from low sensitivities, i.e. a high proportion of false negatives, likely due both to the relatively low intensity of fluorescence signals and the subjective assessment of this low signal on a complex tissue background. Sensitivity limitations lead to

inaccurate tumor detection, i.e., undetected tumor tissue is left unresected, resulting in ALA-induced PpIX imaging being only useful to date for some tumor subtypes that have relatively high PpIX concentration ^{13,38,74,188,200,202-204}. We recently demonstrated a quantitative approach which is significantly more accurate across a range of intracranial tumor histologies: low-grade and high-grade gliomas, meningiomas and metastases. Despite this significant diagnostic improvement, the detection accuracy for low-grade gliomas was still limited ²⁰⁴. Nevertheless, these data demonstrated for the first time that ALA-induced PpIX fluorescence-guided resection has the potential to improve surgery even for low-grade gliomas.

Neoplastic processes, e.g., metabolic-profile changes, abnormal vasculature formation, tissue hypoxia, increased cellular proliferation and differential gene expression profiles, provide a variety of potential biomarker targets ^{45,67,169,202,203,206}. However, inter- and intra- tumor-specific differences, coupled to current technological limitations, significantly restrict the use of these biomarkers for *in vivo* tumor detection. Furthermore, the multifaceted nature of tumor biology and glioma pathophysiology, suggest that any single biomarker is unlikely to provide the required specificity and sensitivity for global tumor tissue identification. Here, we measured *in vivo* multiple optical biomarkers that are potentially predictive of neoplastic processes and developed an accurate and quantitative strategy for resection of gliomas beyond state-of-the-art imaging. The measured biomarkers comprised total hemoglobin, oxygen saturation and optical scattering (related to tissue microstructure), derived from the optical reflectance spectra, and concentration of PpIX and associated photoproducts (related to cell metabolism) from the quantitative fluorescence spectra. We believe this provides a more

comprehensive, biologically relevant approach for intraoperative optical tumor tissue detection, with future studies for validation of the predictive power of this algorithm merited on a larger cohort of patients.

6.2. Materials and Methods

6. 2.1. Patient Selection

The Dartmouth-Hitchcock Medical Center Committee for the Protection of Human Subjects approved this study under a fluorescence-guided brain tumor resection protocol^{121,192,204}. All patients participated under informed consent. Patients with a diagnosis of low-grade glioma (LGG), high-grade glioma (HGG) or recurrent glioma (RCG) were administered an oral dose (20 mg/kg body weight) of ALA (DUSA Pharmaceuticals, Tarrytown, NY, USA) dissolved in 100 ml of water approximately 3 hours prior to the induction of anesthesia. High-resolution post-gadolinium injection pre-operative T1- or T2-weighted images were acquired and used for standard neuronavigation.

6.2.2 Surgical Procedure

The patient was prepared for intracranial tumor resection following standard practice¹⁹². The head was spatially registered with the pre-operative MR images using a StealthStation Treon (Medtronic, Louisville, CO, USA) for image-guided neuronavigation, which relates the position of the focal point of the surgical microscope to the surgical field and image-space coordinates. A Zeiss OPMI Pentero (Carl Zeiss

Surgical, GmbH, Oberkochen, Germany) microscope, modified for fluorescence imaging, was used. This allows the surgeon to switch rapidly between white-light and fluorescence modes during surgery. The microscope is equipped with a 400 nm blue light source for PpIX fluorescence excitation; detection is achieved using a 3-chip charge coupled device (CCD) camera, in front of which optical interference filters are placed. This allows real-time fluorescence images to be acquired within the spectral range from 620-710 nm. PpIX has a fairly broad fluorescence emission spectrum in the red region of the spectrum, which partly compensates for its relatively small quantum efficiency (< 0.01).

At various points during resection, the surgeon switched from white-light to fluorescence mode (blue light) exposure to visualize fluorescence^{121,204,207}. Digital images were recorded in both modes for each biopsy acquisition, and the site was assigned a qualitative visible fluorescence score from 0 to 4 (0 = no visible fluorescence, 1 = minimal fluorescence, 2 = moderate fluorescence, 3 = high fluorescence, 4 = very high fluorescence), based on the subjective impression of the surgeon of the visible fluorescence before tissue removal. The surgeon (DWR) had experience in using this fluorescence imaging system on over 70 patients. Biopsy samples were collected at the beginning, middle and end of resection from areas that displayed both visible (red) fluorescence contrast (if present), as well as non-visibly fluorescent regions that were part of the planned resection volume.

Immediately prior to biopsy acquisition, the surgeon irrigated the location of the intended specimen to ensure clearing of blood and debris, placed the intraoperative fluorescence/reflectance probe (see **Section 6.2.3**), and performed readings of the fluorescence and diffuse reflectance spectra in triplicate²⁰⁴. This took <0.5 s per

acquisition. Control data were also acquired in each case, consisting of spectroscopic measurements in normal brain without a corresponding biopsy. The biopsy specimens were separated into three equal parts for further processing, as follows: one part was placed in formalin; one part was placed in Optimal Cutting Temperature (OCT) compound and frozen in liquid nitrogen; and the final part was placed in a cryogenic vial and frozen in liquid nitrogen. Methodological details can be found in Valdes et al ²⁰⁴. Resection was deemed complete when the surgeon judged that no more tumor tissue that could be safely removed was present.

6.2.3. *In Vivo* Optical Probe Measurements and Quantification

An intra-operative hand-held optical device was used to provide the surgeon with quantitative *in vivo* and *in situ* pathophysiological information that is complementary to the qualitative fluorescence information derived from the state-of-the-art neurosurgical microscope described in Section 2.2.

6.2.3.1. Instrumentation

The spectroscopic probe developed for intraoperative fluorescence and diffuse reflectance measurements (AK, BCW) ^{64,204,208} is illustrated in **Figure 6.1**. It comprises 4 optical fibers arranged linearly at the tip and 260 mm apart (center-to-center). Two fibers act as white-light sources located $d = 260 \mu\text{m}$ and $d = 520 \text{ mm}$ apart from a 3rd detection fiber. The latter is connected to a spectrometer (USB200+: OceanOptics, Dunedin, Florida) with 0.35 nm spectral resolution. The 4th fiber serves as a blue light source

located at $d = 260$ mm from the detector fiber. Each fiber consists of a 200 mm diameter silica core with a numerical aperture of $NA = 0.22$. The fibers were bundled into an 18-gauge stainless steel shaft forming the tissue-contact end of the probe, and connected to a software-controlled data acquisition system through a 3 m long cable. White-light reflectance (450-720 nm) and fluorescence emission spectra (with 405 nm excitation) are collected sequentially during each measurement. As described in detail in Kim et al ^{64,208}, two white-light spectra, corresponding to different source-detector separations are required in order to improve the accuracy of the calculation of the tissue absorption and scattering spectra using a light-transport model ^{64,208} (**Figure 6.1**).

6.2.3.2 Light-transport modeling

Light transport modeling was used in order to estimate the tissue optical properties from the white-light spectra. Optical characterization is achieved assuming that light propagation in tissue is approximated by solutions to the diffusion equation for boundary conditions consistent with a semi-infinite homogeneous turbid medium⁶⁴. Tissue can then be characterized by effective optical properties in the form of the absorption coefficient, $\mu_a(\lambda)$, and the reduced scattering coefficient, $\mu_s'(\lambda)$. Tissue optical properties can be estimated from the white-light reflectance to correct for their distorting effects on the fluorescence emission signal²⁰⁹⁻²¹¹ by minimizing the error between probe measurements and a spectrally constrained model of the diffuse reflectance in a Levenberg-Marquardt algorithm. The resulting quantitative (and corrected) fluorescence spectrum was estimated from the model. This corrected fluorescence emission spectrum was used to quantify PpIX concentration⁶⁴.

Briefly, the fluorescence model assumed that 1) absorption at the excitation wavelength is much larger than absorption at the fluorescence emission wavelengths (i.e., $\mu_{a,x} \gg \mu_{a,m}$ where excitation and emission wavelengths are denoted by the subscripts x and m respectively) because the fluorescent biomarker's contribution to $\mu_{a,x}$ is small when compared to the high absorption of hemoglobin in the range 380 – 450 nm; and 2) fluorescence and reflectance photons travel similar path lengths given the same fiber-optic distance (and $\mu_{a,x} \gg \mu_{a,m}$). Under these assumptions, the measured (uncorrected) fluorescence, $F_{x,m}$, has a linear relationship with reflectance at the emission wavelength, R_m .

$$F_{x,m} = SR_m$$

where S represents the fraction of photons re-emitted as fluorescence which is a function not only of the fluorophore concentration but also the tissue optical properties at the excitation wavelength.

The total diffuse reflectance, $R_{t,x}$, is given by diffusion theory as,

$$R_{t,x} = \frac{a_x'}{1 + 2\kappa(1 - a_x') + \left[1 + \left(\frac{2\kappa}{3}\right)\right]\sqrt{3(1 - a_x')}}}$$

where \mathbf{k} represents the internal reflection parameter as a result of mismatch in refractive index between tissue and the external medium, and \mathbf{a}'_x represents the reduced albedo at

$I_{x,m}$. Given assumption (1), the total absorption can be approximated by $\mu_{a,x}$. The raw (uncorrected) measured fluorescence spectrum is given by

$$F_{x,m} = (1 - R_{t,x}) \left(\frac{Q_{x,m} \mu_{af,x}}{\mu_{a,x}} \right) R_m$$

where $Q_{x,m}$ represents the wavelength-dependent fluorescence quantum yield, and $\mu_{af,x}$ represents the fluorophore absorption coefficient at the excitation wavelength. From these, a closed-form equation for the quantitative (corrected) fluorescence emission spectrum is given by

$$f_{x,m} = (Q_{x,m} \mu_{af,x}) = \left(\frac{\mu_{a,x}}{(1 - R_{t,x})} \right) \left(\frac{F_{x,m}}{R_m} \right)$$

The resulting quantitative (and corrected) fluorescence spectrum was estimated from the model, yielding an emission spectrum, \mathbf{f} . This corrected fluorescence emission spectrum was used to quantify PpIX concentration, c , through a fluorescence basis spectrum, \mathbf{b} , equivalent to unit concentration (mg/ml) from the relation,

$$\mathbf{f} = \mathbf{b}c$$

where \mathbf{f} and \mathbf{b} are column vectors and c is computed by pseudo-inversion as

$$c = (\mathbf{b}^T \mathbf{b})^{-1} \mathbf{b}^T \mathbf{f}$$

Generalization to N fluorescent biomarkers, each with different spectra, is possible by forming a basis matrix, $\mathbf{B} = [\mathbf{b}_1 \mathbf{b}_2 \dots \mathbf{b}_N]$, composed of the individual basis spectra for each fluorescent biomarker, and calculating biomarker concentrations, $\mathbf{c} = [c_1 c_2 \dots c_N]^T$.

The fluorescence model requires prior knowledge of tissue optical properties (i.e., $\mathbf{m}_{a,x}, \mathbf{m}'_{s,x}$) at the excitation wavelength. The geometry of the intraoperative probe allows for one reflectance measurement per wavelength, such that solving for the tissue optical properties requires applying *a priori* knowledge of the absorption and reduced scattering spectra in the forward model. Here we calculated a good model fit of the tissue optical properties over the range 450-720 nm, and extrapolated to the excitation wavelength (i.e., 405 nm).

The absorption spectra can be represented by

$$\mu_a(\lambda) = c_{Hb} \left[S_t O_2 \mu_a(\lambda)^{oxyHb} + (1 - S_t O_2) \mu_a(\lambda)^{deoxyHb} \right]$$

where $\mu_a(l)^{oxyHb}$ and $\mu_a(l)^{deoxyHb}$ are the wavelength-dependent absorption coefficients of oxy- and deoxy-hemoglobin at concentrations of 1 g/mL; c_{Hb} represents the total hemoglobin concentration, and $S_t O_2$ is the oxygen saturation fraction.

The reduced scattering coefficient of tissue fits to a wavelength-dependent power law,

$$\mu'_s(\lambda) = S_A \lambda^{-S_p}$$

where S_A is the scattering amplitude and S_p is the scattering power. A forward model of diffuse reflectance and the *a priori* absorption and scattering spectra are combined and a Levenberg-Marquardt algorithm is used to extract the free parameters – hemoglobin, oxygen saturation, and scattering parameters (**Figure 6.1**). For further details on this algorithm, please refer to Kim et al⁶⁴.

6.2.4. Neuropathological Assessment

Histopathological analysis was performed by an experienced neuropathologist on each biopsy specimen (BTH). Formalin-fixed paraffin-embedded tissues were processed for hematoxylin and eosin (H&E) staining. Each H&E section was assessed for the presence of tumor cells, necrosis and reactive astrocytosis. Tissue samples were classified as normal or abnormal (tumor), based on World Health Organization (WHO) histopathological criteria¹⁵⁷. Biopsy specimens were classified into the following four categories: normal tissue, low-grade glioma (WHO grade I or II), high-grade glioma (WHO grade III or IV) and recurrent glioma. A fifth diagnostic category, labeled ‘all gliomas (AG), was introduced to group all abnormal biopsy specimens together for comparison with normal control measurements.

6.2.5. In Vivo Optical Data Analysis

Prior to biopsy acquisition, *in vivo* optical measurements were acquired at multiple locations in the surgical cavity. The objective is to measure the extent to which the

resulting optical data can be used to accurately classify tissue. The *in situ* intraoperative probe data for each biopsy acquisition were grouped based on the corresponding neuropathological assessment (*e.g.*, tumor or normal).

The raw optical data acquired with the probe come in the form of two reflectance spectra and one fluorescence spectrum. Analyses using the mathematical techniques described in Section 6.2.3.2 – a combination of light transport modeling and curve fitting algorithms – allowed quantitative information to be derived from these raw spectra. More precisely, this biological information comes in the form of concentrations for oxygenated hemoglobin, de-oxygenated hemoglobin, PpIX and associated decay photoproducts resulting from the interaction of the excitation light with the tissue. This molecular information is complemented by measures of the tissue autofluorescence and effective scattering properties, although these are less biologically specific.

For each probe measurement, the white-light reflectance spectrum for which the source-detector distance is $d = 260$ mm is labeled $R_1(\lambda)$ and that for which $d = 520$ mm is labeled $R_2(\lambda)$. For each probe acquisition, a background measurement of the ambient light is acquired, and systematically subtracted from the reflectance spectra. This was also applied to the raw fluorescence spectrum, $F_u(\lambda)$, in the range 450-720 nm.

The model-derived optical spectra consisted of the absorption spectra, $\mu_a(\lambda)$, and reduced scattering spectra, $\mu_s'(\lambda)$, in the range 450-720 nm and diffuse reflectance spectra, $R_{t,x}(l)$, in the range 450–650 nm for each interrogated site. The model-derived biomarkers analyzed were the PpIX concentration (c_{PpIX}), PpIX photoproduct concentration (c_{Pps}), total hemoglobin concentration (c_{Hb}), oxygen saturation fraction (StO_2), scattering amplitude (S_A) and scattering power (S_P).

Kolmogorov-Smirnov tests were used to ascertain normality of distributions. Wilcoxon-rank sum (Mann-Whitney) analyses were used to compare differences between spectral peaks and biomarkers. Receiver operating characteristic (ROC) analysis was used to determine the area under the curve (AUC). This metric serves to quantify and summarize the diagnostic performance, with AUC=1.00 meaning perfect classification and AUC=0.50 meaning classification not significantly different from chance. Data were processed and analyzed with MATLAB® software (Version 2010a, The Mathworks Inc., Natick, MA, USA). Two-sided *P*-values < 0.05 are considered statistically significant.

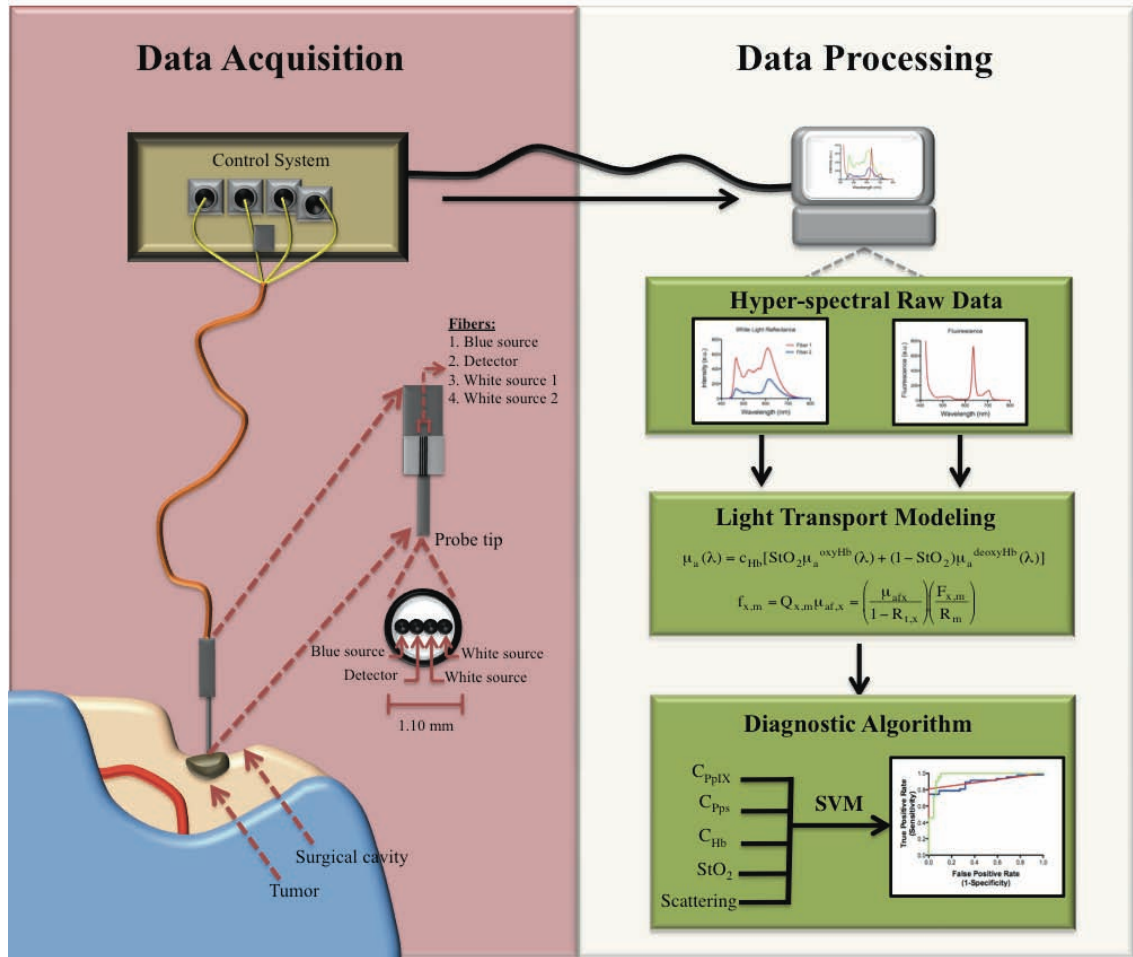


Figure 6.1. Conceptual map. The flow of spectroscopic data acquisition and processing for tumor tissue classification using an SVM diagnostic algorithm is outlined above. *Data Acquisition:* The intraoperative quantitative probe composed of four fibers linearly arranged (blue source, detector, white source at 260 mm, and white source at 520 mm) and a tip end with a diameter of 1.1 mm is placed on the brain. Tissue is irrigated with water to clean out debris. Sequential interrogation with white light sources and blue light sources is followed by collection of white light reflectance and fluorescence spectra using a spectrometer (~0.6 seconds). *Data Processing.* Hyperspectral white light reflectance data is then fed into a spectrally constrained diffuse reflectance model to calculate the

tissue optical properties. The calculated tissue optical properties are then used to correct the raw fluorescence spectrum for variations in tissue optical properties to calculate a quantitative fluorescence spectrum and fluorophore concentrations (~1 second). The calculated biomarkers (e.g., c_{PdIX} , c_{Pps} , c_{Hb}) are then used in a SVM-based diagnostic algorithm to correctly classify tissue as normal or abnormal tumor tissue (~1 second).

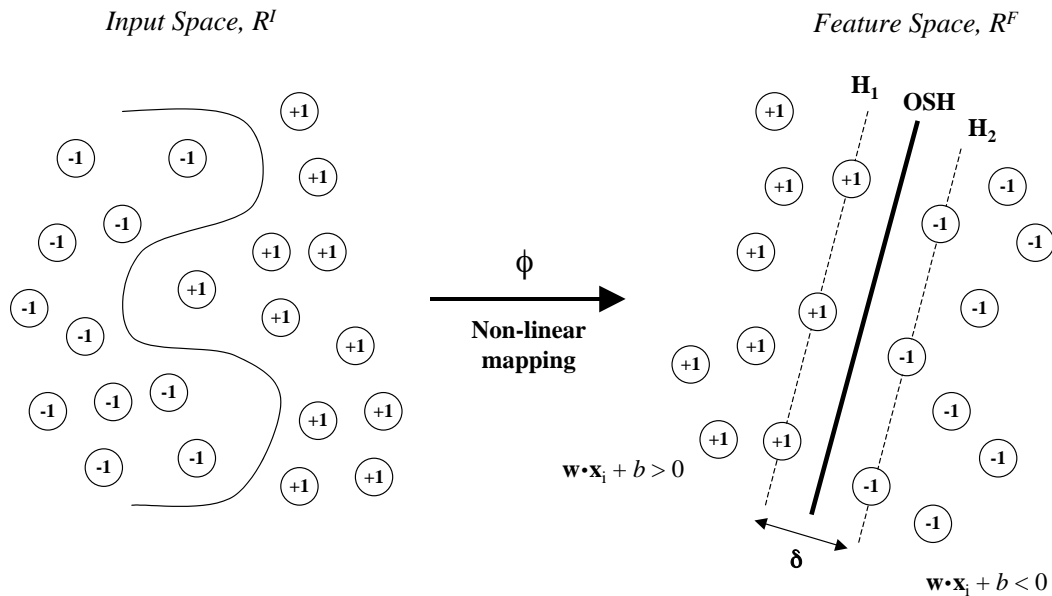


Figure 6.2. SVM algorithm. A training data set contains $n-1$ number of data points (i.e., *objects*). *Objects* are made up of m number of predictor variables (i.e., *attributes*) or coordinates in *input space*. *Feature functions* (f) are computed using a *kernel function* to non-linearly map *objects* (+1,-1) from *input space* unto *feature space*. In *feature space* SVM maximizes the distance (\mathbf{d}) between the margins of both classes (H_1, H_2). *Objects* located on the margins constitute the *support vectors*. Subsequently, SVM computes an

optimal separating hyperplane (**OSH**) to perform linear classification of *objects* in *feature space* (Adapted from Ivanciuc, 2000⁷²¹²).

6.2.6. Diagnostic Algorithm

6.2.6.1 Support Vector Machines Algorithm

The purpose of a diagnostic algorithm is to provide an optimal classification efficiency of data points into their appropriate classes (e.g., tumor vs normal). Here we developed a physiologically relevant diagnostic algorithm composed of the five model-derived biomarkers. Previous studies in brain use various combinations of raw optical data spectral peaks and peak ratios, wavelength-dependent average fluorescence lifetimes, and model-derived diffuse reflectance peaks as predictor variables and/or in multivariate classification algorithms (e.g., linear discriminant analysis)^{49,52,57,62,63,66,116,126,136,206,213-218}. In this study we chose as variables quantitative biomarkers associated with neoplastic changes. Here we hypothesized that inclusion of multiple biomarkers – which in themselves show significant, albeit limited classification potential - in a diagnostic algorithm would provide optimal detection accuracy.

Here we developed a diagnostic algorithm for tissue classification using support vector machines (SVM)²¹⁹⁻²²². SVM algorithms are commonly used in general non-linear classification. The underlying hypothesis of SVM classification is that predictor variables capture important characteristics of an individual data point, and that an appropriate mathematical algorithm (i.e., SVM) can generate accurate relationships between the original data characteristics and a property of interest not previously known for that

object (e.g., class membership). A classification algorithm extracts rules for classification from a training set of data points, with optimal parameters determined by cross-validation (e.g., leave-one-out). The algorithm then applies the derived classification rules to new data points of unknown class and assigns class membership.

A SVM classification algorithm finds the optimal (unique) separating hyperplane (**OSH**) between two classes by maximizing the margin, \mathbf{d} , in *feature space* between the closest point(s) of both classes. Individual data points (e.g., an interrogated tissue site) are known as *objects* and are composed of a set of predictor variables or *attributes* (i.e., the parameters used to describe the individual data points such as $\mathbf{c}_{\text{pIX}}, \mathbf{c}_{\text{Hb}}$). An object, \mathbf{x} , has n *attributes* (i.e., coordinates) in *input space*, R^I , such that $\mathbf{x} = (x_1, x_2, \dots, x_n)$, where x_i is a real number, $x_i \in \mathbb{R}$ for $i = 1, 2, \dots, n$. Each *object* belongs to a given class $y_i \in \{-1, 1\}$. SVM maps *objects* from the original *input space* unto a higher dimensional *feature space* using non-linear functions known as *feature functions* (**Figure 6.2**)^{212,219,221,222}.

We consider a training set T of m *objects* and their *classes*, $T = \{(\mathbf{x}_1, y_1), (\mathbf{x}_2, y_2), \dots, (\mathbf{x}_m, y_m)\}$. Define a set of *features functions* f_1, f_2, \dots, f_n and map any object \mathbf{x} unto a vector $\mathbf{f}(\mathbf{x})$:

$$\mathbf{x} = (x_1, x_2, \dots, x_n) \rightarrow \phi(\mathbf{x}) = (\phi_1(\mathbf{x}), \phi_2(\mathbf{x}), \dots, \phi_n(\mathbf{x}))$$

After mapping, we obtain a set of *objects* in *feature space*, R^F :

$$\phi(T) = [\phi(\mathbf{x}_1, y_1), \phi(\mathbf{x}_2, y_2), \dots, \phi(\mathbf{x}_m, y_m)]$$

The training set in *feature space* (i.e., $f(T)$) can be classified with a linear classifier if the appropriate *feature functions* (i.e., $f(\mathbf{x})$) are used. Transformed *attributes* are known as *features*, and a *vector* is the set of *features* that make up an *object*. *Vectors* that constrain the margin width are known as *support vectors*. In *feature space*, *objects* can be separated by class, with associated error costs in the non-ideal case where no perfect classification is achievable. This becomes a constrained optimization problem for finding the **OSH** (i.e., minimization of a quadratic function under linear constraints) and can be solved by a Lagrangian transformation, which generalizes the problem to both linear and non-linear SVM models. Here we used a Sequential Minimal Optimization algorithm to solve the quadratic optimization problem. In a non-linear SVM the *objects'* class (i.e., \mathbf{x}_k) is given by:

$$\begin{aligned} \text{class}(\mathbf{x}_k) &= \text{sign}[w \cdot \phi(\mathbf{x}_k) + b] \\ &= \text{sign}\left[\sum_{i=1}^m \lambda_i y_i \phi(\mathbf{x}_i) \cdot \phi(\mathbf{x}_k)\right] \end{aligned}$$

where $L = (l_1, l_2, \dots, l_m)$ is the set of Lagrange multipliers from the training *objects* $\mathbf{x} = (x_1, x_2, \dots, x_m)$. Under certain conditions (i.e., Mercer's conditions) an inner product in *feature space* has an equivalent kernel in *input space*. Consequently, simple, non-linear functions known as *kernel functions* can be used to compute $f(\mathbf{x}_i) \cdot f(\mathbf{x}_k)$ and perform the non-linear mapping of *feature function*, such that:

$$K(\mathbf{x}_i, \mathbf{x}_j) = \phi(\mathbf{x}_i) \cdot \phi(\mathbf{x}_j)$$

The training *objects* with $l_i > 0$ represent the *support vectors*. The objects with $l_i = 0$ are not important in the SVM model, and all that is needed to classify *objects* are the *support vectors* and $l_i > 0$ ^{212,219,222}.

We optimized SVM parameters (e.g., *kernels functions*), and applied a commonly used *kernel function* for classification, the Gaussian radial basis function (RBF),

$$K(\mathbf{x}_i, \mathbf{x}_j) = \phi(\mathbf{x}_i) \cdot \phi(\mathbf{x}_j) = e^{-\frac{\|\mathbf{x}_i - \mathbf{x}_j\|^2}{2\sigma^2}}$$

where σ controls the shape of the separating hyperplane. Parameter optimization for σ and the soft margin constraint were determined by performing a grid search from 0.05 to 10 for σ and from 1 to 200 for the soft margin constraint that provided the highest classification efficiency²²². Here, we optimized the algorithm parameters, with a value of $\sigma = 0.2$, a soft margin penalty error of 81 to provide a balance between complexity, overfitting and tolerance of the diagnostic algorithm for misclassification, and an average of 179 support vectors²²².

6.2.6.2. Dataset Training and Testing

The dataset ($n = 264$ data points) was organized into two categories: normal (i.e. control normal brain) and abnormal (i.e. LGG, HGG, RCG) tissue. We used an SVM algorithm in a leave-one-out, cross-validation approach to classify tissue. In this approach, intraoperative probe data for one interrogated site are left out of the dataset. The $n-1$ dataset is used to train the algorithm, avoiding bias introduced by dividing limited amounts of data. The algorithm derived from this training phase was subsequently

applied to the one data point left out (testing phase), a cut-off value was calculated, and the tissue was classified. This process was repeated for each individual interrogated site to build a 2-by-2 table and calculate the overall classification efficiency of the multiple biomarker-based diagnostic algorithm, i.e. to calculate the accuracy, specificity, sensitivity, positive predictive value and negative predictive value.

6.3. Results

6.3.1. Neuropathology

Intraoperative probe data were collected on 10 patients undergoing fluorescence-guided resection: 5 with high-grade gliomas (HGG- glioblastoma multiforme), 2 with low-grade glioma (LGG-mixed oligoastrocytomas) and 3 with recurrent gliomas (RCG). A total of 88 sites were interrogated with the probe (each in triplicate), giving a total of 264 spectra, which included 78 controls and 186 tumor.

6.3.2. *In Vivo* Optical Data

6.3.2.1. Raw Optical Data

The mean spectra \pm SEM for each of $R_1(\lambda)$, $R_2(\lambda)$, and $F_u(\lambda)$ was calculated for normal (i.e., controls) and tumor (i.e., LGG, HGG, RCG) tissue. Wilcoxon rank-sum analysis was used to assess differences in spectral regions for $R_1(\lambda)$, $R_2(\lambda)$, and $F_u(\lambda)$ in the range $\lambda = 450$ -720 nm. For $R_1(\lambda)$ and $R_2(\lambda)$ the whole spectrum in the range $\lambda = 450$

– 720 nm showed statistically-significant differences between normal and tumor, with the most pronounced differences observed in the region corresponding to the two major absorption peaks for hemoglobin (range $\lambda = 400 - 580$ nm) ($P < 0.00001$). For $F_u(\lambda)$ the major regions showing a statistically-significant difference were at $\lambda < 610$ nm and at approximately $\lambda = 650-670$ nm. We also performed an ROC analysis of the same spectral regions and found the regions for $R_1(\lambda)$ and $R_2(\lambda)$ showing the highest classification efficiency for differentiating normal from tumor with AUC values around 0.70 and 0.75, respectively, were $\lambda = 450-580$ nm. For $F_u(\lambda)$ the major regions with the highest classification efficiency were at $\lambda < 610$ nm and the range $\lambda = 650-680$ nm, with AUC values of approximately 0.70 and 0.60, respectively (**Figure 6.3**).

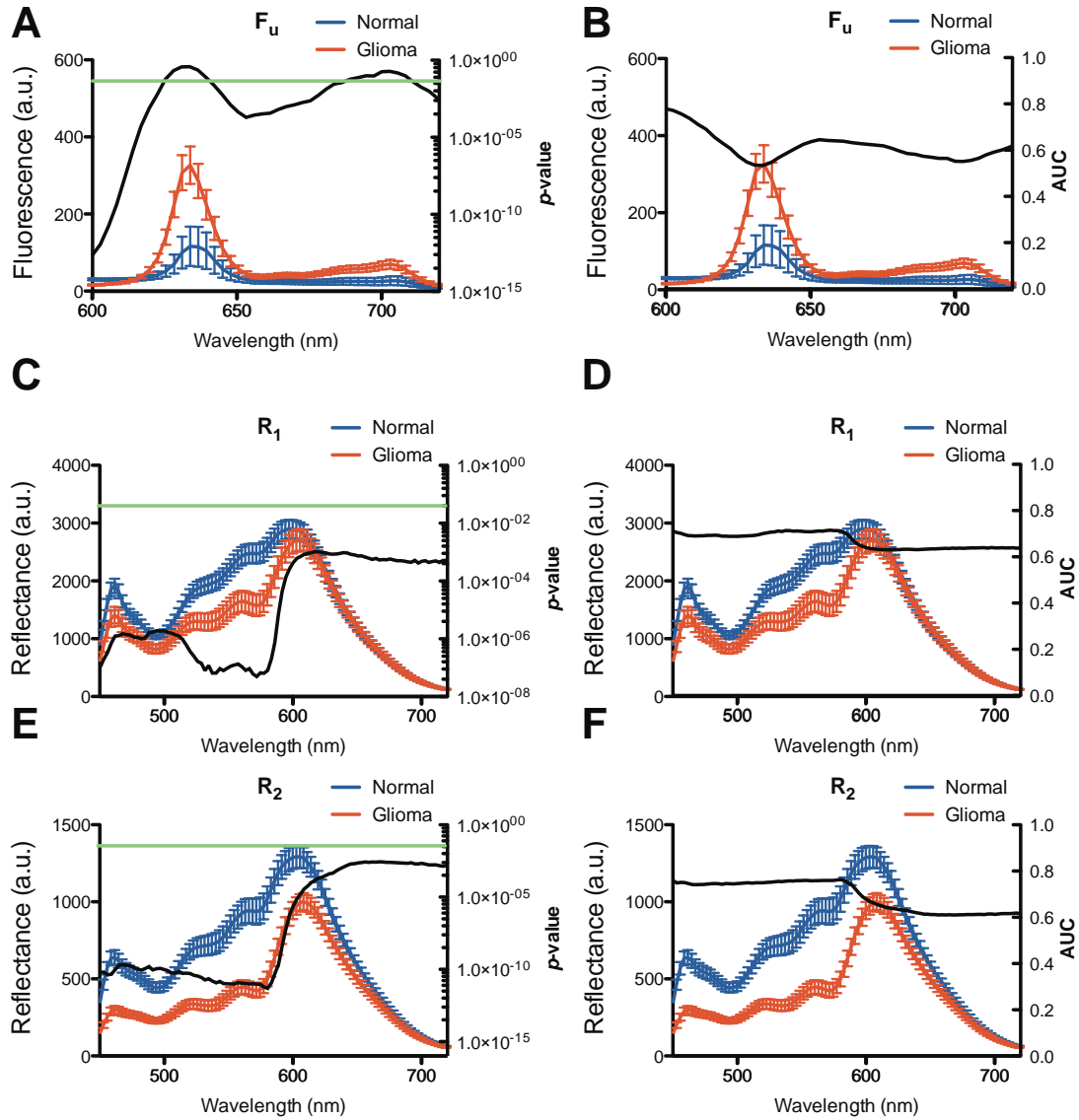


Figure 6.3. Raw reflectance and fluorescence spectra. The mean spectra for each of A, B) $F_u(\lambda)$, C, D) $R_1(\lambda)$, and E, F) $R_2(\lambda)$ was calculated for normal (i.e., controls) (*blue line*) and tumor (i.e., LGG, HGG, RCG) (*red line*) tissue \pm SEM (error bars). Wilcoxon-rank sum analysis was used to test for a significant difference in spectra peaks (*black line, left column*), with the green horizontal line crossing at $p < 0.05$. ROC AUC analysis was used to assess diagnostic performance (*black line, right column*) for individual spectral peaks to discriminate between normal and tumor in the range 450 – 720 nm.

6.3.2.2. Model-derived Optical Spectra

The mean spectra \pm SEM for each of $\mu_s'(\lambda)$, $\mu_a(\lambda)$, and $R_{t,x}(\lambda)$ were calculated for normal and tumor, with Wilcoxon-rank sum analysis to assess differences in spectral regions for $\mu_a(\lambda)$ and $\mu_s'(\lambda)$ in the range $\lambda = 450$ -720 nm, and for $R_{t,x}(\lambda)$ in the range $\lambda = 450 - 650$ nm. For $\mu_a(\lambda)$ the full spectrum in the range $\lambda = 450 - 720$ nm showed a highly statistically-significant difference ($P < 0.00001$), whereas $\mu_s'(\lambda)$ showed a less pronounced statistically-significant difference ($P < 0.05$). For $R_{t,x}(\lambda)$ the whole spectrum in the range $\lambda = 450 - 650$ nm showed statistically-significant differences between normal and tumor, with the most pronounced difference observed in the range $\lambda = 450 - 580$ nm ($P < 0.00001$). We also performed ROC analysis of the same spectral regions, and found the regions for $R_{t,x}(\lambda)$ showing the highest classification efficiency for differentiating normal from tumor were $\lambda = 450 - 580$ nm, with ROC AUC values of approximately 0.65. The AUC values for $\mu_a(\lambda)$ in the range $\lambda = 400 - 580$ nm were approximately 0.65, while the maximum AUC values of approximately 0.75 were observed in the range $\lambda = 600 - 720$ (**Figure 6.4**). The AUC values for the full spectrum range of $\mu_s'(\lambda)$ were all approximately 0.60.

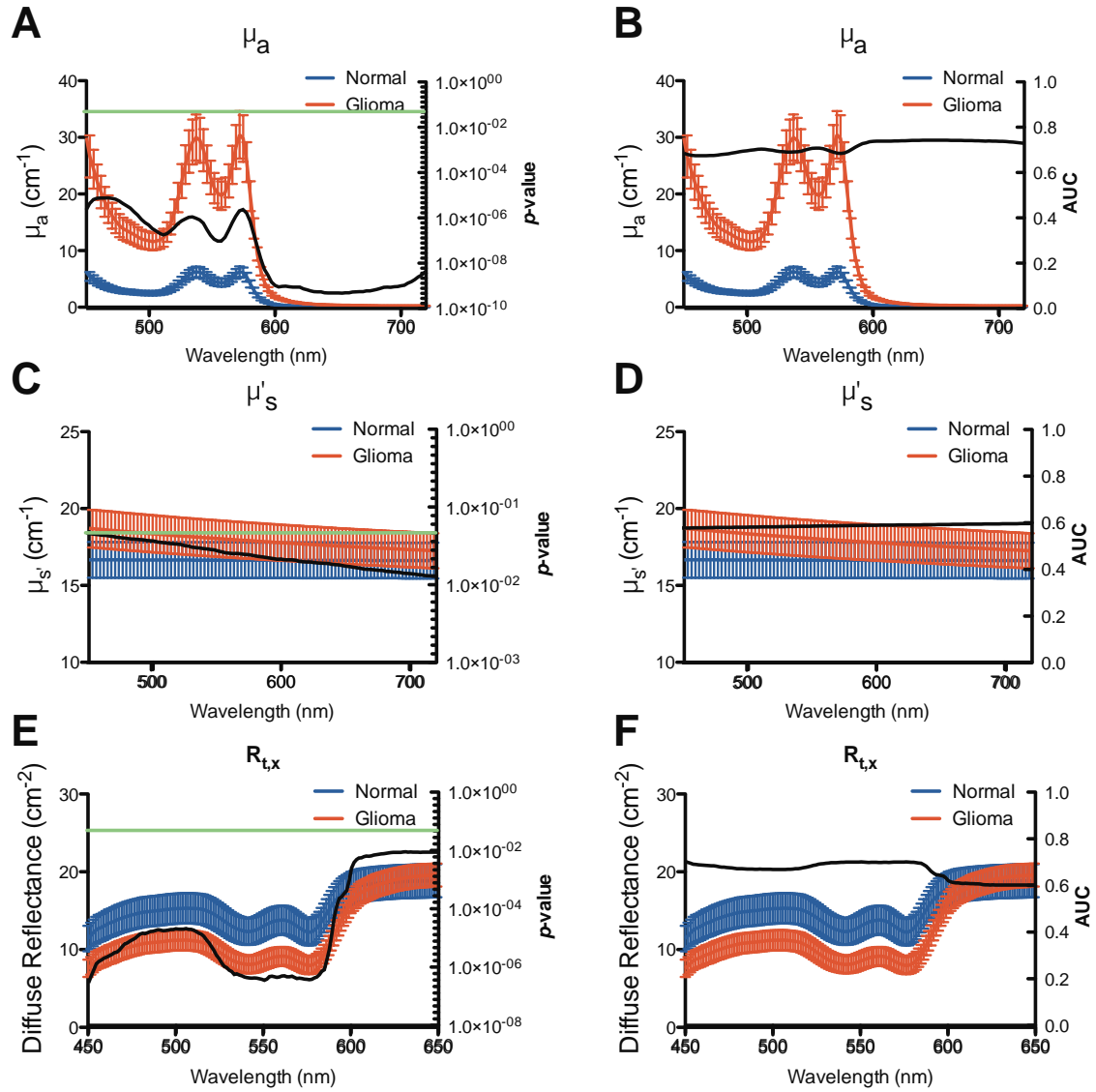


Figure 6.4. Model-derived optical spectra. The mean spectra for each of A, B) $\mu_a(\lambda)$, C, D) $\mu'_s(\lambda)$ and E, F) $R_{t,x}(\lambda)$, was calculated for normal (i.e., controls) (*blue line*) and tumor (i.e., LGG, HGG, RCG) (*red line*) tissue \pm SEM (error bars). Wilcoxon-rank sum analysis was used to test for a significant difference in spectral peaks (*black line, left column*), with the green horizontal line crossing at $p=0.05$. ROC AUC analysis was used

to assess diagnostic performance (*black line, right column*) for individual spectral peaks to discriminate between normal and tumor in the range 450 – 720 nm.

6.3.2.3. Model-derived Optical Biomarkers

The median value and interquartile range for each of c_{PpIX} , c_{Pps} , c_{Hb} , StO_2 , S_A and S_p was calculated for normal and tumor tissue and Wilcoxon-rank sum analysis was performed to assess differences. There was a statistically-significant increase in c_{PpIX} , ($P < 0.0001$), c_{Pps} ($P < 0.0001$), c_{Hb} ($P < 0.01$) and S_p ($P < 0.0001$) in tumor compared to normal tissues, and a statistically-significant decrease ($P < 0.0001$) in StO_2 . No significant difference was observed in S_A ($P = 0.2049$) (**Figure 6.5**). Hence, we chose to include c_{PpIX} , c_{Pps} , c_{Hb} , StO_2 and S_p as predictor variables in the diagnostic algorithm.

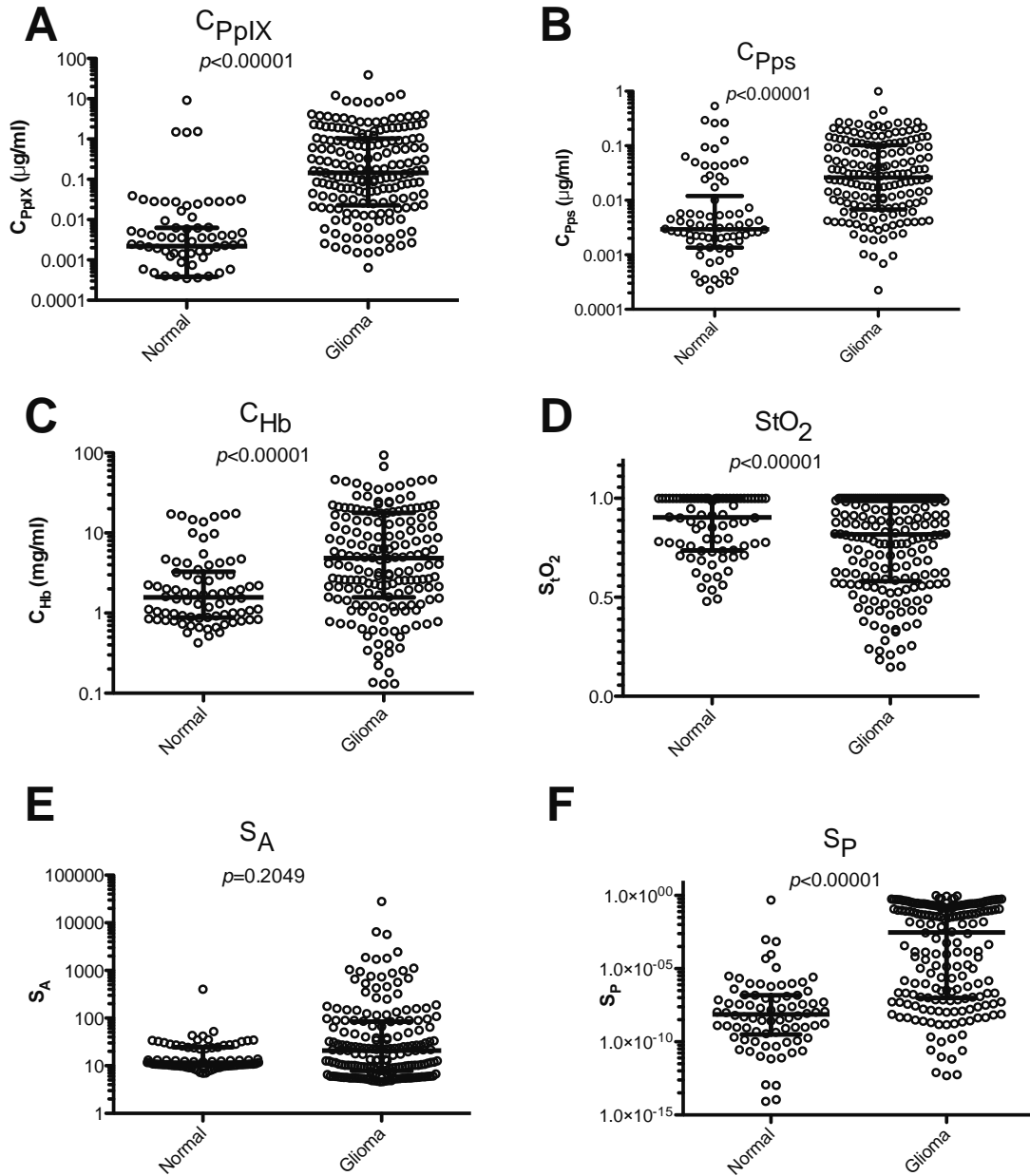


Figure 6.5. Model-derived optical biomarkers. The mean value for each of A) c_{PpIX} , B) c_{Pps} , C) c_{Hb} , D) StO_2 , E) S_A , and F) S_p was calculated for normal (i.e., controls) and tumor (i.e., LGG, HGG, RCG) tissue \pm SEM (error bars). A significant increase in c_{PpIX} , c_{Pps} , c_{Hb} , and S_p and a significant decrease in StO_2 was observed for tumor compared to normal. No significant change was observed for S_A .

6.3.3. Diagnostic Algorithm Classification

We developed a SVM multiple biomarker-based diagnostic algorithm trained and tested on $n = 264$ data points (i.e., 3 spectra for each interrogated site) using leave-one-out cross-validation; these included 78 controls and 186 glioma sites (**Figure 6.5**). The resulting classification efficiency was 94% for all tumors (i.e., LGG, HGG, RCG). We compared the diagnostic performance of this multiple biomarker algorithm to the state-of-the-art qualitative visual imaging approach. **Table 6.1** contains a summary of the ROC AUCs for all gliomas, as well as low-grade, high-grade and recurrent gliomas individually, using the multiple-biomarker algorithm. The optimal classification efficiency for qualitative visual imaging was 64% (specificity= 97%, sensitivity= 45%, positive predictive value= 95%, negative predictive value= 50%) and for the quantitative c_{PpIX} biomarker-only approach was 83% (specificity= 78%, sensitivity= 84%, positive predictive value= 90%, negative predictive value= 68%) compared to a classification efficiency of 94% for the diagnostic algorithm (specificity= 94%, sensitivity= 94%, positive predictive value= 97%, negative predictive value= 87%). **Table 6.2** summarizes the diagnostic performance of the three approaches.

Further, we performed ROC analysis to compare the diagnostic performance of qualitative visual imaging, c_{PpIX} , and our multiple biomarker strategy. The classification algorithm was significantly more accurate with AUC= 0.94 (0.02) than qualitative visible fluorescence with AUC = 0.72(0.03) ($P < 0.00001$), and than our previously reported c_{PpIX} biomarker-only approach with AUC = 0.87(0.03) ($P = 0.0055$).

Table 6.1. Receiver operating characteristic (ROC) analysis of three diagnostic tests

Group	Vis AUC (s.e.)	c_{PpIX} AUC (s.e.)	SVM AUC (s.e.)
AG	0.72 (0.02)	0.87 (0.03)	0.94 (0.02)
LGG	0.54 (0.02)	0.68 (0.07)	0.97 (0.02)
HGG	0.71 (0.03)	0.89 (0.03)	0.91 (0.02)
RCG	0.89 (0.03)	0.98 (0.02)	0.99 (0.01)

Table 6.1. Receiver operating characteristic (ROC) analysis of three diagnostic tests. Vis, qualitative visual imaging; SVM, support vector machines; c_{PpIX} = absolute concentration of PpIX; c_{Hb} = absolute concentration of hemoglobin; StO_2 = oxygen saturation fraction; S_A = scattering amplitude; S_p = scattering power; AUC, area under the curve. AG = all gliomas, LGG = low-grade gliomas, HGG = high-grade gliomas, and RCG = recurrent gliomas; standard error (s.e.) of the ROC AUC (in parenthesis)

Table 6.2. Summary of ROC analysis of diagnostic algorithm

Group	Classification Efficiency (%)	Sn (%)	NPV (%)	Sp (%)	PPV (%)
AG	94	94	87	94	97
LGG	96	94	88	100	100
HGG	92	92	87	91	95
RCG	98	98	86	100	100

Table 6.2. Summary of ROC analysis of diagnostic algorithm. Classification efficiencies, AUCs, sensitivities (Sn), negative predictive values (NPV), specificities (Sp), and positive predictive values (PPV) for tumor tissue diagnosis are tabulated. AG = all gliomas, LGG = low-grade gliomas, HGG = high-grade gliomas, and RCG = recurrent gliomas. The diagnostic performance of this algorithm was based on a retrospective analysis of 6 gliomas and associated SVM model predictions. Future work on a larger cohort of patients would seek to validate the predictive power of the algorithm's model for tissue classification.

6.4. Discussion

Biomarkers hold promise for diagnostics and therapeutics, with discoveries of tumor targeted antibodies and ligands, disease-associated receptors and abnormal gene expression. Many research efforts focus on the discovery and application of disease-specific biomarkers in the treatment and management of disease. Here, we have shown *in vivo* intraoperative measurements and quantification of cancer biomarkers for optimal tissue detection in glioma surgery, based on the use of both the exogenous agent ALA (through its consequent increase in PpIX fluorescence) and endogenous signatures related to hemoglobin concentration, oxygenation status, and structural changes.

6.4.1. Optical Strategies for Brain Tumor Surgery

Three major strategies^{67,223} have been used in optical-based neurosurgical guidance that seek to identify pathophysiological changes and/or tumor biomarkers: 1) wide-field impression of visible levels of fluorescence^{12,13,26,38,41,67,127,132,139,153,192}, 2) fluorescence and/or white-light spectral discrimination^{49,52,57,62,63,66,116,126,136,206,213-218} and 3) biomarker quantification^{204,224}. The most common strategy with wide-field technologies uses PpIX fluorescence imaging in the surgical management of high-grade gliomas. Exogenous administration of ALA leads to selective accumulation of PpIX. Blue light excitation, followed by collection of red fluorescence emission, guides the surgeon^{13,38,192,223,224}.

The majority of strategies based on spectral discrimination use ‘raw’ fluorescence (endogenous or exogenously-induced) and/or white light reflectance spectra, correcting for instrument response. Various research groups use single spectral peaks and/or peak ratios, or combinations of spectral features for tissue identification (e.g., linear discriminant analysis)^{49,116,126,136,206,213-215}. Marcu and colleagues^{61,62,216,217} used fluorescence peaks, peak ratios and fluorescence lifetime- values by themselves or in a linear discriminant classification algorithm. Yaroslavsky et al estimated the tissue optical properties in brain and found distinctive features between tissue types and optical spectra²²⁵. Another group used white-light reflectance to calculate the total model-diffuse reflectance, and assessed the diagnostic value of model-derived spectral peaks²¹⁵.

The third strategy quantifies PpIX biomarker concentrations *in vivo* and uses this for tissue discrimination^{64,204,215}. White-light reflectance spectra acquired *in vivo* are then applied in a spectrally-constrained light-transport model to calculate tissue optical properties (i.e., m_a , m'_s). The measured fluorescence emission is then corrected for the distorting effects of tissue optical attenuation, so that the absolute biomarker

concentrations can be calculated. Our preliminary work with this approach showed significant improvement compared to the state-of-the-art FGR in detection for a range of intracranial tumor histologies.

Here, we assessed the diagnostic value of visible impressions of phenomenological fluorescence, raw optical data, model-derived optical spectra and model-derived biomarkers. We hypothesized that a strategy that accounts for neoplastic processes through quantification and combined use of the predictive potential of multiple tissue biomarkers can detect tumor tissue with high diagnostic fidelity. In previous work we elaborated on visible impressions of fluorescence for tumor tissue delineation in ALA-induced PpIX fluorescence-guided resection^{67,121,192,204,223}. Briefly, qualitative FGR strategies provide a real-time, user-friendly imaging modality for tissue identification using a modified neurosurgical microscope that does not interfere with the surgical workflow. The requirement for high levels of PpIX accumulation to achieve adequate signal and significant contrast for discrimination is the major limitation using current clinical systems. This leads to low detection sensitivity, even in high-grade gliomas; that is, the tumor type where this technology is considered to be most useful.

6.4.2. Summary of Raw Optical Data

We assessed raw optical data – fluorescence and white light reflectance – for spectrally-based tissue discrimination. We found that straightforward spectral intensity determinations provided significant differences between normal and tumor at various wavelengths and wavelength regions (**Figure 6.3**). Interestingly, the fluorescence spectra

did not show significant differences at the two emission maxima of PpIX (635 and 710 nm). We observed significant changes in the full range of the reflectance spectra, with the most pronounced differences in the region of maximum hemoglobin absorption ($\lambda = \sim 450 - 580$ nm). ROC analysis of the raw optical data revealed diagnostic spectral signatures with maximum AUCs values of approximately 0.75 and 0.70 for reflectance and fluorescence, respectively. In comparison to previous studies^{52,57,66,218}, we did not undertake an exhaustive search of peak ratios to ascertain an optimal diagnostic variable, e.g., fluorescence peaks ratios; neither did we develop a multivariate algorithm using intensity peaks or peak ratios, since both strategies are reported in the literature. These strategies are independent of model-derived assumptions, and rely on absolute fluorophore/chromophore differences between normal and tumor and their impact on optical spectra. Such fluorescence ratio approaches have shown promise for tissue diagnostics²⁰⁶. However, parameters used in these discriminative algorithms cannot be linked with direct pathophysiological changes¹²⁴, which make biological interpretation by the clinician difficult for subsequent implementation.

6.4.3. Summary of Model-derived Optical Spectra

We assessed the discriminative potential of model-derived optical spectra: absorption, scattering, and total diffuse reflectance. The trends were similar to those reported in the literature^{136,225,226}. The absorption spectrum in the range $\lambda = \sim 450-580$ nm was dominated by hemoglobin, with characteristic HbO₂ peaks at ~ 540 and 580 nm. In the range $\lambda = 600 - 720$ nm (a subsection of the therapeutic window investigated in this

study), absorption was significantly decreased due to low hemoglobin and water absorption. Reduced scattering spectra showed the inverse relationship between wavelength and scattering predicted by the Rayleigh limit of Mie scattering, with a decrease in scattering with increasing wavelength^{57,226,227}. The shape of the diffuse reflectance spectra showed a strong dependence on the absorption spectrum, whereas the magnitude appeared to be highly influenced by both scattering and absorption, especially in the therapeutic window range²²⁶.

Similar to the raw data, we found significant differences between tumor and normal tissue in the model-derived spectra. The differences were more pronounced in the latter, with significant differences in absorption, scattering, and diffuse reflectance across all wavelengths. Diffuse reflectance showed similar pronounced differences ($P < 0.00001$), in the range $\lambda = \sim 450 - 580$ nm, while the reduced scattering showed less pronounced significant differences between normal and tumor ($P < 0.05$). These trends are similar to previous work in brain^{136,225,226,228}. Note that, in this study normal tissue consists of grey matter, since control measurements were taken from interrogated grey matter cortex following durotomy but prior to the first incision (i.e., prior to the start of brain resection).

For the model-derived spectra, the absorption spectrum showed the highest ROC AUC values of approximately 0.65 in the region dominated by hemoglobin absorption, and maximum ROC AUC values of approximately 0.75 in the range $\lambda = 600 - 720$ nm. Previous studies have reported tissue optical properties (i.e., absorption, scattering) in human brain tissue^{224,225}. For example, Lin et al²¹⁵ elaborated on the diagnostic potential of model-derived spectra peaks for brain tumor resection.

Model-derived optical spectra provide a theoretical framework with which to better understand tissue-light interactions. Differences derived from such investigations depend on fluorophore/chromophore differences between normal and tumor and their impact on the raw optical spectra. In contrast to strategies using raw spectral data, model-derived spectra peak/peaks ratios provide added information by taking into account how light interacts with tissue⁵⁷. Although this strategy uses a biophysical framework, it also has its limitations. Similar to the raw-data approach, it still depends on varying *ad hoc* choices of spectral data (even following optimization) and usually requires large numbers of variables from the spectral data for tissue classification. It also depends on adequate model-data fitting to make valid predictions and it is difficult to identify and quantify the pathophysiological processes measured by these spectral changes, which would negatively impact on clinical utility and acceptance.

6.4.4. Summary of Optical Biomarkers

Adding to the complexity of spectroscopic-based tissue diagnosis, brain neoplasms are highly heterogeneous. Tumors involve complex interdependent changes that result from the interactions between numerous dysregulated pathways, actively proliferating cells, and abnormal tissue-tissue interactions. Brain tumors are diverse, varying in biological aggressiveness, histological differentiation and treatment response^{169,201,229}. Specifically, gliomas are a heterogeneous group of tumors, ranging from well-circumscribed WHO grade I tumors, with minimal histological de-differentiation, to the highly invasive and malignant WHO grade IV, glioblastoma multiforme, with high intra-tumoral

heterogeneity, necrosis, endothelial proliferation and genetic atypia. Conventional histopathological diagnosis of tissue requires a multifaceted assessment of tissue changes, such as nuclear abnormalities, endothelial proliferation, necrosis and increased cell density. Given the complex genetic diversity and gene expression profiles of gliomas, it is unlikely a single biomarker will accurately delineate these tumors ²³⁰. Here, we elaborate on an intuitive approach that incorporates multiple tumor-specific pathophysiological processes and, importantly, quantifies these processes to develop a multiple biomarker-based strategy which provides significant improvement in tissue discrimination.

In this study we examined five optical biomarker groups to develop a physiological diagnostic algorithm: 1) PpIX concentration (c_{PpIX}), 2) PpIX photoproduct concentration (c_{Pps}), 3) total hemoglobin concentration (c_{Hb}), 4) oxygen saturation fraction (S_{tO_2}), and 5) scattering parameters (S_{A} , and S_{p}). PpIX has been shown to accumulate in a highly selective manner in brain tumor following exogenous administration of ALA. Neoplastic changes suggested to induce this selective accumulation of PpIX include: up- and/or down-regulated protein expression (e.g., ferrochelatase), dysregulated substrate uptake mechanisms, microenvironment changes, abnormal metabolism, increased proliferative potential and compromised blood-brain barrier ^{46,67}. We recently demonstrated an intraoperative strategy for quantification of c_{PpIX} as a biomarker. Using an optimized fluorescence detection technology to maximally exploit the tumor-targeting potential of ALA-induced PpIX, we showed significant improvement in tumor detection, including sensitivity in low-grade gliomas, although at a lower level than in high-grade tumor ²⁰⁴. This demonstrated that quantitative assessment of c_{PpIX} and associated photoproducts (i.e.,

c_{Pps}) under blue-light excitation ¹⁹⁵) can serve as promising biomarkers for tumor tissue (Figure 6.5).

Quantitative determination of oxygen saturation fraction (StO_2) and hemoglobin concentration (c_{Hb}) yields different, but highly interrelated and inter-dependent biological processes. Tissue hypoxia (i.e., low levels of StO_2) is associated with malignant progression and is pivotal in many aspects of tumor biology (angiogenesis, balance of aerobic/anaerobic metabolism, cell survival and invasion) ²³¹. Specifically, hypoxia is a critical step in the metabolic adaptation of tumors to anaerobic growth ^{203,232}, i.e., survival adaptation to increased glycolysis. This is in part due to increased metabolism and oxygen needs by the rapidly proliferating cells and decreased oxygen supply that depends on the inter-vessel spacing ²³³. Further, hypoxia may positively alter the diffusely infiltrative nature of gliomas by increasing the acidic conditions of the tumor microenvironment ²²⁹. As a result, oxygen saturation fraction can serve as a biological indicator (i.e., a biomarker) of tissue hypoxia and tumorigenesis. One would expect trends of lower levels of StO_2 in tumor compared to normal tissue (Figure 6.5).

Angiogenesis (formation of new blood vessels) occurs in tumors at increased levels, in a disorganized and inefficient fashion (tortuous dead-ends, over-production of capillary networks, etc.), and with abnormal vascular structure and performance (highly permeable and dilated vessels) ^{203,232,234}. Increased vessel growth is a pre-requisite for tumor formation, growth and progression ²³². Hypoxia and angiogenesis are inter-related neoplastic processes, in which new vessels form partly as a physiologic tumor response to hypoxia ^{229,231,233,235}. Regions of increased vasculature cause increased levels of blood and so raise the total hemoglobin concentration (c_{Hb}). As such, c_{Hb} can serve as an indicator of

increased vasculature, with a trend to increased levels of c_{Hb} in viable tumor compared to normal (**Figure 6.5**).

Tumors undergo morphological changes at the tissue, cellular and sub-cellular levels. Changes in nuclear size and shape, organelle content and morphology occur at the cellular and sub-cellular levels, whereas increased nuclear density, disorganized tissue networks and vasculature occur at the tissue level. Elastic scattering is one of the two most important forms of light interaction with tissue, with a relationship between size and shape of scatterers, and derived modeling-predictions^{57,227,236 237}. Here, we used a wavelength-dependent power law $\mu'_s = S_A \lambda^{-S_p}$ to model the reduced scattering spectrum, $\mu'_s(\lambda)$, of tissue. This yields quantitative scattering parameters, S_A and S_p , corresponding to the scattering amplitude and power. Scattering parameters can serve as biomarkers of morphological changes that occur at the tissue, cellular and sub-cellular levels; in tumor, scattering inhomogeneities increase, tissue becomes optically denser, and scattering increases²²⁷ (**Figure 6.5**).

These quantitative biomarkers serve as indicators of important biological processes (e.g., angiogenesis, hypoxia) occurring in gliomas. Given the inter- and intra-tumor heterogeneity of gliomas, and multifaceted nature of neoplastic processes, individual biomarkers are not sufficient for comprehensive interpretation of data and for achieving accurate tumor tissue diagnosis (**Table 6.1**). Intuitively, we hypothesized that the use of multiple factors (i.e., biomarkers) is necessary to maximize the diagnostic and predictive power of optical technologies for tumor tissue delineation.

4.4. Summary of Diagnostic Algorithm

Here, we developed a support vector machines (SVM) algorithm, used for general, non-linear problems ²¹⁹⁻²²¹, to ‘synthesize’ the information of all five quantitative biomarkers. That is, our strategy incorporates the individual predictive and diagnostic contributions of the 5 model-derived biomarkers (i.e., c_{PpIX} , c_{Pps} , c_{Hb} , StO_2 , S_p) for tissue classification. In this study we observed the superior diagnostic capability of this multiple biomarker-based strategy (classification efficiency = 94%; ROC AUC = 0.94(0.02)) compared to raw spectroscopic fluorescence, model-derived spectra, and the state-of-the-art in fluorescence-guided resection, namely visual impression of fluorescence (classification efficiency = 64%; ROC AUC = 0.72(0.02)).

In this work, state-of-the-art ALA-induced PpIX fluorescence-guided surgery using a surgical microscope shows a diagnostic capability in LGG that is no greater than chance, with an AUC of 0.54(0.02). As expected, visible fluorescence in HGG shows significantly better diagnostic capabilities, with an AUC of 0.71(0.03). As previously reported, this qualitative approach still suffers from significant sensitivity issues. Using the single biomarker approach with c_{PpIX} , the AUC for HGG is 0.89(0.03) and that for LGG also improves to 0.68(0.07). It is interesting to note that the diagnostic capability for LGG using the single-biomarker approach has a comparable diagnostic performance as the qualitative fluorescence imaging approach for HGGs. Yet, despite improvements, the use of c_{PpIX} alone is still not sufficient for accurate tumor detection in LGG. Here, we show a significantly improved diagnostic performance ($P < 0.00001$) using a multiple biomarker approach (**Table 2**). We see a marked increase in diagnostic performance for LGG: from 0.54(0.02) using visible fluorescence, to 0.68(0.07) using c_{PpIX} alone, to

0.97(0.02) using the quantitative multiple biomarker approach, as well as high accuracy for all gliomas with each individual glioma subtype having an accuracy greater than 94%. These are encouraging results, as they suggest the ability of a quantitative multiple biomarker approach to detect both tumor bulk and infiltrating glioma tissues, especially in low-grade gliomas where the impact on patient prognosis and survival could be substantial.

It is important to note this is a non-randomized study with a limited number of patients. The purpose of this work was to test the hypothesis that quantification of multiple biomarkers provides improved glioma detection compared to current optical approaches. As a proof-of-concept study, we have shown this strategy significantly improves detection of tumor tissue. We will further validate the predictive power of this multiple-biomarker approach in a larger cohort of gliomas. Another limitation of this study is the spatial restrictions imposed by a probe-based technology, which interrogates only a small region of tissue and minimally interrupts the surgical work-flow. This could be resolved by development of quantitative methods for real-time fluorescence imaging and work is in progress on this challenge.

6.5. Conclusions

We believe that our multiple biomarker strategy represents a significant improvement in intraoperative tumor detection for gliomas that goes beyond current optics-based strategies, including fluorescence image-guided resection and/or white light reflectance, on our cohort of 10 gliomas. Future work will be directed at validating the predictive

power of this algorithm on a larger group of patients. The use of a point-spectroscopic approach to interrogate tissue and light-transport modeling to quantify biomarkers opens the door to more comprehensive, multiple biomarker-based strategies in ‘optical-guided surgery’, beyond the traditional single-biomarker (e.g., PpIX), single-imaging modality (e.g., fluorescence), or ‘black-box’ multiple-wavelength approaches. Our strategy accounts for multiple aspects of tumor biology to accurately diagnose tissue, showing promise for neurosurgical diagnostics and therapeutics.

Chapter 7. Gene expression profile changes in ALA-induced PpIX visibly fluorescent tissue compared to non-visibly fluorescent tissue

7.1. Introduction

Gliomas are the most common primary brain tumors, accounting for over 70% of all cases, with glioblastoma multiforme (GBM) accounting for approximately 60-80% of all gliomas. Evidence suggests that extent of resection is a significant factor influencing both the recurrence and prognosis of disease in GBM^{9,11,13,205}.

Over the last decade, numerous studies have shown that GBM tumors accumulate the fluorescent biomarker, protoporphyrin IX (PpIX), following exogenous administration of the pro-drug 5-aminolevulinic acid (ALA). Accumulated levels of PpIX result in intraoperative levels of visible fluorescence in tissue⁶⁷. Numerous studies have been conducted to investigate the biological processes and reasons for increased PpIX accumulation in tissue. Hypoxic changes, pH levels, proliferation, and enzymatic up- and down-regulation have been proposed as contributing factors in differential PpIX production, among others^{67,177,238}.

To the best of our knowledge, no published study has investigated the biological changes associated with ALA-induced PpIX accumulation in GBM tissue using gene expression microarrays. Gene expression microarray technologies allow simultaneous, global assessment of gene expression profiles^{203,239-241}. Recent studies have correlated MR imaging features and gene expression changes in GBM, providing exciting results regarding inter- and intra-tumoral heterogeneity, and revealing molecular signatures

associated with GBM and changes on MR imaging²⁴⁰⁻²⁴². Here we followed a methodology similar to that by Pope et al²⁴² and Barajas et al²⁴¹, and compared the gene expression profiles of paired GBM tissue samples and their binary imaging phenotype groups (i.e., negative (-F) or positive (+F) PpIX visible fluorescence levels). We hypothesized that ALA-induced PpIX fluorescence signatures in GBM reflect underlying differences in gene-expression, and that intratumoral heterogeneity at the gene expression level can be resolved intraoperatively using ALA-induced PpIX fluorescence. Our preliminary results show that PpIX fluorescent tissues display a more aggressive phenotype as evidenced by over-expression of proliferation, angiogenesis, extracellular-matrix (ECM), immune response, cell death and survival, and locomotion related genes.

7.2. Materials and Methods

7.2.1. Patients and Samples

The Dartmouth-Hitchcock Medical Center Committee for the Protection of Human Subjects approved this study under a fluorescence-guided brain tumor resection protocol. All patients participated under informed consent. Patients with a first-time diagnosis of glioblastoma multiforme were included in this study. Approximately three hours prior to the induction of anesthesia, patients were administered an oral dose (20 mg/kg body weight) of ALA (DUSA Pharmaceuticals, Tarrytown, NY, USA) dissolved in 100 ml of water.

The patient was prepared following standard practice for tumor resection. The patient's head was registered with a StealthStation Treon for image-guided neuronavigation and a Zeiss OPMI Pentero (Carl Zeiss Surgical, GmbH, Oberkochen,

Germany) microscope modified for fluorescence imaging with a 400 nm light source for excitation and a 620-710 nm bandpass filter to collect fluorescence was used for fluorescence imaging and co-registered with the surgical field.

The surgeon switched from white to blue light exposure to visualize fluorescence at various points during surgery. Digital images were recorded under white and blue light for each biopsy acquisition and the site was assigned a fluorescence score from 0 to 4 (0 = no fluorescence, 1 = minimal fluorescence, 2 = moderate fluorescence, 3 = high fluorescence) based on the impression of the surgeon of the visible fluorescence before tissue removal. Biopsy specimens were collected at the beginning, middle, and end of resection, as well as in both fluorescing (if present) and non- fluorescing regions within the preoperatively planned resection volume, and were identified as corresponding to either the center or the edge of tumor. Biopsy specimens were separated into three equal parts for further processing as follows: one part was placed in formalin; another part was placed in Optimal Cutting Temperature (OCT) compound and frozen in liquid nitrogen; and the final part was placed in a cryogenic vial and frozen in liquid nitrogen. Resection was continued until the surgeon judged that no more malignant tissue that could be safely removed was present.

7.2.2 RNA Isolation and Gene Expression Microarray Analysis

Tissues samples frozen at -80° C were used for RNA isolation and subsequent microarray analysis. Briefly, each individual tissue sample was homogenized in 1 ml of TRIZOL. Then 200 ml of chloroform were added per 1 ml of TRIZOL, and incubated at room temperature for 3 min. Samples were centrifuged at 12,000g for 15 min at 4° C. Aqueous

phase containing the RNA isolate was transferred, 500 ml of isopropanol were added, mixed, incubated at room temperature for 10 min, and centrifuged at 12,000g for 10 min at 4° C. To further purify RNA, supernatant was removed, pellet washed with 1 ml of 75% cold ethanol, and centrifuged at 10,000g for 10 min. Then ethanol was removed and RNA pellet was left to air dry at room temperature, dissolved in RNase-free water for incubation for 10 min at room temperature, and tested to ensure RNA purity. We used a Human HT-12v3 Expression BeadChip (Illumina), which targets more than 25,000 annotated genes with more than 48,000 probes derived from the Nation Center for Biotechnology Information Reference Sequence (NCBI) RefSeq (Build 36.2, Rel 22) and the UniGene (Build 199) databases. Gene expression data from the Illumina oligonucleotide microarrays were quantile normalized and \log_2 transformed for further analysis using GeneSifter® (Geospiza). Genes showing a two-fold change or greater in expression between negatively (fluorescence score = 0) and positively fluorescent (fluorescence scores = 1, 2, or 3) samples and a quality threshold of >0.5 were analyzed. To assess a statistically significant difference *Student's* t-tests were used with a Benjamini and Hochberg False Discovery Rate for multiple testing correction, which provides a balance between not identifying false positives and discovery of significant expression changes. *P*-values <0.05 were considered statistically significant.

7.2.3 Histopathology and *Ex Vivo* PpIX Quantification

Formalin-fixed paraffin embedded tissue sections corresponding to each individual sample were assessed for histopathological score, tumor burden, and necrosis score as previously described in Roberts et al¹⁹². Briefly, hematoxylin-and-eosin-stained sections

are assessed and assigned a histopathological grade (based on the WHO grading scheme - 0 - IV). Then each tissue section is assigned a tumor burden score (0 = no tumor; 1 = up to 33% of the tissue with the presence of tumor cells; 2 = 33-66% of tissue with the presence of tumor cells, and 3 = >66% of tissue with the presence of tumor cells) and a necrosis score of 0-3 corresponding to the same levels of change as tumor burden for the presence of necrosis.

Ten (10) tissue samples in a cryogenic vial were stored at -80°C prior to *ex vivo* fluorimetric quantification of PpIX following a modified protocol from Lilge et al²⁴³. Briefly, the tissue was combined with 1 mL of Solvable (Dupont-Biotechnology Systems, Boston, MA, USA) and placed in an undulating water bath at 50°C for 1 hr. The tissue-Solvable solution was homogenized with a Tissue Tearor tool in the original cryogenic vial. The tissue homogenate (0.500 mL) was then combined with 1.125 mL of distilled water and 0.375 mL of Solvable. This solution was incubated in a 50°C water bath for 1 hr and then transferred to a quartz cuvette. The optical density of the solution was tested with a spectrophotometer to ensure an optical density less than 0.1. The cuvette was analyzed with a fluorimeter using an excitation wavelength of 401 nm and a slit width of 5 nm. A standard curve for quantification of PpIX was constructed by serially diluting PpIX by factors of 2 in a solution of distilled water (75% v/v) and Solvable (25% v/v).

Spectral decomposition was used to separate the contributions of PpIX, its photoproducts¹⁹⁵, and tissue autofluorescence. Autofluorescence was modeled as a linear combination of the emission spectra of reduced nicotinamide adenine dinucleotide (NADH), flavin adenine dinucleotide (FAD) and lipofuscin - components known to exist in brain tissue. Total tissue fluorescence was modeled as a linear combination of all

fluorescent species, with a non-negative least squares algorithm to extract the contribution from each species, and determine the PpIX concentration in each specimen. A Wilcoxon-Rank (Mann-Whitney) tests was used to assess for a significant difference in PpIX concentrations between fluorescent and non-fluorescent groups.

7.3. Results

7.3.1. Neuropathology and *Ex Vivo* PpIX Quantification

A total of five (5) patients with a first-time diagnosis of GBM were included in this study. Paired samples for each of four cases for a total of eight (8) samples and an additional two pairs of samples for one patient for a total of twelve (12) samples were assigned a histopathological score, tumor burden, and necrotic score. Paired samples were chosen for analysis as either negatively fluorescent (fluorescence score = 0) (i.e., six samples) or positively fluorescent (fluorescence scores = 1, 2, or 3) (i.e., six samples) (**Table 7.1**). PpIX concentrations between positively and negatively fluorescent tissue showed a statistically significant difference (positively fluorescent, median = 4.4858 mg/ml, interquartile range [4.2452 – 4.5227]; negatively fluorescent, median = 0.2951 mg/ml, interquartile range [0.0638 – 0.6234]; $p = 0.009$). This demonstrates that tissue displaying visible fluorescence had significantly more PpIX accumulation by approximately one order of magnitude.

Table 7.1. Samples for Gene Expression Microarray Analysis

Sample	HS	TS	NS	Vis
1A	3	3	0	-
1B	4	3	1	+
2A	4	2	0	-
2B	4	3	0	+
3A	2	3	0	-
3B	4	3	1	+
4A	4	3	1	-
4B	4	3	1	+
5A	2	1	0	-
5B	2	1	0	+
2C	2	1	0	-
2D	4	3	0	+

HS=histopathological score; TS=tumor burden score;

NS=necrotic score; Vis=negative (-) or positive (+) levels of visible fluorescence.

Table 7.2. List of Gene Expression Profile Changes in PpIX Fluorescence Guided Resection

Gene Identifier	Gene ID	Gene Title	Expression	Chromosome
NM_001845	COL4A1	Collagen, type IV, alpha 1	+	13
NM_000090	COL3A1	Collagen, type III, alpha 1	+	2
NM_003254	TIMP1	TIMP metalloproteinase inhibitor 1	+	X
NM_203416	CD163	CD163 molecule	+	12
NM_000089	COL1A2	Collagen, type I, alpha 2	+	7
XM_936128	-	PREDICTED: major histocompatibility complex, class II, DQ alpha 1, transcript variant 10 (HLA-DQA1), mRNA.	+	-
NM_203416	CD163	CD163 molecule	+	12
NM_021983	HLA-DRB4	Major histocompatibility complex, class II, DR beta 4	+	6
XM_001719804	-	PREDICTED: similar to hCG2042724 (LOC100133678), partial mRNA.	+	-
NM_000597	IGFBP2	Insulin-like growth factor binding protein 2, 36kDa	+	2
NM_012072	CD93	CD93 molecule	+	20
NM_000089	COL1A2	Collagen, type I, alpha 2	+	7
NM_001613	ACTA2	Actin, alpha 2, smooth muscle, aorta	+	10
NM_001615	ACTG2	Actin, gamma 2, smooth muscle,	+	2

		enteric		
		PREDICTED: similar to HLA class II histocompatibility antigen, DRB1-9 beta chain precursor (MHC class I antigen DRB1*9) (DR-9) (DR9), transcript variant 2 (LOC649143), mRNA.	+	-
XM_944822	-			
NM_033554	HLA-DPA1	Major histocompatibility complex, class II, DP alpha 1	+	6
NM_052871	-	non-protein coding RNA 152	+	-
		PREDICTED: similar to major histocompatibility complex, class II, DQ beta 1, transcript variant 2 (LOC100133583), mRNA.		
XM_001714074	-		+	-
NM_133505	DCN	Decorin	+	12
		PREDICTED: hypothetical LOC730415, transcript variant 2 (LOC730415), mRNA.		
XM_001720835	-		+	-
NM_000358	TGFBI	Transforming growth factor, beta-induced, 68kDa	+	5
NM_000088	COL1A1	Collagen, type I, alpha 1	+	17
		Major histocompatibility complex, class II, DR alpha		
NM_019111	HLA-DRA		+	6
		Membrane-spanning 4-domains, subfamily A, member 6A		
NM_152851	MS4A6A	CD74 molecule, major histocompatibility complex, class II invariant chain	+	11
NM_001025159	CD74		+	5
NM_001002858	ANXA2	Annexin A2	+	15
NM_003380	VIM	Vimentin	+	10
		Superoxide dismutase 2, mitochondrial		
NM_001024465	SOD2		+	6
		Sushi-repeat-containing protein, X-linked 2		
NM_014467	SRPX2		+	X
NM_001846	COL4A2	Collagen, type IV, alpha 2	+	13
		major histocompatibility complex, class II, DR beta 6 (pseudogene)		
NR_001298	-		+	-
		Membrane-spanning 4-domains, subfamily A, member 6A		
NM_152851	MS4A6A		+	11
NM_004244	CD163	CD163 molecule	+	12
		Tumor necrosis factor receptor superfamily, member 12A		
NM_016639	TNFRSF12A		+	16
NM_003380	VIM	Vimentin	+	10
		Growth arrest and DNA-damage-inducible, alpha		
NM_001924	GADD45A		+	1
NM_001002	RPLP0	Ribosomal protein, large, P0	+	12
NM_000393	COL5A2	Collagen, type V, alpha 2	+	2
		Complement component 1, r subcomponent		
NM_001733	C1R		+	12
NM_005746	NAMPT	Nicotinamide	+	7

		phosphoribosyltransferase		
NM_004048	B2M	Beta-2-microglobulin	+	15
NM_001463	FRZB	Frizzled-related protein	+	2
NM_001924	GADD45A	Growth arrest and DNA-damage-inducible, alpha	+	1
NM_172369	C1QC	Complement component 1, q subcomponent, C chain	+	1
NM_001102	ACTN1	Actinin, alpha 1	+	14
NM_015419	MXRA5	Matrix-remodelling associated 5	+	X
NM_001288	CLIC1	Chloride intracellular channel 1	+	6
NM_003651	CSDA	Cold shock domain protein A	+	12
NM_001953	TYMP	Thymidine phosphorylase	+	22
NM_001901	CTGF	Connective tissue growth factor	+	6
NM_032048	EMILIN2	Elastin microfibril interfacier 2	+	18
NR_001562	-	annexin A2 pseudogene 1	+	-
NM_003246	THBS1	Thrombospondin 1	+	15
NM_005531	IFI16	Interferon, gamma-inducible protein 16	+	1
NM_014220	TM4SF1	Transmembrane 4 L six family member 1	+	3
NM_019029	CPVL	Carboxypeptidase, vitellogenic-like	+	7
NM_005841	SPRY1	Sprouty homolog 1, antagonist of FGF signaling (Drosophila)	+	4
NM_000491	C1QB	Complement component 1, q subcomponent, B chain	+	1
NM_138455	CTHRC1	Collagen triple helix repeat containing 1	+	8
NM_001235	SERPINH1	Serpin peptidase inhibitor, clade H (heat shock protein 47), member 1, (collagen binding protein 1)	+	11
NM_005504	BCAT1	Branched chain aminotransferase 1, cytosolic	+	12
NM_015150	RFTN1	Raftlin, lipid raft linker 1	+	3
NM_020404	CD248	CD248 molecule, endosialin	+	11
NM_021642	FCGR2A	Fc fragment of IgG, low affinity IIa, receptor (CD32)	+	1
NM_001008490	-	Kruppel-like factor 6	+	-
NM_002155	HSPA6	Heat shock 70kDa protein 6 (HSP70B')	+	1
NM_002291	LAMB1	Laminin, beta 1	+	7
NM_007350	PHLDA1	Pleckstrin homology-like domain, family A, member 1	+	12
NM_001135239	LDHA	Lactate dehydrogenase A	+	11
NM_199327	SPRY1	Sprouty homolog 1, antagonist of FGF signaling (Drosophila)	+	4
NM_000442	PECAM1	Platelet/endothelial cell adhesion molecule	+	17
XR_019265	LOC728698	Similar to eukaryotic translation initiation factor 4A, isoform 1	+	12

NM_020663	RHOJ	Ras homolog gene family, member J	+	14
NM_005797	MPZL2	Myelin protein zero-like 2	+	11
NM_014867	KBTBD11	Kelch repeat and BTB (POZ) domain containing 11	-	8
XM_001715395	-	PREDICTED: hypothetical protein LOC100129129 (LOC100129129), mRNA.	-	-
NM_020225	STOX2	Storkhead box 2	-	4
NM_138284	IL17D	Interleukin 17D	-	13
NM_004750	CRLF1	Cytokine receptor-like factor 1	-	19
NM_138328	RHBDL3	Rhomboid, veinlet-like 3 (Drosophila)	-	17
NM_198573	ENHO	Energy homeostasis associated	-	9
NM_000835	GRIN2C	Glutamate receptor, ionotropic, N-methyl D-aspartate 2C	-	17
NM_201539	NDRG2	NDRG family member 2	-	14
NM_198573	ENHO	Energy homeostasis associated	-	9
NM_006741	PPP1R1A	Protein phosphatase 1, regulatory (inhibitor) subunit 1A	-	12
NM_000849	GSTM3	Glutathione S-transferase mu 3 (brain)	-	1

Table 7.2. List of Gene Expression Profile Changes in PpIX Fluorescence Guided Resection

Table 7.3. List of Over-expressed Genes in PpIX Fluorescent Tissue		
Gene ID	Gene Title	Biological Process
COL4A1	Collagen, type IV, alpha 1	angiogenesis epithelial cell differentiation cell differentiation anatomical structure morphogenesis anatomical structure formation involved in morphogenesis developmental process cellular process multicellular organismal process anatomical structure development vasculature development epithelium development blood vessel development multicellular organismal development blood vessel morphogenesis tissue development system development cellular developmental process
COL3A1	Collagen, type III, alpha 1	organ development skeletal system development blood vessel development

		<ul style="list-style-type: none"> cell-matrix adhesion transforming growth factor beta receptor signaling pathway integrin-mediated signaling pathway response to radiation peptide cross-linking platelet activation collagen fibril organization collagen biosynthetic process response to cytokine stimulus wound healing fibril organization negative regulation of immune response vasculature development extracellular structure organization cell surface receptor linked signaling pathway transmembrane receptor protein serine/threonine kinase signaling pathway extracellular matrix organization response to stress
TIMP1	TIMP metalloproteinase inhibitor 1	<ul style="list-style-type: none"> positive regulation of cell proliferation positive regulation of cellular process cellular protein metabolic process cell maturation
CD163	CD163 molecule	<ul style="list-style-type: none"> homeostatic process acute-phase response acute inflammatory response response to stress
COL1A2	Collagen, type I, alpha 2	<ul style="list-style-type: none"> blood vessel development transforming growth factor beta receptor signaling pathway Ras protein signal transduction vasculature development extracellular structure organization extracellular matrix organization
-	PREDICTED: major histocompatibility complex, class II, DQ alpha 1, transcript variant 10 (HLA-DQA1), mRNA. Major histocompatibility complex, class II, DR beta 4	<ul style="list-style-type: none"> antigen processing and presentation of peptide or polysaccharide antigen via MHC class II immune response
HLA-DRB4	4	
-	PREDICTED: similar to hCG2042724 (LOC100133678), partial mRNA.	
IGFBP2	Insulin-like growth factor binding protein 2, 36kDa	<ul style="list-style-type: none"> regulation of cell growth response to stress regulation of insulin-like growth factor receptor signaling pathway

		transmembrane receptor protein tyrosine kinase signaling pathway insulin-like growth factor receptor signaling pathway regulation of cell size phagocytosis cell-cell adhesion macrophage activation leukocyte activation macrophage activation
CD93	CD93 molecule	
ACTA2	Actin, alpha 2, smooth muscle, aorta	muscle contraction regulation of blood pressure vasoconstriction
ACTG2	Actin, gamma 2, smooth muscle, enteric	muscle contraction
-	PREDICTED: similar to HLA class II histocompatibility antigen, DRB1-9 beta chain precursor (MHC class I antigen DRB1*9) (DR-9) (DR9), transcript variant 2 (LOC649143), mRNA.	
HLA-DPA1	Major histocompatibility complex, class II, DP alpha 1	antigen processing and presentation of peptide or polysaccharide antigen via MHC class II immune response
-	non-protein coding RNA 152	
-	PREDICTED: similar to major histocompatibility complex, class II, DQ beta 1, transcript variant 2 (LOC100133583), mRNA.	
DCN	Decorin	peptide cross-linking via chondroitin 4-sulfate glycosaminoglycan extracellular matrix organization wound healing
-	PREDICTED: hypothetical LOC730415, transcript variant 2 (LOC730415), mRNA.	
TGFBI	Transforming growth factor, beta-induced, 68kDa	negative regulation of cell adhesion cell proliferation extracellular matrix organization
COL1A1	Collagen, type I, alpha 1	blood vessel development response to hydrogen peroxide cellular response to growth factor stimulus cell differentiation extracellular matrix organization

HLA-DRA	Major histocompatibility complex, class II, DR alpha	antigen processing and presentation of peptide or polysaccharide antigen via MHC class II immune response
MS4A6A	Membrane-spanning 4-domains, subfamily A, member 6A	receptor activity signal transducer activity
CD74	CD74 molecule, major histocompatibility complex, class II invariant chain	activation of MAPK activity immune response cell proliferation negative regulation of apoptosis negative regulation of DNA damage response, signal transduction by p53 class mediator positive regulation of fibroblast proliferation positive regulation of ERK1 and ERK2 cascade cell differentiation positive regulation of MAP kinase activity negative regulation of cell death ERK1 and ERK2 cascade
ANXA2	Annexin A2	angiogenesis blood vessel morphogenesis extracellular matrix organization
VIM	Vimentin	cellular component movement interspecies interaction between organisms intermediate filament-based process
SOD2	Superoxide dismutase 2, mitochondrial	response to superoxide response to hypoxia release of cytochrome c from mitochondria age-dependent response to oxidative stress glutathione metabolic process anti-apoptosis mitochondrion organization respiratory electron transport chain negative regulation of apoptosis
SRPX2	Sushi-repeat-containing protein, X-linked 2	angiogenesis cell-cell adhesion positive regulation of cell migration involved in sprouting angiogenesis regulation of localization blood vessel endothelial cell migration positive regulation of locomotion regulation of endothelial cell migration cellular component movement sprouting angiogenesis regulation of cell migration involved in sprouting angiogenesis cell migration locomotion

COL4A2	Collagen, type IV, alpha 2 major histocompatibility complex, class II, DR beta 6 (pseudogene)	extracellular matrix organization
-	Membrane-spanning 4-domains, subfamily A, member 6A	
MS4A6A CD163	CD163 molecule	molecular transducer activity inflammatory response
TNFRSF12A	Tumor necrosis factor receptor superfamily, member 12A	angiogenesis cellular component movement positive regulation of cellular component organization axon extension positive regulation of axon extension positive regulation of cell growth positive regulation of axonogenesis blood vessel morphogenesis cell migration axonogenesis positive regulation of cell size regulation of cyclin-dependent protein kinase activity G2/M transition of mitotic cell cycle negative regulation of protein kinase activity cell cycle arrest DNA repair cellular response to stress response to DNA damage stimulus
GADD45A	Growth arrest and DNA-damage-inducible, alpha	
RPLP0	Ribosomal protein, large, P0	translation ribosome biogenesis gene expression
COL5A2	Collagen, type V, alpha 2	collagen fibril organization extracellular structure organization extracellular matrix organization
C1R	Complement component 1, r subcomponent	immune response complement activation, classical pathway innate immune response positive regulation of immune system process activation of plasma proteins involved in acute inflammatory response
NAMPT	Nicotinamide phosphoribosyltransferase	nicotinamide metabolic process positive regulation of cell proliferation insulin receptor signaling pathway pyridine nucleotide biosynthetic process positive regulation of nitric-oxide synthase biosynthetic process nucleobase, nucleoside, nucleotide and nucleic acid biosynthetic process nucleobase, nucleoside and nucleotide

		<ul style="list-style-type: none"> biosynthetic process positive regulation of metabolic process transmembrane receptor protein tyrosine kinase signaling pathway
B2M	Beta-2-microglobulin	<ul style="list-style-type: none"> positive regulation of T cell mediated cytotoxicity antigen processing and presentation of peptide antigen via MHC class I immune response
FRZB	Frizzled-related protein	<ul style="list-style-type: none"> negative regulation of Wnt receptor signaling pathway cell differentiation
C1QC	Complement component 1, q subcomponent, C chain	<ul style="list-style-type: none"> immune response complement activation, classical pathway
ACTN1	Actinin, alpha 1	<ul style="list-style-type: none"> regulation of apoptosis
MXRA5	Matrix-remodelling associated 5	<ul style="list-style-type: none"> extracellular region
CLIC1	Chloride intracellular channel 1	<ul style="list-style-type: none"> ion transport
CSDA	Cold shock domain protein A	<ul style="list-style-type: none"> negative regulation of transcription from RNA polymerase II promoter negative regulation of apoptosis
TYMP	Thymidine phosphorylase	<ul style="list-style-type: none"> positive regulation of organ growth mitochondrial genome maintenance angiogenesis DNA replication chemotaxis mitochondrion organization
CTGF	Connective tissue growth factor	<ul style="list-style-type: none"> cartilage condensation angiogenesis positive regulation of protein amino acid phosphorylation DNA replication cell-matrix adhesion integrin-mediated signaling pathway positive regulation of cell proliferation fibroblast growth factor receptor signaling pathway positive regulation of gene expression positive regulation of cell death cell migration extracellular matrix constituent secretion positive regulation of G0 to G1 transition extracellular matrix organization
EMILIN2	Elastin microfibril interfacier 2	<ul style="list-style-type: none"> cell adhesion
-	annexin A2 pseudogene 1	
THBS1	Thrombospondin 1	<ul style="list-style-type: none"> activation of MAPK activity
IFI16	Interferon, gamma-inducible protein 16	<ul style="list-style-type: none"> regulation of transcription, DNA-dependent cell proliferation positive regulation of programmed cell death

		apoptosis DNA damage response, signal transduction positive regulation of apoptosis
TM4SF1	Transmembrane 4 L six family member 1	
CPVL	Carboxypeptidase, vitellogenic-like	proteolysis
SPRY1	Sprouty homolog 1, antagonist of FGF signaling (Drosophila)	metanephros development negative regulation of cell proliferation negative regulation of MAP kinase activity negative regulation of Ras protein signal transduction negative regulation of nerve growth factor receptor signaling pathway negative regulation of ERK1 and ERK2 cascade
C1QB	Complement component 1, q subcomponent, B chain	complement activation, classical pathway positive regulation of immune system process
CTHRC1	Collagen triple helix repeat containing 1 Serpin peptidase inhibitor, clade H (heat shock protein 47), member 1, (collagen binding protein 1)	cell migration
SERPINH1	Serpine peptidase inhibitor 1	response to unfolded protein peptidase inhibitor activity
BCAT1	Branched chain aminotransferase 1, cytosolic	G1/S transition of mitotic cell cycle cell proliferation
RFTN1	Raftlin, lipid raft linker 1	
CD248	CD248 molecule, endosialin	
FCGR2A	Fc fragment of IgG, low affinity IIa, receptor (CD32)	
-	Kruppel-like factor 6	regulation of transcription, DNA-dependent cytokine-mediated signaling pathway positive regulation of transcription from RNA polymerase II promoter cell differentiation positive regulation of biosynthetic process
HSPA6	Heat shock 70kDa protein 6 (HSP70B')	response to unfolded protein
LAMB1	Laminin, beta 1	cell adhesion positive regulation of cell migration neuron projection development positive regulation of cell proliferation positive regulation of cellular component movement

PHLDA1	Pleckstrin homology-like domain, family A, member 1	induction of apoptosis
LDHA	Lactate dehydrogenase A	glycolysis
PECAM1	Platelet/endothelial cell adhesion molecule	phagocytosis cell adhesion cell motility
LOC728698	Similar to eukaryotic translation initiation factor 4A, isoform 1	
RHOJ	Ras homolog gene family, member J	small GTPase mediated signal transduction Rho protein signal transduction regulation of cell shape actin cytoskeleton organization
MPZL2	Myelin protein zero-like 2	cell adhesion

Table 7.3. List of Over-expressed Genes in PpIX Fluorescent Tissue

Table 7.4. List of Under-expressed Genes in PpIX Fluorescent Tissue		
Gene ID	Gene Title	Biological Process
KBTD11	Kelch repeat and BTB (POZ) domain containing 11 PREDICTED: hypothetical protein LOC100129129 (LOC100129129), mRNA.	protein binding
-		
STOX2	Storkhead box 2	
IL17D	Interleukin 17D	inflammatory response
CRLF1	Cytokine receptor-like factor 1	
RHBDL3	Rhomboid, veinlet-like 3 (Drosophila)	signaling process
ENHO	Energy homeostasis associated	extracellular region
GRIN2C	Glutamate receptor, ionotropic, N-methyl D-aspartate 2C	N-methyl-D-aspartate selective glutamate receptor activity ion transport glutamate signaling pathway
NDRG2	NDRG family member 2	signal transduction cell differentiation
PPP1R1A	Protein phosphatase 1, regulatory (inhibitor) subunit 1A	carbohydrate metabolic process glycogen metabolic process energy reserve metabolic process protein serine/threonine phosphatase inhibitor activity
GSTM3	Glutathione S-transferase mu 3 (brain)	establishment of blood-nerve barrier endothelium development

Table 7.4. List of Under-expressed Genes in PpIX Fluorescent Tissue

7.3.2. Gene Expression Profile of PpIX Fluorescent GBM Samples

A total of 86 genes showed a statistically significant two-fold or greater change in their gene expression levels between negatively and positively fluorescent tissue following a Benjamini and Hochberg False Discovery Rate for multiple testing correction at a *P*-value <0.05. A summary list of all identified genes is given in **Table 7.2**. A list of identified genes showing a two-fold or greater over-expression and their corresponding biological processes are presented in **Table 7.3**, and genes showing a two-fold or greater under-expression and their corresponding biological processes are presented in **Table 7.4**.

Identified genes were then parsed into several broad functional categories including genes related to cellular proliferation (**Table 7.5**), immune response (**Table 7.6**), locomotion (**Table 7.7**), cell death (**Table 7.8**), extra-cellular matrix (ECM) interactions (**Table 7.9**), and angiogenesis (**Table 7.10**).

Table 7.5. Gene Expression Changes of Genes Associated with Cellular Proliferation

Gene ID	Gene Title	Chromosome	Mean Relative Expression (+F)	Mean Relative Expression (-F)
TIMP1	TIMP metalloproteinase inhibitor 1	X	12.2655	10.141
TGFBI	Transforming growth factor, beta-induced, 68kDa	5	9.77087	8.13772
CD74	CD74 molecule, major histocompatibility complex, class II invariant chain	5	9.39076	7.83115
SOD2	Superoxide dismutase 2, mitochondrial	6	10.1912	8.72979
NAMPT	Nicotinamide phosphoribosyltransferase	7	7.91243	6.60247

CTGF	Connective tissue growth factor	6	11.7031	10.4452
THBS1	Thrombospondin 1	15	7.38143	6.14504
IFI16	Interferon, gamma-inducible protein 16	1	9.25923	8.03338
SPRY1	Sprouty homolog 1, antagonist of FGF signaling (Drosophila)	4	9.17893	7.97457
BCAT1	Branched chain aminotransferase 1, cytosolic	12	8.75193	7.602
LAMB1	Laminin, beta 1	7	8.12411	7.06295
SPRY1	Sprouty homolog 1, antagonist of FGF signaling (Drosophila)	4	8.66805	7.62021

Table 7.5. Gene Expression Changes of Genes Associated with Cellular Proliferation

7.3.2.1 Cellular Proliferation GEP

This set of genes contained mostly genes involved in positive regulation of cellular proliferation (e.g., *TIMP1*, *TGFBI*). These included genes involved in positive regulation of mitogen activated protein kinase (MAPK) activity and/or ERK1/ERK2 signaling cascade (e.g., *THBS1*, *CD74*). Genes involved in metabolic processes and proliferation were also identified (e.g., *NAMPT*); including a gene involved in G1/S transition of the mitotic cell cycle (e.g., *BCAT1*) (**Table 7.5**). This data further supports the idea that cellular proliferation is a key factor in the increased accumulation of PpIX in tumor tissue.

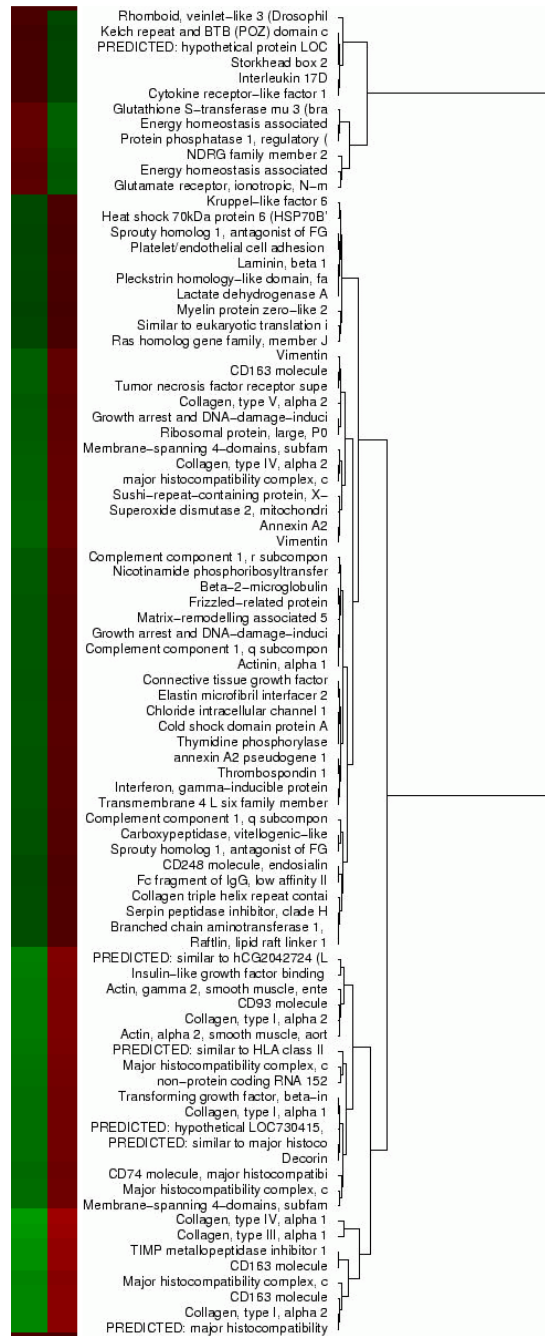


Figure 7.1. Gene expression profile changes in ALA-induced PpIX GBM tissue. GBM tissue samples were separated into negatively fluorescent (-F) or positively fluorescent (+F) groups. Analysis of gene expression data and hierarchical clustering using a Euclidean distance metric is shown. Under-expression is shown in green and over-expression is shown in red.

Gene ID	Gene Title	Chromosome	Mean Relative Expression (+F)	Mean Relative Expression (-F)
COL3A1	Collagen, type III, alpha 1	2	9.43366	7.17835
TIMP1	TIMP metalloproteinase inhibitor 1	X	12.2655	10.141
HLA-DRB4	Major histocompatibility complex, class II, DR beta 4	6	11.011	9.04514
CD93	CD93 molecule	20	9.59629	7.78173
HLA-DPA1	Major histocompatibility complex, class II, DP alpha 1	6	11.8781	10.1658
HLA-DRA	Major histocompatibility complex, class II, DR alpha	6	12.2649	10.6657
CD74	CD74 molecule, major histocompatibility complex, class II invariant chain	5	9.39076	7.83115
SOD2	Superoxide dismutase 2, mitochondrial	6	10.1912	8.72979
C1R	Complement component 1, r subcomponent	12	8.15299	6.83633
B2M	Beta-2-microglobulin	15	12.7317	11.431
C1QC	Complement component 1, q subcomponent, C chain	1	12.0864	10.7982
THBS1	Thrombospondin 1	15	7.38143	6.14504
IFI16	Interferon, gamma-inducible protein 16	1	9.25923	8.03338
C1QB	Complement component 1, q subcomponent, B chain	1	12.2217	11.0381
-	Kruppel-like factor 6	-	9.4293	8.34469
PECAM1	Platelet/endothelial cell adhesion molecule	17	8.80485	7.7592

Table 7.6. Gene Expression Changes of Genes Associated with Immune Response

7.3.2.2 Immune Response GEP

Genes related to immune response were the largest cluster of sixteen (16) over-expressed genes. These included genes found in antigen presenting cells such as macrophages and microglia (e.g., *MHC class II* genes such as *HLA-DRB4*, *HLA-DPA1*, *HLA-DRA*). These

results are consistent with the known high infiltration of antigen presenting cells in GBM²⁴⁰. Genes involved in complement activation for inflammatory response were also shown to be over-expressed in fluorescent areas (e.g., *CIR*, *CIQC*, *CIQB*). Leukocyte migration to tumors is a known characteristic of GBMs. We found over-expression of a gene involved in leukocyte migration, which is found on the surface of leukocytes and endothelial cell intercellular junctions (e.g., *PECAMI*).

Table 7.7. Gene Expression Changes of Genes Associated with Cellular Locomotion

Gene ID	Gene Title	Chromosome	Mean Relative Expression (+F)	Mean Relative Expression (-F)
SRPX2	Sushi-repeat-containing protein, X-linked 2	X	7.94934	6.50132
TNFRSF12A	Tumor necrosis factor receptor superfamily, member 12A	16	8.87211	7.48622
TYMP	Thymidine phosphorylase	22	10.9251	9.66222
CTGF	Connective tissue growth factor	6	11.7031	10.4452
THBS1	Thrombospondin 1	15	7.38143	6.14504
CTHRC1	Collagen triple helix repeat containing 1	8	8.4131	7.24779
LAMB1	Laminin, beta 1	7	8.12411	7.06295
PECAM1	Platelet/endothelial cell adhesion molecule	17	8.80485	7.7592
GRIN2C	Glutamate receptor, ionotropic, N-methyl D-aspartate 2C	17	7.62528	8.93981

Table 7.7. Gene Expression Changes of Genes Associated with Cellular Locomotion

7.3.2.3 Cellular Locomotion GEP

The highly infiltrative and migratory nature of GBM tumor cells is a major cause of recurrence and poor prognosis. We see an over-expression of cellular locomotion or migratory gene signatures in areas of increased fluorescence. Genes involved in cell-cell adhesion and cell migration were identified (e.g., *SRPX2*, *CTGF*, *LAMB1*). Further, substrate bound cell-migration is key for the infiltrative nature of gliomas, with over-expression of *TNFRSF12A* an important player.

Table 7.8. Gene Expression Changes of Genes Associated with Cell Death

Gene ID	Gene Title	Chromosome	Mean Relative Expression (+F)	Mean Relative Expression (-F)
CD74	CD74 molecule, major histocompatibility complex, class II invariant chain	5	9.39076	7.83115
SOD2	Superoxide dismutase 2, mitochondrial	6	10.1912	8.72979
TNFRSF12A	Tumor necrosis factor receptor superfamily, member 12A	16	8.87211	7.48622
GADD45A	Growth arrest and DNA-damage-inducible, alpha	1	9.1664	7.8039
B2M	Beta-2-microglobulin	15	12.7317	11.431
GADD45A	Growth arrest and DNA-damage-inducible, alpha	1	9.69591	8.40388
ACTN1	Actinin, alpha 1	14	11.0895	9.80175
CSDA	Cold shock domain protein A	12	10.9192	9.65407
CTGF	Connective tissue growth factor	6	11.7031	10.4452
THBS1	Thrombospondin 1	15	7.38143	6.14504
IFI16	Interferon, gamma-inducible protein 16	1	9.25923	8.03338
PHLDA1	Pleckstrin homology-like domain, family A, member 1	12	9.58853	8.52973

Table 7.8. Gene Expression Changes of Genes Associated with Cell Death

7.3.2.4 Cell Death GEP

Aberrant cell survival and apoptosis are key changes observed in GBM as a result of bypass of normal cell cycle checkpoints by tumors cells, which allow prolonged survival and growth. Here we identified mostly genes associated with aberrant cell cycle control, with an increase in expression in genes involved in negative regulation of apoptosis (e.g., *CD74*, *SOD2*). Further, negative regulation and induction of cyclin-dependent kinase 4 (CDK4) for G1/S progression has been shown for *CSDA*, which was identified as over-expressed in fluorescent regions. Further, we found an increased expression of *GADD45A* and *IFI16* in fluorescent regions, which have been shown to induce cell cycle arrest as a response to DNA damage in cells.

Table 7.9. Gene Expression Changes of Genes Associated with ECM Interactions

Gene ID	Gene Title	Chromosome	Mean Relative Expression (+F)	Mean Relative Expression (-F)
COL4A1	Collagen, type IV, alpha 1	13	11.3396	9.01301
COL3A1	Collagen, type III, alpha 1	2	9.43366	7.17835
COL1A2	Collagen, type I, alpha 2	7	9.19028	7.17232
COL1A2	Collagen, type I, alpha 2	7	8.91125	7.10748
COL1A1	Collagen, type I, alpha 1	17	8.61645	6.98949
COL4A2	Collagen, type IV, alpha 2	13	8.53317	7.10373
COL5A2	Collagen, type V, alpha 2	2	8.76176	7.4232
THBS1	Thrombospondin 1	15	7.38143	6.14504
LAMB1	Laminin, beta 1	7	8.12411	7.06295

Table 7.9. Gene Expression Changes of Genes Associated with ECM interactions

7.3.2.4 ECM-related GEP

Here we see over-expression of ECM-related signature genes in fluorescent regions which included multiple collagens (e.g., *COL1A1*, *COL1A2*, *COL3A1*, *COL4A1*, *COL4A2*, *COL5A1*) not usually found in normal brain, but commonly found in brain vasculature. Specifically, *COL4A1*, *COL1A2*, *COL1A1*, and *COL3A1* have been shown to be present in proliferating microvasculature. ECM-related changes also provide the necessary environment in tumor for the infiltrative phenotype changes found in GBM tumor cells, in which we see over-expression of the ECM matrix glycoprotein, *LAMB1* - a positive regulator of migration.

Table 7.10. Gene Expression Changes of Genes Associated with Angiogenesis

Gene ID	Gene Title	Chromosome	Mean Relative Expression (+F)	Mean Relative Expression (-F)
COL4A1	Collagen, type IV, alpha 1	13	11.3396	9.01301
TGFBI	Transforming growth factor, beta-induced, 68kDa	5	9.77087	8.13772
ANXA2	Annexin A2	15	11.617	10.1452
SRPX2	Sushi-repeat-containing protein, X-linked 2	X	7.94934	6.50132
COL4A2	Collagen, type IV, alpha 2	13	8.53317	7.10373
TNFRSF12A	Tumor necrosis factor receptor superfamily, member 12A	16	8.87211	7.48622
CTGF	Connective tissue growth factor	6	11.7031	10.4452
THBS1	Thrombospondin 1	15	7.38143	6.14504
LAMB1	Laminin, beta 1	7	8.12411	7.06295

Table 7.10. Gene Expression Changes of Genes Associated with Angiogenesis

7.3.2.4 Angiogenesis GEP

Here we find a cluster of over-expressed genes in fluorescent regions that are involved in angiogenesis. The increased expression of various collagens (e.g., *COL4A1*, *COL4A2*, *COL1A2*, *COL3A1*) are most likely related to sprouting of new vessels and their constituent ECM. Other over-expressed genes include those involved in sprouting vessel growth and/or endothelial cell migration such as *ANXA2*, *SRPX2*, *TNFRSF12*.

7.4. Discussion

The tumor-associated changes that lead to an over-production of PpIX following exogenous administration of ALA still remains an unanswered question despite efforts to further elucidate its mechanisms^{46,238}. Studies to date have shown tumor-associated correlations with specific enzymes (e.g., down-regulation of ferrochelatase), cellular phenotypes (e.g., increased proliferation), and tissue-wide changes (e.g., tissue section histological features)⁶⁷, to name a few. To the best of our knowledge, no group has undertaken a gene expression study of GBM tissues to better elucidate the gene expression profile changes associated with differing levels of ALA-induced PpIX fluorescence. Here we present a preliminary analysis of gene expression microarray data on GBM tissue undergoing ALA-induced PpIX fluorescence guided resection.

This study sought to provide insight into the biological changes at the transcriptome level which help explain the increased accumulation of PpIX in tissue, as determined by using a binary classification of either positively (+) or negatively (-) fluorescent tissue as assessed by the surgeon in the operating room. As a preliminary exploration into the

expression changes of GBM, we examined 5 patients with a first time diagnosis of GBM and compared the expression changes between paired fluorescent and non-visibly fluorescent tumor samples. We used a standard Illumina array which targets more than 25,000 genes, and found 86 genes that showed a statistically significant two-fold or greater change in expression following a Benjamini and Hochberg False Discovery Rate for multiple testing correction (i.e., this approach provides a balance between not identifying false positives and discovery of significant expression changes).

A systematic approach was taken to identify key gene clusters associated with functional changes of importance for tumorigenesis and glioma progression (e.g., cell proliferation, angiogenesis, immune response). We found strong gene over-expression in fluorescent tissue of gene clusters that underwent specific investigation. Previously, we showed a strong correlation between tissue proliferation (assessed using proliferation labeling indices of tissue sections) and PpIX concentrations. Here we see a strong over-expression of genes involved in cell proliferation and regulation of cell cycle in fluorescent tissue. These results further corroborate at the transcriptome level, our previous work, suggesting the essential role cell proliferation plays in the increased production of PpIX in tumor tissue. Further, our results identified clusters of genes related to immune response with increased expression profiles. This data agrees with our understanding of substantial immune cell infiltrates in gliomas, and the pro-tumorigenic role of immune cells (e.g., microglia).

Angiogenesis is a common change observed in glioma progression and growth. Here we found a strong over-expression of angiogenesis and ECM-interaction related genes in fluorescent tissue. This data support the idea of increased vasculature and ECM changes

associated with GBM growth and tumor aggressiveness. Closely associated with the observed ECM gene changes are over-expressed genes related to cellular locomotion in fluorescent tissue. That is, since the diffusely infiltrative character of tumor cells in gliomas play a key role in its recurrence and invasion, and our gene expression data suggest a more invasive and increased migratory character for fluorescent when compared to non-fluorescent tissue.

An important conclusion to be drawn from this pilot data set and analysis is that increased levels of accumulated PpIX, which lead to visible levels of fluorescence, is associated with tumor changes leading to a more aggressive glioma phenotype. This data is comparable to recent work showing increased aggressive cellular features (e.g., angiogenesis, cell survival, proliferation, migration) on T1-weighted contrast enhancing compared to non-contrast enhancing GBM tissues²⁴¹. That is, high levels of accumulated PpIX are predictive of gene expression profile changes associated with a more aggressive cellular phenotype in tumor tissue, such as increased cellular proliferation, angiogenesis, and migration. These results suggest that accumulated PpIX levels are dependent on not just one or a few transcriptome-level changes, but on the interplay between numerous signaling pathways and expression patterns affecting the overall phenotype of tumor cells towards a more aggressive, infiltrative character.

Although the present study presents promising data regarding the changes associated with increased PpIX levels in GBM at the gene expression levels, limitations of this study should be considered. First, the numbers in this study are low with only 5 different GBM cases and 12 paired samples. GBMs are highly heterogeneous tumors at both the intra-tumoral and inter-tumoral levels. As such, future work examining the gene expression

changes associated with increased PpIX levels will need a larger cohort of patients. Increased numbers would enable a more rigorous hierarchical clustering analysis of the data, to enable further segmentation and identification of over- or under-expressed functional groups of genes. Second, gene expression microarrays studies such as these are excellent tools for exploratory analysis. Nevertheless, to validate gene expression results a combination of further analysis using immunohistochemistry, real time quantitative PCR, and western blotting, for example, is required. Future work will seek to validate targets genes of interest. Finally, another important limitation of this study is the assumption that ALA-induced PpIX fluorescence is an all-or-none phenomenon (i.e., yes or no). As we have shown previously, PpIX can accumulate at high levels without tissue displaying visible fluorescence. Future studies will study the relationships between not just visible levels of fluorescence but between specific concentrations of PpIX accumulation in tissue and their gene expression profile.

7.5. Conclusions

Here we show the gene expression profile changes associated with different levels of visible ALA-induced PpIX in GBMs undergoing fluorescence-guided resection. Our results show initial data and corresponding analysis suggesting an overall more aggressive phenotype in tissue with visible levels of fluorescence compared to non-visibly fluorescent tissue. Further, our data suggest that numerous factors at the transcriptome level are predictive of PpIX accumulation. This work provides a preliminary analysis which suggests the need for further gene expression studies and

subsequent validation of target genes of interest to better understand the phenomenon of increased PpIX concentrations and fluorescence in GBM.

Chapter 8. ALA-induced PpIX concentration correlates with tissue histopathological measures of malignancy

8.1. Introduction

Gliomas account for over 70% of all primary brain tumors^{169,201,244}. Currently brain tumor research seeks to find diagnostic and prognostic biomarkers for gliomas that would inform both surgical and/or medical treatment. Extent of resection is increasingly accepted as critical to optimal surgical treatment and patient prognosis^{11,205}. Image-guidance facilitates neurosurgical resection but is subject to intraoperative brain shift, which degrades the accuracy of relating navigational information with the surgical field presented to the surgeon^{18,20,22,23,245-247}.

The use of ALA-induced PpIX fluorescence-guided resection (FGR) of brain tumors has gained increased clinical interest¹⁹³. FGR provides the operating surgeon with an intuitive, real-time surgical guidance tool for delineating tumor tissue which mitigates some of the challenges of image-guided neuro-navigation caused by intraoperative brain shift and deformation. ALA-induced PpIX FGR studies support its utility as a surgical tool for intraoperative delineation of tumor. For example, the largest study to date, a multicenter, randomized phase III clinical study of ALA-induced PpIX for FGR of malignant gliomas showed a significant improvement in gross total resection of the contrast-enhancing tumor (65% vs 36%) as well as a higher 6-month progression free survival (41.1% vs 21.1%) in the FGR group compared to the conventional white-light treatment group^{12,13,132}.

In a recent study of malignant gliomas, we found that visible levels of ALA-induced PpIX fluorescence correlate with tumor burden and WHO histopathological score of resected specimens¹⁹². To date, intraoperative detection of PpIX fluorescence for tumor delineation has largely been subjective (i.e., a modified surgical microscope is used to visualize “pink” fluorescence)^{13,15,38,121,132,192,248}. This approach is limited in its sensitivity for identifying low (but significant) levels of accumulated PpIX in tumor, potentially leaving some amount of resectable tumor unidentified²⁴⁹. Indeed, we recently reported preliminary *in vivo* results in human brain tumors²⁵⁰ that indicate PpIX fluorescence may be a tumor-targeting biomarker with a diagnostic performance which exceeds subjective visible assessments when measured quantitatively with a new fiber optic approach²⁵¹. Thus, even though ALA-induced PpIX fluorescence has been shown to be a successful biomarker for surgical resection of malignant glioma, the subjective assessments used to date do not appear to be sufficiently sensitive or quantitative to exhaust its full potential. As a result, establishing the underlying relationships between ALA-induced PpIX concentration in brain tumor tissues and their histologically-determined malignancy profile is critical to further development and optimization of FGR.

Towards this end, we investigated the hypothesis that quantitative *ex vivo* measurements of PpIX more sensitively differentiate areas of increasing malignancy in tumor than intraoperative visually subjective assessments of the same tissue. We tested our hypothesis by evaluating quantitative *ex vivo* measurements of PpIX concentration (C_{PpIX}) with proliferation indices and neoplasm subtypes on histopathology. We show that *ex vivo* quantitative measurement of PpIX concentration in tissue is more sensitive at identifying regions of increasing malignancy in both low- and high-grade gliomas than

current intraoperative fluorescence imaging. These findings suggest a need for improved intraoperative PpIX fluorescence detection to achieve better sensitivity and quantification of PpIX as a brain tumor biomarker, which in turn could lead to optimal surgical resection.

Table 1. Summary of patient characteristics

Patient No.	Diagnosis	Grade	Gender	Age	Visible Fluorescence
1	Dysembryoplastic neuroepithelial tumor	I	M	20.0	No
2	Dysembryoplastic neuroepithelial tumor	I	M	22.3	No
3	Recurrent glioma	N/A	F	50.6	Yes
4	Glioblastoma	IV	M	60.9	Yes
5	Anaplastic astrocytoma	III	F	24.7	Yes
6	Glioblastoma	IV	M	52.8	Yes
7	Glioblastoma	IV	M	79.9	Yes
8	Glioblastoma	IV	F	54.9	Yes
9	Glioblastoma	IV	M	68.8	Yes
10	Anaplastic mixed oligoastrocytoma	III	F	43.6	Yes
11	Glioblastoma	IV	F	41.3	Yes
12	Anaplastic oligodendroglioma	III	M	73.3	Yes
13	Glioblastoma	IV	F	77.0	Yes
14	Glioblastoma	IV	M	59.2	Yes
15	Ganglioglioma	I	F	22.2	No
16	Dysembryoplastic neuroepithelial tumor	I	F	38.0	No
17	Gliosarcoma	IV	F	70.6	Yes
18	Recurrent glioma	N/A	F	56.6	Yes
19	Glioblastoma	IV	F	76.5	Yes
20	Glioblastoma	IV	M	60.5	Yes
21	Glioblastoma	IV	M	55.7	Yes
22	Mixed oligoastrocytoma	II	M	50.4	Yes
23	Mixed oligoastrocytoma	II	D	27.5	No

Visible fluorescence: No-the surgeon did not observe red, visible fluorescence; **Yes**-the surgeon did observe red, visible fluorescence

Table 8.1. Summary of patient characteristics.

8.2. Methods

8.2.1 Specimen Acquisition

Tissue specimens evaluated in this study were obtained under informed consent from patients participating in our FGR protocol approved by the Dartmouth-Hitchcock Medical Center Committee for the Protection of Human Subjects. Patients were administered a 20 mg/kg body weight oral dose of ALA (DUSA Pharmaceuticals, Tarrytown, NY, USA) dissolved in 100 mL of water approximately three hours prior to the induction of anesthesia. The operating room was equipped with a Zeiss OPMI Pentero® operating microscope (Carl Zeiss Surgical GmbH, Oberkochen, Germany) enabled with fluorescence imaging and a Medtronic's StealthStation® Treon® (Medtronic, Louisville, CO, USA) for neurosurgical navigation. The operating microscope was modified for fluorescence imaging of PpIX with a 400 nm light source for excitation and a 620-710 nm bandpass filter for selectively recording PpIX fluorescence.

The primary guide for resection was conventional neurosurgical technique with white light illumination assisted by neuro-navigational guidance. Only tissue judged reasonably part of the planned resection volume, or abnormal tissue by other assessments (i.e., texture, non-fluorescent color, etc.) was included in the resection. In no instance was tissue resected on the basis of fluorescence alone. At different times during resection, the surgeon switched to 400 nm excitation light to visualize fluorescence. Biopsy specimens were collected at the beginning, middle, and end of resection, and digital images in white and blue light modes were recorded concurrently for each biopsy acquisition. Biopsy sites were assigned a fluorescence level by the study surgeon (DWR) of *0-no fluorescence, 1-low fluorescence, 2-moderate fluorescence, or 3-high fluorescence*. For each patient, multiple biopsy specimens were collected in both non-fluorescing and fluorescing (if present) regions within the preoperatively planned resection volume.

Each excised specimen was immediately separated into three equal parts for further processing as follows: 1) one part was placed in 10% buffered formalin for hematoxylin and eosin (H&E) and immunohistochemistry (IHC) staining; 2) a second part was placed in Optimal Cutting Temperature (OCT) compound and frozen in liquid nitrogen; 3) the third part was placed in a cryogenic vial and also frozen in liquid nitrogen for *ex vivo* fluorimetric quantification of PpIX.

8.2.2 Histopathology

Neuropathological analysis was performed on formalin-fixed paraffin-embedded biopsy tissue processed for H&E staining. A single neuropathologist (BTH) analyzed the H&E tissue slides blinded to the clinical, radiographic, and pathological diagnoses derived from the main surgical specimen in each case. Each H&E tissue section was assigned a histopathological score (0-IV) based on the current WHO grading criteria for the particular neoplasms observed¹⁵⁷. The following histopathological characteristics were used for each of the biopsies and judged independently regardless of the overall WHO grade assigned: (0) normal or fully necrotic tissue section with no viable tumor cells observed; (I) tissue section with low number of infiltrating tumor cells (reserved for specific types of glial or glioneuronal neoplasms such as pilocytic astrocytomas, dysembryoplastic neuroepithelial tumors, and gangliogliomas); (II) tissue section with higher number of infiltrating, pleomorphic cells and no observable necrosis, mitotic figures, or endothelial proliferation; (III) tissue section with highly pleomorphic tumor cells with mitotic figures, increased neoplastic cell density, and no observable necrosis or endothelial proliferation, (IV) tissue section with highly pleomorphic tumor cells with

mitotic figures, increased neoplastic cell density, and either observable necrosis and/or endothelial proliferation). The percentage of area occupied by necrotic tissue compared to non-necrotic tissue in each slide was determined for each tissue (as estimated by two observers -- BTH, PV).

8.2.3 Immunohistochemistry

Formalin-fixed paraffin embedded tissues near adjacent to the tissue sections used for H&E histopathological diagnosis were sectioned into 4 μm thick sections. To immunostain for the proliferation marker, Ki-67 antigen, tissue sections (n=133) were first hydrated, followed by antigen retrieval with hydrated autoclaving at 121°C for 10 min. Samples were blocked for endogenous peroxidase activity using 3% H_2O_2 for 10 min followed by a blocking step for non-specific binding using 10% fetal bovine serum (FBS) in phosphate buffered saline (PBS) for 20 min at room temperature. Tissue sections were incubated overnight with MIB-1 (1:150) anti-Ki-67 primary mouse IgG (Dako) in PBS and 1% FBS at 4°C. Tissue sections were then incubated for 2.5 hours with biotinylated (1:200) secondary anti-mouse IgG (Vector laboratories) in PBS at 37°C. Biopsy sections were then treated with ABC solution (Vector Laboratories) for 30 min and incubated with 3,3'-diaminobenzidine tetrahydrochloride (DAB) substrate for 1 hr. Samples were counterstained with hematoxylin (Fisher Scientific) and mounted. Appropriate negative controls were routinely obtained by substitution of the primary antibody with PBS only.

Tissue levels of proliferation were determined by calculating the MIB-1 proliferation index (PI)²⁵²⁻²⁵⁶. Briefly, for each tissue section, three high-power fields (400x) from non-overlapping regions in which the tissue displayed the greatest levels of positively-stained

MIB-1 nuclei (i.e., DAB positive) were chosen and corresponding images acquired using an Olympus bright field microscope. Manual counting of MIB-1 immunoreactive positive nuclei and non-reactive nuclei visualized by hematoxylin counterstain was performed on each image. For each tissue section, the PI was calculated as the ratio of positive MIB-1 nuclei over the sum of positive MIB-1 and non-reactive nuclei multiplied by 100. Tissues which were mostly necrotic with minimal viable cells (<33%) were excluded from the analysis.

8.2.4 Ex Vivo PpIX Fluorimetry

Tissue samples (n=133) placed in a cryogenic vial were stored at -80°C prior to fluorimetric quantification of PpIX following a modified protocol from Lilge et al²⁴³. Average tissue weight was 14.7 ± 10.1 mg (range, 1.1 – 56.1 mg). Briefly, the tissue was combined with 1 mL of Solvable (Dupont-Biotechnology Systems, Boston, MA, USA) and placed in an undulating water bath at 50°C for 1 hr. The tissue-Solvable solution was homogenized with a Tissue Tearor tool in the original cryogenic vial. The tissue homogenate (0.500 mL) was then combined with 1.125 mL of distilled water and 0.375 mL of Solvable. This solution was incubated in a 50°C water bath for 1 hr and then transferred to a quartz cuvette. The optical density of the solution was tested with a spectrophotometer to ensure an optical density less than 0.1. The cuvette was analyzed with a fluorimeter using an excitation wavelength of 401 nm and a slit width of 5 nm. A standard curve for quantification of PpIX was constructed by serially diluting PpIX by factors of 2 in a solution of distilled water (75% v/v) and Solvable (25% v/v).

Spectral decomposition was used to separate the contributions of PpIX, its photoproducts¹⁹⁵, and tissue autofluorescence. Autofluorescence was modeled as a linear combination of the emission spectra of reduced nicotinamide adenine dinucleotide (NADH), flavin adenine dinucleotide (FAD) and lipofuscin - components known to exist in brain tissue. Total tissue fluorescence was modeled as a linear combination of all fluorescent species, with a non-negative least squares algorithm to extract the contribution from each species, and determine the PpIX concentration in each specimen (C_{PpIX}).

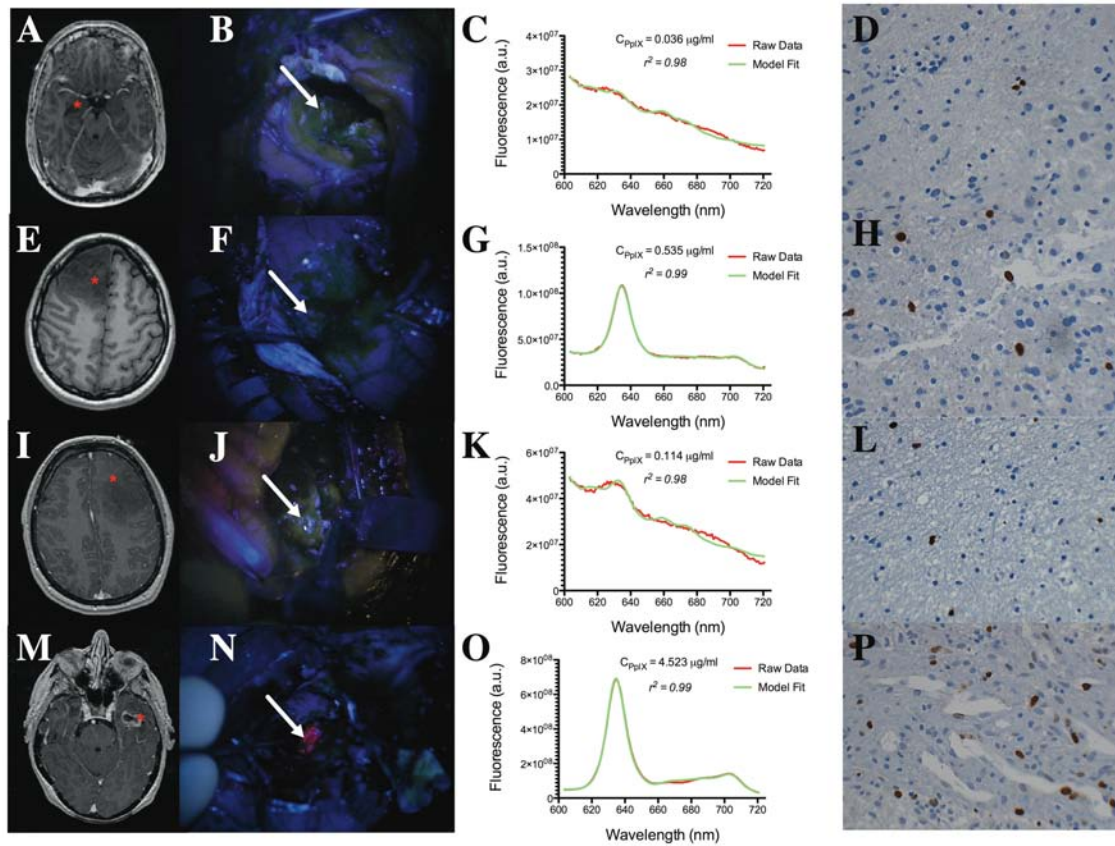


Figure 8.1. Illustrative examples of PpIX fluorescence characteristics and proliferative potential of low- and high-grade gliomas. Low and high-grade gliomas display distinct PpIX fluorescence characteristics and proliferative potential. A WHO grade I glioma (top

row), a WHO grade II glioma (second row), a WHO grade III glioma (third row), and one WHO grade IV glioma (fourth row) are shown, with their (A,E,I,M) post-gadolinium injection, T1-weighted axial images with red asterisks (*) corresponding to the image-guidance coordinates of a biopsy acquisition; (B,F,J,N) intraoperative blue light image of the surgical field with white arrows pointing to the location where the biopsy specimens were resected; (C,G,K,O) *ex vivo* PpIX fluorimetry spectral results from the samples (raw data spectra in red and model fit spectra in green); and (D,H,L,P) Ki-67 IHC of the resected tissues (original magnification 400x). The two low-grade and the one WHO grade III glioma samples shown here displayed no visible fluorescence. WHO grade I gliomas contained low, but detectable levels of accumulated C_{PpIX} (0.036 $\mu\text{g/mL}$) and minimal cellular proliferation (top row). The WHO grade II glioma contained intermediate to high levels of accumulated C_{PpIX} (0.535 $\mu\text{g/mL}$) and intermediate cellular proliferation (second row). The WHO grade III glioma contained low to intermediate levels of accumulated C_{PpIX} (0.114 $\mu\text{g/mL}$) and low to intermediate cellular proliferation. The high-grade glioma (GBM) illustrates an instance of high visible fluorescence, high levels of accumulated C_{PpIX} (4.523 $\mu\text{g/mL}$) and high cellular proliferation (fourth row). Ordinate, arbitrary units (a.u.); abscissa, nm.

8.2.5 Statistical Analysis

Kolmogorov-Smirnov analyses were used to assess normality of distributions. Wilcoxon-rank sum (Mann-Whitney) analyses were used to compare differences between groups. To further validate the statistical results and to accommodate for the multiple specimens per patient, a robust generalized estimating equation model²⁵⁷ was used to

perform a clustered data analysis of variance to attest for difference between groups. Medians and interquartile ranges were used to summarize differences in visible fluorescence and C_{ppIX} or PI, and across histopathological scores and qualitative visible fluorescence level. The differences were evaluated with a Kruskal-Wallis test with a post-test analysis for multiple comparisons using Dunn's procedure. Spearman's rank or Pearson's correlation analyses were used to assess a correlation for non-parametric or parametric variables, respectively. A *P* value of <0.05 was considered statistically significant for all tests. Data was processed with MATLAB® software (Version 2010a, The Mathworks Inc., Natick, MA, USA). STATA 11.0 (Stata Corporation, College Station, TX, USA) was used for statistical analyses.

8.3. Results

8.3.1 Patient and Data Characteristics

Specimens (n=133) from a total of 23 patients who underwent fluorescence-guided resection (10 men, 11 women) were collected and evaluated. As summarized in Table 8.1, the clinical diagnoses of cases studied were: 3 dysembryoplastic neuroepithelial tumors (Grade I), 1 ganglioglioma (Grade I), 2 mixed oligoastrocytomas (Grade II), 1 anaplastic astrocytoma (Grade III), 1 anaplastic mixed oligoastrocytoma (Grade III), 1 anaplastic oligodendroglioma (Grade III), 1 gliosarcoma (Grade IV), 11 glioblastoma multiforme (Grade IV), and 2 recurrent gliomas. The mean patient age was 51.6 years (range, 20.0-79.9 years). All high-grade gliomas (n=17) showed varying levels of visible fluorescence. No WHO grade I gliomas (n=4) showed visible fluorescence. One out of two WHO grade II gliomas showed visible levels of fluorescence. Figure 8.1 provides

examples of data collected in the study which illustrate relationships between visual (intraoperative) fluorescence, C_{PpIX} (as measured by ex-vivo fluorimetry) and immunohistochemical presentation of cellular proliferation (Ki-67 antigen) from specimens acquired during individual low- and high-grade glioma surgeries.

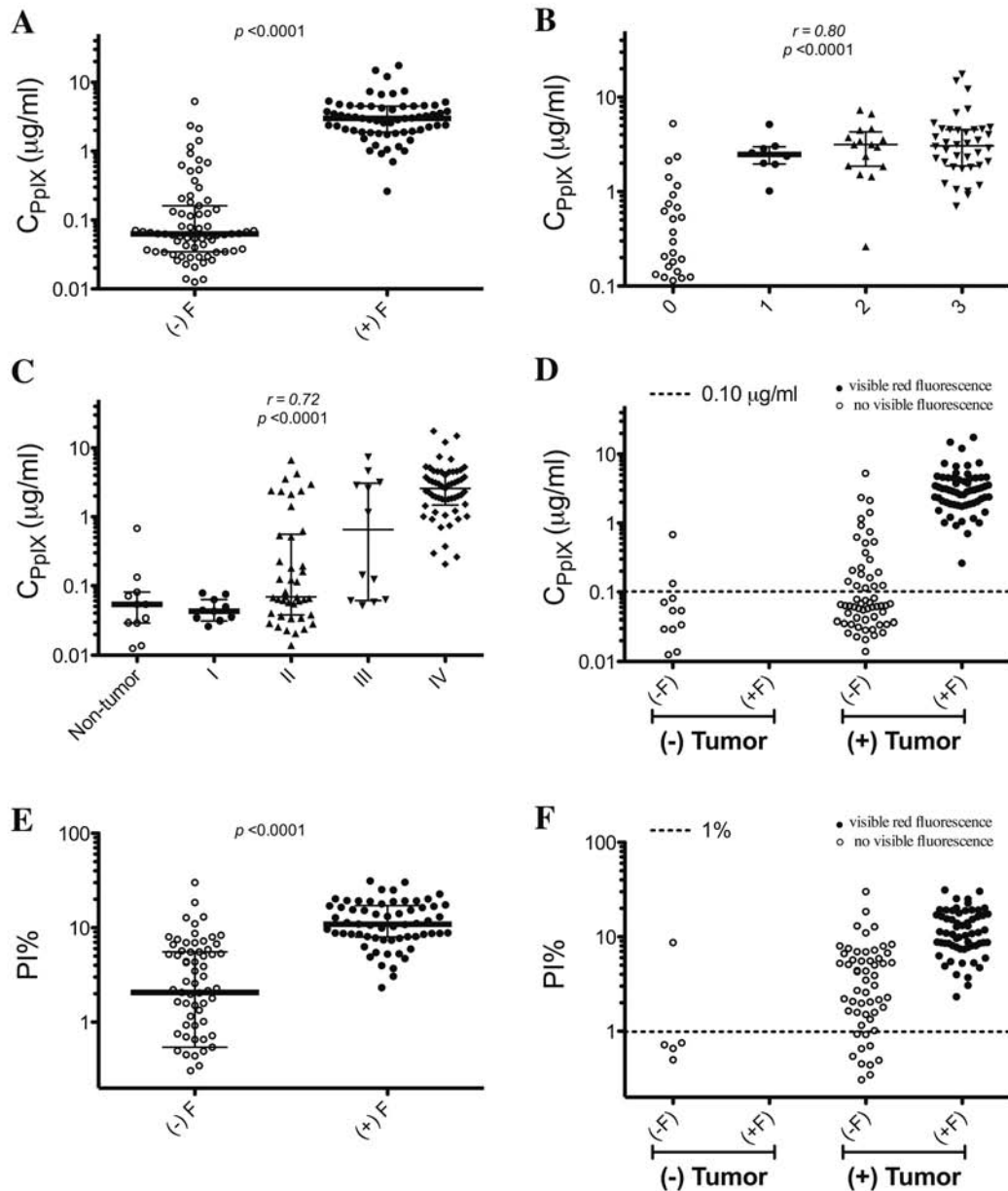


Figure 8.2. Intraoperative Visible Fluorescence, PpIX Concentrations, and Proliferation Index. A) Median and interquartile range of C_{PpIX} in tissues with no visible fluorescence, (-)F, or positive visible fluorescence, (+)F. Median C_{PpIX} is statistically different in the two groups (P value <0.0001). B) Median and interquartile range of C_{PpIX} in tissues with varying visible fluorescence scores (0-3) (Spearman's correlation analysis, $r = 0.80$, P value <0.0001). C) Median and interquartile range of C_{PpIX} in tissues with varying histopathological scores (Spearman's correlation analysis, $r = 0.72$, P value <0.0001). D) C_{PpIX} in specimens categorized as either tumor-negative, (-) Tumor, or tumor-positive, (+) Tumor, with no visible fluorescence, (-)F, or positive visible fluorescence, (+)F, in each category. Non-visibly fluorescent tumor tissues (~40%) accumulated levels of C_{PpIX} ($> 0.1\mu\text{g/ml}$) that were not detected with intraoperative fluorescence imaging. E) Median and interquartile range of PI percentage in tissues with no visible fluorescence, (-)F, or positive visible fluorescence, (+)F. Median PI is statistically different in the two groups (P value <0.0001). F) PI in specimens categorized as either tumor-negative, (-) Tumor, or tumor-positive, (+) Tumor, with no visible fluorescence, (-)F, or positive visible fluorescence, (+)F, in each category.

8.3.2 Association Between Intraoperative Visible Fluorescence, C_{PpIX} and PI

We performed Wilcoxon-rank sum (Mann-Whitney) analyses and further validated these results to accommodate for the multiple specimens per patient using a robust generalized estimating equations model to perform a clustered data analysis of variance to attest for a significant difference between the intraoperative visual fluorescence

characteristics (i.e, (-) F, no visible fluorescence and (+) F, positive visible fluorescence) of tissues and the two quantitative parameters, C_{PpIX} and PI. As shown in Figures 8.2A and 8.2E, we found significantly higher levels of accumulated C_{PpIX} and PI in tissues displaying visible levels of fluorescence compared to tissues displaying no visible fluorescence (P value <0.0001). These results corroborate the expectation that visible levels of fluorescence are dependent on the accumulated concentrations of PpIX.

We found a statistically significant difference using Kruskal-Wallis analyses with a Dunn's post-test for multiple comparisons in C_{PpIX} levels between groups classified as non-tumor and IV, I and III, I and IV, II and IV (P value <0.0001) and a statistically significant difference in visible fluorescence levels and C_{PpIX} only between fluorescence scores of 0 and 1, 0 and 2, and 0 and 3 (P value <0.0001). Further, the corresponding analysis for PI also showed a similar trend, with statistically significant differences in PI between non-tumor and IV, I and II, I and III, I and IV, II and IV, and III and IV (P value <0.0001). We see the same trend with statistically significant differences in visible fluorescence levels and PI only between fluorescence scores of 0 and 1, 0 and 2, and 0 and 3 (P value <0.0001).

Approximately 40% of the tumor-positive biopsy sites (22 samples), which were non-visibly fluorescent under the operating microscope, had C_{PpIX} levels greater than 0.1 mg/ml as measured by the fluorimetric assay whereas only two specimens above this threshold were negative for tumor (Figure 8.2D). Recent work using the quantitative intraoperative probe²⁰⁴ shows that greater than ~95% of normal tissue contains C_{PpIX} levels below 0.1 $\mu\text{g/ml}$. Here we chose this concentration as the cut-off value. One of these displayed high vascularity at the choroid plexus and showed no visible fluorescence (-F),

but presented with a particularly high level of C_{PpIX} ($\sim 0.6 \mu\text{g/ml}$). We also found that three quarters (75%) of the tumor-positive biopsies which did not visually fluoresce during surgery had PIs greater than 1% (Figure 8.2F).

8.3.3 Correlation Between Intraoperative Visible Fluorescence, C_{PpIX} and PI

We have previously shown that intraoperative visible PpIX fluorescence strongly correlates with tissue histopathological score (based on WHO grading criteria)¹⁹². We performed a non-parametric Spearman's rank analysis to test if a significant correlation also exists with PpIX concentrations (C_{PpIX}) and found a strong correlation between levels of C_{PpIX} in tissue and the levels of intraoperatively visible fluorescence ($r=0.80$, P value <0.0001) (Figure 8.2B) and the histopathological score ($r=0.72$, P value <0.0001) (Figure 8.2C). A similarly strong correlation between PI and histopathological score resulted from the same non-parametric Spearman's rank analysis ($r=0.61$, P value <0.0001). We also found a statistically significant correlation between the subjective levels of intraoperatively visible fluorescence (scored from 0-3) and the PI of tissue ($r=0.54$, P value <0.0001).

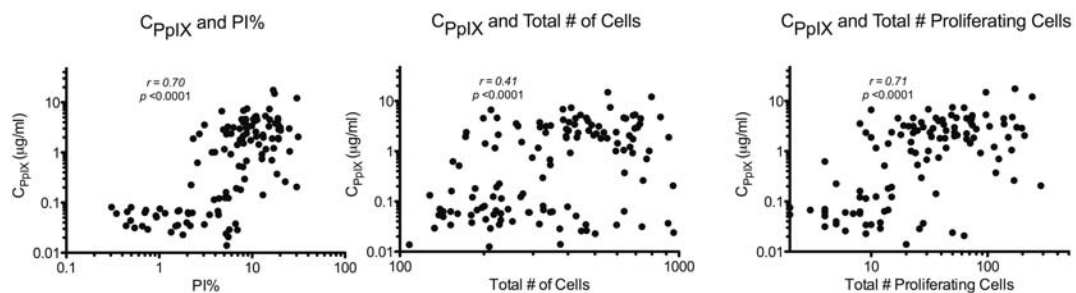


Figure 8.3. PpIX Concentration and Quantitative Histopathological Parameters of Malignancy. Pearson's correlation analysis (n=133) of A) scatter plot of log C_{PpIX} vs. log PI ($r = 0.70$, P value <0.0001), B) scatter plot of log C_{PpIX} vs log of total number of cells ($r = 0.41$, P value <0.0001) and C) scatter plot of log C_{PpIX} vs. log of total number of proliferating cells ($r = 0.71$, P value <0.0001). PI, total number of cells, and total number of proliferating cells were counted in three high power fields from tissues processed for anti-Ki-67 IHC.

8.3.4 Correlation Between C_{PpIX} and Quantitative Histopathological Parameters of Malignancy

To assess whether PpIX concentrations (i.e., C_{PpIX}) are able to quantitatively differentiate between discrete levels of malignancy, we used Pearson's analysis to test for a significant correlation between C_{PpIX} and three quantitative histopathological parameters: (1) PI, (2) total number of cells, and (3) total number of proliferating cells. We found the strongest correlations (on a log-log scale, see Figure 3) between levels of C_{PpIX} and PI ($r=0.70$, P value <0.0001) and total number of proliferating cells ($r=0.71$, P value <0.0001) relative to total number of cells ($r=0.41$, P value <0.0001). This statistically significant linear correlation between C_{PpIX} and quantitative histopathological parameters demonstrate that microscopic levels of malignancy can be differentiated by accumulated tissue levels of C_{PpIX} .

8.4. Discussion

Extent of resection is a major prognostic factor in brain tumor patients. Further, accurate identification during surgery of the more malignant regions of tumor is important for subsequent neuropathological diagnosis, which determines the chemo- and radio-therapeutic regime and patient prognosis. Image-guidance can help the neurosurgeon to better delineate the tumor margins for surgical removal and subsequent neuropathological assessment. Nevertheless, image-guidance suffers from intraoperative brain shift and deformation which degrade and limit navigational accuracy^{18,20,22,23,245-247}.

The major clinical implementations of FGR have only used subjective assessments of intraoperative fluorescence (i.e., negative or positive visible fluorescence). One major limitation of this approach is that subjective FGR suffers from inter-observer variability in correctly assessing low levels of fluorescence. A further limitation of subjective ALA-induced PpIX FGR is its inability to detect fluorescence that may be obscured by physical effects such as variation in tissue optical properties (i.e., optical absorption and transport scattering properties) and camera orientation to the resection cavity. The tissue optical absorption in particular varies between tissue sites and can greatly impact the resultant subjective fluorescence assessment. This can lead to tumor tissue that contains high levels of accumulated PpIX biomarker but is incorrectly identified (i.e., non-visibly fluorescent) (Fig. 1). In a recent study we used a fiber-optic approach that takes into account tissue optical properties to quantify PpIX concentrations *in vivo* and showed that significant levels of PpIX concentrations are present in a variety of intracranial tumor histologies below the threshold of visual detection²⁵⁰.

In this study we have shown that C_{PpIX} evaluated in specimens resected during surgery is identified with regions of increasing malignancy assessed histologically in low- and

high-grade gliomas beyond the capabilities of current fluorescence imaging. As expected, a statistically significant difference in C_{PpIX} occurred between tissues with no visual fluorescence (-F) intraoperatively and those with positive visual fluorescence (+F). A significant trend also occurred between C_{PpIX} and the subjective fluorescence levels observed intraoperatively which produced a positive correlation. All but two non-tumor tissue specimens contained C_{PpIX} levels below $0.1 \mu\text{g/mL}$, while ~40% of non-visibly fluorescent tumor tissues were above this threshold (Figure 8.2D). These results suggest that improvements in the detection of fluorescence intraoperatively is likely to identify more tumor tissue (especially in low-grade glioma) and if quantitative detection of C_{PpIX} can be achieved during surgery, it may be possible to define a threshold which maximizes the diagnostic performance of PpIX fluorescence for tumor resection.

Although the exact mechanism(s) that leads to preferential accumulation of PpIX in tumor tissue is not well known, cellular proliferation, cell density, mitochondrial content, vascular proliferation, structural changes, and enzymatic up-/down-regulation (e.g., ferrochelatase)^{46,91,258,259} have been suggested as contributing factors. Since all of these factors correlate with the degree of tissue malignancy, we also assessed relationships between PpIX fluorescence and measures of tissue malignancy quantified with a (MIB-1) proliferation index (PI) using Ki-67 antigen as the biomarker. We found a statistically significant difference in PI between non-fluorescent (-F) and positively-fluorescent (+F) biopsies (Figure 8.2) as well as a strong correlation between PI and subjective levels of fluorescence. Further, the results assessing a difference in C_{PpIX} levels and PI across histopathological scores and visible fluorescence levels (i.e., Kruskal-Wallis analyses) further show that C_{PpIX} levels and PI display similar trends of statistically significant

differences between groups. This data further supports our hypothesis that quantitative levels of C_{PpIX} can serve as a useful biomarker to ascertain tumor regions of more proliferative and anaplastic tissue.

Further, we show that quantitative *ex vivo* measurements of C_{PpIX} correlate with quantitative histopathological measures of tissue malignancy by showing a strong, statistically significant correlation between PI and C_{PpIX} (Figure 8.3A). However, PI index is a relative term quantifying the percentage of abnormal cells over the total number of cells in a given tissue which does not fully relate measures of tissue malignancy to accumulation of C_{PpIX} . To further elucidate the quantitative relationship between *ex vivo* measurements of PpIX and tissue malignancy, we also determined the correlation between cell density and number of abnormal, proliferating cells as additional factors affecting accumulation of PpIX in tissue. We found a statistically significant correlation (Figures 8.3B and C) between C_{PpIX} and total number of cells as well as between C_{PpIX} and total number of abnormal cells. More importantly, these results as well as similarly strong correlations between C_{PpIX} ($r=0.72$) and PI ($r=0.61$) with tissue histopathological score, indicate the ability of C_{PpIX} to differentiate between varying degrees of tissue malignancy at the microscopic level comparable to the gold standard, i.e., Ki-67 proliferation index. The predictive value of both qualitative levels of visible fluorescence and C_{PpIX} levels for predicting phenotype (e.g., proliferation, histopathological grade) is provided by our correlation coefficients, r , which show a statistically significant, strong correlation between C_{PpIX} and cellular proliferation ($r = 0.71$) and histopathological score ($r = 0.72$). Previous studies have shown that MIB index, although not an absolute marker of tumor malignancy, is positively correlated with WHO grade in gliomas as well as negatively

correlated with prognosis²⁶⁰⁻²⁶³. As such, in this study we have focused on gliomas, as we present a quantitative approach to identifying areas of more aggressive, highly proliferative tissue in the resection of gliomas. Further, we have also shown a positive correlation between cell density and C_{PpIX} , but in this study we show a stronger correlation between C_{PpIX} and cellular proliferation, which argues that the latter is a stronger, more significant predictor of C_{PpIX} levels in glioma tissue.

They also show that a quantitative and more sensitive determination of PpIX concentration can be used to identify microscopic levels of increasing tumor cell proliferation, and thus, regions of increasing malignancy. More importantly, quantitative measurements of C_{PpIX} can be used as a tissue biomarker to accurately identify non-visibly fluorescent, proliferative tumor tissue. Quantitative assessments open the door for more sensitive intraoperative determination of tumor malignancy in both visibly fluorescent and perhaps more importantly, non-visibly fluorescent tissue (e.g., non-fluorescing regions of anaplastic astrocytomas). Further, such biomarker determinations can guide the neurosurgeon in representative biopsy sampling to achieve a more accurate neuropathological diagnosis and inform patient treatment. For example, it is of importance to note that all WHO grade III tumors in this study were heterogeneous tumors with anaplastic foci. This point is of importance to our study, since our results show a correlation between increased proliferation and C_{PpIX} , arguing that such anaplastic foci in heterogeneous gliomas could be more easily identified by noting increased levels of C_{PpIX} .

Previous work suggests that blood-brain barrier status is a contributing factor to observable levels of PpIX fluorescence^{13,38,67}. Stummer et al showed a strong association between post-operative contrast-enhancement on MR imaging and levels of red visible

fluorescence at the end of surgery. Further, we have recently shown a significant association between intraoperative levels of PpIX fluorescence and two MR imaging metrics of contrast-enhancement¹⁹². These studies are inconclusive, since they suffer from brain shift, which degrades the accuracy of associating tissue fluorescence and MR imaging. Further, to our knowledge, no study has undertaken a quantitative assessment un-affected by brain shift (e.g., brain biopsy cases) and correlated histopathological and imaging findings with quantitative levels of PpIX. It is important to note that the strong positive correlation of $r = 0.70$, $P \text{ value} < 0.0001$ observed in this study for proliferation index and PpIX accumulation argues that: 1) PpIX accumulation in gliomas is strongly dependent on cellular proliferation status (i.e., cellular proliferation status in gliomas is a strong predictor of PpIX accumulation); 2) despite the strong correlation observed between C_{PpIX} and cellular proliferation, PpIX accumulation is a multifaceted biological process which cannot be accounted solely on the basis of cellular proliferation; and 3) that the strong correlation presented here suggests the predictive power of C_{PpIX} for tissue proliferation. These conclusions are in agreement with previous studies which show that PpIX accumulation is dependent upon factors such as enzymatic up- and down-regulation, cellular proliferation, oxygenation status, and mitochondrial content, among others^{67,238,264}. The current study investigated the relationship specifically between cellular proliferation and PpIX accumulation in gliomas. The relationship between PpIX accumulation and blood-brain barrier status is of great importance to the field, but beyond the scope of this study.

A limitation of the study is that C_{PpIX} measurements were performed ex vivo, which for purposes of intraoperative guidance is impractical. Utsuki et al⁴⁴ report on a

spectroscopy device for real-time feedback of fluorescence signal which shows improved detection of tumor with no visible fluorescence. Spectroscopic devices are known to improve detection of fluorescence signals from tissue due to geometries optimized for excitation and light collection, which maximize detection of fluorescent light while minimizing bleed-through of extraneous signals. Despite improved detection of low levels of fluorescence or fluorescence not visible by a modified surgical microscope, this simplified fluorescence spectroscopic devices are still limited in their inability to quantitatively determine absolute levels of PpIX. More specifically, the system by Utsuki et al is limited by its inability to accurately quantify fluorescence that may be obscured by physical effects such as variation in tissue optical properties (i.e., optical absorption and transport scattering properties). The tissue optical absorption in particular varies between tissue sites and can greatly impact the resultant fluorescence assessment^{57,64,124,265}. We have reported on an intraoperative fiber-optic system which measures C_{PpIX} levels in vivo and which accounts for such variations in tissue optical properties - providing significantly improved diagnostic performance compared to simplified fluorescence spectroscopy. This quantitative probe is able to quantify the absolute levels of C_{PpIX} in tissue despite variations in tissue optical properties^{64,204}. The results presented in this study are a proof-of-principle of the value of C_{PpIX} measurements for detection of more malignant, proliferative regions of tissue in gliomas. Since the ability to quantify PpIX levels in tissue for the ex vivo assay correlates with the *in vivo* quantitative probe, the results from this study are translatable to a real-time *in vivo* quantification procedure which can be implemented using the quantitative probe. One important observation and possible limitation to this study is the validity of operating on recurrent gliomas with the

assumption that C_{PpIX} positively correlates with cellular proliferation. Recurrent gliomas following chemotherapy are known to contain significant levels of inflammatory cells which in turn are known to have increased levels of C_{PpIX} fluorescence²³⁸. This fact could be a confounding factor leading to increased C_{PpIX} levels in recurrent glioma as a result of inflammatory cell presence and not increased proliferation. In our study, all recurrent glioma specimens did not contain any significant component of inflammatory cells, and were either diffusely infiltrated with rare tumor cells and had low levels of C_{PpIX} , or were densely infiltrated by tumor cells with high levels of C_{PpIX} . Future studies will further inform the surgeon regarding the utility of C_{PpIX} determination for the resection of recurrent gliomas. Another limitation of this study is possible sampling error when dividing the biopsy specimens into three parts for histopathological and biochemical analysis; though generally samples are quite small (less than 0.5 cm in greatest dimension) and the three parts should have similar pathology.

8.5. Conclusions

The findings reported here provide rationale for developing the improved PpIX fluorescence detection needed to achieve better sensitivity and quantification of the biomarker in tissue. Quantitative and more sensitive detection of PpIX fluorescence would better enable the neurosurgeon to achieve a more informed real-time assessment of the surgical field, leading to optimal tumor resection.

Chapter 9. Conclusions and future directions

9.1. Conclusions

Broadly speaking, the main objective of this thesis was to explore the role of ALA-induced PpIX as an intraoperative fluorescent biomarker for neurosurgical resection of brain tumors. Specifically, this thesis systematically assessed two main aspects of ALA-induced PpIX in fluorescence guided surgery so as to inform the community on the detection capabilities and biological correlates of ALA-induced PpIX in brain tumors.

This thesis started with a presentation on the relevant background for intraoperative fluorescence guided surgery. First, it elaborated on the four major factors to consider for *in vivo* fluorescence detection: properties of fluorophores, biological origin of fluorescence contrast, the role of intrinsic tissue properties, and available detection technologies. It then provided a thorough overview of current work in fluorescence guided neurosurgery, and specifically, on ALA-induced PpIX fluorescence guided surgery. This introductory chapter (i.e., *Chapter 1*) provided the necessary background knowledge to inform subsequent studies presented in this thesis.

An initial study (i.e., *Chapter 2*) was conducted to serve as a baseline experience on the current-state-of-the-art in ALA-induced PpIX fluorescence imaging to inform and help guide future studies. In this study we were able to replicate previous work in FGR of gliomas (e.g., Stummer's experience), which up until this point was considered the most current and elaborate experience on ALA-induced PpIX FGR. Further, this study yielded two major lessons which drove the subsequent work presented in this thesis. First, it provided a basic understanding on the important biological parameters associated with

accumulated PpIX fluorescence in tissue. It gave insight into the biological significance of accumulated levels of PpIX in GBMs. Specifically, we learned the importance of tumor aggressiveness and blood-brain barrier breakdown as predictors of PpIX fluorescence. Broadly, it provided us with a baseline understanding on the multifaceted nature of PpIX accumulation in brain tumors, which this study suggested was a factor of both intrinsic tumor metabolic changes (e.g., increased growth and associated requirements) as well as tumor induced structural changes (i.e., blood-brain barrier breakdown as assessed by contrast enhancement on T1-weighted MR imaging). Second, it explored what is clinically the state-of-the-art in ALA-induced PpIX fluorescence detection technologies – the Zeiss OPMI Pentero microscope modified for PpIX fluorescence imaging. This analysis provided a standard against which to compare any future studies regarding the detection capabilities of PpIX fluorescence – using the Pentero microscope - for tumor tissue detection. The major lesson learned from this experience was the severely limited detection capabilities of the state-of-the-art in FGR (e.g., negative predictive value = 0.26; sensitivity = 0.75). That is, current fluorescence imaging showed significant limitations in its sensitivity for detecting abnormal tumor tissue. This would imply inaccurate detection of tumor during resection, thus leaving significant amounts of tumor tissue behind (i.e., unresected).

Finally, we learned in *Chapter 2* and *Chapter 3* that ALA-induced PpIX fluorescence provides predictive as well as complementary information to MR imaging features and image-guidance during resection of malignant gliomas; results which support the role of FGR as an adjuvant to MR image guidance for its real-time feedback, correlates with MR imaging, and added information about tumor not provided by MR imaging features.

Despite the added value of FGR as an adjuvant to MR image guidance (e.g., FGR combined with updated MR image guidance from *Chapter 3* which showed perfect accuracy in detecting tumor tissue), our ‘baseline’ experience highlighted 1) the limitations in detection capabilities for FGR in brain tumor resection, and 2) the lack of a clear understanding regarding the biological basis of PpIX as an intraoperative biomarker for brain tumors that would inform neurosurgeons for future implementations. As such, before any further investigation into the role of FGR in combination with MR image guidance, this initial work prompted subsequent studies to address the following two questions:

- 1) How ‘good’ of an intraoperative brain tumor biomarker is ALA-induced PpIX? That is, what is the extent to which PpIX can serve as a biomarker to accurately detect abnormal tumor tissue for intraoperative applications.
- 2) What is the biological basis of ALA-induced PpIX in brain tumors? That is, what are significant predictors of PpIX accumulation in brain tumors that would inform the neurosurgeon when using this technology.

The studies in this thesis were undertaken to address both of these questions in parallel over the years of study.

Others have shown (and we corroborated in our initial studies) that current state-of-the-art FGR detection technologies (i.e., surgical microscope modified for fluorescence imaging) suffers from low detection accuracies, leaving significant amounts of tumor undetected. Such an observation would argue against the utility of PpIX as a useful intraoperative biomarker for brain tumors. This prompted investigation into two

approaches for improving PpIX fluorescence for tumor detection: 1) artificially enhance PpIX levels; and 2) improve the detection technologies to maximally exploit the targeting potential of PpIX. That is, we sought to answer the question of “how accurate is PpIX for intraoperative detection?”

The initial approach could be labeled as the ‘brute force’ approach, in which we would seek to artificially increase PpIX levels to overcome both technological and PpIX targeting limitations. PpIX is known to undergo addition of an iron atom by the enzyme ferrochelatase to form heme. *In vitro* work has shown the value of iron chelation for enhancing PpIX fluorescence. As such, the initial approach in a xenograft rodent model of GBM was to treat animals with an iron chelator to enhance PpIX fluorescence. This artificial increase in PpIX fluorescence showed an increase in overall PpIX levels of approximately 50% following therapy. Nevertheless, although the increase was statistically significant, the burden of iron chelation therapy and the modest increase in PpIX production, did not warrant further pursuit of this approach for improving tumor detection with PpIX. An added concern of clinical relevance is the fact that iron chelation therapy (as an adjuvant to ALA administration) would require further approvals, toxicity, and associated requirements for application in humans. Such added hurdles impeded pursuit of this avenue of research.

The next approach was the use and validation of improved detection technologies that would maximally exploit the inherent targeting capabilities of ALA-induced PpIX fluorescence. State-of-the-art in FGR uses a surgical microscope with appropriate excitation and emission filters to detect PpIX fluorescence. Detected PpIX fluorescence is enhanced by means of collection with a CCD camera, but no further processing or

corrections are applied. Lessons from the field of tissue optics have informed us that the observed fluorescence emissions from tissues are multifactorial. The intrinsic tissue properties such as tissue autofluorescence impact the observed PpIX fluorescence. More importantly, tissue optical properties such as scattering and absorption significantly impact both the ability of tissue fluorophores (i.e., PpIX) to be excited and for the fluorescence emissions to be detected. As such, the variations in tissue optical properties and their effects on the observed fluorescence emissions will significantly impact the utility of a fluorescent biomarker for intraoperative use. As such, the current state-of-the-art approach is highly prone to subjectivity in interpreting the observed fluorescence emissions, since they do not accurately quantify the levels of fluorophore present. That is, the current clinical approach is at best subjective and qualitative in assessing ‘true’ PpIX fluorescence. An optimal detection technology would take into account the contribution of variations in tissue optical properties to extract the ‘intrinsic’ or ‘quantitative’ fluorescence in tissue, which would be directly proportional to the actual concentration of fluorescent biomarker accumulated.

The work in *Chapter 5* validated a spectroscopic-based detection technology that maximally exploits the targeting potential of ALA-induced PpIX in tumors. Simultaneous measurement of the tissue optical properties and fluorescence spectrum of interrogated tissues provided the necessary information to extract the ‘quantitative’ fluorescence spectrum. Subsequently, the absolute concentrations of accumulated PpIX in tissues could be determined. A systematic comparison of the diagnostic capabilities of this ‘quantitative’ approach to the ‘qualitative’ approach showed that PpIX is a more accurate biomarker for tumor tissue than previously believed (qualitative approach accuracy =

66% vs quantitative approach accuracy=87%). These results showed significantly improved detection potential of PpIX as a surgical marker for a variety of tumor histologies, including low- and high-grade gliomas, meningiomas, and metastases. This study demonstrated that FGR using PpIX has great potential, achieving accuracies of ~90% for tumor tissue identification - if improved detection technologies other than the current state-of-the-art are used. That is, current clinical implementations of fluorescence imaging suffer from significant sensitivity and detection limitations, but using a technology that accurately quantifies the intrinsic tissue fluorescence can provide substantial improvement in detecting tumor. The work in *Chapter 5* showed that to maximally exploit ALA-induced PpIX, a more sophisticated optical detection technology, which takes into account the variations in tissue optical properties is required; such that, PpIX has the potential to be a highly accurate tumor targeting biomarker.

This work in intraoperative quantitative fluorescence has prompted future work in developing quantitative fluorescence imaging and detection technologies (Please refer to section 9.2 for further discussion). Although these results are promising, two important lessons on the targeting and detection potential for low-grade gliomas were learned. First, the accuracy for low-grade gliomas using this quantitative approach (i.e., accuracy = 76%) was almost identical to that of current fluorescence imaging using a surgical microscope for high-grade gliomas (i.e., GBM). These results significantly change the ‘dogma’ in the field of FGR which suggested that PpIX fluorescence does not provide diagnostic benefit for low-grade gliomas. Instead, this data demonstrates that with improved detection technologies, PpIX FGR for low-grade gliomas has the potential to

improve resection in this tumor sub-type. This is of great significance, since improved resection in this tumor sub-type has the potential for profound clinical benefit. Second, although detection was significantly improved for all tumor sub-types, the accuracy for low-grade gliomas lagged behind. Our understanding of the complexity in tumor biology supports these results. Low-grade gliomas are different entities than high-grade gliomas, displaying distinct differences at both the histopathological and gene expression levels. It is almost 'silly' to think that one particular biomarker would be all-encompassing and display comparable targeting capabilities for such distinct biological entities.

This work informed the subsequent study presented in *Chapter 6*. Neoplastic processes are multifaceted, involving a complex interplay of changes including angiogenesis, hypoxia, changes in gene expression profiles, increased growth and resistance to death-inducing signals, and structural changes at both the intracellular (e.g., increased mitochondria) and intercellular (e.g., extra-cellular matrix modifications) levels. Pathologists use a combination of various assessments at the histopathological level to accurately discriminate between low-grade and high-grade gliomas (e.g., endothelial proliferation, pleomorphic changes, necrosis, nuclear atypia, etc.). Given our understanding of the numerous changes associated with neoplastic progression and growth (e.g., from low- to high-grade glioma), it would only be reasonable that accurate detection of tissue *in vivo* might require assessment of multiple biomarkers other than just one (i.e., PpIX). In this study on only gliomas interrogated with the intraoperative probe, a diagnostic algorithm was developed, which takes into account the predictive power of several biomarkers of relevance to neoplastic processes, to improve detection accuracy for gliomas. The diagnostic algorithm accounted for changes in angiogenesis, tissue

hypoxia, PpIX accumulation, and associated morphological changes (e.g., increased nuclear density and intracellular changes), by means of hemoglobin concentration, oxygen saturation fraction, PpIX (and associated photoproducts) concentration, and scattering parameters. The multiple biomarker diagnostic algorithm showed significantly improved detection accuracy of 96% for gliomas. More specifically, the detection for low-grade gliomas also significantly improved, achieving an accuracy of 96%. This study opened the door to the use of quantitative biomarkers and development of the first truly multiple biomarker approach (and algorithm) for resection of brain tumors. This work is the logical progression and extension of our initial quantitative study using PpIX as the sole biomarker. Here, use of multiple biomarkers which account for the multifaceted nature of gliomas provided significantly improved (almost ideal) tumor tissue detection. This simple, practical diagnostic algorithm could in principle be applied intraoperatively and *in vivo*, as it depends only on the initial model used for classification. Further, this study sheds light and provides a basis for future development of FGR technologies which take into account not just PpIX fluorescence but also endogenous biomarkers predictive of neoplastic processes. That is, this work opens the door to not just fluorescence guidance in neurosurgery, but to a more comprehensive approach which could more accurately be described as optical guidance.

All the studies investigating the biomarker targeting capabilities, e.g., sensitivity, of PpIX accumulation in tissues assumes a particular relationship between PpIX and tumor tissue; namely, PpIX selectively accumulates in abnormal compared to normal tissue in brain tumors to provide significant fluorescence contrast for differentiation. This assumes that PpIX production is increased in tumors relative to normal brain as a result of tumor-

specific changes. Previous work has already reviewed and elaborated on many possible factors affecting PpIX production in cells^{46,67,238}. Nevertheless, despite efforts to address the overproduction of PpIX in tumors, no clear consensus and understanding exists regarding its accumulation.

Given this lack in the ALA-induced PpIX FGR literature, studies were conducted in this thesis to inform the neurosurgical community on key histopathological correlates that make up a significant component for the biological basis of PpIX-selectivity for brain tumors. The importance of this information is of great importance for future implementations of this targeting biomarker. First, a more complete understanding regarding the selective nature of PpIX accumulation would inform the neurosurgeon on the patient population (e.g., tumor sub-types) that are good candidates for FGR. Second, a clear understanding of the biological basis of PpIX overproduction will inform future technological developments in FGR. For example, we have seen that although PpIX accumulates at significant levels in low-grade gliomas, evidence suggests that PpIX is not an optimal biomarker for this tumor type (e.g., classification accuracies are < 80%).

The initial experience presented in *Chapter 2* informed future work. This initial study showed correlates of aggressiveness (e.g., a positive correlation in histopathological score and tumor burden with visible levels of fluorescence). More importantly, this initial study shed light on multiple factors that are predictive of PpIX accumulation. This data prompted the study in *Chapter 7* – a comprehensive and exploratory analysis of gene expression changes in tissue displaying distinct fluorescence characteristics.

Gene expression microarrays are a powerful tool to look at over 20,000 genes and their expression profiles simultaneously – endowing the researcher with a global outlook

on feasible biological targets to explain the phenomenon (or phenomena) of interest. In this initial study the approach was conservative but highly informative if successful: compare the gene expressions profile changes between positively and negatively fluorescent tissue in paired specimens from GBM cases. One of the major limitations to take into account when performing gene expression microarray studies is the high false positive rate of “identified targets”. In this study, this was dealt with by using a Benjamini and Hochberg False Discovery Rate for multiple testing correction, which provides a balance between decreasing the false positive rate and increasing the discovery of significant expression changes. Analysis of the microarray data showed significant gene expression profiles changes in over 80 genes. Specifically, particular gene clusters were significantly overexpressed in positively fluorescent tissue; among the significant gene clusters were cellular proliferation, angiogenesis, extra-cellular matrix modifications, locomotion, cell death, and immune response.

These results provided a global perspective of likely explanatory factors for increased ALA-induced PpIX fluorescence in gliomas. The main lesson learned from this data was further confirmation of the multifaceted changes that might account for PpIX overproduction. That is, PpIX overproduction in tumors is most likely not the result of one or a few dysregulated pathways. Rather, the selective accumulation of PpIX in tumors is more likely explained by a synergistic and multifactorial interplay of numerous pathways gone awry. This would explain the broad targeting potential of PpIX as an intraoperative biomarker. PpIX accumulates at significant levels across a range of tumor histologies beyond just GBM, including such distinct entities as low-grade gliomas, metastases, and meningiomas. Further, this multifaceted nature of PpIX overproduction

can also explain how, despite its characteristics as a broad targeting biomarker, PpIX does not provide optimal targeting in entities such as low-grade gliomas, e.g., they are growing at a significantly slower rate, structural and associated metabolic changes are minimal compared to other faster growing, malignant tumors like GBM, etc. Another important lesson learned from this global assessment on PpIX production and GBM was the explanatory and predictive power of certain gene clusters for overproduction of PpIX. These results informed further studies presented in *Chapter 8*.

Gene expression profile changes showed a significant increase in overexpression of proliferation genes in positively fluorescent tissue; a likely explanation is that increased cellular proliferation in tumors accounts for increased PpIX accumulation. The value of this observation lies in the fact that cellular proliferation shows a strong correlation with histopathological grade and patient prognosis. Such that, if PpIX levels are predictive of proliferation, then PpIX can serve not just a tumor targeting biomarker, but more specifically, as a biomarker for identifying anaplastic regions within and across tumors. Thus, the hypothesis guiding this study was that cellular proliferation correlates with PpIX levels, such that highly sensitive and quantitative measurements of increasing PpIX levels are predictive of increasing levels of proliferation in tissue; a hypothesis that arose out of the initial experience (*Chapter 2*) and our gene expression analysis (*Chapter 7*).

This study demonstrated a strong correlation between quantitative measurements of PpIX (i.e., absolute PpIX concentrations in tissue) and cellular proliferation across a broad range of gliomas – WHO grade I, II, III, and IV gliomas. These results validate the gene expression analysis, since it supports the idea that cellular proliferation plays a significant role in the selective accumulation of PpIX in tissues. Further, and of greater

practical importance, increasing levels of PpIX correlate with increasing levels of cellular proliferation. These results are of profound clinical impact, since it informs the neurosurgeon on the utility of PpIX as not just a tumor biomarker, but a biomarker of anaplasticity. Further, it provides a framework upon which the surgeon can better understand the multifaceted nature of PpIX accumulation in tumors. Although the correlation between proliferation and PpIX was strong and highly significant, it was not perfect, which further corroborates our gene expression results – which shed light on multifactorial explanations for PpIX accumulation in tissues. That is, other factors in addition to proliferation are also predictive of PpIX accumulation in tumors.

Further, our initial experience (i.e., baseline study) showed a significant correlation between contrast-enhancement on pre-operative T1-weighted images and visible levels of fluorescence. This is in agreement with previous work showing a significant association between contrast-enhancement on post-operative T1-weighted images and levels of residual intraoperative visible fluorescence. These results, among others, suggest that blood-brain barrier (BBB) breakdown plays a role in PpIX accumulation; to the extent that the neurosurgical community has the implicit understanding that low-grade gliomas (which generally do not display BBB breakdown as assessed by contrast-enhancement) do not accumulate significant levels of PpIX for adequate fluorescence contrast and as such are not good candidates for FGR.

The results from *Chapter 5* argue against this view, suggesting that although PpIX targeting for low-grade gliomas is less accurate than for high-grade gliomas, it can identify tumor tissue with diagnostic fidelity. That is, PpIX is produced in high enough amounts in low-grade glioma tissue compared to normal brain to provide sufficient

fluorescence contrast for tumor tissue identification; this is despite the unimpaired (that is to say, radiologically unimpaired) BBB observed in a majority of these tumors.

Nevertheless, BBB breakdown does appear to play an important role. Analysis of the gene expression profile differences showed significant upregulation of genes associated with angiogenesis and extra-cellular matrix (ECM) interactions. Angiogenic and ECM changes in brain tumors will alter the BBB, likely leading to breakdown and increased permeability. In summary, our results suggest that anaplasticity and associated neoplastic changes of more aggressive tumor are major determinants of PpIX accumulation, and should provide a venue for future investigation into the major correlates of PpIX overproduction in these tumors.

Exploratory analysis into the biological basis of PpIX accumulation in brain tumors as presented in this thesis provides new insights, with substantial amounts of data to the FGR community. First, it provides a global assessment of gene expression changes associated with PpIX fluorescence in gliomas. Second, it provides a strong basis pointing to the multifaceted and multifactorial nature of PpIX overproduction in tumors. Third, it presents a quantitative study validating the significant role of cellular proliferation for overproduction of PpIX – suggesting PpIX as a targeting biomarker for anaplasticity. Investigation into the biological basis of PpIX overproduction in tumors as presented in this thesis provides an in-depth assessment which informs the FGR community on the biological correlates of PpIX fluorescence, and provides a strong foundation on which to continue further exploration into this question.

This thesis demonstrates that PpIX is a broad targeting biomarker across a range of different tumor histologies, given the multifaceted nature of factors accounting for the

fluorescence contrast provided by PpIX. Further, this thesis shows that to maximally exploit the highly selective and targeting potential of PpIX for intraoperative brain tumor detection, more sophisticated technologies that account for variations in tissue optical properties are required to objectively measure PpIX levels in tissues. To the best of our knowledge this thesis presented the first quantitative and systematic analysis of the targeting potential of PpIX for brain tumors. In addition, this thesis demonstrates that PpIX can be used even more specifically, not just as a brain tumor biomarker, but as a biomarker of anaplasticity in gliomas.

As expected, although PpIX displays broad targeting potential because of the multiple factors contributing to its overproduction, optimal tumor tissue detection is likely to require more than just one simple biomarker. As a result of the multifaceted nature of neoplastic process, FGR is likely to require detection of more than just one biomarker to provide maximal surgical guidance. In light of these findings, which elaborate on the biological basis of PpIX and its limitations as an all-encompassing targeting biomarker, this thesis developed a logical extension to quantitative ALA-induced PpIX FGR as developed in *Chapter 5*. We developed a more comprehensive quantitative FGR diagnostic algorithm which takes into account multiple biomarker to achieve accuracies of 96% or greater across a range of different glioma histologies – from low-grade to high grade – opening the door to optical guidance in resection of tumors (fluorescence guidance coupled with adjuvant optical methods).

In summary, this thesis presented a systematic and quantitative assessment on the detection capabilities and factors to achieve maximal exploitation of the tumor targeting potential of ALA-induced PpIX. This work elaborated on the important and contributing

biological factors which form the basis of PpIX accumulation in tumors, informing future development of FGR technologies. The ground-work for future investigations on the biological basis of FGR is presented, providing a strong baseline for future studies. Finally, this thesis provides the FGR neurosurgical community strong evidence suggesting the need for improved and more sophisticated optical detection technologies to achieve maximal guidance for the resection of tumors. Overall, we provide a biologically and technologically informed approach in ALA-induced PpIX fluorescence guidance as an adjuvant for improved resection of brain tumors.

9.2. Future Directions

In this final section of the thesis I wish to briefly discuss possible future directions for this project. In this section, I will follow the same organizational outline as the thesis, discussing ideas in detection improvements, and followed by suggestions for further understanding the biological basis of PpIX. First, the quantitative intraoperative probe approach should be further validated in a larger cohort of patients. Such a study would continue to inform the neurosurgical community regarding the guidance potential of quantitative PpIX FGR. Along these lines, we are currently working on extending the intraoperative probe approach from a “point” approach (i.e., $\sim 1 \text{ mm}^2$ of interrogated tissue) to an imaging approach. That is, for quantitative PpIX FGR to likely take hold in the neurosurgical community, an imaging modality (rather than a point spectroscopic approach) should be developed and validated. Future work should then focus on implementing the exciting results from our quantitative approach, to a wide-field imaging technology, capable of performing real time, quantitative PpIX FGR. Further, and in line

with the results presented in this thesis, an imaging approach to PpIX is likely to provide improved detection with inclusion of multiple biomarkers, e.g., hemoglobin content, oxygen saturation fraction. Thus, a suggestion for future directions stemming from this thesis is development of a quantitative multiple biomarker imaging system, analogous to the “point” approach presented in *Chapter 6*.

Future work should continue to focus on further investigation into the biological basis of PpIX accumulation in tumors. A logical extension from this study would involve further microarray expression studies, followed by appropriate validation, e.g., IHC, western blotting, etc. Such data would provide further insight into the biological basis of this phenomenon, by elaborating on the key pathways and neoplastic processes which account for PpIX accumulation. This would require future work involving histopathological as well as molecular biology studies into the key biological factors influencing the accumulation of PpIX in cells and tissues.

Another future direction of interest, given that we have already provided an understanding on the targeting potential for PpIX and validated technologies for such evaluations, is investigation into the role of PpIX FGR in image guided surgery. One key study that would greatly inform the community is one that would seek to more accurately correlate the levels of PpIX with MR imaging features. We have found a correlation between imaging features and PpIX visible fluorescence. But our study had two major limitations: 1) it used relative metrics of enhancement; and 2) it was plagued by significant intraoperative brain shift. Future work should perform quantitative MR imaging to ascertain gadolinium concentrations at the moment of imaging. Further, a stereotactic biopsy (closed cranium) study would be minimally influenced by brain shift

and deformation. With such a study design and subsequent determination of tissue fluorescence, the neurosurgical community could have a more informed, accurate understanding on the correlation between contrast enhancement on MR imaging and PpIX accumulation.

Future work should also seek to evaluate application of PpIX FGR beyond tumor resection. We are currently assessing the utility of PpIX FGR in a rodent model of temporal lobe epilepsy. We have found significant PpIX fluorescence contrast in regions known to compose the epileptic foci. As such, we hope that such a study would translate to application in humans and extension of PpIX FGR for epilepsy resection.

The possible avenues of research on both the engineering and biological fronts are numerous, especially given the promise PpIX FGR shows for intraoperative neurosurgical guidance. In this thesis we presented work that will inform the community using or planning to use AA-induced PpIX FGR. Finally, we concluded with some suggestions for future directions on the PpIX FGR project.

Appendices

Automated 3D Rigid and Non-Rigid Image Registration Graphical User Interface

Use of MR image-guidance is standard practice in neurosurgical resection of brain tumors. In this work, biopsy specimens were mapped to their intraoperative image-space coordinates which were obtained from the StealthStation Treon navigation system. MR image sequences used intraoperatively were either high resolution (i.e., in the z-direction) post-contrast injection T1-weighted or T2-weighted images. The studies conducted in *Chapter 2* and *Chapter 3* required analysis of only T1-weighted images. As such, the need arose to create a user friendly, multimodality, and 3D image registration toolbox. For example, a common need involved registration of T2-weighted images with T1-weighted images from low-grade gliomas, where T2-weighted images were usually used for registration. Following registration, intraoperative navigation coordinates could be mapped from the T2-weighted to the T1-weighted images with an appropriate transformation.

For the purpose of this thesis, an automated 3D image registration toolbox for registering MR images was developed. The toolbox and associated functions are controlled by means of a user-friendly graphical user interface (GUI) developed and run through MATLAB. All basic image processing and image displays are performed through MATLAB, but the core of the 3D registration computations are performed using ITK Rigid and Non-rigid algorithms. Image registration is performed using mutual information as a similarity metric between images. As such, in a mutual information

registration algorithm, the optimal registration between images is achieved when the mutual information is maximized^{266,267}. The image registration GUI is equipped with both rigid and non-rigid capabilities for registration of 3D brain images. Given the nature of mutual information and use of only intensity value between images, the registration algorithms allow for multimodality registration – a key requirement for this toolbox.

Screen-shots of the GUI are provided below, which display some of the key functionalities – input/outputs.

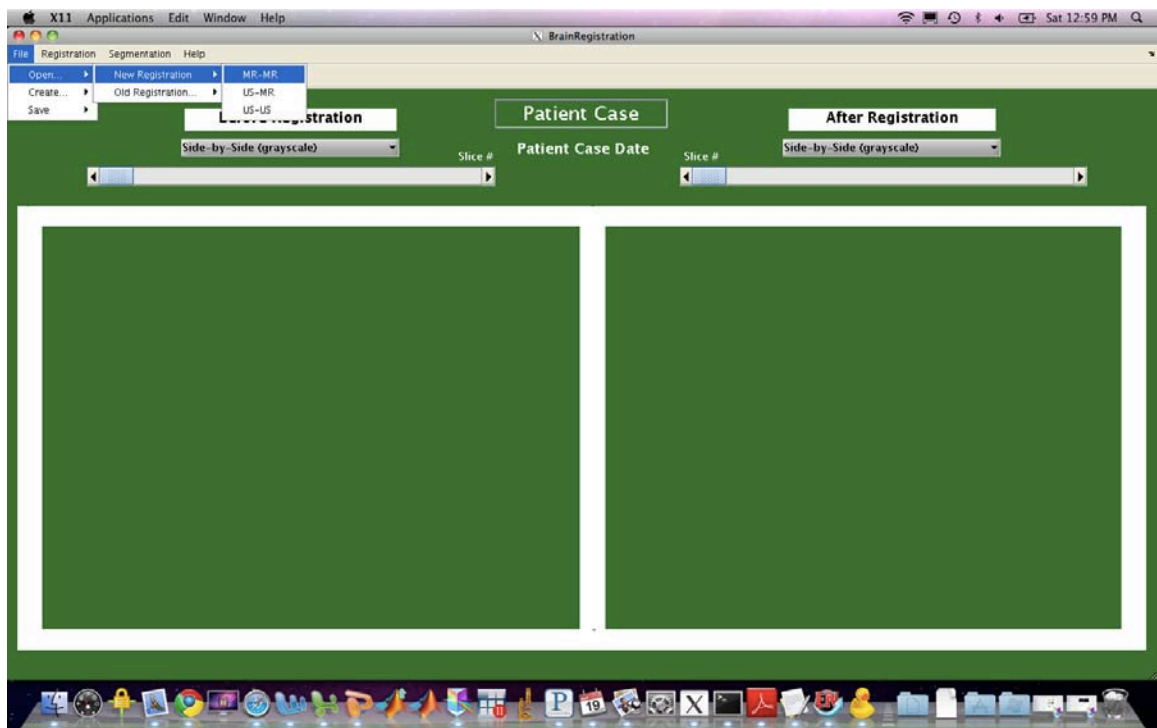


Figure Appendix A1. Registration selection. The GUI allows selection of image registration between inter- and intra-modality rigid and non-rigid registration.

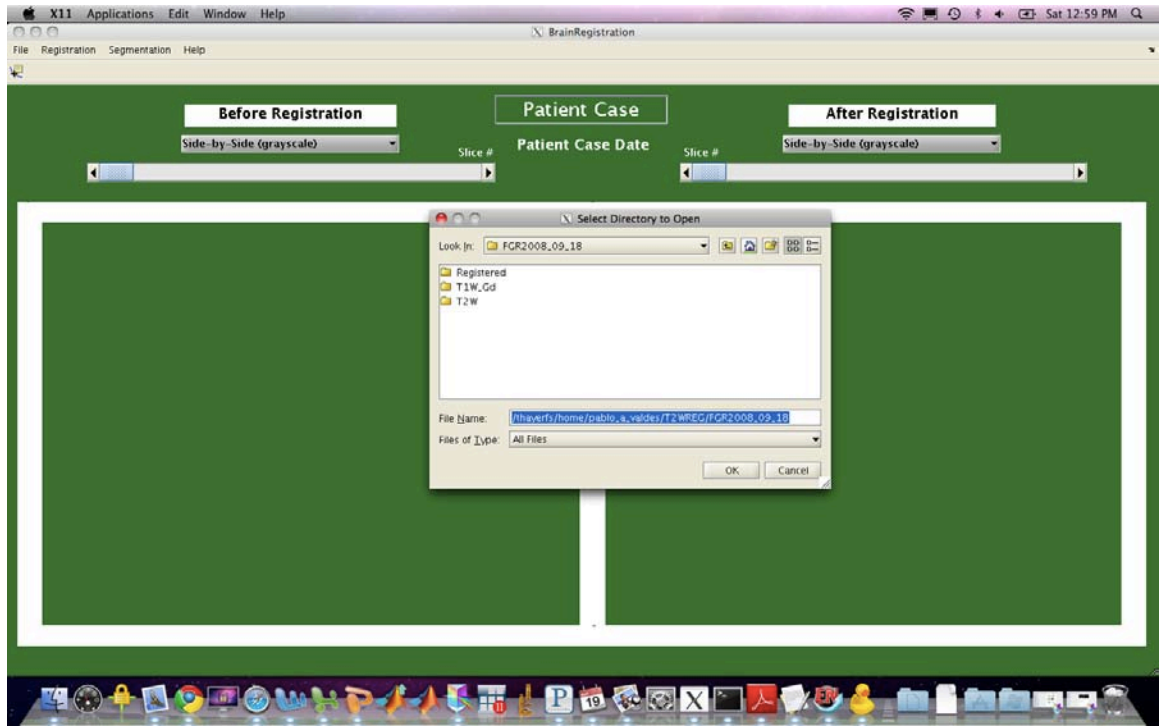


Figure Appendix A2. Directory selection. The GUI allows user friendly selection of directory containing files for registration

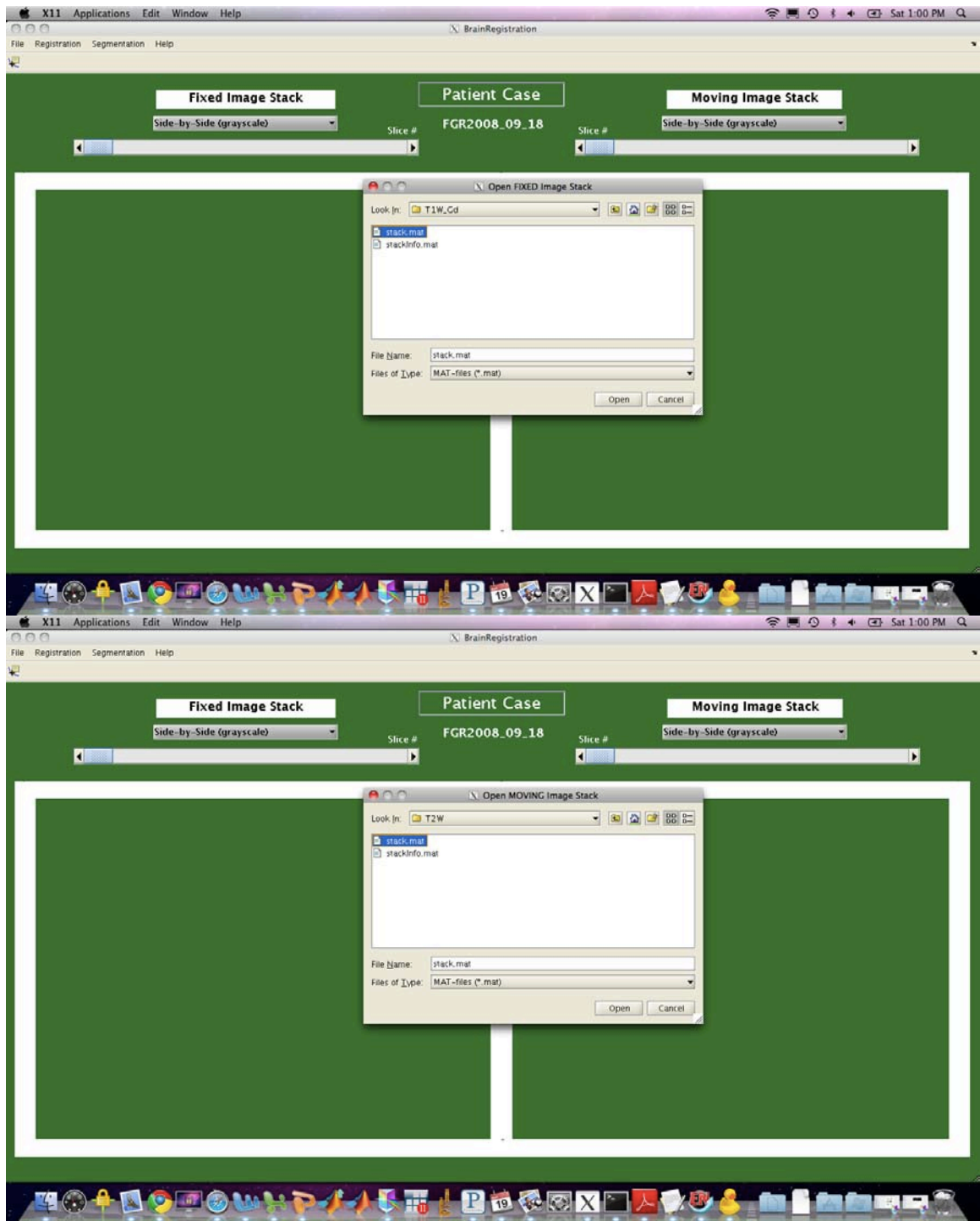


Figure Appendix A3. Fixed and moving stack selection. The GUI allows the user to specify which images will be the “fixed” and “moving” images. The “fixed” image is the

image stack that remains immovable in image space, meanwhile a “moving” image is rotated and translated (e.g., in rigid registration) in image space with respect to the “fixed” image to calculate the optimal mutual information.

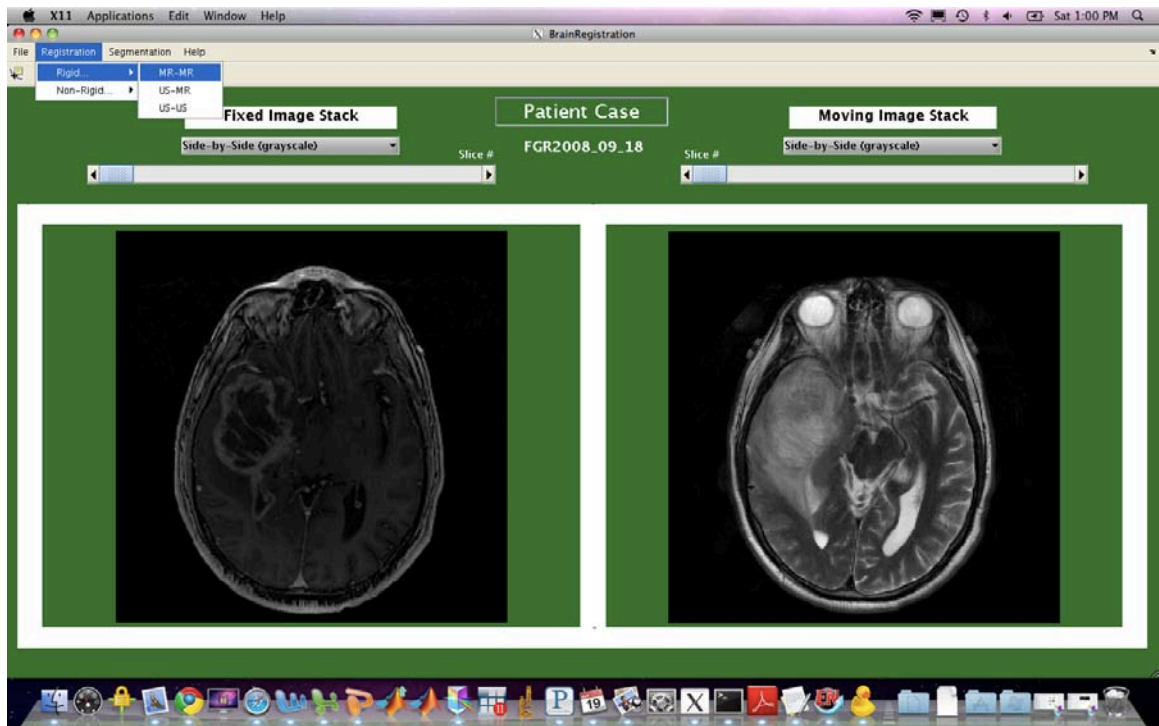


Figure Appendix A4. Registration type and image visualization. The GUI allows the user to visualize the image stacks to be registered prior to selection of registration type. The two types of registration supported by the GUI are rigid and non-rigid registration.



Figure Appendix A5. Registration parameters. The GUI allows the user to select registration parameters to optimize registration and timing. In this case, the user can select the number of iterations (default, 200) and the sampling ratio (default, 50) of the images to use to calculate the mutual information of the two images during rigid registration.

References

1. Nabavi, A., Black, P. M., Gering, D. T., Westin, C. F., Mehta, V., Pergolizzi, R. S., Jr., Ferrant, M., Warfield, S. K., Hata, N., Schwartz, R. B., Wells, W. M., 3rd, Kikinis, R., Jolesz, F. A.: Serial intraoperative magnetic resonance imaging of brain shift. **Neurosurgery** **48**:787-797; discussion 797-788, 2001
2. Black, P. M., Moriarty, T., Alexander, E., 3rd, Stieg, P., Woodard, E. J., Gleason, P. L., Martin, C. H., Kikinis, R., Schwartz, R. B., Jolesz, F. A.: Development and implementation of intraoperative magnetic resonance imaging and its neurosurgical applications. **Neurosurgery** **41**:831-842; discussion 842-835, 1997
3. Matula, C., Rossler, K., Reddy, M., Schindler, E., Koos, W. T.: Intraoperative computed tomography guided neuronavigation: concepts, efficiency, and work flow. **Comput Aided Surg** **3**:174-182, 1998
4. Nakao, N., Nakai, K., Itakura, T.: Updating of neuronavigation based on images intraoperatively acquired with a mobile computerized tomographic scanner: technical note. **Minim Invasive Neurosurg** **46**:117-120, 2003
5. Uhl, E., Zausinger, S., Morhard, D., Heigl, T., Scheder, B., Rachinger, W., Schichor, C., Tonn, J. C.: Intraoperative computed tomography with integrated navigation system in a multidisciplinary operating suite. **Neurosurgery** **64**:231-239; discussion 239-240, 2009
6. Gronningsaeter, A., Kleven, A., Ommedal, S., Aarseth, T. E., Lie, T., Lindseth, F., Lango, T., Unsgard, G.: SonoWand, an ultrasound-based neuronavigation system. **Neurosurgery** **47**:1373-1379; discussion 1379-1380, 2000

7. Keles, G. E., Lamborn, K. R., Berger, M. S.: Coregistration accuracy and detection of brain shift using intraoperative sononavigation during resection of hemispheric tumors. **Neurosurgery** **53**:556-562; discussion 562-554, 2003
8. Letteboer, M. M., Willems, P. W., Viergever, M. A., Niessen, W. J.: Brain shift estimation in image-guided neurosurgery using 3-D ultrasound. **IEEE Trans Biomed Eng** **52**:268-276, 2005
9. Albert, F. K., Forsting, M., Sartor, K., Adams, H. P., Kunze, S.: Early postoperative magnetic resonance imaging after resection of malignant glioma: objective evaluation of residual tumor and its influence on regrowth and prognosis. **Neurosurgery** **34**:45-60; discussion 60-41, 1994
10. Barker, F. G., 2nd, Prados, M. D., Chang, S. M., Gutin, P. H., Lamborn, K. R., Larson, D. A., Malec, M. K., McDermott, M. W., Sneed, P. K., Wara, W. M., Wilson, C. B.: Radiation response and survival time in patients with glioblastoma multiforme. **J Neurosurg** **84**:442-448, 1996
11. Lacroix, M., Abi-Said, D., Fournay, D. R., Gokaslan, Z. L., Shi, W., DeMonte, F., Lang, F. F., McCutcheon, I. E., Hassenbusch, S. J., Holland, E., Hess, K., Michael, C., Miller, D., Sawaya, R.: A multivariate analysis of 416 patients with glioblastoma multiforme: prognosis, extent of resection, and survival. **J Neurosurg** **95**:190-198, 2001
12. Pichlmeier, U., Bink, A., Schackert, G., Stummer, W.: Resection and survival in glioblastoma multiforme: an RTOG recursive partitioning analysis of ALA study patients. **Neuro Oncol** **10**:1025-1034, 2008

13. Stummer, W., Pichlmeier, U., Meinel, T., Wiestler, O. D., Zanella, F., Reulen, H. J.: Fluorescence-guided surgery with 5-aminolevulinic acid for resection of malignant glioma: a randomised controlled multicentre phase III trial. **Lancet Oncol** **7**:392-401, 2006
14. Stummer, W., Reulen, H. J., Meinel, T., Pichlmeier, U., Schumacher, W., Tonn, J. C., Rohde, V., Opperl, F., Turowski, B., Woiciechowsky, C., Franz, K., Pietsch, T.: Extent of resection and survival in glioblastoma multiforme: identification of and adjustment for bias. **Neurosurgery** **62**:564-576, 2008
15. Stummer, W., Stocker, S., Wagner, W., Stepp, H., Clemens, F., Goetz, C., Goetz, A., Kiefmann, R., Reulen, H. J.: Intraoperative Detection of Malignant Gliomas by 5-Aminolevulinic Acid-induced Porphyrin Fluorescence. **Neurosurgery** **42**:518 - 526, 1998
16. Hill, D. L., Maurer, C. R., Jr., Maciunas, R. J., Barwise, J. A., Fitzpatrick, J. M., Wang, M. Y.: Measurement of intraoperative brain surface deformation under a craniotomy. **Neurosurgery** **43**:514-526, 1998
17. Ji, S., Roberts, D. W., Hartov, A., Paulsen, K. D.: Brain-skull contact boundary conditions in an inverse computational deformation model. **Med Image Anal** **13**:659-672, 2009
18. Lunn, K. E., Paulsen, K. D., Liu, F., Kennedy, F. E., Hartov, A., Roberts, D. W.: Data-guided brain deformation modeling: evaluation of a 3-D adjoint inversion method in porcine studies. **IEEE Trans Biomed Eng** **53**:1893-1900, 2006
19. Nimsky, C., Ganslandt, O., Cerny, S., Hastreiter, P., Greiner, G., Fahlbusch, R.: Quantification of, visualization of, and compensation for brain shift using

- intraoperative magnetic resonance imaging. **Neurosurgery** **47**:1070-1079; discussion 1079-1080, 2000
20. Sun, H., Lunn, K. E., Farid, H., Wu, Z., Roberts, D. W., Hartov, A., Paulsen, K. D.: Stereopsis-guided brain shift compensation. **IEEE Trans Med Imaging** **24**:1039-1052, 2005
 21. Sun, H., Roberts, D. W., Farid, H., Wu, Z., Hartov, A., Paulsen, K. D.: Cortical surface tracking using a stereoscopic operating microscope. **Neurosurgery** **56**:86-97; discussion 86-97, 2005
 22. Grunert, P., Darabi, K., Espinosa, J., Filippi, R.: Computer-aided navigation in neurosurgery. **Neurosurg Rev** **26**:73-99; discussion 100-101, 2003
 23. Lunn, K. E., Paulsen, K. D., Lynch, D. R., Roberts, D. W., Kennedy, F. E., Hartov, A.: Assimilating intraoperative data with brain shift modeling using the adjoint equations. **Med Image Anal** **9**:281-293, 2005
 24. Valdes, P. A., Fan, X., Ji, S., Harris, B. T., Paulsen, K. D., Roberts, D. W.: Estimation of Brain Deformation for Volumetric Image Updating in Protoporphyrin IX Fluorescence-Guided Resection. **Stereotact Funct Neurosurg**:[in press], 2009
 25. Eljamel, M. S., Goodman, C., Moseley, H.: ALA and Photofrin fluorescence-guided resection and repetitive PDT in glioblastoma multiforme: a single centre Phase III randomised controlled trial. **Lasers Med Sci** **23**:361-367, 2008
 26. Hefti, M., von Campe, G., Moschopoulos, M., Siegner, A., Looser, H., Landolt, H.: 5-aminolevulinic acid induced protoporphyrin IX fluorescence in high-grade

- glioma surgery: a one-year experience at a single institution. **Swiss Med Wkly** **138**:180-185, 2008
27. Kajimoto, Y., Kuroiwa, T., Miyatake, S., Ichioka, T., Miyashita, M., Tanaka, H., Tsuji, M.: Use of 5-aminolevulinic acid in fluorescence-guided resection of meningioma with high risk of recurrence. Case report. **J Neurosurg** **106**:1070-1074, 2007
 28. Koc, K., Anik, I., Cabuk, B., Ceylan, S.: Fluorescein sodium-guided surgery in glioblastoma multiforme: a prospective evaluation. **Br J Neurosurg** **22**:99-103, 2008
 29. Kremer, P., Mahmoudreza, F., Ding, R., Pritsch, M., Zoubaa, S., Frei, E.: Intraoperative fluorescence staining of malignant brain tumors using 5-aminofluorescein-labeled albumin. **Neurosurgery** **64**:53-60, 2009
 30. Kuroiwa, T., Kajimoto, Y., Ohta, T.: Development of a Fluorescein Operative Microscope for use During Malignant Glioma Surgery: A Technical Note and Preliminary Report. **Surgical Neurology** **50**:41-49, 1998
 31. Kuroiwa, T., Kajimoto, Y., Ohta, T.: Comparison between operative findings on malignant glioma by a fluorescein surgical microscopy and histological findings. **Neurological Research** **21**:130-134, 1999
 32. Moore, G. E., Peyton, W. T., French, L. A., Walker, W. W.: The clinical use of fluorescein in neurosurgery: The localization of brain tumors. **Journal of Neurosurgery** **5**:392-398, 1948
 33. Morofuji, Y., Matsuo, T., Hayashi, Y., Suyama, K., Nagata, I.: Usefulness of intraoperative photodynamic diagnosis using 5-aminolevulinic acid for

- meningiomas with cranial invasion: technical case report. **Neurosurgery** **62**:102-103; discussion 103-104, 2008
34. Murray, K. J.: Improved surgical resection of human brain tumors: Part 1. A preliminary study. **Surgical Neurology** **17**:316-319, 1982
35. Okuda, T., Kataoka, K., Taneda, M.: Metastatic brain tumor surgery using fluorescein sodium: technical note. **Minim Invasive Neurosurg** **50**:382-384, 2007
36. Shinoda, J., Yano, H., Yoshimura, S., Okumura, A., Kaku, Y., Iwama, T., Sakai, N.: Fluorescence-guided resection of glioblastoma multiforme by using high-dose fluorescein sodium. Technical note. **J Neurosurg** **99**:597-603, 2003
37. Stepp, H., Beck, T., Pongratz, T., Meinel, T., Kreth, F. W., Tonn, J., Stummer, W.: ALA and malignant glioma: fluorescence-guided resection and photodynamic treatment. **J Environ Pathol Toxicol Oncol** **26**:157-164, 2007
38. Stummer, W., Novotny, A., Stepp, H., Goetz, C., Bise, K., Reulen, H. J.: Fluorescence-guided resection of glioblastoma multiforme by using 5-aminolevulinic acid-induced porphyrins: a prospective study in 52 consecutive patients. **J Neurosurg** **93**:1003-1013, 2000
39. Stummer, W., Reulen, H. J., Novotny, A., Stepp, H., Tonn, J. C.: Fluorescence-guided resections of malignant gliomas--an overview. **Acta Neurochir Suppl** **88**:9-12, 2003
40. Stummer, W., Stepp, H., Moller, G., Ehrhardt, A., Leonhard, M., Reulen, H. J.: Technical principles for protoporphyrin-IX-fluorescence guided microsurgical

- resection of malignant glioma tissue. **Acta Neurochir (Wien)** **140**:995-1000, 1998
41. Utsuki, S., Miyoshi, N., Oka, H., Miyajima, Y., Shimizu, S., Suzuki, S., Fujii, K.: Fluorescence-guided resection of metastatic brain tumors using a 5-aminolevulinic acid-induced protoporphyrin IX: pathological study. **Brain Tumor Pathol** **24**:53-55, 2007
 42. Utsuki, S., Oka, H., Miyajima, Y., Shimizu, S., Suzuki, S., Fujii, K.: Auditory alert system for fluorescence-guided resection of gliomas. **Neurol Med Chir (Tokyo)** **48**:95-97, 2008
 43. Utsuki, S., Oka, H., Sato, S., Shimizu, S., Suzuki, S., Tanizaki, Y., Kondo, K., Miyajima, Y., Fujii, K.: Histological examination of false positive tissue resection using 5-aminolevulinic acid-induced fluorescence guidance. **Neurol Med Chir (Tokyo)** **47**:210-213, 2007
 44. Utsuki, S., Oka, H., Sato, S., Suzuki, S., Shimizu, S., Tanaka, S., Fujii, K.: Possibility of using laser spectroscopy for the intraoperative detection of nonfluorescing brain tumors and the boundaries of brain tumor infiltrates. Technical note. **J Neurosurg** **104**:618-620, 2006
 45. Weissleder, R., Pittet, M. J.: Imaging in the era of molecular oncology. **Nature** **452**:580-589, 2008
 46. Collaud, S., Juzeniene, A., Moan, J., Lange, N.: On the selectivity of 5-aminolevulinic acid-induced protoporphyrin IX formation. **Curr Med Chem Anticancer Agents** **4**:301-316, 2004

47. Friesen, S. A., Hjortland, G. O., Madsen, S. J., Hirschberg, H., Engebraten, O., Nesland, J. M., Peng, Q.: 5-Aminolevulinic acid-based photodynamic detection and therapy of brain tumors (review). **International Journal of Oncology** **21**:577-582, 2002
48. Kennedy, J. C., Marcus, S. L., Pottier, R. H.: Photodynamic therapy (PDT) and photodiagnosis (PD) using endogenous photosensitization induced by 5-aminolevulinic acid (ALA): mechanisms and clinical results. **J Clin Laser Med Surg** **14**:289-304, 1996
49. Ishihara, R., Katayama, Y., Watanabe, T., Yoshino, A., Fukushima, T., Sakatani, K.: Quantitative spectroscopic analysis of 5-aminolevulinic acid-induced protoporphyrin IX fluorescence intensity in diffusely infiltrating astrocytomas. **Neurol Med Chir (Tokyo)** **47**:53-57; discussion 57, 2007
50. Pogue, B. W., Gibbs-Strauss, S., Valdes, P. A., Samkoe, K., Roberts, D. W., Paulsen, K. D.: Review of Neurosurgical Fluorescence Imaging Methodologies. **IEEE J Sel Top Quantum Electron**, In Press, 2010
51. Wagnieres, G. A., Star, W. M., Wilson, B. C.: In vivo fluorescence spectroscopy and imaging for oncological applications. **Photochem Photobiol** **68**:603-632, 1998
52. Sokolov, K., Follen, M., Richards-Kortum, R.: Optical spectroscopy for detection of neoplasia. **Curr Opin Chem Biol** **6**:651-658, 2002
53. Fitzmaurice, M.: Principles and pitfalls of diagnostic test development: implications for spectroscopic tissue diagnosis. **J Biomed Opt** **5**:119-130, 2000

54. Leblond, F., Davis, S. C., Valdes, P. A., Pogue, B. W.: Pre-clinical whole-body fluorescence imaging: Review of instruments, methods and applications. **J Photochem Photobiol B** **98**:77-94
55. Moghissi, K., Stringer, M. R., Dixon, K.: Fluorescence photodiagnosis in clinical practice. **Photodiagnosis Photodyn Ther** **5**:235-237, 2008
56. Lakowicz, J. R.: **Principles of Fluorescence Spectroscopy, ed 3**: Springer, 2006
57. Richards-Kortum, R., Sevick-Muraca, E.: Quantitative optical spectroscopy for tissue diagnosis. **Annu Rev Phys Chem** **47**:555-606, 1996
58. Leblond, F., Davis, S. C., Valdes, P. A., Pogue, B. W.: Pre-clinical whole-body fluorescence imaging: Review of instruments, methods and applications. **J Photochem Photobiol B** **98**:77-94, 2010
59. Roberts, W. G., Hasan, T.: Role of neovasculature and vascular permeability on the tumor retention of photodynamic agents. **Cancer Res** **52**:924-930, 1992
60. Ennis, S. R., Ren, X. D., Betz, A. L.: Transport of alpha-aminoisobutyric acid across the blood-brain barrier studied with in situ perfusion of rat brain. **Brain Res** **643**:100-107, 1994
61. Butte, P. V., Pikul, B. K., Hever, A., Yong, W. H., Black, K. L., Marcu, L.: Diagnosis of meningioma by time-resolved fluorescence spectroscopy. **J Biomed Opt** **10**:064026, 2005
62. Marcu, L., Jo, J. A., Butte, P. V., Yong, W. H., Pikul, B. K., Black, K. L., Thompson, R. C.: Fluorescence lifetime spectroscopy of glioblastoma multiforme. **Photochem Photobiol** **80**:98-103, 2004

63. Yong, W. H., Butte, P. V., Pikul, B. K., Jo, J. A., Fang, Q., Papaioannou, T., Black, K., Marcu, L.: Distinction of brain tissue, low grade and high grade glioma with time-resolved fluorescence spectroscopy. **Front Biosci** **11**:1255-1263, 2006
64. Kim, A., Khurana, M., Moriyama, Y., Wilson, B. C.: Quantification of in vivo fluorescence decoupled from the effects of tissue optical properties using fiber-optic spectroscopy measurements. **J Biomed Opt** **15**:067006, 2010
65. Bradley, R. S., Thorniley, M. S.: A review of attenuation correction techniques for tissue fluorescence. **J R Soc Interface** **3**:1-13, 2006
66. Ramanujam, N.: Fluorescence spectroscopy of neoplastic and non-neoplastic tissues. **Neoplasia** **2**:89-117, 2000
67. Pogue, B. W., Gibbs-Strauss, S., Valdes, P. A., Samkoe, K., Roberts, D. W., Paulsen, K. D.: Review of Neurosurgical Fluorescence Imaging Methodologies. **IEEE J Sel Top Quantum Electron** **16**:493-505, 2010
68. Cheong, W. F., Prah, S. A., Welch, A. J.: A review of the optical properties of biological tissues. **IEEE J Quant Electron** **26**:2166-2185, 1990
69. Wilson, B. C., Jeeves, W. P., Lowe, D. M., Adam, G.: Light propagation in animal tissues in the wavelength range 375-825 nanometers, in Doiron, D. R., Gomer, C. J. (eds): **Porphyrin Localization and Treatment of Tumors**. New York: Alan R. Liss, 1984, pp 115-132
70. Kim, A., Roy, M., Dadani, F., Wilson, B. C.: A fiberoptic reflectance probe with multiple source-collector separations to increase the dynamic range of derived tissue optical absorption and scattering coefficients. **Opt Express** **18**:5580-5594, 2010

71. Sturgis, M.: Design and Use of the Surgical Microscope in Fluorescence-Guided Surgery, in Rosenthal, E., Zinn, K. R. (eds): **Optical Imaging of Cancer: Clinical Applications**: Springer, 2009, pp 49-58
72. Nguyen, N. Q., Biankin, A. V., Leong, R. W., Chang, D. K., Cosman, P. H., Delaney, P., Kench, J. G., Merrett, N. D.: Real time intraoperative confocal laser microscopy-guided surgery. **Ann Surg** **249**:735-737, 2009
73. Kuroiwa, T., Kajimoto, Y., Ohta, T.: Development of a fluorescein operative microscope for use during malignant glioma surgery: a technical note and preliminary report. **Surg Neurol** **50**:41-48; discussion 48-49, 1998
74. Kuroiwa, T., Kajimoto, Y., Ohta, T.: Development and clinical application of near-infrared surgical microscope: preliminary report. **Minim Invasive Neurosurg** **44**:240-242, 2001
75. Jocham, D., Stepp, H., Waidelich, R.: Photodynamic diagnosis in urology: state-of-the-art. **Eur Urol** **53**:1138-1148, 2008
76. Andersson-Engels, S., Johansson, J., Svanberg, K., Svanberg, S.: Fluorescence imaging and point measurements of tissue: applications to the demarcation of malignant tumors and atherosclerotic lesions from normal tissue. **Photochem Photobiol** **53**:807-814, 1991
77. Shah, K., Weissleder, R.: Molecular optical imaging: applications leading to the development of present day therapeutics. **NeuroRx** **2**:215-225, 2005
78. Lee, J. H., Yigit, M. V., Mazumdar, D., Lu, Y.: Molecular diagnostic and drug delivery agents based on aptamer-nanomaterial conjugates. **Adv Drug Deliv Rev**

79. Taylor, E. L., Brown, S. B.: The advantages of aminolevulinic acid photodynamic therapy in dermatology. **J Dermatolog Treat** **13 Suppl 1**:S3-11, 2002
80. Dolmans, D. E., Fukumura, D., Jain, R. K.: Photodynamic therapy for cancer. **Nat Rev Cancer** **3**:380-387, 2003
81. Hirschberg, H., Sorensen, D. R., Angell-Petersen, E., Peng, Q., Tromberg, B., Sun, C. H., Spetalen, S., Madsen, S.: Repetitive photodynamic therapy of malignant brain tumors. **J Environ Pathol Toxicol Oncol** **25**:261-279, 2006
82. Hopper, C.: Photodynamic therapy: a clinical reality in the treatment of cancer. **Lancet Oncol** **1**:212-219, 2000
83. Dougherty, T. J., Gomer, C. J., Henderson, B. W., Jori, G., Kessel, D., Korbek, M., Moan, J., Peng, Q.: Photodynamic therapy. **J Natl Cancer Inst** **90**:889-905, 1998
84. Henderson, B. W., Dougherty, T. J.: How does photodynamic therapy work? **Photochem Photobiol** **55**:145-157, 1992
85. Kondo, M., Hirota, N., Takaoka, T., Kajiwar, M.: Heme-biosynthetic enzyme activities and porphyrin accumulation in normal liver and hepatoma cell lines of rat. **Cell Biol Toxicol** **9**:95-105, 1993
86. Reinhold, H. S., Endrich, B.: Tumour microcirculation as a target for hyperthermia. **Int J Hyperthermia** **2**:111-137, 1986
87. Reddi, E.: Role of delivery vehicles for photosensitizers in the photodynamic therapy of tumours. **J Photochem Photobiol B** **37**:189-195, 1997

88. Gibson, S. L., Havens, J. J., Foster, T. H., Hilf, R.: Time-dependent intracellular accumulation of delta-aminolevulinic acid, induction of porphyrin synthesis and subsequent phototoxicity. **Photochem Photobiol** **65**:416-421, 1997
89. Navone, N. M., Polo, C. F., Dinger, R. M., Batlle, A. M.: Heme regulation in mouse mammary carcinoma and liver of tumor bearing mice--I. Effect of allyl-isopropylacetamide and veronal on delta-aminolevulinic acid synthetase, cytochrome P-450 and cytochrome oxidase. **Int J Biochem** **22**:1005-1008, 1990
90. Valdes, P. A., Samkoe, K., O'Hara, J. A., Roberts, D. W., Paulsen, K. D., Pogue, B. W.: Deferoxamine Iron Chelation Increases delta-Aminolevulinic Acid Induced Protoporphyrin IX in Xenograft Glioma Model. **Photochem Photobiol**, 2009
91. Ohgari, Y., Nakayasu, Y., Kitajima, S., Sawamoto, M., Mori, H., Shimokawa, O., Matsui, H., Taketani, S.: Mechanisms involved in delta-aminolevulinic acid (ALA)-induced photosensitivity of tumor cells: relation of ferrochelatase and uptake of ALA to the accumulation of protoporphyrin. **Biochem Pharmacol** **71**:42-49, 2005
92. Ohgari, Y., Sawamoto, M., Yamamoto, M., Kohno, H., Taketani, S.: Ferrochelatase consisting of wild-type and mutated subunits from patients with a dominant-inherited disease, erythropoietic protoporphyria, is an active but unstable dimer. **Hum Mol Genet** **14**:327-334, 2005
93. Gibbs, S. L., Chen, B., O'Hara, J. A., Hoopes, P. J., Hasan, T., Pogue, B. W.: Protoporphyrin IX level correlates with number of mitochondria, but increase in

- production correlates with tumor cell size. **Photochem Photobiol** **82**:1334-1341, 2006
94. Peng, Q., Warloe, T., Berg, K., Moan, J., Kongshaug, M., Giercksky, K. E., Nesland, J. M.: 5-Aminolevulinic acid-based photodynamic therapy. Clinical research and future challenges. **Cancer** **79**:2282-2308, 1997
95. Pottier, R., Truscott, T. G.: The photochemistry of haematoporphyrin and related systems. **Int J Radiat Biol Relat Stud Phys Chem Med** **50**:421-452, 1986
96. Pottier, R. H., Chow, Y. F., LaPlante, J. P., Truscott, T. G., Kennedy, J. C., Beiner, L. A.: Non-invasive technique for obtaining fluorescence excitation and emission spectra in vivo. **Photochem Photobiol** **44**:679-687, 1986
97. Dalton, J. T., Yates, C. R., Yin, D., Straughn, A., Marcus, S. L., Golub, A. L., Meyer, M. C.: Clinical pharmacokinetics of 5-aminolevulinic acid in healthy volunteers and patients at high risk for recurrent bladder cancer. **J Pharmacol Exp Ther** **301**:507-512, 2002
98. Ennis, S. R., Novotny, A., Xiang, J., Shakui, P., Masada, T., Stummer, W., Smith, D. E., Keep, R. F.: Transport of 5-aminolevulinic acid between blood and brain. **Brain Res** **959**:226-234, 2003
99. Garcia, S. C., Moretti, M. B., Garay, M. V., Batlle, A.: Delta-aminolevulinic acid transport through blood-brain barrier. **Gen Pharmacol** **31**:579-582, 1998
100. Novotny, A., Xiang, J., Stummer, W., Teuscher, N. S., Smith, D. E., Keep, R. F.: Mechanisms of 5-aminolevulinic acid uptake at the choroid plexus. **J Neurochem** **75**:321-328, 2000

101. Stummer, W., Stocker, S., Novotny, A., Heimann, A., Sauer, O., Kempfski, O., Plesnila, N., Wietzorrek, J., Reulen, H. J.: In vitro and in vivo porphyrin accumulation by C6 glioma cells after exposure to 5-aminolevulinic acid. **J Photochem Photobiol B** **45**:160-169, 1998
102. Roberts, D. W., Valdes, P. A., Harris, B. T., Fontaine, K. M., Hartov, A., Fan, X., Ji, S., Lollis, S. S., Pogue, B. W., Leblond, F., Tosteson, T. D., Wilson, B. C., Paulsen, K. D.: Co-registered Fluorescence-Enhanced Tumor Resection of Malignant Glioma: Relationships between ALA-Induced PpIX Fluorescence, MRI Enhancement and Neuropathological Parameters **J Neurosurg**, In Press, 2010
103. Engel, E., Schraml, R., Maisch, T., Kobuch, K., Konig, B., Szeimies, R. M., Hillenkamp, J., Baumler, W., Vasold, R.: Light-induced decomposition of indocyanine green. **Invest Ophthalmol Vis Sci** **49**:1777-1783, 2008
104. Baker, K. J.: Binding of sulfobromophthalein (BSP) sodium and indocyanine green (ICG) by plasma alpha-1 lipoproteins. **Proc Soc Exp Biol Med** **122**:957-963, 1966
105. Yoneya, S., Saito, T., Komatsu, Y., Koyama, I., Takahashi, K., Duvoll-Young, J.: Binding properties of indocyanine green in human blood. **Invest Ophthalmol Vis Sci** **39**:1286-1290, 1998
106. Miller, D. E., Gleason, W. L., Mc, I. H.: A comparison of the cardiac output determination by the direct Fick method and the dye-dilution method using indocyanine green dye and a cuvette densitometer. **J Lab Clin Med** **59**:345-350, 1962

107. Maarek, J. M., Holschneider, D. P., Yang, J., Pniak, S. N., Rubinstein, E. H.: Transcutaneous fluorescence dilution cardiac output and circulating blood volume during hemorrhagic hypovolemia. **Anesthesiology** **102**:774-782, 2005
108. Wheeler, H. O., Cranston, W. I., Meltzer, J. I.: Hepatic uptake and biliary excretion of indocyanine green in the dog. **Proc Soc Exp Biol Med** **99**:11-14, 1958
109. Hunton, D. B., Bollman, J. L., Hoffman, H. N.: Hepatic removal of indocyanine green. **Proc Staff Meet Mayo Clin** **35**:752-755, 1960
110. Narayanan, R., Kenney, M. C., Kamjoo, S., Trinh, T. H., Seigel, G. M., Resende, G. P., Kuppermann, B. D.: Toxicity of indocyanine green (ICG) in combination with light on retinal pigment epithelial cells and neurosensory retinal cells. **Curr Eye Res** **30**:471-478, 2005
111. Hope-Ross, M., Yannuzzi, L. A., Gragoudas, E. S., Guyer, D. R., Slakter, J. S., Sorenson, J. A., Krupsky, S., Orlock, D. A., Puliafito, C. A.: Adverse reactions due to indocyanine green. **Ophthalmology** **101**:529-533, 1994
112. Reiff, R., Barndt, R.: Letter: Reducing substances in certain heparin preparations: a source of error in the measurement of indocyanine green. **Am Heart J** **92**:542, 1976
113. Yang, Y. L., Ye, Y. M., Li, F. M., Li, Y. F., Ma, P. Z.: Characteristic autofluorescence for cancer diagnosis and its origin. **Lasers Surg Med** **7**:528-532, 1987

114. Chung, Y. G., Schwartz, J. A., Gardner, C. M., Sawaya, R. E., Jacques, S. L.: Diagnostic potential of laser-induced autofluorescence emission in brain tissue. **J Korean Med Sci** **12**:135-142, 1997
115. Croce, A. C., Fiorani, S., Locatelli, D., Nano, R., Ceroni, M., Tancioni, F., Giombelli, E., Benericetti, E., Bottirolì, G.: Diagnostic potential of autofluorescence for an assisted intraoperative delineation of glioblastoma resection margins. **Photochem Photobiol** **77**:309-318, 2003
116. Majumder, S. K., Gebhart, S., Johnson, M. D., Thompson, R., Lin, W. C., Mahadevan-Jansen, A.: A probability-based spectroscopic diagnostic algorithm for simultaneous discrimination of brain tumor and tumor margins from normal brain tissue. **Appl Spectrosc** **61**:548-557, 2007
117. Majumder, S. K., Keller, M. D., Boulos, F. I., Kelley, M. C., Mahadevan-Jansen, A.: Comparison of autofluorescence, diffuse reflectance, and Raman spectroscopy for breast tissue discrimination. **J Biomed Opt** **13**:054009, 2008
118. Qu, J. Y., Chang, H., Xiong, S.: Fluorescence spectral imaging for characterization of tissue based on multivariate statistical analysis. **J Opt Soc Am A Opt Image Sci Vis** **19**:1823-1831, 2002
119. Imizu, S., Kato, Y., Sangli, A., Oguri, D., Sano, H.: Assessment of incomplete clipping of aneurysms intraoperatively by a near-infrared indocyanine green-video angiography (Niicg-Va) integrated microscope. **Minim Invasive Neurosurg** **51**:199-203, 2008
120. Troyan, S. L., Kianzad, V., Gibbs-Strauss, S. L., Gioux, S., Matsui, A., Oketokoun, R., Ngo, L., Khamene, A., Azar, F., Frangioni, J. V.: The FLARE

- intraoperative near-infrared fluorescence imaging system: a first-in-human clinical trial in breast cancer sentinel lymph node mapping. **Ann Surg Oncol** **16**:2943-2952, 2009
121. Valdes, P. A., Fan, X., Ji, S., Harris, B. T., Paulsen, K. D., Roberts, D. W.: Estimation of brain deformation for volumetric image updating in protoporphyrin IX fluorescence-guided resection. **Stereotact Funct Neurosurg** **88**:1-10, 2010
122. Stummer, W., Stocker, S., Wagner, S., Stepp, H., Fritsch, C., Goetz, C., Goetz, A. E., Kiefmann, R., Reulen, H. J.: Intraoperative detection of malignant gliomas by 5-aminolevulinic acid-induced porphyrin fluorescence. **Neurosurgery** **42**:518-525; discussion 525-516, 1998
123. Sterenborg, H. J., Saarnak, A. E., Frank, R., Motamedi, M.: Evaluation of spectral correction techniques for fluorescence measurements on pigmented lesions in vivo. **J Photochem Photobiol B** **35**:159-165, 1996
124. Volynskaya, Z., Haka, A. S., Bechtel, K. L., Fitzmaurice, M., Shenk, R., Wang, N., Nazemi, J., Dasari, R. R., Feld, M. S.: Diagnosing breast cancer using diffuse reflectance spectroscopy and intrinsic fluorescence spectroscopy. **J Biomed Opt** **13**:024012, 2008
125. Song, J. J., Ren, Y., Yan, F.: Classification for high-throughput data with an optimal subset of principal components. **Comput Biol Chem** **33**:408-413, 2009
126. Toms, S. A., Lin, W. C., Weil, R. J., Johnson, M. D., Jansen, E. D., Mahadevan-Jansen, A.: Intraoperative optical spectroscopy identifies infiltrating glioma margins with high sensitivity. **Neurosurgery** **57**:382-391; discussion 382-391, 2005

127. Eljamel, M. S., Leese, G., Moseley, H.: Intraoperative optical identification of pituitary adenomas. **J Neurooncol** **92**:417-421, 2009
128. Kabuto, M., Kubota, T., Kobayashi, H., Nakagawa, T., Ishii, H., Takeuchi, H., Kitai, R., Kodera, T.: Experimental and clinical study of detection of glioma at surgery using fluorescent imaging by a surgical microscope after fluorescein administration. **Neurol Res** **19**:9-16, 1997
129. Miyatake, S., Kuroiwa, T., Kajimoto, Y., Miyashita, M., Tanaka, H., Tsuji, M.: Fluorescence of non-neoplastic, magnetic resonance imaging-enhancing tissue by 5-aminolevulinic acid: case report. **Neurosurgery** **61**:E1101-1103; discussion E1103-1104, 2007
130. Moore, G. E., Peyton, W. T., et al.: The clinical use of fluorescein in neurosurgery; the localization of brain tumors. **J Neurosurg** **5**:392-398, 1948
131. Murray, K. J.: Improved surgical resection of human brain tumors: Part I. A preliminary study. **Surg Neurol** **17**:316-319, 1982
132. Stummer, W., Reulen, H. J., Meinel, T., Pichlmeier, U., Schumacher, W., Tonn, J. C., Rohde, V., Opperl, F., Turowski, B., Woiciechowsky, C., Franz, K., Pietsch, T.: Extent of resection and survival in glioblastoma multiforme: identification of and adjustment for bias. **Neurosurgery** **62**:564-576; discussion 564-576, 2008
133. Haj-Hosseini, N., Richter, J., Andersson-Engels, S., Wardell, K.: Optical touch pointer for fluorescence guided glioblastoma resection using 5-aminolevulinic acid. **Lasers Surg Med** **42**:9-14

134. Utsuki, S., Oka, H., Miyajima, Y., Shimizu, S., Suzuki, S., Fujii, K.: Auditory alert system for fluorescence-guided resection of gliomas. **Neurol Med Chir (Tokyo)** **48**:95-97; discussion 97-98, 2008
135. Yang, V. X., Muller, P. J., Herman, P., Wilson, B. C.: A multispectral fluorescence imaging system: design and initial clinical tests in intra-operative Photofrin-photodynamic therapy of brain tumors. **Lasers Surg Med** **32**:224-232, 2003
136. Lin, W. C., Toms, S. A., Johnson, M., Jansen, E. D., Mahadevan-Jansen, A.: In vivo brain tumor demarcation using optical spectroscopy. **Photochem Photobiol** **73**:396-402, 2001
137. Tonn, J. C., Stummer, W.: Fluorescence-guided resection of malignant gliomas using 5-aminolevulinic acid: practical use, risks, and pitfalls. **Clin Neurosurg** **55**:20-26, 2008
138. Westphal, M., Lamszus, K.: Other experimental therapies for glioma. **Recent Results Cancer Res** **171**:155-164, 2009
139. Nabavi, A., Thurm, H., Zountsas, B., Pietsch, T., Lanfermann, H., Pichlmeier, U., Mehdorn, M.: Five-aminolevulinic acid for fluorescence-guided resection of recurrent malignant gliomas: a phase ii study. **Neurosurgery** **65**:1070-1076; discussion 1076-1077, 2009
140. Tamura, Y., Kuroiwa, T., Kajimoto, Y., Miki, Y., Miyatake, S., Tsuji, M.: Endoscopic identification and biopsy sampling of an intraventricular malignant glioma using a 5-aminolevulinic acid-induced protoporphyrin IX fluorescence imaging system. Technical note. **J Neurosurg** **106**:507-510, 2007

141. Zilidis, G., Aziz, F., Telara, S., Eljamel, M. S.: Fluorescence image-guided surgery and repetitive Photodynamic Therapy in brain metastatic malignant melanoma. **Photodiagnosis Photodyn Ther** **5**:264-266, 2008
142. Hayashi, Y., Nakada, M., Tanaka, S., Uchiyama, N., Kita, D., Hamada, J.: Implication of 5-aminolevulinic acid fluorescence of the ventricular wall for postoperative communicating hydrocephalus associated with cerebrospinal fluid dissemination in patients with glioblastoma multiforme: a report of 7 cases. **J Neurosurg**, 2009
143. Zimmermann, A., Ritsch-Marte, M., Kostron, H.: mTHPC-mediated photodynamic diagnosis of malignant brain tumors. **Photochem Photobiol** **74**:611-616, 2001
144. Kremer, P., Mahmoudreza, F., Ding, R., Pritsch, M., Zoubaa, S., Frei, E.: Intraoperative fluorescence staining of malignant brain tumors using 5-aminofluorescein-labeled albumin. **Neurosurgery** **64**:53-60; discussion 60-51, 2009
145. Suzuki, K., Kodama, N., Sasaki, T., Matsumoto, M., Ichikawa, T., Munakata, R., Muramatsu, H., Kasuya, H.: Confirmation of blood flow in perforating arteries using fluorescein cerebral angiography during aneurysm surgery. **J Neurosurg** **107**:68-73, 2007
146. Khurana, V. G., Seow, K., Duke, D.: Intuitiveness, quality and utility of intraoperative fluorescence videoangiography: Australian Neurosurgical Experience. **Br J Neurosurg** **24**:163-172

147. Li, J., Lan, Z., He, M., You, C.: Assessment of microscope-integrated indocyanine green angiography during intracranial aneurysm surgery: a retrospective study of 120 patients. **Neurol India** **57**:453-459, 2009
148. Raabe, A., Beck, J., Gerlach, R., Zimmermann, M., Seifert, V.: Near-infrared indocyanine green video angiography: a new method for intraoperative assessment of vascular flow. **Neurosurgery** **52**:132-139; discussion 139, 2003
149. Raabe, A., Beck, J., Seifert, V.: Technique and image quality of intraoperative indocyanine green angiography during aneurysm surgery using surgical microscope integrated near-infrared video technology. **Zentralbl Neurochir** **66**:1-6; discussion 7-8, 2005
150. Woitzik, J., Horn, P., Vajkoczy, P., Schmiedek, P.: Intraoperative control of extracranial-intracranial bypass patency by near-infrared indocyanine green videoangiography. **J Neurosurg** **102**:692-698, 2005
151. Raabe, A., Nakaji, P., Beck, J., Kim, L. J., Hsu, F. P., Kamerman, J. D., Seifert, V., Spetzler, R. F.: Prospective evaluation of surgical microscope-integrated intraoperative near-infrared indocyanine green videoangiography during aneurysm surgery. **J Neurosurg** **103**:982-989, 2005
152. Woitzik, J., Pena-Tapia, P. G., Schneider, U. C., Vajkoczy, P., Thome, C.: Cortical perfusion measurement by indocyanine-green videoangiography in patients undergoing hemicraniectomy for malignant stroke. **Stroke** **37**:1549-1551, 2006

153. Kuroiwa, T., Kajimoto, Y., Ohta, T.: Comparison between operative findings on malignant glioma by a fluorescein surgical microscopy and histological findings. **Neurol Res** **21**:130-134, 1999
154. Kuroiwa, T., Kajimoto, Y., Ohta, T.: Surgical management for supratentorial astrocytic tumors. **Minim Invasive Neurosurg** **42**:182-186, 1999
155. Friesen, S. A., Hjortland, G. O., Madsen, S. J., Hirschberg, H., Engebraten, O., Nesland, J. M., Peng, Q.: 5-Aminolevulinic acid-based photodynamic detection and therapy of brain tumors (review). **Int J Oncol** **21**:577-582, 2002
156. Utsuki, S., Oka, H., Sato, S., Shimizu, S., Suzuki, S., Tanizaki, Y., Kondo, K., Miyajima, Y., Fujii, K.: Histological examination of false positive tissue resection using 5-aminolevulinic acid-induced fluorescence guidance. **Neurol Med Chir (Tokyo)** **47**:210-213; discussion 213-214, 2007
157. Louis, D. N., Ohgaki, H., Wiestler, O. D., Cavenee, W. K., Burger, P. C., Jouvett, A., Scheithauer, B. W., Kleihues, P.: The 2007 WHO classification of tumours of the central nervous system. **Acta Neuropathol** **114**:97-109, 2007
158. Pijl, M. E., Doornbos, J., Wasser, M. N., van Houwelingen, H. C., Tollenaar, R. A., Bloem, J. L.: Quantitative analysis of focal masses at MR imaging: a plea for standardization. **Radiology** **231**:737-744, 2004
159. Fitzmaurice, G. M., Laird, N. M., Ware, J. H.: **Applied Longitudinal Analysis, ed 1**. Hoboken, NJ: John Wiley & Sons, 2004
160. Bogaards, A., Varma, A., Collens, S. P., Lin, A., Giles, A., Yang, V. X., Bilbao, J. M., Lilge, L. D., Muller, P. J., Wilson, B. C.: Increased brain tumor resection

- using fluorescence image guidance in a preclinical model. **Lasers Surg Med** **35**:181-190, 2004
161. Hill, D. L., Maurer, C. R., Jr., Maciunas, R. J., Barwise, J. A., Fitzpatrick, J. M., Wang, M. Y.: Measurement of intraoperative brain surface deformation under a craniotomy. **Neurosurgery** **43**:514-526; discussion 527-518, 1998
162. Ji, S., Roberts, D. W., Hartov, A., Paulsen, K. D.: Brain-skull contact boundary conditions in an inverse computational deformation model. **Med Image Anal**, 2009
163. Pallatroni, H., Hartov, A., McInerney, J., Platenik, L. A., Miga, M. I., Kennedy, F. E., Paulsen, K. D., Roberts, D. W.: Coregistered ultrasound as a neurosurgical guide. **Stereotact Funct Neurosurg** **73**:143-147, 1999
164. Hartov, A., Roberts, D. W., Paulsen, K. D.: A comparative analysis of coregistered ultrasound and magnetic resonance imaging in neurosurgery. **Neurosurgery** **62**:91-99; discussion 99-101, 2008
165. Wu, Z., Paulsen, K. D., Sullivan, J. M., Jr.: Adaptive model initialization and deformation for automatic segmentation of T1-weighted brain MRI data. **IEEE Trans Biomed Eng** **52**:1128-1131, 2005
166. Ji, S., Hartov, A., Roberts, D. W., Paulsen, K. D.: Data assimilation using a gradient descent method for estimation of intraoperative brain deformation. **Med Image Anal**, 2009
167. Grunert, P., Muller-Forell, W., Darabi, K., Reisch, R., Busert, C., Hopf, N., Perneczky, A.: Basic principles and clinical applications of neuronavigation and intraoperative computed tomography. **Comput Aided Surg** **3**:166-173, 1998

168. Roberts, D. W., Miga, M. I., Hartov, A., Eisner, S., Lemery, J. M., Kennedy, F. E., Paulsen, K. D.: Intraoperatively updated neuroimaging using brain modeling and sparse data. **Neurosurgery** **45**:1199-1206; discussion 1206-1197, 1999
169. Wen, P. Y., Kesari, S.: Malignant gliomas in adults. **N Engl J Med** **359**:492-507, 2008
170. Stummer, W., Pichlmeier, U., Meinel, T., Wiestler, O. D., Zanella, F., Reulen, H. J., Group, A. L.-G. S.: Fluorescence-guided surgery with 5-aminolevulinic acid for resection of malignant glioma: a randomised controlled multicentre phase III trial.[see comment]. **Lancet Oncology** **7**:392-401, 2006
171. Vecht, C. J., Avezaat, C. J., van Putten, W. L., Eijkenboom, W. M., Stefanko, S. Z.: The influence of the extent of surgery on the neurological function and survival in malignant glioma. A retrospective analysis in 243 patients. **J Neurol Neurosurg Psychiatry** **53**:466-471, 1990
172. Sinha, A. K., Anand, S., Ortel, B. J., Chang, Y., Mai, Z., Hasan, T., Maytin, E. V.: Methotrexate used in combination with aminolaevulinic acid for photodynamic killing of prostate cancer cells. **Br J Cancer** **95**:485-495, 2006
173. Sato, N., Moore, B. W., Keevey, S., Drazba, J. A., Hasan, T., Maytin, E. V.: Vitamin D enhances ALA-induced protoporphyrin IX production and photodynamic cell death in 3-D organotypic cultures of keratinocytes. **J Invest Dermatol** **127**:925-934, 2007
174. Ortel, B., Sharlin, D., O'Donnell, D., Sinha, A. K., Maytin, E. V., Hasan, T.: Differentiation enhances aminolevulinic acid-dependent photodynamic treatment of LNCaP prostate cancer cells. **Br J Cancer** **87**:1321-1327, 2002

175. Ortel, B., Chen, N., Brissette, J., Dotto, G. P., Maytin, E., Hasan, T.: Differentiation-specific increase in ALA-induced protoporphyrin IX accumulation in primary mouse keratinocytes. **Br J Cancer** **77**:1744-1751, 1998
176. Berg, K., Anholt, H., Bech, O., Moan, J.: The influence of iron chelators on the accumulation of protoporphyrin IX in 5-aminolaevulinic acid-treated cells. **Br J Cancer** **74**:688-697, 1996
177. Curnow, A., Pye, A.: Biochemical manipulation via iron chelation to enhance porphyrin production from porphyrin precursors. **J Environ Pathol Toxicol Oncol** **26**:89-103, 2007
178. Chang, S. C., MacRobert, A. J., Porter, J. B., Bown, S. G.: The efficacy of an iron chelator (CP94) in increasing cellular protoporphyrin IX following intravesical 5-aminolaevulinic acid administration: an in vivo study. **J Photochem Photobiol B** **38**:114-122, 1997
179. Collaud, S., Juzeniene, A., Moan, J., Lange, N.: On the selectivity of 5-aminolevulinic acid-induced protoporphyrin IX formation. **Current Medicinal Chemistry Anti Cancer Agents** **4**:301-316, 2004
180. Bech, O., Phillips, D., Moan, J., MacRobert, A. J.: A hydroxypyridinone (CP94) enhances protoporphyrin IX formation in 5-aminolaevulinic acid treated cells. **J Photochem Photobiol B** **41**:136-144, 1997
181. Choudry, K., Brooke, R. C., Farrar, W., Rhodes, L. E.: The effect of an iron chelating agent on protoporphyrin IX levels and phototoxicity in topical 5-aminolaevulinic acid photodynamic therapy. **Br J Dermatol** **149**:124-130, 2003

182. Casas, A., Batlle, A. M., Butler, A. R., Robertson, D., Brown, E. H., MacRobert, A., Riley, P. A.: Comparative effect of ALA derivatives on protoporphyrin IX production in human and rat skin organ cultures. **Br J Cancer** **80**:1525-1532, 1999
183. Bernhardt, P. V.: Coordination chemistry and biology of chelators for the treatment of iron overload disorders. **Dalton Trans**:3214-3220, 2007
184. Bring, P., Partovi, N., Ford, J. A., Yoshida, E. M.: Iron overload disorders: treatment options for patients refractory to or intolerant of phlebotomy. **Pharmacotherapy** **28**:331-342, 2008
185. Maggio, A.: Light and shadows in the iron chelation treatment of haematological diseases. **Br J Haematol** **138**:407-421, 2007
186. Hershko, C., Abrahamov, A., Konijn, A. M., Breuer, W., Cabantchik, I. Z., Pootrakul, P., Link, G.: Objectives and methods of iron chelation therapy. **Bioinorg Chem Appl**:151-168, 2003
187. Aldridge, M. D.: Acute iron poisoning: what every pediatric intensive care unit nurse should know. **Dimens Crit Care Nurs** **26**:43-48; quiz 49-50, 2007
188. Clinical Pharmacology [database online], in, **ed 2008**, 2009, Vol 2009
189. Cappellini, M. D., Pattoneri, P.: Oral iron chelators. **Annu Rev Med** **60**:25-38, 2009
190. Iinuma, S., Farshi, S. S., Ortel, B., Hasan, T.: A mechanistic study of cellular photodestruction with 5-aminolaevulinic acid-induced porphyrin. **Br J Cancer** **70**:21-28, 1994

191. Floeth, F. W., Stummer, W.: The value of metabolic imaging in diagnosis and resection of cerebral gliomas. **Nat Clin Pract Neurol** **1**:62-63, 2005
192. Roberts, D. W., Valdes, P. A., Harris, B. T., Fontaine, K. M., Hartov, A., Fan, X., Ji, S., Lollis, S. S., Pogue, B. W., Leblond, F., Tosteson, T. D., Wilson, B. C., Paulsen, K. D.: Coregistered fluorescence-enhanced tumor resection of malignant glioma: relationships between delta-aminolevulinic acid-induced protoporphyrin IX fluorescence, magnetic resonance imaging enhancement, and neuropathological parameters. **J Neurosurg**, 2010
193. Pogue, B. W., Gibbs-Strauss, S. L., Valdes, P. A., Samkoe, K. S., Roberts, D. W., Paulsen, K. D.: Review of Neurosurgical Fluorescence Imaging Methodologies. **Selected Topics in Quantum Electronics, IEEE Journal of** **16**:493-505, 2010
194. Widhalm, G., Wolfsberger, S., Minchev, G., Woehrer, A., Krssak, M., Czech, T., Prayer, D., Asenbaum, S., Hainfellner, J. A., Knosp, E.: 5-Aminolevulinic acid is a promising marker for detection of anaplastic foci in diffusely infiltrating gliomas with nonsignificant contrast enhancement. **Cancer** **116**:1545-1552, 2010
195. Dysart, J. S., Patterson, M. S.: Photobleaching kinetics, photoproduct formation, and dose estimation during ALA induced PpIX PDT of MLL cells under well oxygenated and hypoxic conditions. **Photochem Photobiol Sci** **5**:73-81, 2006
196. Shapiro, D. E.: The interpretation of diagnostic tests. **Stat Methods Med Res** **8**:113-134, 1999
197. Galloway, R. L., Jr.: The process and development of image-guided procedures. **Annu Rev Biomed Eng** **3**:83-108, 2001

198. Uematsu, Y., Owai, Y., Okita, R., Tanaka, Y., Itakura, T.: The usefulness and problem of intraoperative rapid diagnosis in surgical neuropathology. **Brain Tumor Pathol** **24**:47-52, 2007
199. Brenner, H., Gefeller, O.: Variation of sensitivity, specificity, likelihood ratios and predictive values with disease prevalence. **Stat Med** **16**:981-991, 1997
200. Pouratian, N., Asthagiri, A., Jagannathan, J., Shaffrey, M. E., Schiff, D.: Surgery Insight: the role of surgery in the management of low-grade gliomas. **Nat Clin Pract Neurol** **3**:628-639, 2007
201. DeAngelis, L. M.: Brain tumors. **N Engl J Med** **344**:114-123, 2001
202. Jansen, M., Yip, S., Louis, D. N.: Molecular pathology in adult gliomas: diagnostic, prognostic, and predictive markers. **Lancet Neurol** **9**:717-726, 2010
203. Van Meir, E. G., Hadjipanayis, C. G., Norden, A. D., Shu, H. K., Wen, P. Y., Olson, J. J.: Exciting new advances in neuro-oncology: the avenue to a cure for malignant glioma. **CA Cancer J Clin** **60**:166-193, 2010
204. Valdes, P. A., Leblond, F., Kim, A., Harris, B. T., Wilson, B. C., Fan, X., Tosteson, T. D., Hartov, A., Ji, S., Erkmen, K., Simmons, N., Paulsen, K. D., Roberts, D. W.: Quantitative fluorescence in intracranial tumor: implications for ALA-induced PpIX as an intraoperative biomarker. **J Neurosurg**, 2011
205. McGirt, M. J., Chaichana, K. L., Gathinji, M., Attenello, F. J., Than, K., Olivi, A., Weingart, J. D., Brem, H., Quinones-Hinojosa, A. R.: Independent association of extent of resection with survival in patients with malignant brain astrocytoma. **J Neurosurg** **110**:156-162, 2009

206. Richter, J. C., Haj-Hosseini, N., Andersson-Engel, S., Wardell, K.: Fluorescence spectroscopy measurements in ultrasonic navigated resection of malignant brain tumors. **Lasers Surg Med** **43**:8-14, 2011
207. Roberts, D. W., Valdes, P. A., Harris, B. T., Fontaine, K. M., Hartov, A., Fan, X., Ji, S., Lollis, S. S., Pogue, B. W., Leblond, F., Tosteson, T. D., Wilson, B. C., Paulsen, K. D.: Coregistered fluorescence-enhanced tumor resection of malignant glioma: relationships between delta-aminolevulinic acid-induced protoporphyrin IX fluorescence, magnetic resonance imaging enhancement, and neuropathological parameters. **J Neurosurg** **114**:595-603, 2011
208. Kim, A., Roy, M., Dadani, F., Wilson, B. C.: A fiberoptic reflectance probe with multiple source-collector separations to increase the dynamic range of derived tissue optical absorption and scattering coefficients. **Opt Express** **18**:5580-5594, 2010
209. Wu, J., Feld, M. S., Rava, R. P.: Analytical model for extracting intrinsic fluorescence in turbid media. **Appl Opt** **32**:3585-3595, 1993
210. Weersink, R., Patterson, M. S., Diamond, K., Silver, S., Padgett, N.: Noninvasive measurement of fluorophore concentration in turbid media with a simple fluorescence /reflectance ratio technique. **Appl Opt** **40**:6389-6395, 2001
211. Muller, M. G., Georgakoudi, I., Zhang, Q., Wu, J., Feld, M. S.: Intrinsic fluorescence spectroscopy in turbid media: disentangling effects of scattering and absorption. **Appl Opt** **40**:4633-4646, 2001

212. Ivanciuc, O.: Applications of Support Vector Machines in Chemistry, in Lipkowitz, K. B., Cundari, T. R. (eds): **Reviews in Computational Chemistry**. Hoboken, NJ: John Wiley & Sons, 2007, Vol 23, pp 291-400
213. Haj-Hosseini, N., Richter, J., Andersson-Engels, S., Wardell, K.: Optical touch pointer for fluorescence guided glioblastoma resection using 5-aminolevulinic acid. **Lasers Surg Med** **42**:9-14, 2010
214. Lin, W. C., Sandberg, D. I., Bhatia, S., Johnson, M., Morrison, G., Ragheb, J.: Optical spectroscopy for in-vitro differentiation of pediatric neoplastic and epileptogenic brain lesions. **J Biomed Opt** **14**:014028, 2009
215. Lin, W. C., Sandberg, D. I., Bhatia, S., Johnson, M., Oh, S., Ragheb, J.: Diffuse reflectance spectroscopy for in vivo pediatric brain tumor detection. **J Biomed Opt** **15**:061709, 2010
216. Butte, P. V., Fang, Q., Jo, J. A., Yong, W. H., Pikul, B. K., Black, K. L., Marcu, L.: Intraoperative delineation of primary brain tumors using time-resolved fluorescence spectroscopy. **J Biomed Opt** **15**:027008, 2010
217. Butte, P. V., Mamelak, A. N., Nuno, M., Bannykh, S. I., Black, K. L., Marcu, L.: Fluorescence lifetime spectroscopy for guided therapy of brain tumors. **Neuroimage** **54S1**:S125-S135, 2011
218. Toms, S. A., Konrad, P. E., Lin, W. C., Weil, R. J.: Neuro-oncological applications of optical spectroscopy. **Technol Cancer Res Treat** **5**:231-238, 2006
219. Burges, C. J. C.: A tutorial on Support Vector Machines for pattern recognition. **Data Mining and Knowledge Discovery** **2**:121-167, 1998

220. Duda, R. O., Hart, P. E., Stork, D. G.: **Pattern classification, ed 2nd**. New York: Wiley, 2001
221. Noble, W. S.: What is a support vector machine? **Nat Biotechnol** **24**:1565-1567, 2006
222. Brereton, R. G., Lloyd, G. R.: Support vector machines for classification and regression. **Analyst** **135**:230-267, 2010
223. Valdes, P. A., Jacobs, V. L., Paulsen, K. D., Roberts, D. W., Leblond, F.: In vivo fluorescence detection in surgery: A review of principles, methods, and applications. **Curr Med Imaging Rev**, 2011
224. Johansson, J. D.: Spectroscopic method for determination of the absorption coefficient in brain tissue. **J Biomed Opt** **15**:057005, 2010
225. Yaroslavsky, A. N., Schulze, P. C., Yaroslavsky, I. V., Schober, R., Ulrich, F., Schwarzmaier, H. J.: Optical properties of selected native and coagulated human brain tissues in vitro in the visible and near infrared spectral range. **Phys Med Biol** **47**:2059-2073, 2002
226. Gebhart, S. C., Lin, W. C., Mahadevan-Jansen, A.: In vitro determination of normal and neoplastic human brain tissue optical properties using inverse adding-doubling. **Phys Med Biol** **51**:2011-2027, 2006
227. Boustany, N. N., Boppart, S. A., Backman, V.: Microscopic imaging and spectroscopy with scattered light. **Annu Rev Biomed Eng** **12**:285-314, 2010
228. Lin, W. C., Toms, S. A., Motamedi, M., Jansen, E. D., Mahadevan-Jansen, A.: Brain tumor demarcation using optical spectroscopy; an in vitro study. **J Biomed Opt** **5**:214-220, 2000

229. Brat, D. J., Mapstone, T. B.: Malignant glioma physiology: cellular response to hypoxia and its role in tumor progression. **Ann Intern Med** **138**:659-668, 2003
230. Deighton, R. F., McGregor, R., Kemp, J., McCulloch, J., Whittle, I. R.: Glioma pathophysiology: insights emerging from proteomics. **Brain Pathol** **20**:691-703, 2010
231. Semenza, G. L.: Targeting HIF-1 for cancer therapy. **Nat Rev Cancer** **3**:721-732, 2003
232. Bergers, G., Benjamin, L. E.: Tumorigenesis and the angiogenic switch. **Nat Rev Cancer** **3**:401-410, 2003
233. Liao, D., Johnson, R. S.: Hypoxia: a key regulator of angiogenesis in cancer. **Cancer Metastasis Rev** **26**:281-290, 2007
234. Carmeliet, P.: Mechanisms of angiogenesis and arteriogenesis. **Nat Med** **6**:389-395, 2000
235. Grier, J. T., Batchelor, T.: Low-grade gliomas in adults. **Oncologist** **11**:681-693, 2006
236. Rolfe, P.: In vivo near-infrared spectroscopy. **Annu Rev Biomed Eng** **2**:715-754, 2000
237. Srinivasan, S., Pogue, B. W., Jiang, S., Dehghani, H., Kogel, C., Soho, S., Gibson, J. J., Tosteson, T. D., Poplack, S. P., Paulsen, K. D.: Interpreting hemoglobin and water concentration, oxygen saturation, and scattering measured in vivo by near-infrared breast tomography. **Proc Natl Acad Sci U S A** **100**:12349-12354, 2003

238. Krammer, B., Plaetzer, K.: ALA and its clinical impact, from bench to bedside. **Photochem Photobiol Sci** **7**:283-289, 2008
239. Yoshino, A., Ogino, A., Yachi, K., Ohta, T., Fukushima, T., Watanabe, T., Katayama, Y., Okamoto, Y., Naruse, N., Sano, E., Tsumoto, K.: Gene expression profiling predicts response to temozolomide in malignant gliomas. **Int J Oncol** **36**:1367-1377, 2010
240. Liang, Y., Diehn, M., Watson, N., Bollen, A. W., Aldape, K. D., Nicholas, M. K., Lamborn, K. R., Berger, M. S., Botstein, D., Brown, P. O., Israel, M. A.: Gene expression profiling reveals molecularly and clinically distinct subtypes of glioblastoma multiforme. **Proc Natl Acad Sci U S A** **102**:5814-5819, 2005
241. Barajas, R. F., Jr., Hodgson, J. G., Chang, J. S., Vandenberg, S. R., Yeh, R. F., Parsa, A. T., McDermott, M. W., Berger, M. S., Dillon, W. P., Cha, S.: Glioblastoma multiforme regional genetic and cellular expression patterns: influence on anatomic and physiologic MR imaging. **Radiology** **254**:564-576, 2010
242. Pope, W. B., Chen, J. H., Dong, J., Carlson, M. R., Perlina, A., Cloughesy, T. F., Liau, L. M., Mischel, P. S., Nghiemphu, P., Lai, A., Nelson, S. F.: Relationship between gene expression and enhancement in glioblastoma multiforme: exploratory DNA microarray analysis. **Radiology** **249**:268-277, 2008
243. Lilge, L., O'Carroll, C., Wilson, B. C.: A solubilization technique for photosensitizer quantification in ex vivo tissue samples. **J Photochem Photobiol B** **39**:229-235, 1997

244. Bondy, M. L., Scheurer, M. E., Malmer, B., Barnholtz-Sloan, J. S., Davis, F. G., Il'yasova, D., Kruchko, C., McCarthy, B. J., Rajaraman, P., Schwartzbaum, J. A., Sadetzki, S., Schlehofer, B., Tihan, T., Wiemels, J. L., Wrensch, M., Buffler, P. A.: Brain tumor epidemiology: consensus from the Brain Tumor Epidemiology Consortium. **Cancer** **113**:1953-1968, 2008
245. Lunn, K. E., Paulsen, K. D., Roberts, D. W., Kennedy, F. E., Hartov, A., West, J. D.: Displacement estimation with co-registered ultrasound for image guided neurosurgery: a quantitative in vivo porcine study. **IEEE Trans Med Imaging** **22**:1358-1368, 2003
246. Miga, M. I., Roberts, D. W., Kennedy, F. E., Platenik, L. A., Hartov, A., Lunn, K. E., Paulsen, K. D.: Modeling of retraction and resection for intraoperative updating of images. **Neurosurgery** **49**:75-84; discussion 84-75, 2001
247. Willems, P. W., van der Sprenkel, J. W., Tulleken, C. A., Viergever, M. A., Taphoorn, M. J.: Neuronavigation and surgery of intracerebral tumours. **J Neurol** **253**:1123-1136, 2006
248. Widhalm, G., Wolfsberger, S., Minchev, G., Woehrer, A., Krssak, M., Czech, T., Prayer, D., Asenbaum, S., Hainfellner, J. A., Knosp, E.: 5-Aminolevulinic acid is a promising marker for detection of anaplastic foci in diffusely infiltrating gliomas with nonsignificant contrast enhancement. **Cancer** **116**:1545-1552
249. Johansson, A., Palte, G., Schnell, O., Tonn, J. C., Herms, J., Stepp, H.: 5-Aminolevulinic Acid-induced Protoporphyrin IX Levels in Tissue of Human Malignant Brain Tumors. **Photochem Photobiol**

250. Valdés, P. A., Leblond, F., Kim, A., Harris, B. T., Wilson, B. C., Fan, X., Tosteson, T. D., Hartov, A., Ji, S., Paulsen, K. D., Roberts, D. W.: Quantitative fluorescence in intracranial tumor: implications for ALA-induced PpIX as a surgical biomarker to guide resection procedures. **J Neurosurg (In Press)**, 2010
251. Kim, A., Khurana, M., Moriyama, Y., Wilson, B. C.: Quantification of in vivo fluorescence decoupled from the effects of tissue optical properties using fiberoptic spectroscopy measurements. **J Biomedical Optics (In Press)**, 2010
252. Sarkar, C., Karak, A. K., Nath, N., Sharma, M. C., Mahapatra, A. K., Chattopadhyay, P., Sinha, S.: Apoptosis and proliferation: correlation with p53 in astrocytic tumours. **J Neurooncol** **73**:93-100, 2005
253. McKeever, P. E.: Insights about brain tumors gained through immunohistochemistry and in situ hybridization of nuclear and phenotypic markers. **J Histochem Cytochem** **46**:585-594, 1998
254. Etienne, M. C., Formento, J. L., Lebrun-Frenay, C., Gioanni, J., Chatel, M., Paquis, P., Bernard, C., Courdi, A., Bensadoun, R. J., Pignol, J. P., Francoual, M., Grellier, P., Frenay, M., Milano, G.: Epidermal growth factor receptor and labeling index are independent prognostic factors in glial tumor outcome. **Clin Cancer Res** **4**:2383-2390, 1998
255. Preusser, M., Heinzl, H., Gelpi, E., Hoftberger, R., Fischer, I., Pipp, I., Milenkovic, I., Wohrer, A., Popovici, F., Wolfsberger, S., Hainfellner, J. A.: Ki67 index in intracranial ependymoma: a promising histopathological candidate biomarker. **Histopathology** **53**:39-47, 2008

256. Higano, S., Yun, X., Kumabe, T., Watanabe, M., Mugikura, S., Umetsu, A., Sato, A., Yamada, T., Takahashi, S.: Malignant astrocytic tumors: clinical importance of apparent diffusion coefficient in prediction of grade and prognosis. **Radiology** **241**:839-846, 2006
257. Fitzmaurice, G. M., Laird, N. M., Ware, J. H.: **Applied Longitudinal Analysis**. Hoboken, NJ : John Wiley & Sons, 2004
258. Wyld, L., Burn, J. L., Reed, M. W., Brown, N. J.: Factors affecting aminolaevulinic acid-induced generation of protoporphyrin IX. **Br J Cancer** **76**:705-712, 1997
259. Valdes, P. A., Samkoe, K., O'Hara, J. A., Roberts, D. W., Paulsen, K. D., Pogue, B. W.: Deferoxamine iron chelation increases delta-aminolevulinic acid induced protoporphyrin IX in xenograft glioma model. **Photochem Photobiol** **86**:471-475, 2010
260. Zuber, P., Hamou, M. F., de Tribolet, N.: Identification of proliferating cells in human gliomas using the monoclonal antibody Ki-67. **Neurosurgery** **22**:364-368, 1988
261. Coons, S. W., Johnson, P. C.: Regional heterogeneity in the proliferative activity of human gliomas as measured by the Ki-67 labeling index. **J Neuropathol Exp Neurol** **52**:609-618, 1993
262. McKeever, P. E., Strawderman, M. S., Yamini, B., Mikhail, A. A., Blaivas, M.: MIB-1 proliferation index predicts survival among patients with grade II astrocytoma. **J Neuropathol Exp Neurol** **57**:931-936, 1998

263. Sallinen, P. K., Haapasalo, H. K., Visakorpi, T., Helen, P. T., Rantala, I. S., Isola, J. J., Helin, H. J.: Prognostication of astrocytoma patient survival by Ki-67 (MIB-1), PCNA, and S-phase fraction using archival paraffin-embedded samples. **J Pathol** **174**:275-282, 1994
264. Kennedy, J. C., Pottier, R. H.: Endogenous protoporphyrin IX, a clinically useful photosensitizer for photodynamic therapy. **J Photochem Photobiol B** **14**:275-292, 1992
265. Georgakoudi, I., Jacobson, B. C., Muller, M. G., Sheets, E. E., Badizadegan, K., Carr-Locke, D. L., Crum, C. P., Boone, C. W., Dasari, R. R., Van Dam, J., Feld, M. S.: NAD(P)H and collagen as in vivo quantitative fluorescent biomarkers of epithelial precancerous changes. **Cancer Res** **62**:682-687, 2002
266. Hawkes, D. J.: Algorithms for radiological image registration and their clinical application. **J Anat** **193 (Pt 3)**:347-361, 1998
267. Pluim, J. P., Maintz, J. B., Viergever, M. A.: Mutual-information-based registration of medical images: a survey. **IEEE Trans Med Imaging** **22**:986-1004, 2003